UNIVERSITY OF CALIFORNIA SAN DIEGO

Electron vortices subject to imposed strain flows

A Dissertation submitted in partial satisfaction of the
requirements for the degree
Doctor of Philosophy

in

Physics

by

Noah Carlson Hurst

Committee in charge:

Professor Clifford M. Surko, Chair
Professor C. Fred Driscoll
Professor Daniel H. E. Dubin
Professor Stefan G. Llewellyn-Smith
Professor George R. Tynan
Professor William R. Young

2018

The Dissertation of Noah Carlson Hurst is approved, and it is acceptable in quality and form for publication on microfilm and electronically:

_____

_____

_____

_____

_____

_____

Chair

University of California, San Diego

2018

DEDICATION

To my parents, Mike and Caryn, for teaching me to be curious and creative.

EPIGRAPH

Many times I've wondered how much there is to know

— Robert Plant

TABLE OF CONTENTS

Signature Page iii

Dedication iv

Epigraph v

Table of Contents vi

List of Figures ix

List of Tables xii

Acknowledgements xiii

Vita xvi

Abstract of the Dissertation xviii

Chapter 1 Introduction 1
1.1 Vorticity and strain in a 2D ideal fluid 1
1.2 Electron plasmas as 2D fluids 7
1.3 An electron plasma experiment to study vortex dynamics in strain flows 10
1.4 Other examples of nearly ideal 2D fluids 12
1.5 Related work on strained vortices and electron plasma fluids 15
1.6 Outline of the dissertation 21

Chapter 2 Experimental procedures 22
2.1 The plasma/fluid analogy 22
2.2 Experimental apparatus 26
2.3 External flow properties 31
2.4 Run sequence 35
2.5 Data analysis 38
2.6 Calibration 41
2.7 Non-fluid behavior 47
2.8 Vortex-in-cell simulations 50

Chapter 3 Theoretical description of vortices in strain flows 54
3.1 Introduction 54
3.2 The elliptical patch model 57
3.2.1 The K81 system under constant strain 59
3.2.2 The K81 system under time-dependent strain 68

3.2.3 Instabilities . . . 72
3.3 Vortex dynamics beyond the patch model . . . 76
3.3.1 Overview of methodology . . . 76
3.3.2 The Okubo-Weiss criterion . . . 79
3.3.3 A few examples . . . 80

Chapter 4 Experiments with constant strain flows . . . 86
4.1 Tests of the elliptical patch model . . . 86
4.1.1 K81 orbits . . . 87
4.1.2 MS71 equilibria . . . 91
4.1.3 Stability threshold measurements . . . 92
4.2 Physics beyond the elliptical patch model . . . 94
4.2.1 The stream function separatrix and the Okubo-Weiss criterion . . . 94
4.2.2 Shifted stability limits . . . 98
4.2.3 Stripping of peripheral circulation . . . 100
4.2.4 Inviscid damping of K81 orbits . . . 102

Chapter 5 Experiments with time-dependent strain flows . . . 106
5.1 Introduction . . . 106
5.2 Square pulses . . . 110
5.3 Double square pulse . . . 116
5.4 Gaussian pulses . . . 117
5.5 Sinusoidal strain . . . 121

Chapter 6 Summary and conclusions . . . 126
6.1 Recap of the strained vortex problem . . . 126
6.2 Summary of experimental data and results . . . 128
6.2.1 Development of an apparatus for strained vortex experiments . . . 128
6.2.2 Experiments with quasi-flat profiles . . . 129
6.2.3 Experiments with smooth profiles . . . 130
6.2.4 Experiments with time-dependent strain . . . 131
6.3 Implications for other quasi-2D fluid systems . . . 133
6.4 Ideas for future experiments . . . 136

Appendix A Experiments with the multi-cell trap . . . 139
A.1 Introduction . . . 139
A.2 Plasma pinning during the fill process . . . 144
A.3 Cell-to-cell transfer . . . 150
A.4 Autoresonant plasma positioning . . . 156
A.5 Bounce-average orbits . . . 161
A.6 Trapped off-axis plasmas . . . 166

A.7 High-voltage experiments 168
A.8 Vortex destruction in the MCT 175
A.9 Summary and Conclusions 177

Appendix B List of mathematical symbols 181

Bibliography 188

LIST OF FIGURES

Figure 1.1: Example of a 2D fluid in a circular container which is organized into many discrete vortex structures. 5
Figure 1.2: Cartoon of vorticity and strain. 6
Figure 1.3: An example of electron fluid data for vortices under strain. 11

Figure 2.1: Cartoon of electron motion in a Penning-Malmberg trap. 23
Figure 2.2: Schematic diagram of 8ST apparatus in the (y,z) plane. 28
Figure 2.3: Models and photographs of the 8ST apparatus. 29
Figure 2.4: Choices of boundary conditions for electrode II, and the corresponding external flow field. 32
Figure 2.5: Serial steps in the experimental procedure, shown as voltage traces on the 8ST electrodes. 37
Figure 2.6: Demonstration of RW vorticity profile conditioning. 38
Figure 2.7: Analysis of a CCD image. 40
Figure 2.8: Examples of initial vorticity profiles obtained using the RW technique. 41
Figure 2.9: Demonstration of the elliptical fitting routine, for two different instances of vorticity data (a) and (b). 42
Figure 2.10: Spatial calibration of the CCD diagnostic. 43
Figure 2.11: Vorticity calibration process. 43
Figure 2.12: Strain calibration process. 45
Figure 2.13: Photograph of the segments of electrode II. 47
Figure 2.14: A quasi-flat initial vorticity profile (solid), and the same profile after 10 s of free relaxation in the absence of strain (dashed). 51
Figure 2.15: Demonstration of electron re-entry after a straining event. 51
Figure 2.16: Vortex-in-cell simulations of a quasi-flat vortex subject to applied strain. 53

Figure 3.1: Geometry of an elliptical vortex in a background simple strain flow. 58
Figure 3.2: Contours of the K81 Hamiltonian (Eq. 3.9) in polar $(\lambda \geq 1, \xi)$ space. 62
Figure 3.3: Contours of the K81 Hamiltonian (Eq. 3.11) in polar (p,q) space. . 63
Figure 3.4: Contours of the K81 Hamiltonian (Eq. 3.9) in polar $(\lambda - 1, q)$ space. 64
Figure 3.5: Color maps of the K81 Hamiltonian H (Eq. 3.9) in polar $(\lambda - 1, q)$ space. 65
Figure 3.6: Fixed points of the K81 system and maximum aspect ratio curves. . 67
Figure 3.7: Temporal behavior of K81 orbits with circular initial condition. . . 69
Figure 3.8: Temporal behavior of open (unstable) K81 orbits with circular initial condition. 70
Figure 3.9: Response of the K81 system to an external strain which is ramped up linearly in time. 73
Figure 3.10: Response of the K81 system to an external strain with Gaussian time dependence. 74

Figure 3.11: Normalized squared growth rates versus λ for (a) Love instabilities, and (b) MS71 instabilities. 77
Figure 3.12: Normalized squared growth rates versus normalized wavenumber $2bk$ for the KH instability on a strip of piecewise constant vorticity. . . . 78
Figure 3.13: Examples of theoretical vorticity profiles. 81
Figure 3.14: Flow geometry for a circular vortex patch (left) and a parabolic vorticity distribution (right). 83

Figure 4.1: Comparison of experimental data and K81 predictions for dynamical orbits in $(\lambda, 2\xi)$ space. 87
Figure 4.2: Comparison of experimental data and K81 predictions for $\lambda(t^*)$ and $\xi(t^*)$. 88
Figure 4.3: Dynamics of unstable elliptical vortices above the critical strain threshold. 90
Figure 4.4: Demonstration of MS71 strained vortex equilibria. 91
Figure 4.5: Stability threshold measurements versus peak vorticity. 92
Figure 4.6: Evolution of the vorticity distribution, stream function, and Okubo-Weiss criterion. 95
Figure 4.7: Local stability inside a vortex versus time. 97
Figure 4.8: Dynamical stability threshold $\varepsilon_d^*(C=1)$ for constant strain versus smoothness exponent α. 99
Figure 4.9: Experimental evolution of vorticity (color maps) and stream function (lines) for (a) a Gaussian profile, and (b) a quasi-flat profile with $\alpha \approx 8$. 100
Figure 4.10: Fraction of the circulation remaining in a vortex after a straining event. 101
Figure 4.11: Evidence of inviscid damping of K81 orbits in $(\lambda, 2\xi)$ space. 103
Figure 4.12: Vorticity (color maps) and stream function (black lines) evolution during inviscid damping of the K81 orbit. 104

Figure 5.1: Various time dependencies of the applied strain flow. 109
Figure 5.2: Free relaxation of a stretched vortex with $\omega_0 = 440$ krad/s and initial aspect ratio $\lambda \approx 7.5$. 111
Figure 5.3: Free relaxation of a stretched vortex with $\omega_0 = 440$ krad/s and initial aspect ratio $\lambda \approx 11.5$. 112
Figure 5.4: Free relaxation of vorticity filaments for $\omega_0 = 440$ krad/s and filament half-thickness $b/r_w =$ (a) 0.036; (b) 0.014; (c) 0.007. 115
Figure 5.5: Number of daughter vortices N_d versus normalized filament half-thickness b/r_w, or aspect ratio λ. 116
Figure 5.6: The Kelvin-Helmholtz instability under applied strain. 118
Figure 5.7: Residual elliptical distortion of a vortex with $\omega_0 = 228$ krad/s following a Gaussian strain pulse of varying width. 120
Figure 5.8: Map of vortex response to a Gaussian strain pulse. 122
Figure 5.9: A vortex subjected to six periods of sinusoidal strain. 124
Figure 5.10: Cartoon of vortex behavior under periodic strain. 125

Figure A.1: Computer model (a) and photograph (b) of the MCT electrode structure. 141
Figure A.2: Schematic diagram of the MCT geometry and procedure. 143
Figure A.3: Schematic diagram of the plasma generation process. 145
Figure A.4: Data showing the de-pinning of the trapped electron population as its particle number increases. 147
Figure A.5: Contours of the beam-plasma Hamiltonian given by Eq. A.2. 149
Figure A.6: Schematic diagram of transferring plasma into an on-axis storage cell. 151
Figure A.7: Data showing the efficiency of transferring plasma into an on-axis storage cell, as a function of (a) time, and (b) voltage applied to the storage cell electrodes. 153
Figure A.8: Calculated plasma length plotted over vacuum electric potentials for the master cell (a) and a storage cell (b). 158
Figure A.9: Comparison of diocotron frequency data with a numerical model (solid) and an analytical one (dashed) in the master cell. 160
Figure A.10: Data and a simple model of bounce-average diocotron orbits for plasmas spanning the master and storage cells. 162
Figure A.11: Data for a bounce-average plasma located at the stationary point. . . 165
Figure A.12: Images of plasmas trapped in each of the storage cells (not simultaneously). 167
Figure A.13: Data showing the RW compression and free expansion of an off-axis plasma. 169
Figure A.14: Radial profiles of high-voltage plasmas during filling and relaxation. 171
Figure A.15: Evolution of the trapped particle number for high-voltage plasmas. . 172
Figure A.16: Images of the electron density distribution of high-voltage plasmas during the fill and relaxation periods. 174
Figure A.17: Stripping of a plasma in the MCT due to an applied asymmetric potential. 176

LIST OF TABLES

Table B.1: List of mathematical symbols and abbreviations. 181

ACKNOWLEDGEMENTS

First and foremost, I would like to acknowledge my thesis advisor Cliff Surko, and my de facto co-advisor James Danielson. It has been a great pleasure to work with these gentlemen. They have taught me so much over the years about physics and science, as well as politics, technology, history, and a wealth of other lunch table debate topics. I would also like to thank the other group members I have had the good fortune of working with, including Mike Natisin, Adric Jones, Chris Baker, Soumen Ghosh, and the late Gene Jerzewski (1940–2015). The Surko group suffered a great loss with Gene's passing. He was a kind, friendly, talented man whose laboratory expertise was unrivaled. I would also like to thank our secretaries Judy Winstead and Susan Marshall for their guidance with administrative matters.

A handful of other professors, researchers, and teachers have been integral to my graduate education here at UCSD. I would like to extend my gratitude to the professors serving on my committee, they have been very supportive and helpful in guiding my research. Particularly, I appreciate collaboration with Dan Dubin, who is a co-PI on our grant and a co-author on a few of our recent papers, and from Bill Young, who has generously reviewed our work and provided to us a bridge to the world of fluid dynamics. I also appreciate enlightening conversations with other professors outside of my committee, including Tom O'Neil, Pat Diamond, John McGreevy, and Rick Salmon.

None of this work would have been possible without the continued love and support from my wonderful family over the years. It was a great joy of mine to be able to visit

home frequently to see my parents Mike and Caryn, and my grandparents Genevieve and Richard. The Carlson family mourns the passing of my grandfather Richard Carlson (1928–2015). The closeness of our family reflects his love and dedication, and many of our various successes in life can be traced back to his hard-working attitude.

A big round of applause for all of my awesome friends in San Diego and elsewhere, my life in graduate school has been so much fun thanks to all of you. Special shout-outs to JonesCorp and the WonderDogs. Thank you so much to the beautiful Sarah Wise for everything, this last year has been amazing!

Some of the work and discussion in Chapter 2 is taken from N. C. Hurst, J. R. Danielson, and C. M. Surko, "An electron plasma experiment to study vortex dynamics subject to externally imposed flows," *AIP Conf. Proc.* **1928**, 020007 (2017). The author of the dissertation led the research and was the primary investigator and author of this paper.

Some of the work and discussion in Chapter 4 is taken from N. C. Hurst, J. R. Danielson, D. H. E. Dubin, and C. M. Surko, "Experimental study of the stability and dynamics of a two-dimensional ideal vortex under external strain," submitted to *J. Fluid Mech.* (2017), and from N. C. Hurst, J. R. Danielson, D. H. E. Dubin, and C. M. Surko, "Evolution of a vortex in a strain flow," *Phys. Rev. Lett.* **117**, 235001 (2016). The author of the dissertation led the research and was the primary investigator and author of these papers.

Some of the work and discussion in Appendix A is taken from N. C. Hurst, J. R. Danielson, C. J. Baker, and C. M. Surko, "Electron plasma orbits from competing diocotron drifts," *Phys. Rev. Lett.* **113**, 025004 (2014), and from N. C. Hurst, J. R. Danielson, C. J.

Baker, and C. M. Surko, "Finite-length, large-amplitude diocotron mode dynamics," *AIP Conf. Proc.* **1668**, 020003 (2015). The author of the dissertation led the research and was the primary investigator and author of these papers.

Finally, I would like to acknowledge our funding sources. Early stages of the vortex dynamics experiments were supported by funds from the UCSD Foundation. Following that, the plasma partership grant No. DE-SC0016532 from the Department of Energy has supported these experiments for the last couple of years. I also acknowledge support from the U.S. Defense Threat Reduction Agency, which has funded our experiments with the multi-cell trap.

VITA

2011	B.S. in Engineering Mechanics & Astronautics, Physics, and Astronomy, University of Wisconsin Madison
2011	Teaching Assistant, University of California San Diego
2012-2018	Research Assistant, University of California San Diego
2013	M.S. in Physics, University of California San Diego
2015	C.Phil. in Physics, University of California San Diego
2018	Ph.D. in Physics, University of California San Diego

PUBLICATIONS

N. C. Hurst, J. R. Danielson, D. H. E. Dubin, and C. M. Surko,"Experimental study of the stability and dynamics of a two-dimensional ideal vortex under external strain," submitted to *J. Fluid Mech.* (2018)

N. C. Hurst, J. R. Danielson, and C. M. Surko, "An electron plasma experiment to study vortex dynamics subject to externally imposed flows," *AIP Conf. Proc.* **1928**, 020007 (2018)

N. C. Hurst, J. R. Danielson, D. H. E. Dubin, and C. M. Surko, "Evolution of a vortex in a strain flow," *Phys. Rev. Lett.* **117**, 235001 (2016)

N. C. Hurst, J. R. Danielson, C. J. Baker, and C. M. Surko, "Finite-length, large-amplitude diocotron mode dynamics," *AIP Conf. Proc.* **1668**, 020003 (2015)

N. C. Hurst, J. R. Danielson, and C. M. Surko, "Magnetic field extraction of trap-based electron beams using a high-permeability grid," *Phys. Plasmas* **22**, 073503 (2015)

C. J. Baker, J. R. Danielson, N. C. Hurst, and C. M. Surko, "Electron plasma dynamics during autoresonant excitation of the diocotron mode," *Phys. Plasmas* **22**, 022302 (2015)

N. C. Hurst, J. R. Danielson, C. J. Baker, and C. M. Surko, "Electron plasma orbits from competing diocotron drifts," *Phys. Rev. Lett.* **113**, 025004 (2014)

J. R. Danielson, N. C. Hurst, and C. M. Surko, "Progress towards a practical multicell positron trap," *AIP Conf. Proc.* **1521**, 101 (2013)

M. R. Natisin, N. C. Hurst, J. R. Danielson, and C. M. Surko, "Recent progress in tailoring trap-based positron beams," *AIP Conf. Proc.* **1521**, 154 (2013)

W. S. Harris, D. J. Den Hartog, and N. C. Hurst, "Initial operation of a pulse-burst laser system for high-repetition-rate Thomson scattering," *Rev. Sci. Instrum.* **81**, 10D505 (2010)

E. Parke, D. J. Den Hartog, L. A. Morton, H. D. Stephens, C. P. Kasten, J. A. Reusch, W. S. Harris, M. T. Borchardt, A. F. Falkowski, N. C. Hurst, A. Plunkett, and J. Goglio, "Improvements to the calibration of the MST Thomson scattering diagnostic," *Rev. Sci. Instrum.* **83**, 10E324 (2012)

N. C. Hurst & S. S. Harilal, "Pulse shaping of transversely excited atmospheric CO2 laser using a simple plasma shutter," *Rev. Sci. Instrum.* **80**, 035101 (2009)

ABSTRACT OF THE DISSERTATION

Electron vortices subject to imposed strain flows

by

Noah Carlson Hurst

Doctor of Philosophy in Physics

University of California, San Diego, 2018

Professor Clifford M. Surko, Chair

The stability and dynamics of two-dimensional (2D) ideal fluid vortices are studied under the influence of externally imposed irrotational strain flows. Laboratory experiments are conducted using pure electron plasmas. This is made possible by the isomorphism between the Drift-Poisson equations describing the dynamics of a single-component plasma perpendicular to the magnetic field and the 2D Euler equations describing inviscid, incompressible (ideal) fluids. Here, electron density is the analog of vorticity in a neutral fluid. The experimental apparatus used in this work was designed specifically to study vortex

dynamics under the influence of external flows. It features a long, cylindrical electrode spanning the length of the plasma which is divided into eight azimuthal segments that can be electrically biased. Advantages of using electron plasmas to study 2D ideal fluid dynamics are that the system is dissipationless over many vortex rotation periods, the vorticity can be diagnosed directly, and the initial vorticity profile and boundary conditions can be precisely controlled. Quasi-flat, axisymmetric vorticity profiles are prepared and subjected to external strain. The results are in quantitative agreement with a dynamical theory assuming the vorticity is piecewise-constant inside an elliptical boundary. Dynamical oscillations of the ellipses are observed, as well as stationary modes, and stretching modes that lead to vortex destruction. When non-flat (e.g., Gaussian) radial vorticity profiles are used, the vortices suffer loss of outer circulation, the stability threshold for vortex destruction is lowered, and the dynamical orbits undergo inviscid damping, thus driving the system toward a stationary elliptical state. Preliminary experiments are also described in which the strength of the strain flow was varied in time. The relationship of these results to other theoretical, experimental, and numerical work is discussed, as are prospects for future research studying the dynamics of electron vortices in strain and shear flows.

Chapter 1

Introduction

1.1 Vorticity and strain in a 2D ideal fluid

Throughout history, humans have been intrigued by the motion of fluids [1]. There is a unique visual appeal to the intricate patterns and structures which emerge in the air and water around us. Few other natural systems are so ubiquitous in our everyday lives yet so difficult to analyze scientifically. In many cases, both the beauty and the challenge of fluid dynamics are due to the advective nonlinearity – a term arising in the fluid equations which describes self-transport of the fluid velocity field. It is this nonlinearity which gives rise to structure formation, self-organization, and turbulence in a fluid.

However, no natural structure or pattern is permanent; due to the second law of thermodynamics, the captivating features of a fluid flow are removed over time in favor of homogeneity. Dissipation in a fluid is described at the simplest level by viscosity. Although we often think of fluids as continuous systems, they are typically aggregates of

many discrete microscopic particles (i.e., atoms or molecules). Viscosity is an approximate description of the friction arising from collisions between these particles, which converts kinetic energy of the flow into thermal energy at small scales.

Viscous fluids are described by the Navier-Stokes equations, where the viscosity appears as a diffusion term acting on the fluid velocity field. When the fluid velocity $\mathbf{v}$ is small compared to the sound speed, the fluid is said to be incompressible, meaning that the fluid density ρ is a constant and the divergence of the velocity field $\nabla \cdot \mathbf{v}$ is zero. In this case, the Navier-Stokes equations are given by

$$(\partial_t + \mathbf{v} \cdot \nabla)\mathbf{v} = -\rho^{-1}\nabla p + \nu\nabla^2\mathbf{v}, \tag{1.1}$$

where p is the fluid pressure, ν is the kinematic viscosity, and the second term is the advective nonlinearity. Therefore, the nonlinearity, which tends to generate structure in a fluid, is in direct competition with the viscosity, which tends to dissipate structure. This competition is quantified by the Reynolds number *Re*, which is defined as the ratio of the nonlinear term to the viscous term in Eq. 1.1. If the viscosity is sufficiently weak, then *Re* is large and the nonlinearity is dominant. Although the second law still holds true, on short timescales the fluid behaves as if the viscosity were inactive. Such a system is called an inviscid fluid.

The differential equations describing inviscid fluid flow were first published in 1757 by Leohnard Euler (1707-1783) [2]. The so-called "Euler equations" are identical to the incompressible Navier-Stokes equations (Eq. 1.1) with the viscosity set to zero. Since they are dissipationless, Euler fluids conserve total energy. Furthermore, the specific internal energy is locally conserved along streamlines, and so thermal forces and sound waves are

absent [3]. Euler fluids are the simplest fluid system featuring the advective nonlinearity, therefore they represent an excellent laboratory for nonlinear fluid physics including self-organization and turbulence. This dissertation focuses on the dynamics of an inviscid, incompressible fluid (called an ideal or perfect fluid) as described by the Euler equations, although the effects of viscosity are discussed briefly.

Euler originally formulated his ideal fluid equations in three spatial dimensions (3D). However, in certain fluid systems, flows can be regarded as two-dimensional (2D), and so many authors have studied the 2D Euler equations [4]. For example, a shallow layer of fluid in a flat container under the influence of gravity moves primarily along the bottom surface, and the motion of the fluid normal to the boundary is negligible. Such is the case for the large-scale dynamics of the atmospheres and oceans of Earth and other planets, as well as a variety of other important fluid systems. The scope of this dissertation is narrowed further to the dynamics of 2D ideal fluids.

It was recognized early on by Lagrange, Helmholtz, Lord Kelvin, and others, that rotation plays a key role in the dynamics of inviscid fluids [1]. Fluid rotation is quantified locally by the vorticity, which is the curl of the velocity field, $\omega = \nabla \times \mathbf{v}$. In 2D, the fluid velocity is confined to a plane $\mathbf{v} = \mathbf{v}(x,y)$ and so the vorticity is a scalar field where the direction of rotation is normal to the flow, $\omega = \omega\hat{\mathbf{z}}$. By taking the curl of Eq. 1.1 with $\nu = 0$, the 2D Euler equations can be written in terms of the vorticity and the stream function ψ,

$$(\partial_t - \nabla\psi \times \hat{\mathbf{z}} \cdot \nabla)\omega = 0;\ \nabla^2\psi = \omega, \tag{1.2}$$

where ψ is a scalar field related to the velocity by $\mathbf{v} = -\nabla\psi \times \hat{\mathbf{z}}$. Thus the flow advects

the vorticity, which is locally conserved in the Lagrangian frame (i.e., ω is a constant in a frame moving with the flow). The entire flow field at an instant is specified by the vorticity distribution and boundary conditions through the Poisson equation.

It has been observed that 2D inviscid fluids tend to organize themselves such that the vorticity is localized to discrete clumps [5]. These clumps of vorticity are known generally as *vortices* (singular *vortex*). They are isolated, coherent regions of the flow where the fluid is locally rotating. Figure 1.1 shows an example of a vorticity distribution for a 2D fluid with a few isolated vortices. Well-known examples of vortex-like structures include hurricanes, tornadoes, whirlpools (for example, the Maelstrom or the bathtub vortex [6]), Earth's polar vortices [7], and wingtip vortices generated by aircraft [8], although in many of these cases 3D effects play a role.

In accordance with the observations, both the Euler equations and the Navier-Stokes equations are known to have vortex solutions [9]. For a 2D ideal fluid, the Euler equations are solved exactly by the so-called vortex patch distribution, where the vorticity is piece-wise constant within a bounded area (for example, the Rankine vortex or the Kirchoff vortex). For a 2D viscous fluid, the Navier-Stokes equations are solved exactly by the Lamb-Oseen vortex solution, where the vorticity has a Gaussian spatial distribution which spreads over time. Since natural fluids exist in a wide range from viscous to approximately inviscid, one might expect a spectrum of vortex profiles ranging from smooth, Gaussian distributions to flat, patch-like distributions.

In addition to rotational motion, 2D fluids can also undergo stretching in the plane perpendicular to ω, as depicted in Fig. 1.2. These are the two most basic types of fluid

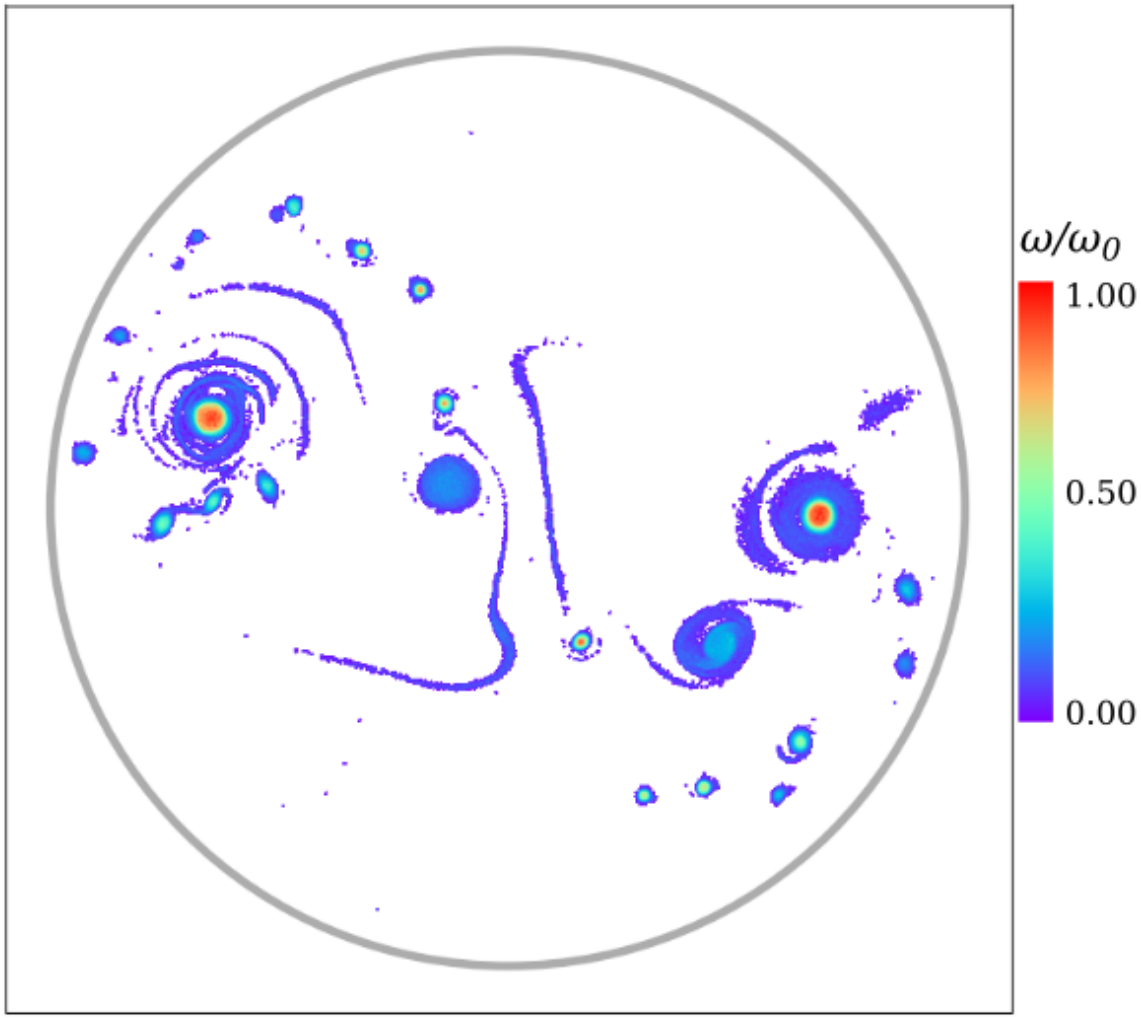

Figure 1.1: Example of a 2D fluid in a circular container which is organized into many discrete vortex structures. The colormap corresponds to the vorticity ω, normalized to its maximum value ω_0. The data were obtained using an electron fluid; a detailed description of this technique is given in Chapter 2.

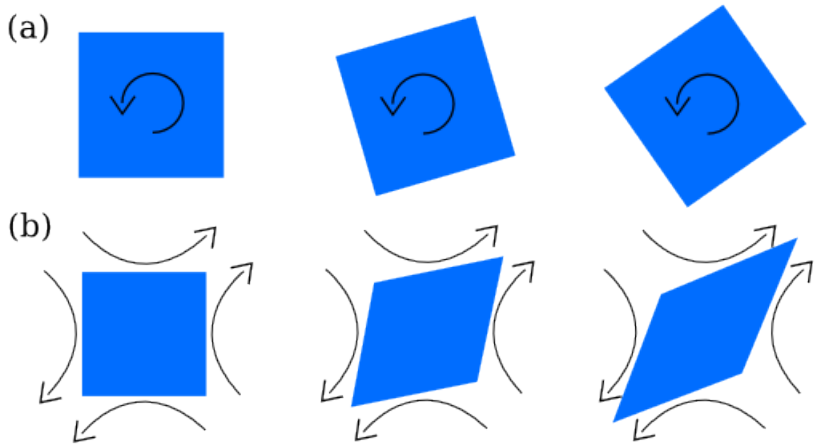

Figure 1.2: Cartoon of vorticity and strain. Vorticity (a) corresponds to a rigid rotation of a fluid element, whereas strain (b) corresponds to deformation.

motion (other than the trivial case of uniform flow). While rotation is quantified by the vorticity, stretching is described by a quantity called strain[1]. Strain and vorticity are mathematical counterparts, being associated with the symmetric and antisymmetric parts of the velocity gradient tensor, respectively. Strain flows are hyperbolic and incoherent, whereas vortical flows are elliptical and periodic. Thus, the local dynamics at any point in a fluid can be understood as a competition between these two basic motions, parameterized by the ratio of strain to vorticity. Generally, regions of strain flow are created by the long-range influence of vortices and/or boundary conditions (both of which source flow *via* the Poisson equation), where the influence of the sources decreases gradually with distance.

Consider the case of a fluid vortex within a more complicated 2D flow. If the vortex is well isolated (i.e., significantly separated from other comparable sources), then it is in a region of weak strain. In this case, it is well known that vortices tend towards axisymmetry

[1] Although strain and vorticity are discussed here in the context of 2D fluids, these concepts are perfectly valid in 3D as well.

[5, 10]. However, when the vortex approaches another vortex or a boundary, it experiences an externally imposed strain flow which can cause deformations (for example, see Fig. 1.1). In some cases, the vortex can be partially or totally destroyed during an encounter. Upon destruction, the circulation within the vortex loses coherence, succumbing to whatever flow pattern exists around it. ***Vortex deformation and destruction events in a 2D ideal fluid are precisely the subject of this dissertation.***

1.2 Electron plasmas as 2D fluids

It is well known that many types of strongly magnetized plasmas exhibit quasi-2D fluid-like drift dynamics perpendicular to the magnetic field [11, 12]. Two-dimensional fluid behavior is observed in toroidal quasineutral plasmas for magnetized fusion experiments [13], as well as in cyclotrons, accelerators, etc. [14, 15]. For certain types of confined non-neutral plasma, the analogy is rigorous, and the perpendicular dynamics of the plasma are identical to those of a 2D ideal fluid [16, 17]. A common non-neutral plasma confinement device for fluid studies is the Penning-Malmberg (PM) trap [18]. It is a device with cylindrical geometry, where electrons are confined axially by applied electrostatic potentials and radially by a strong applied magnetic field. In the plane perpendicular to the magnetic field, the plasma obeys guiding-center $\mathbf{E} \times \mathbf{B}$ drift dynamics [19], where $\mathbf{E}$ and $\mathbf{B}$ are the electric and magnetic fields. Here, the electrons perform miniscule, high-frequency gyro-orbits, and the macroscopic motion in the plane perpendicular to the magnetic field is given by the drift velocity, $\mathbf{v} = B^{-1}\, \mathbf{E} \times \hat{\mathbf{z}}$. The electron distribution is self-advected by its

own electric field, just as the velocity in a fluid is self-advected.

The electron plasma typically forms a cylindrical column. It generates a radial electric field which causes it to rotate azimuthally about its axis, as would a fluid vortex. Electron motion parallel to the field consists of rapid bounce motion which is decoupled from the slower cross-field drift dynamics. In the absence of dissipation (collisions, viscosity, etc.) the drift dynamics of the electron plasma are given by the 2D Euler equations, Eq. 1.2 [17]. Here, the electron density behaves as the vorticity, and the electric potential as the fluid stream function. Vortical flows are generated in such a device by injecting electrons; irrotational strain flows can be generated by manipulating the boundary electric potential. ***In this dissertation, electron plasmas in a PM trap are studied in the laboratory in order to understand the dynamics of fluid vortices in response to externally imposed strain flows.*** Further details of the analogy between electron plasmas and fluid vortices are given in Chapter 2, including a schematic diagram of electron motion in a PM trap.

Electron plasmas offer distinct advantages over traditional methods of experimentally studying 2D ideal fluid dynamics. Many aspects of 2D fluid physics have been studied in the laboratory using tanks of water, wind tunnels, and other similar devices. Here, flows can be generated by pumps or by moving boundaries; and they can be diagnosed using particle imaging velocimetry, other optical techniques [20], or pressure transducers, etc. However, ideal fluid behavior is quite difficult to realize using traditional fluids in the laboratory. Water or air features roughly the same kinematic viscosity ($\nu \sim 10^{-6}$ and 15×10^{-6} m^2/s at 20° C, respectively) in the laboratory as in the oceans and atmosphere, but the length scales differ by many orders of magnitude, and thus so does the Reynolds

number, which is defined as $Re = vL/\nu$ where v and L are characteristic velocity and length scales. For example, in laboratory water tanks $Re \sim 10^2$ [21], whereas for vortices in the oceans and atmosphere, Re can have values up to $\sim 10^6$ [22]. Therefore, viscous effects are typically present in traditional fluid experiments in the laboratory, whereas, to a good level of approximation the large-scale motion of geophysical fluids is inviscid.

Viscosity in an electron plasma is a complicated subject. In a neutral fluid, collisions between particles are simple in the sense that the particles interact only at short distances (roughly speaking, when the particles are in contact). On the other hand, charged particles such as electrons have long-range coulomb interactions due to the electric field, leading to a significant enhancement of the viscosity relative to neutral fluids [23]. The collisional behavior of a plasma can be further complicated by the presence of magnetic fields. Additionally, the viscosity in an electron plasma depends on the particle density (i.e., on the vorticity), and so its effect is somewhat different from that of a neutral fluid. Despite these subtleties, attempts to define an effective Reynolds number based on the outward electron transport rate yield $Re \sim 10^6$ (see Chapter 2 for details), due in part to the strong electric field which can generate drift velocities on the order $v \sim 1$ km/s. As such, these plasmas represent an excellent testbed for 2D inviscid fluid physics.

In contrast with traditional fluids, detailed control of the electron fluid is possible. The stream function at the boundary can be specified by applying an electrical bias to the conducting walls of the PM trap – as simple as just connecting a battery! By choosing the boundary conditions in this way, externally imposed electric fields are created which advect the electron density (i.e., the vorticity) *via* the $\mathbf{E} \times \mathbf{B}$ drift. In some cases, the response

of the plasma to these boundary conditions is well-known, and so a particular vorticity distribution can be selected in a repeatable manner [24, 25].

Additionally, 2D electron fluids can be diagnosed relatively simply and accurately. At some point during the evolution of the fluid, the electrons can be deconfined in the axial direction and accelerated onto a phosphor screen, and the resulting flourescent light imaged by a camera. This technique provides a destructive measurement of the 2D vorticity field (i.e., the electron density integrated over the axial direction). With a vorticity measurement and knowledge of the boundary conditions, the entire flow field at an instant is determined. Measurements can typically be repeated once every few seconds. By gathering many images at different times during the evolution, the complete spatial and temporal behavior of the electron fluid can be determined. Coarse diagnosis of the plasma *in situ* can also be accomplished by receiving electrical signals due to the electron motion [26].

1.3 An electron plasma experiment to study vortex dynamics in strain flows

In this dissertation, fluid experiments are presented using a PM trap device in which a long electrode surrounding the plasma is divided into eight equal azimuthal segments. This allows for the application of boundary conditions without introducing 3D effects that break the plasma/fluid analogy. In this way, the response of an electron plasma vortex to an external flow can be studied in detail.

An example of data obtained using this apparatus is shown in Fig. 1.3. Here, an

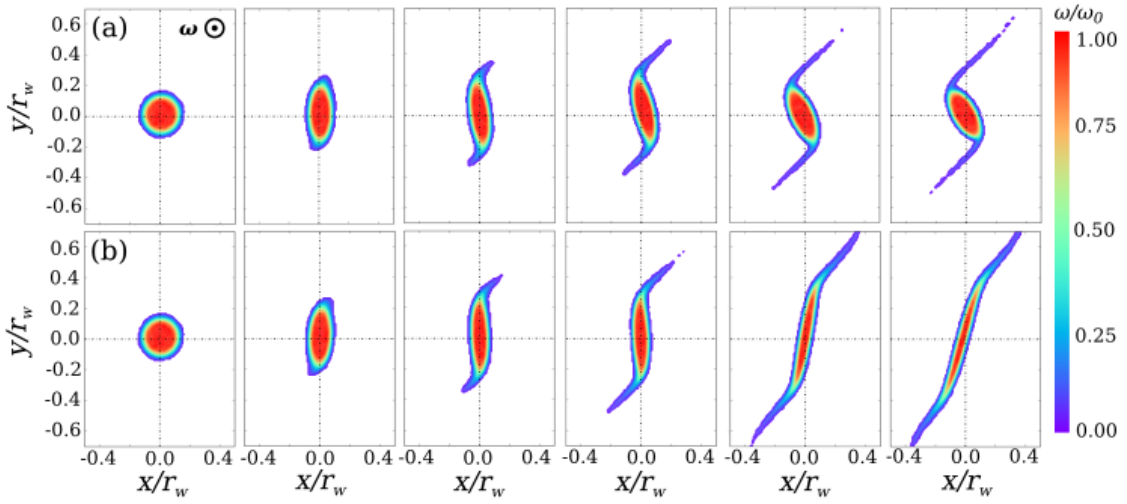

Figure 1.3: An example of electron fluid data for vortices under strain. Shown are vorticity measurements (colormap) in response to an applied strain flow at equal intervals over 100 μs ($22.8\omega_0^{-1}$), where the peak vorticity is $\omega_0 = 228$ krad/s, and the strain-to-vorticity ratio is $\varepsilon^* =$ (a) 0.116, and (b) 0.130. Spatial coordinates are scaled to the wall radius r_w.

initially axisymmetric, quasi-flat electron vortex is prepared, and subjected to a simple strain flow, where the stream function and velocity are given by

$$\psi = \frac{1}{2}\varepsilon(x^2 - y^2);\ \mathbf{v} = \varepsilon(y\hat{\mathbf{x}} + x\hat{\mathbf{y}}). \tag{1.3}$$

In Fig. 1.3 (a), the ratio of the external strain rate ε to the peak vorticity ω_0 is $\varepsilon/\omega_0 \equiv \varepsilon^* = 0.116$, where $\omega_0 = 228$ krad/s. Although small filaments of vorticity are stripped away from the vortex periphery by the strain, the core survives and continues to rotate. In row (b), $\varepsilon^* = 0.13$, and the strain is sufficiently strong that the vortex is destroyed (i.e., stretched into a thin filament aligned with the strain axis). These and other data are analyzed in Chapter 4, and details of the experimental technique are given in Chapter 2.

1.4 Other examples of nearly ideal 2D fluids

Inviscid fluids and 2D fluids do not strictly exist in nature; dissipation and 3D effects are always present at some level. However, the 2D Euler equations provide a simple, approximate description of many natural and man-made systems across a broad range of spatiotemporal scales [4]. Thus, beyond interest in the 2D Euler system from a purely academic perspective, it can also be used to understand the dynamics of real fluids and to make predictions of their behavior. As examples, approximate 2D vortices are commonly observed in geophysical fluids, strongly magnetized plasmas, astrophysical disks, and a variety of other flows in engineering and industrial settings.

In order to behave as a 2D system, the planar dynamics of a fluid must be sufficiently decoupled from the dynamics normal to the plane. This typically arises due to a separation of scales, where the wavelength of the planar motion is far removed from that of the normal dimension, and so the two do not interact significantly. For this to happen, the 3D translation symmetry of a fluid must be broken by some external influence. Common examples of symmetry-breaking agents include gravity, rotation, and magnetic fields.

In many geophysical and astrophysical scenarios, fluids are confined to a spherical shell by the force of gravity, leading to quasi-2D dynamics in the plane of the shell. For example, quasi-2D vortices form regularly in the oceans and atmospheres of Earth and other planets [27]. In this case, the characteristic scales of fluid motion on the shell can be much greater than those in the normal direction; in the Earth's atmosphere, the scales can be separated by a factor of $\sim 10^2$. Vortices in these systems provide an efficient means of

transporting heat, chemical species, and momentum across the surface of the globe; as such, they can have a profound impact on the planetary climate. The dynamics and stability of these vortex structures have broad implications for humanity, ranging from agriculture, to natural disasters, to navigation and transportation. Hurricanes and tornados are well-known examples of atmospheric vortices, however these objects are typically not well-described by the 2D Euler equations due to strong 3D or non-ideal effects. Quasi-2D fluids with spherical shell geometry are also known to occur in stellar systems; one example is the solar tachocline [28]. Interestingly, in the context of general relativity, recent theoretical work suggests the existence of a 2D fluid-like flows of spacetime near the event horizon of large black holes [29].

The Earth and many systems like it also feature rotation, and so the dynamics are altered relative to that of a pure 2D fluid due to the Coriolis acceleration. The resulting physics can be described approximately using the so-called "β-plane" model [30], which belongs to a wider class of quasi-2D fluids known generally as "potential vorticity" (PV) systems. Whereas the 2D Euler equations preserve the vorticity ω along streamlines (i.e., in the Lagrangian frame), these systems preserve a generalized quantity ζ called the PV. For example, fluid flow on a β-plane is described by a PV model in which $\zeta = \omega + \beta y$, where y is a spatial coordinate corresponding to the latitude, and β is a constant related to the rotation. Similar models have been used to describe magnetized plasmas [12] and astrophysical disks [31]. One ubiquitous feature of PV systems is the formation of so-called "zonal flows," or banded flow structures which are clearly seen, for example, in images of Jupiter.

Another interesting consequence of planetary rotation is the common occurence of polar vortices, which are rotational flow structures routinely observed at the poles of the Earth and other planets [27]. The stability and dynamics of these structures are thought to be of great importance to global weather patterns. The Earth's arctic polar vortex has a habit of periodically fragmenting due to large-amplitude distortions – these fragments are often advected southward, resulting in a blast of frigid air to the mid-latitudes. The antarctic polar vortex is quite stable in the winter, although a remarkable splitting event occurred in 2002 [7].

In some astrophysical systems, rotational effects can dominate over gravity, leading to the formation of disk-like structures which can also behave as quasi-2D fluids. Common examples of astrophysical disk geometry are protoplanetary or protostellar disks, as well as some types of galaxies [32], and accretion disks around compact objects (such as neutron stars or black holes). Many of these systems are characterized by a background Keplerian shear [33], as well as a fluid density which decreases with radius [31]. It is thought that vortices forming in these disks could be important for momentum transport [34] and planet formation [35].

Strong magnetic fields in a plasma cause anisotropy which can result in quasi-2D fluid behavior perpendicular to the field [11, 12]. In this case, motion parallel to the field is unimpeded and therefore rapid, while cross-field drift motion is slower, and so once again the separation of scales leads to a decoupling of the parallel and perpendicular dynamics. This phenomenology is applicable to a wide range of laboratory and astrophysical plasmas, including magnetically-confined plasmas with toroidal geometry for controlled nuclear fu-

sion (i.e., tokamaks, stellarators, and related devices). Efforts to achieve sustained fusion in laboratory plasmas have been frustrated by cross-field turbulent transport which carries heat, momentum, and particles out of the hot plasma core towards the wall of the confinement chamber, similar to the way 2D turbulent transport in a geophysical system causes mixing between the hot equatorial regions and cold polar regions. It is now accepted that the turbulent transport can be reduced by the formation of shear layers (i.e., zonal flows) which serve to decorrelate turbulent eddies [13, 36], similar to the vortex destruction process shown in Fig. 1.3 (b).

The stability and behavior of 2D vortices is also of importance in various engineering flows including, for example, airfoil wakes [8] and mixing processes [37]. Finally, it should be noted that the formation of vorticity filaments in response to strain [shown in Fig. 1.3 (b)] is a ubiquitous process in vortex dynamics; it is closely related to the forward enstrophy cascade familiar to 2D turbulence theory [4]. Therefore, the competition between vorticity and strain in a 2D fluid is applicable to a broad range of important topics, both academic and practical.

1.5 Related work on strained vortices and electron plasma fluids

The first investigations of deformed vortices took place in the late 19th century. In 1880, Lord Kelvin studied small-amplitude linear oscillations of a circular vortex patch (sometimes called a Rankine vortex), where the vorticity is a constant inside the patch

boundary and zero elsewhere. These modes are known as "Kelvin waves" (not to be confused with Kelvin waves in the geophysical context); they can be excited by weak external disturbances. Kirchoff, in his 1883 work *Mechanik*, generalized the Kelvin wave with azimuthal wave number $m = 2$ to arbitrarily large amplitude, providing an exact nonlinear vortex solution to the Euler equations. The Kirchoff vortex is a patch with elliptical shape, where the rotation rate decreases relative to the linear rate as the ellipticity increases. Thanks to Kirchoff, the "elliptical patch model" was born, variants of which have been studied in detail by many authors; it forms the theoretical basis for much of the work presented in this dissertation. Although the Kirchoff vortex is an exact solution, Love found in 1893 that perturbations to the elliptical patch could be unstable for sufficiently large ellipticity. Discussions of these early results are given in Refs. [9] and [38].

More recently, the elliptical patch model has been implemented by Moore and Saffman [8] and Kida [39] (henceforth MS71 and K81) in the presence of externally imposed strain flows. MS71 found stationary solutions for strained elliptical vortex patches, while K81 found dynamical solutions. Most importantly, MS71 showed that no stationary solutions exist when the ratio of the external strain rate to the patch vorticity exceeds a certain value, implying that vortices under conditions of strong strain must be unstable. K81 found that different types of dynamical solutions were possible depending on the initial conditions and the strain-to-vorticity ratio; these include nutational modes, rotational modes, stationary modes, and extensional modes. The nutating and rotating solutions correspond to stable periodic orbits in phase space. The stationary solutions are identical to those found by MS71, and so the MS71 work can be considered a limiting case of K81.

Finally, the extending solutions correspond to vortices which succumb to the external strain and lose stability; these vortices experience infinite stretching, where the aspect ratio of the ellipse increases without bound. Thus, the idea that sufficiently strong strain could effectively "destroy" a vortex was implied by the MS71 results, and shown rigorously by K81[2]. Soon thereafter, it was shown that the K81 model could be described as a limiting case of a Hamiltonian theory for many interacting vortex patches by truncating the patch distortions at wavenumber $m = 2$ [40].

Though the vortex patch model is relatively simple and manageable, its utility in describing realistic vortices is questionable, since the patch vorticity is discontinuous and therefore unphysical. On the other hand, theoretical analysis of a smooth vorticity distribution in the presence of external strain is a challenging task. While the K81 model is a dynamical system with two degrees of freedom (the ellipse aspect ratio and orientation), a smooth vorticity distribution, as described by the Euler equations, has infinite dimensionality (i.e., where the dynamical variables are the continuous spatial coordinates [41]). Progress has been made so far only in situations where the nonlinearity can be handled perturbatively. For example, in the limit of weak strain, distortions of the vortex are small and can be treated using an expansion about the axisymmetric distribution [42, 43, 44]. In the opposite limit, when the strain is large, the vorticity can be treated passively or perturbatively; this approach is closely related to a technique known as "rapid distortion theory" [45]. However, near the stability threshold of a strained vortex, the strain and vorticity

[2]Note that MS71 and K81 considered the more general case of both external shear and strain. In general, the behavior is qualitatively similar in each case, the key difference being that the shear can be either adverse or cooperative depending on its relative sign. This dissertation focuses primarily on the case of external strain.

are of comparable strength, and so these techniques are not appropriate. In this case, it is sometimes useful to consider the behavior of the system on short timescales. The simplest example is to consider only the initial flow field given by the initial vorticity distribution and the boundary conditions. On a more advanced level is the work of Okubo [46] and Weiss [47], in which spatial derivatives of the flow field are used to find short-term, approximate solutions for the evolution of the vorticity gradients. This technique has been used widely as a criterion to identify turbulent cascade activity in various fluids. It has also been extended by other authors to higher orders of approximation [48, 49], as well as to 3D flows [50].

Other approaches to studying smooth profiles involve truncating the Euler equations (i.e., considering lower-dimensional approximations). For example, one technique involves approximating a smooth vorticity profile with a series of nested contours of piecewise-constant vorticity. Here, analytical progress was made under the assumption that each contour remains elliptical [51, 52] (assumptions that, as we will see, are not necessarily justified). For nested vorticity contours of arbitrary shape, the dynamics of each contour are relatively simple to solve numerically. This approach is known as "contour dynamics," and it has been used extensively in the literature [53], since it is much less computationally expensive than solving the continuous Euler equations using other numerical methods. Contour dynamics simulations have been used to study vortex stripping events, or partial destruction events where outer low-vorticity contours are destabilized and pulled away by the strain [54], as well as total destruction events. One shortcoming of the contour dynamics method is that the contours can be heavily stretched and distorted such that the

numerical solution becomes stiff; in this case, an ad-hoc small-scale reconnection scheme known as "contour surgery" has been implemented [55].

Another way to truncate the Euler system is by using a point vortex approximation [56]. Here, a smooth vorticity distribution is represented by a distribution of N discrete point vortices, which is an $N-$dimensional Hamiltonian system. Although theoretical analysis shows that the dynamics can be chaotic for $N \geq 3$ [57], numerical solutions are quite tractable. When the stream function is discretized to a grid (further reducing the computational load), the numerical procedure is known as a "Vortex-In-Cell" (VIC) simulation [58], in analogy with the popular "particle-in-cell" codes frequently used in plasma physics.

Attempts to study strained vortices in the laboratory have relied heavily on experiments with water tanks [21, 59]. However, in these systems, viscosity plays an important role. Here, the Reynolds number is roughly $Re \sim 10^2$, and the fluid vortices are best described by the Lamb-Oseen model [9], where the vorticity profile is a Gaussian curve that decays over time. Although vortex stripping and destruction events were observed for sufficiently large values of shear or strain, quantitative comparison with the MS71 and K81 predictions was not possible due to viscous effects. Another interesting way to study 2D fluid physics is by using soap films where the fluid flow is confined to a planar geometry [60]. However, to our knowledge, no rigorous studies of vortex deformation and destruction have been conducted in this system.

It has long been known that magnetized plasmas behave as quasi-2D fluids under certain conditions [11, 12]. The analogy is closer yet for magnetized non-neutral plasmas [16], specifically when confined in a Penning-Malmberg trap geometry [17]. This analogy

has been exploited by many authors as a tool to study the dynamics of 2D ideal fluids in the laboratory. Electron plasmas have been used to study vortex merger events [61, 62, 63, 64]. The formation of vortex crystals from decaying turbulence was observed and studied using electron plasmas [65, 66, 67], and the stability of these crystals was studied in detail [68]. Further studies have focused on turbulent cascades in 2D [69, 70] and the guiding principles of 2D turbulence [71, 72]. Other aspects of 2D vortex dynamics which have been investigated using electron plasmas include vortex axisymmetrization (also known as "inviscid damping" or "spatial Landau damping") [44] and shear instabilities [73, 74].

The above electron plasma experiments all involved the free relaxation of some initial vorticity distribution (i.e., under symmetric boundary conditions). Other researchers have implemented asymmetric boundary conditions, including studies of non-axisymmetric equilibria [75, 76] and studies of cascading turbulence under external forcing [77]. However, in many of these studies the asymmetric potential was applied by a segmented electrode extending over only a portion of the plasma, and so 3D effects (namely, axial trapping of particles) may have been present. Most notable is the work of Eggleston [78], who studied the destruction of electron vortices under externally imposed irrotational shear by applying a radial electric field. Here, the vorticity profiles were roughly Gaussian, and the measured stability threshold was found to be in disagreement with theoretical predictions.

Despite the relatively large body of work on this subject, a rigorous quantitative test of the K81 system is lacking. Specifically, to our knowledge, the dynamical orbits predicted by K81 have not been previously studied in the laboratory. Additionally, key questions remain as to the effect of profile smoothness on the vortex dynamics.

1.6 Outline of the dissertation

The remainder of the dissertation is organized as follows. In Chapter 2, details of the experimental procedure are given, including a description of the apparatus, data analysis and calibration techniques, and further discussion of the plasma/fluid analogy. In Chapter 3, the theory of a vortex under strain is discussed, including the elliptical patch approach as well as theoretical efforts regarding smooth profiles. In Chapter 4, experimental data and numerical data from vortex-in-cell simulations are presented for the case of strain flows which are constant in time. In Chapter 5, preliminary experimental data is presented regarding time-dependent strain flows. In Chapter 6, the results are summarized and discussed, and conclusions are made. The dissertation also includes an appendix in which a series of other related electron plasma experiments that the author participated in are discussed, and a second appendix containing a dictionary of mathematical symbols.

Chapter 2

Experimental procedures

2.1 The plasma/fluid analogy

Non-neutral plasmas consisting only of electrons are routinely confined in a cylindrical geometry using a strong, constant axial magnetic field $\mathbf{B} = B\hat{\mathbf{z}}$ for radial confinement and electrostatic potentials $\phi(z)$ for axial confinement. This configuration is known as a Penning-Malmberg (PM) trap [79]. A schematic diagram of this type of apparatus is shown in Fig. 2.1. Confinement in these traps is sufficiently good that the electrons can reach a state of thermal equilibrium, described by a temperature T. In the presence of a strong magnetic field, the electrons perform small, high-frequency gyro-orbits perpendicular to the magnetic field with radius $r_g = m_e v_T/eB$ and frequency $f_g = eB/2\pi m$, where $v_T = (T/m_e)^{1/2}$ is the thermal velocity, and e and m_e are the electron charge and mass. Furthermore, when electric fields are present, the gyrating electrons drift perpendicular to $\mathbf{B}$ with velocity $\mathbf{v} = \mathbf{E} \times \mathbf{B}/B^2$ [19]. Electric fields are generated by the non-neutral plasma it-

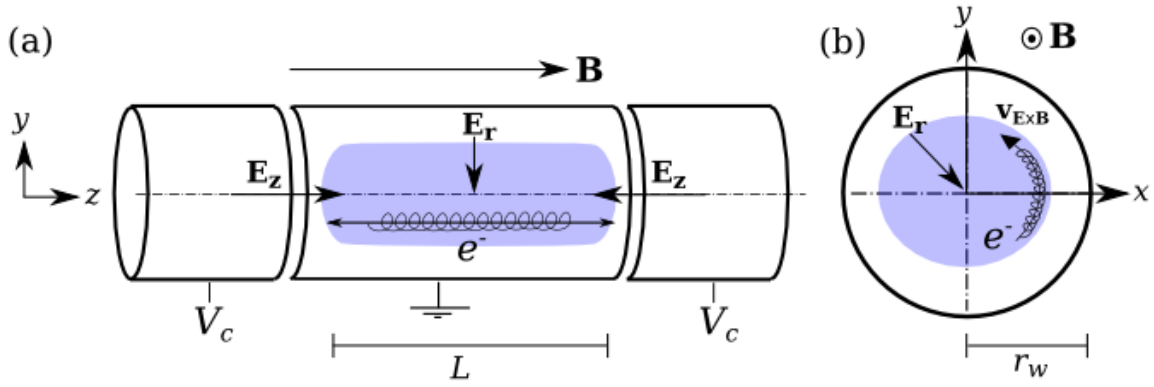

Figure 2.1: Cartoon of electron motion in a Penning-Malmberg trap. (a) (y,z) and (b) (x,y) views are shown, with axial confinement voltages V_c, axial and radial electric fields $\mathbf{E_z}$ and $\mathbf{E_r}$, and magnetic field $\mathbf{B}$. Electron trajectories are depicted, including the small-scale gyromotion, (a) axial bounce motion, and (b) perpendicular $\mathbf{E}\times\mathbf{B}$ drift motion.

self and by the boundary conditions *via* the Poisson equation, $\nabla^2\phi = en/\varepsilon_0$ (SI units), where ϕ is the electric potential, n is the electron density and ε_0 is the permittivity of free space. Often, the plasma density is axisymmetric and quasi-uniform within the plasma "vortex" radius r_v (c.f. Fig. 2.8), so the self electric field is radial, and the drift motion is azimuthal and periodic about the plasma centroid with frequency $f_v = en/4\pi B\varepsilon_0$ [80]. Parallel to the magnetic field, electrons bounce rapidly between the endcap confinement potentials at frequency $f_b = v_T/2L$, where L is the plasma length. The axial motion, perpendicular drift motion, and small-scale gyration of the electrons are depicted schematically in Fig. 2.1. Collisions between electrons occur at a rate per particle given roughly by $f_c \sim nv_T e^4/T^2$, although they are significantly more complicated than particle collisions in a neutral fluid [81].

When the magnetic field is large, the gyroradius is very small compared to the plasma radius ($r_g/r_v \ll 1$), and the gyrofrequency is large compared to the frequency of

the drift motion ($f_g/f_v \gg 1$) . Typically, the plasma temperature is high enough that the axial bounce frequency is large compared to the frequency scale of the perpendicular drift motion ($f_b/f_v \gg 1$). Additionally, PM traps are often designed so that the aspect ratio is large, i.e. $L/r_w \gg 1$ where r_w is the wall radius. In this way, 3D effects due to the end confinement fields are small, and so the dynamics are two-dimensional to a good degree of approximation. Furthermore, when the drift dynamics are rapid compared to collisional frequency scales ($f_c/f_v \ll 1$), a collisionless description is appropriate, and so the system is dissipationless. In summary, when the frequency scales are ordered as $f_g \gg f_b \gg f_v \gg f_c$ and spatial scales as $r_g \ll r_v < r_w \ll L$, the electrons behave as rigid line charges which move in 2D (i.e., in the plane perpendicular to $\mathbf{B}$) as point-like particles under dissipationless $\mathbf{E} \times \mathbf{B}$ drift dynamics.

In this regime, the thermal energy is small compared to the electrostatic energy, $e\phi/T \gg 1$, so the electron dynamics are described by the Hamiltonian

$$H = \frac{e}{L}\sum_{i=1}^{N} \phi_s(\mathbf{r_i}) + \left(\frac{e}{L}\right)^2 \sum_{i \neq j} G(\mathbf{r_i}, \mathbf{r_j}), \tag{2.1}$$

where ϕ_s is the potential associated with the applied boundary conditions, and $G(\mathbf{r_i}, \mathbf{r_j})$ is the Green's function for the Poisson equation in 2D [79]. If the electrons are all far away from the conducting boundary ($r_i/r_w \ll 1$), then image fields can be neglected, and the Green's function is logarithmic: $G(\mathbf{r_i}, \mathbf{r_j}) = \ln(|\mathbf{r_i} - \mathbf{r_j}|)$. The momentum of the electrons is dominated by the magnetic vector potential, and so the canonical coordinates for a given particle are (p_θ, θ), where $p_\theta = eBr^2/2L$ [75, 82]. Therefore, the electron drift dynamics are analogous to point vortex dynamics, where the electron charge per unit length corre-

sponds to the point vortex circulation [9, 41]. Since the PM trap confines only a single sign of charge, the corresponding vorticity also has a single sign, i.e. $\omega \geq 0$. In principle, both signs of vorticity could be studied by simultaneously confining electrons and positrons (i.e., anti-electrons), however in practice this is quite difficult to accomplish [80].

When the electron density is sufficiently large, a continuum description is appropriate, in the same way that 2D point vortex dynamics can be used to approximate the 2D Euler equations (Eqs. 1.2) [56]. In this case, the electron distribution is advected perpendicular to $\mathbf{B}$ by its own electric field *via* the $\mathbf{E} \times \mathbf{B}$ drift. These dynamics are given by the Drift-Poisson equations,

$$\left[\partial_t - \frac{1}{B}(\nabla\phi \times \hat{\mathbf{z}}) \cdot \nabla\right] n = 0; \; \nabla^2\phi = en/\varepsilon_0, \tag{2.2}$$

(SI units) where $n = n(x,y)$, $\phi = \phi(x,y)$, and the drift velocity is $\mathbf{v} = -\nabla\phi \times \hat{\mathbf{z}}/B$. Equations 2.2 are isomorphic to the 2D Euler equations (Eqs. 1.2) under the transformations $\phi/B \to \psi$ and $en/B\varepsilon_0 \to \omega$ [17]. Thus, the perpendicular drift motion of the electron plasma described by the Drift-Poisson equations is directly analogous to the motion of a 2D ideal fluid, with electric potential playing the role of the fluid stream function and electron density that of the fluid vorticity. Therefore, a collection of electrons (i.e., an electron plasma) will rotate coherently as a 2D fluid vortex.

This plasma/fluid analogy has been exploited to study the dynamics of 2D ideal fluids in a way inaccessible to traditional fluid experiments (i.e., using water or air). Advantages of this technique include simple diagnosis of the vorticity distribution, precise control over initial conditions and boundary conditions, weak dissipation, and slow radial

transport of the vorticity – remarkably, the electron vortices discussed here can be approximately static over 10^6 rotations (c.f. Fig. 2.14). Most prior work using this plasma/fluid analogy focused on the free relaxation of an initial vorticity distribution. However, when the electrical boundary conditions of the cylindrical confining electrodes are specified, an externally imposed, irrotational $\mathbf{E} \times \mathbf{B}$ flow can be created which advects the vorticity.

This chapter contains a description of an apparatus called the 8-Segment Trap (8ST) and the experimental procedures that have recently been developed to study ideal 2D fluid dynamics in the presence of externally imposed flows. A key feature of the apparatus is that the boundary conditions can be varied without violating the assumptions of the plasma/fluid analogy. It consists of a specially designed Penning-Malmberg trap for electron plasma confinement, where the boundary is divided into eight equal azimuthal segments that extend axially over the entire length of the plasma (i.e., as opposed to other PM devices where the segmented electrode extends axially only over a portion of the plasma). A report of the first results from this device can be found in Refs. [83, 84]. Discussed here are the experimental apparatus and operating procedure, data analysis and calibration procedures, and limitations of the plasma/fluid analogy.

2.2 Experimental apparatus

Figure 2.2 shows a schematic diagram of the 8ST apparatus. Shown are the electron source (A), cryopump (B), electrode structure (C), superconducting coils (D), and diagnostic equipment (E, F, G). The coils produce an axial magnetic field $B = 4.8$ T which is

approximately uniform over the electrodes (with variations $\delta B/B \sim 0.01$). The cryopump maintains a pressure of $\lesssim 10^{-9}$ torr inside the chamber. The electron source is a heated tungsten cathode located in the flaring field region where $B_z \approx 0.03$ T. It produces electron beams of width ~ 5 mm and currents ~ 1 μA. Electrodes I, III, and V are used for axial confinement; they are typically biased to $V_c = -100$ V. Electrode II is divided azimuthally into eight equal segments which can be independently biased; this is the region in which the fluid experiments take place. Electrode IV is divided azimuthally into four equal segments; these electrodes are used to control the plasma density (vorticity) profile *via* the Rotating Wall (RW) technique [80]. Pictures of the 8ST apparatus are shown in Fig. 2.3, including computer models as well as the actual device before and after gold-plating.[1]

The wall radius of the 8ST is $r_w = 13$ mm, the length of the entire electrode structure is 440 mm, and the length of electrode II is 260 mm. Typical plasma parameters are total electron number $N = 10^8 - 10^9$, peak electron density (in the center of the plasma) $n_0 = 10^{13} - 10^{15}$ m^{-3}, temperature $T \approx 0.1$ eV, and plasma radius $r_v = 1 - 5$ mm. In the 8ST, $f_g = 130$ GHz, $f_b \approx 1$ MHz, $f_v = 50 - 250$ kHz, $f_c \approx 3$ kHz, $r_g = 0.5\mu$m, $r_v = 0.1 - 10$ mm, $r_w = 13$ mm, $L \sim 240$ mm, and the areal density of the electrons is roughly $nL \sim 10^{13}$ m^{-2}. Thus, the separation of temporal and spatial scales discussed in Sec. 2.1 is satisfied, and so the plasma/fluid analogy is expected to be valid. However, it is important to be able to recognize non-fluid behavior if and when it occurs, so a discussion of plasma behavior when these conditions are violated is given in Sec. 2.7.

[1]The electrodes are gold-plated so that applied potentials can be uniform over the surfaces, since gold is mostly unreactive with background molecules in the vacuum system. In contrast, aluminum can form insulating oxide layers on its surface which can collect charge and create non-uniform potentials, thus affecting the plasma behavior.

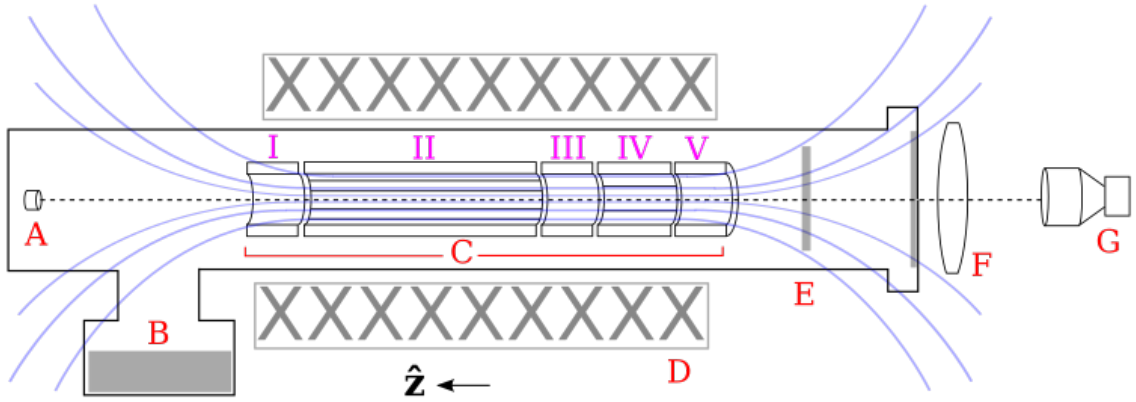

Figure 2.2: Schematic diagram of 8ST apparatus in the (y,z) plane. Shown are the electron source (A), cryopump (B), 8ST electrodes (C), magnet coils (D), phosphor screen (E), optical lens (F), and CCD camera (G). Magnetic field lines are shown schematically (blue), as is a vacuum chamber enclosing the electrodes.

The diagnostic system consists of a phosphor screen which is electrically biased to +5 kV, coupled to a CCD camera. The phosphor screen is located in the flaring field region opposite the electron source, where $B_z \approx 1.2$ T (see Fig. 2.2), so the electron distribution is magnified by a factor of two as the particles travel adiabatically along field lines between the 8ST electrodes and the phosphor screen. Fluorescent light emitted from the phosphor screen passes first through a window in the vacuum chamber. Then it passes through an achromatic doublet lens with focal length 600 mm and diameter 150 mm which is placed 380 mm from the phosphor screen. Finally, it is focused onto a 15 mm^2, 4.2 megapixel CCD chip by a compound lens system mounted to the camera housing, located 340 mm from the doublet lens with a focal length 105 mm and diameter 53 mm.

The optical system was designed in this way for the following reasons. The two main goals of the optical system are to maximize the signal-to-noise ratio (SNR) and to maximize the pixel resolution. However, these two criteria are inversely related, so a com-

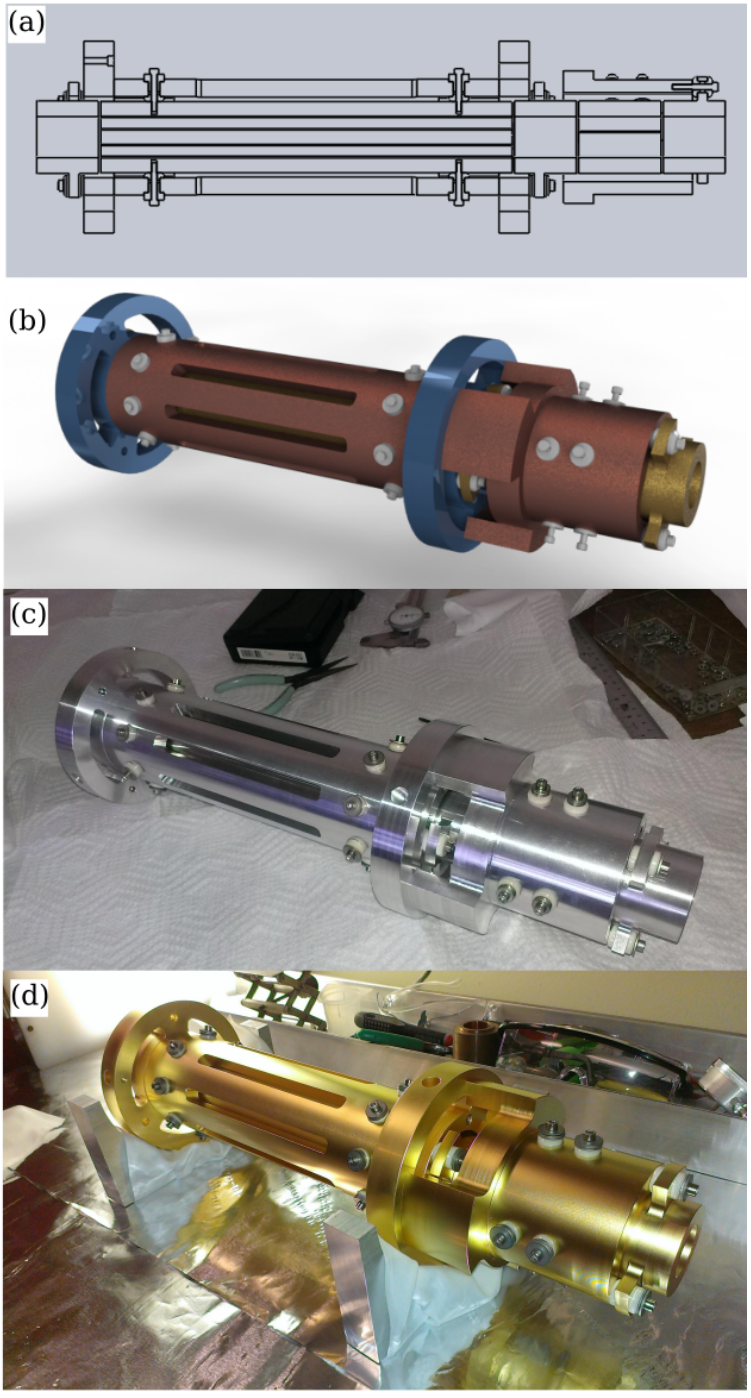

Figure 2.3: Models and photographs of the 8ST apparatus. Shown are (a) a section view of a wireframe computer model; (b) a solid computer model; (c) the assembled device prior to, and (d) after gold-plating the electrodes.

promise must be reached. The SNR is improved by cooling the CCD chip to $\sim -15^\circ$ C using a Peltier thermoelectric cooler coupled to a forced air system[2]. Furthermore, the 2048×2048 pixel CCD chip data is binned by a factor of two, resulting in a stronger signal but lower resolution. The primary constraint is that the camera fails in a magnetic field of $\gtrsim 0.03$ T, thus it is placed far from the magnet where $B \sim 0.02$ T. The optical signal decreases as r^{-2}, where r is the distance from the source to the camera, so the doublet lens is placed closer to the magnet in order to maximize the amount of light collected. The focal lengths and distances are chosen in order to obtain a magnification factor where the 8ST trap domain fills the CCD chip, thus maximizing the number of pixels used. Given these constraints and the available equipment, the optical setup described here represents our best effort to simultaneous maximize the resolution and the SNR. Here, the magnification factor between the phosphor screen and the CCD chip is 0.226, the resolution is roughly $r_w = 390$ pixels, and the SNR for these experiments (based on the peak signal at the center of the plasma) ranges from 10-50.

Possible ways to improve the optical diagnostic system include the following. Most importantly, it is advantageous to place the CCD chip as close as possible to the phosphor screen. Ideally, one could purchase a camera which is engineered to work in a strong magnetic field, although we have yet to find a good option which is not prohibitively expensive. Otherwise, the system could be improved dramatically by building a "magnetic shield" of high-permeability metal around the camera in order to reduce B. Alternatively, the dou-

[2]The stock camera system was cooled by a small fan mounted to the back of the housing. Since the fan failed in a magnetic field of $B \gtrsim 0.01$ T, it was removed and replaced with an externally pressurized air source which was mounted directly to the camera housing.

blet lens could be replaced by a better lens with a large diameter, small focal length, and aberration corrections; however, such a lens is difficult to manufacture and therefore expensive. Plans are being made to implement some combination of these techniques for future experiments in the 8ST.

2.3 External flow properties

During the fluid experiments, the segments of electrode II are biased, creating vacuum electric fields which give rise to an irrotational $\mathbf{E} \times \mathbf{B}$ flow that advects the trapped electrons (i.e., the vorticity). In 2D, the vacuum electric potential inside the trap volume satisfies the Laplace equation $\nabla^2 \phi = 0$ with

$$\phi(r,\theta) = \sum_{m=0}^{\infty} \Big[A_m \cos(m\theta) + B_m \sin(m\theta) \Big] \Big(\frac{r}{r_w} \Big)^m, \tag{2.3}$$

where the A_m and B_m are expansion coefficients, given by

$$A_m = \frac{1}{\pi} \int \mathrm{d}\theta \cos(m\theta) \phi(r_w,\theta); \; B_m = \frac{1}{\pi} \int \mathrm{d}\theta \sin(m\theta) \phi(r_w,\theta), \tag{2.4}$$

where $\phi(r_w,\theta)$ is the applied boundary condition. Plasmas are typically centered at $r = 0$ with $r_v \ll r_w$, so the lowest-order expansion terms are dominant. With the segmented electrodes aligned with the coordinate axes, the boundary conditions can often be chosen such that all $B_m = 0$.

Different choices of boundary conditions and the resulting vacuum potentials are shown in Fig. 2.4, where the equipotential contours are analogous to fluid streamlines. An external flow with a dominant $m = 1$ term can be created by biasing the segments

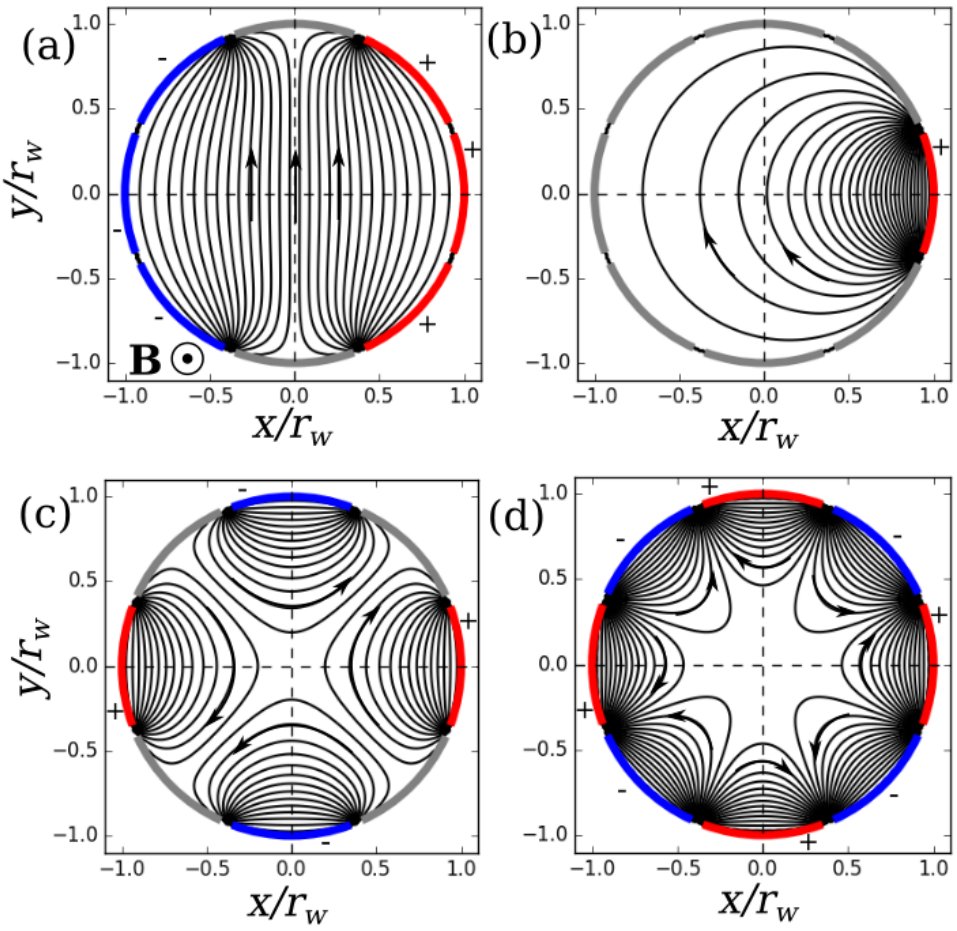

Figure 2.4: Choices of boundary conditions for electrode II, and the corresponding external flow field. Shown are (a) a uniform vertical flow, (b) an irrotational shear flow, (c) a simple strain flow, and (d) an octupolar flow. Boundary conditions are shown as $+V_a$ (red), $-V_a$ (blue), and $V_a = 0$ (gray). Streamlines are shown in black, with arrows indicating flow direction. The direction of the magnetic field is shown in panel (a). The simple strain flow shown in panel (c) is used for the majority of the experiments discussed here.

of electrode II to voltages $V_a(1,1,0,-1,-1,-1,0,1)$ [Fig. 2.4 (a)], beginning with the segment along the positive x-axis. This results in an approximately uniform flow field $\mathbf{v} = A_1\hat{\mathbf{y}}/Br_w$ near the axis, where $A_1 = 1.18V_a$; the next largest coefficient is $A_3 = -0.16V_a$. This flow initially advects the plasma away from the axis with no distortion; however at later times, the image charge induced in the wall leads to interesting dynamical orbits of the plasma [85]. Alternatively, the voltage configuration $V_a(1,0,0,0,0,0,0,0)$ [shown in Fig. 2.4 (b)] generates an irrotational shear flow similar to that which would be produced by a nearby vortex structure.

A flow with a dominant $m = 2$ component can be generated by the voltage configuration $V_a(1,0,-1,0,-1,0,-1,0)$ [Fig. 2.4 (c)]. The second order flow velocity for this configuration is given by $\mathbf{v} = \varepsilon(y\hat{\mathbf{x}} + x\hat{\mathbf{y}})$, where $A_2 = 0.9V_a$, and the next nonzero coefficient is $A_6 = 0.3V_a$, and

$$\varepsilon \equiv 2A_2/Br_w^2. \tag{2.5}$$

This flow is identified as the "simple strain flow" given in Eq. 1.3, where ε is the applied strain magnitude. Another interesting possibility, not yet exploited, involves a quadrupolar voltage pattern which rotates about the trap axis. In the rotating frame, this appears as a simple shear flow [39]. Additionally, an octupolar flow (with a dominant $m = 4$ term) can be generated using the boundary conditions $V_a(1,-1,1,-1,1,-1,1,-1)$ [Fig. 2.4 (d)].

A uniform potential associated with nonzero A_0 can modify the length of the plasma, and therefore change the density (vorticity). Typically, the boundary conditions are chosen such that $A_0 = 0$ to avoid this complication. Another issue is that the external flow can lead

to a net translation of the vorticity away from the axis of the trap, for example, due to an $m = 1$ component of the flow, or due to an $m > 1$ flow where the plasma is not initially centered on the axis [76]. When the vorticity is advected away from the origin, r/r_w is no longer a small parameter, and so higher-order terms in Eq. 2.3 can become important. In practice, this translational instability is avoided by carefully centering the initial vorticity distribution at the origin, and by working on timescales short compared to the instability. The distribution is centered using a damping circuit (described below), where a small asymmetry voltage (~ 0.1 V) is applied to a segment of electrode II in order to tune the location of the vortex center [85].

For the flows discussed above, the A_m are proportional to V_a, so the magnitude of the external flow velocity can be adjusted by varying V_a over time. The temporal dependence of the external strain is set using waveform generators. The only limitation is RC filtering from the electrical circuit, which presently has a ~ 1 μs time constant.

The influence of these external flows on an initially stable, axisymmetric vortex is an important topic in fluid dynamics, which can be studied in the 8ST. Moreover, these external flows can be implemented serially in order to generate other non-axisymmetric initial vorticity distributions (e.g., elliptical vortices or thin filaments). This dissertation focuses primarily on the case of an initially axisymmetric vortex subjected to a simple strain flow [shown in Fig. 2.4 (c)].

2.4 Run sequence

The procedure for a single run cycle of the 8ST is shown in Fig. 2.5, where voltages applied to the electrodes are represented schematically. A run cycle typically takes 5 - 10 s. The majority of this time is occupied by the preparation of the initial vorticity profile, with the fluid experiment itself taking < 500 μs. At the end of each run, the vorticity is diagnosed destructively using the phosphor screen diagnostic. Steps in this process are given below.

- **Programming.** First, waveform generators with 1 μs resolution are programmed to drive the segments of electrode II with the desired voltage and time dependence.

- **Electron injection.** Next, the trap is filled by injecting electrons. Electrode V is biased to the confinement voltage $V_c = -100$ V and electrode I is biased to the "lip voltage" V_l where $|V_l| < |V_c|$. The electron source is biased to an intermediate voltage V_e, where $|V_l| < |V_e| < |V_c|$ such that electrons have sufficient energy to transit electrode I but not electrode V. Electrons become confined between electrodes I and V by scattering energy from the parallel to perpendicular direction, either through collisions or conceivably by a two-stream instability [86]. This process continues for 0.1 - 1 s, until the desired total electron number is achieved. Then, electrode I is ramped to voltage V_c to prevent further filling.

- **First diocotron damp.** The initial electron density distribution is typically offset from the symmetry axis, resulting in an $m = 1$ diocotron mode [80], where m is an

azimuthal wave number. This mode is damped in 100 - 300 ms using a feedback circuit connected to two segments of electrode II.

- **Profile conditioning.** Then, the Rotating Wall (RW) technique is used to condition the radial density profile [80]. Here, the 4 segments of electrode IV are biased to generate a uniform electric field near the origin which rotates azimuthally at frequency f_w (either with or against the rotation of the plasma). In this way, angular momentum is either injected into or removed from the plasma, and the vorticity profile $\omega(r)$ can be changed. A few examples of profile evolution in response to the RW are shown in Fig. 2.6, and some examples of final profiles obtained in this manner are shown in Fig. 2.8.

- **Plasma cutting.** The RW profile control is conducted with plasma confined between electrodes I and V, however the fluid experiments must be conducted with plasma confined between electrodes I and III. Therefore, the plasma is "cut" by ramping electrode III abruptly from ground to voltage V_c. The plasma remaining between electrodes III and V is discarded.

- **Second diocotron damp.** The cutting process can result in a small amplitude $m = 1$ diocotron mode. Thus, the damping circuit is once again implemented to position the plasma centroid as close as possible to the symmetry axis.

- **Plasma cooling.** The plasma is held for about 500 ms, and the plasma cools *via* cyclotron radiation to $T \sim 0.1$ eV with a time constant of $\tau_c = 150$ ms [87]. At this point, the plasma has the properties necessary for experiments in the fluid regime.

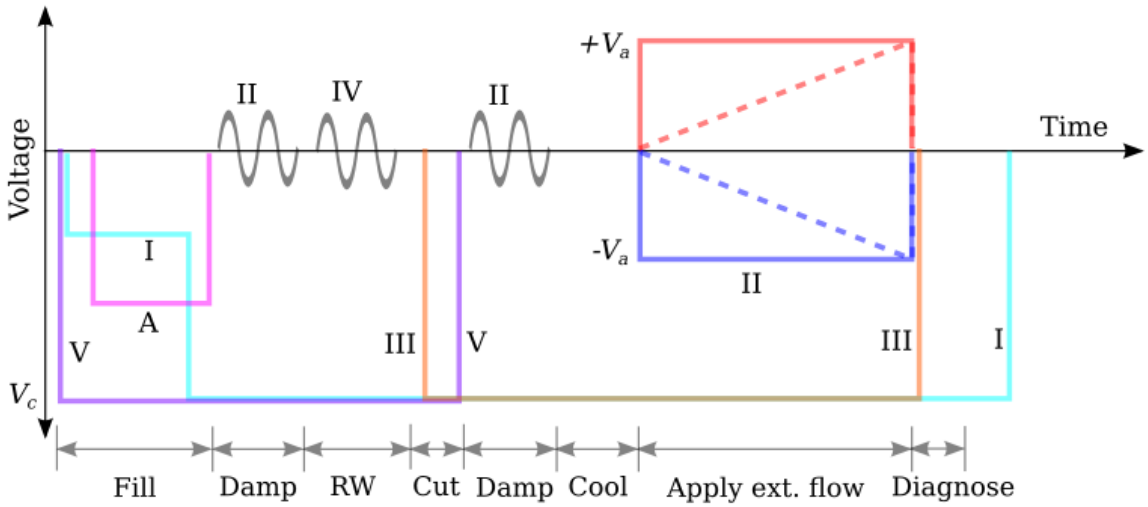

Figure 2.5: Serial steps in the experimental procedure, shown as voltage traces on the 8ST electrodes. Labels A, I-V correspond to the electron source and electrodes in Fig. 2.2. Shown are a square pulse (solid) and linear ramp (dashed) external flow time dependence, with bipolar boundary conditions.

- **Fluid experiment.** Prior to the fluid experiment, the CCD camera is triggered with an exposure time long enough to capture the event. Then, the external flow is applied by triggering the waveform generators. The system is allowed to evolve for some time, then the segments of electrode II are grounded, and immediately thereafter electrode III is grounded such that the electrons stream along the field and impinge on the phosphor screen. The resulting light is measured with the CCD camera.

- **Dark exposure.** After diagnosis, another camera exposure is taken in the absence of plasma, and the two exposures are subtracted to eliminate background noise.

The end result is a CCD image of the electron density distribution integrated over the axial direction [see, for example, Fig. 2.7 (a)]. This data represents a measurement of the 2D vorticity field at each CCD pixel. Runs can be repeated to reduce noise, or the

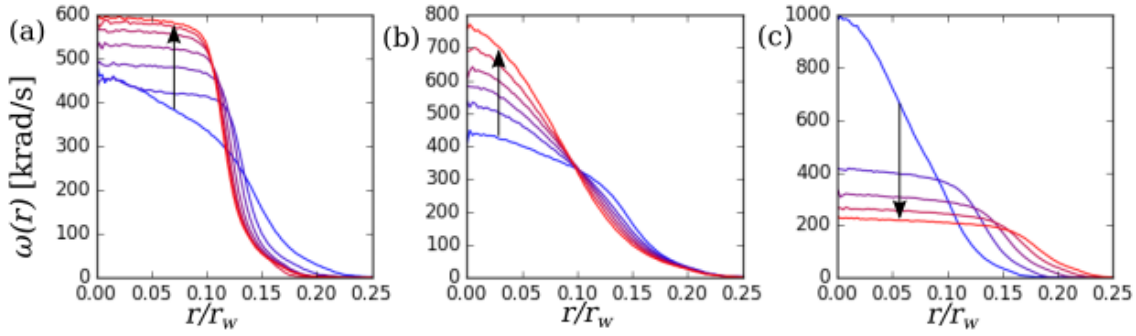

Figure 2.6: Demonstration of RW vorticity profile conditioning. (a) compression to a quasi-flat profile with $f_w = 50$ kHz over 3 s (blue to red); (b) compression to a Gaussian profile with $f_w = 1$ MHz over 500 ms; (c) reverse RW expansion to a quasi-flat profile with $f_w = -1$ MHz over 1 s.

protocol can be varied, for example to record time series data of the vorticity evolution.

2.5 Data analysis

Using the vorticity data and knowledge of the applied boundary conditions, the Poisson equation $\nabla^2\psi = \omega$ is solved using a numerical finite-difference algorithm to find the stream function at each CCD pixel. Then the velocity components (v_x, v_y) are determined by numerically differentiating the stream function. Second derivatives of the stream function are then found and used to calculate quantities such as the local strain eigenvalue $s(x,y) = \pm[4\psi_{xy}^2 + (\psi_{xx} - \psi_{yy})^2]^{1/2}$ (where subscripts indicate partial derivatives), and the Okubo-Weiss local stability parameter $Q(x,y) = s^2 - \omega^2$ [47] (see Chapter 3 for further discussion of these quantities). Figure 2.7 (a) shows a CCD image of an axisymmetric vortex centered on the domain axis with a quasi-flat profile and central vorticity $\omega_0 = 228$ krad/s, and panel (b) shows the same image overlaid with contours of the stream function due to an

applied strain flow with $\varepsilon^* \equiv \varepsilon/\omega_0 = 0.116$. Panel (c) shows a close-up view of the stream function separatrix and velocity magnitude $|\mathbf{v}|$, and panel (d) shows the separatrix and the strain eigenvalue s.

For axisymmetric vortices, it is useful to perform an azimuthal average of the vorticity data to extract the radial profile, $\omega(r) = (2\pi)^{-1} \int \omega d\theta$. It is observed that the profiles are often well-described by the simple formula

$$\omega(r) = \omega_0 \exp\left[-(r/r_v)^{\alpha}\right]. \tag{2.6}$$

This formula is numerically fit to the profiles using a least-squares routine to extract the fitted peak vorticity ω_0, vortex radius r_v, and smoothness exponent α. Examples of profiles and fits obtained in this manner are shown in Fig. 2.6. Low-order spatial moments of the vorticity distribution are also calculated, including the total circulation $\Gamma = \int \omega dA$, the centroid $\Gamma^{-1} \int r_i \omega dA$, and the quadrupole tensor $\Gamma^{-1} \int (3 r_i r_j - r^2 \delta_{ij}) \omega dA$, where r_i are the spatial coordinates and δ_{ij} is the Kronecker delta function.

Elliptical modes of a vortex can be excited, for example, by an external strain flow (Eq. 1.3) [39]. However, filamentary structures which form outside the vortex core can influence the quadrupole moment (c.f. Fig. 1.3). In order to diagnose elliptical distortions of the core, a numerical routine is used to fit an ellipse to the half-maximum vorticity contour. Here, the aspect ratio λ and orientation ξ of the ellipse are fit to the set of CCD pixels with vorticity in the range $0.4 \leq \omega/\omega_0 \leq 0.6$, where ω_0 is the peak vorticity. In this way, a robust representation of elliptical distortions of the vortex core is obtained. Examples of the elliptical fitting routine are shown in Fig. 2.9.

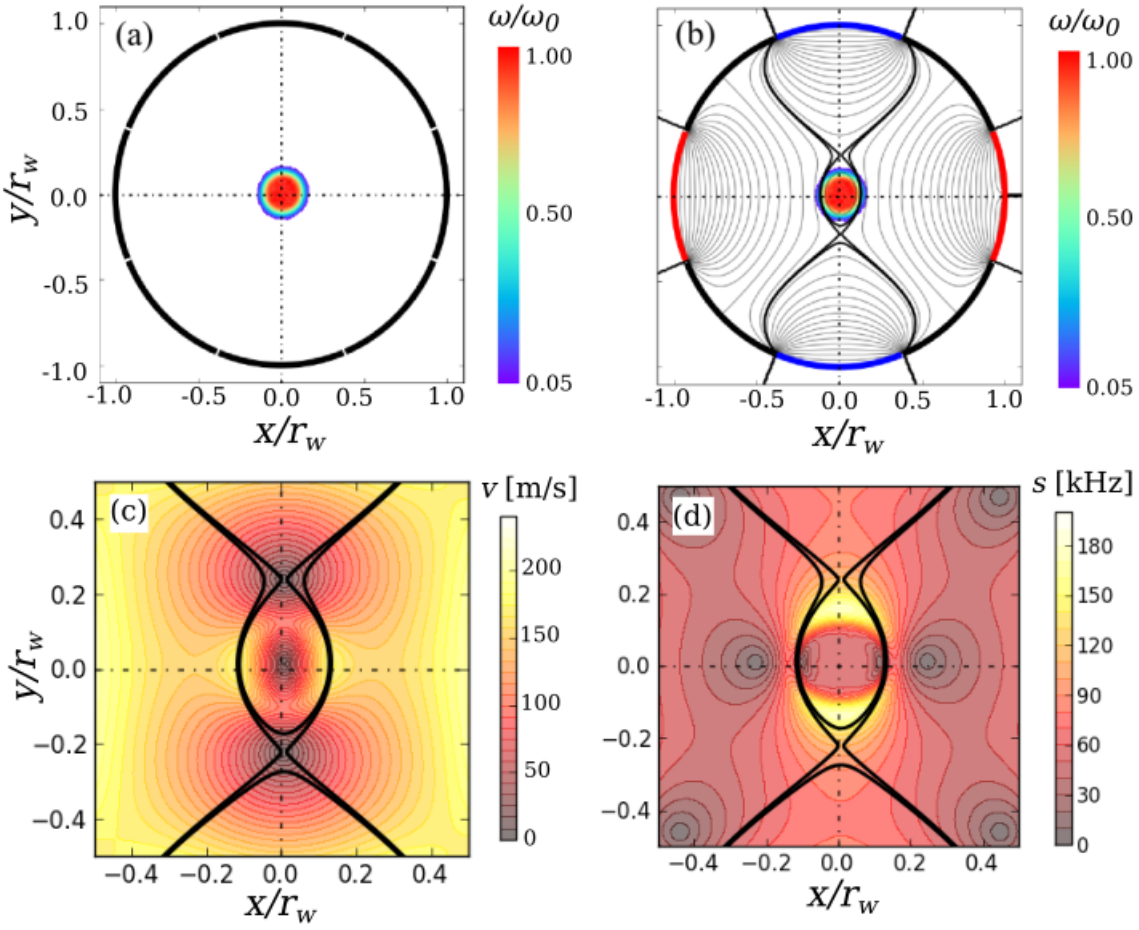

Figure 2.7: Analysis of a CCD image. (a) vorticity data (color map) with $\omega_0 = 228$ krad/s, truncated at $0.05\omega_0$; (b) vorticity overlaid with numerically calculated streamlines (black lines) and separatrix (thick black line) under applied strain with $\varepsilon^* = 0.116$; (c) close-up of separatrix and velocity magnitude (color map); (d) close-up of separatrix and strain eigenvalue s (color map).

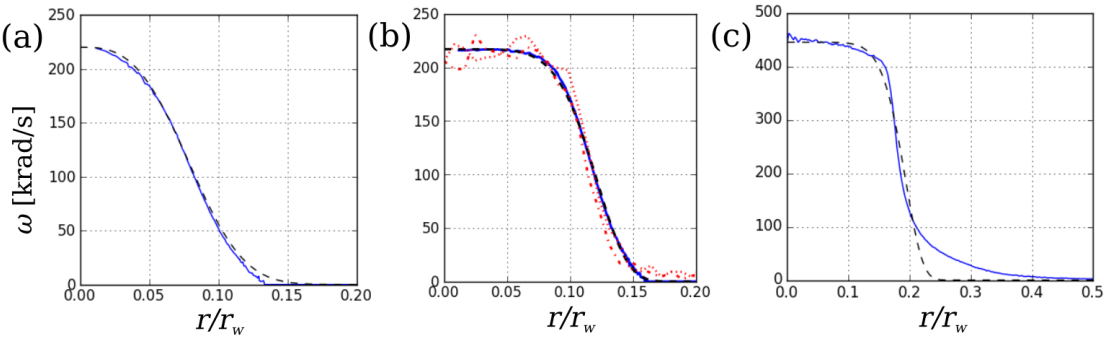

Figure 2.8: Examples of initial vorticity profiles obtained using the RW technique. Shown are data (blue) and fits to Eq. 2.6 (dashed), for (a) a smooth profile with $\alpha \sim 3$; (b) a quasi-flat profile with $\alpha \sim 6$; and (c) a quasi-flat profile with $\alpha \sim 8$ where the fit fails to capture a tail in the distribution at the vortex periphery. In panel (b), vertical (dashed) and horizontal (dash-dot) slices of the vorticity data are shown in red.

2.6 Calibration

In order to obtain quantitative data, the spatial resolution and signal magnitude of the CCD diagnostic must be calibrated. From the confinement region to the phosphor screen, the electron distribution is magnified by a factor of approximately two due to the flaring magnetic field. The flourescent light from the phosphor screen is then focused onto the CCD chip through an optical lens system. The total magnification factor can be found *in situ* by preparing a plasma which fills the entire trap volume, as shown in Fig. 2.10 (a), thus providing a measurement of r_w on the CCD image. Alternatively, the spatial calibration can be obtained using a plasma subjected to a strong external strain flow [83], as shown in Fig. 2.10 (b). In this case, the plasma collapses to a thin filament which is advected through small gaps between the segmented electrodes. The orientation of the filament and the point at which the signal disappears give a calibration of r_w and the orientation of the segments. Figure 2.10 (c) shows the electrode geometry fitted to data using these techniques. For the

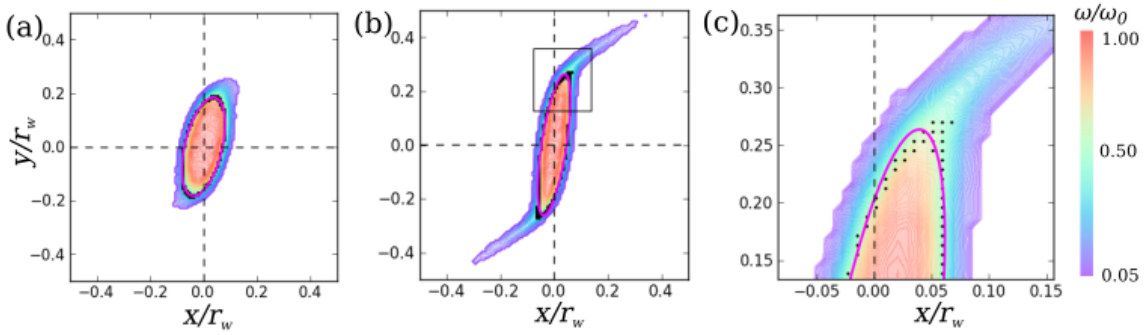

Figure 2.9: Demonstration of the elliptical fitting routine, for two different instances of vorticity data (a) and (b). Panel (c) shows a close-up region given by the square in panel (b). Pixels with vorticity between 40-60% of ω_0 are highlighted (black dots), and the elliptical fit to these points is shown (magenta line).

work presented here, the pixel calibration factor is approximately 1 pixel $= 33$ μm.

The vorticity is calibrated by measuring the rotation rate of a slightly elliptical vortex. A quasi-flat vorticity profile is prepared, and a low-amplitude elliptical distortion is excited using an external strain flow; then the strain is removed and the vortex is allowed to rotate freely at approximately the linear rate $d\xi/dt = \omega_0/4$ [9]. The orientation angle $\xi(t)$ is measured using the fitting routine described above. Using this procedure, the measured vorticity is calibrated to the CCD signal magnitude in the vortex core. Figure 2.11 shows the free evolution of (λ, ξ) for three different initial values of λ. Although the aspect ratio decreases due to inviscid damping [44], the rotation rate is initially constant for $1.2 \leq \lambda \leq 1.8$, and a robust calibration of the vorticity magnitude is obtained.

The external flow field is completely specified by the electrode geometry and knowledge of the boundary conditions. However, it is frequently observed that the strength of the external flow differs slightly from the calculated value. For this reason, the external strain magnitude ε is calibrated *in situ* using the plasma, and this calibrated value is used for

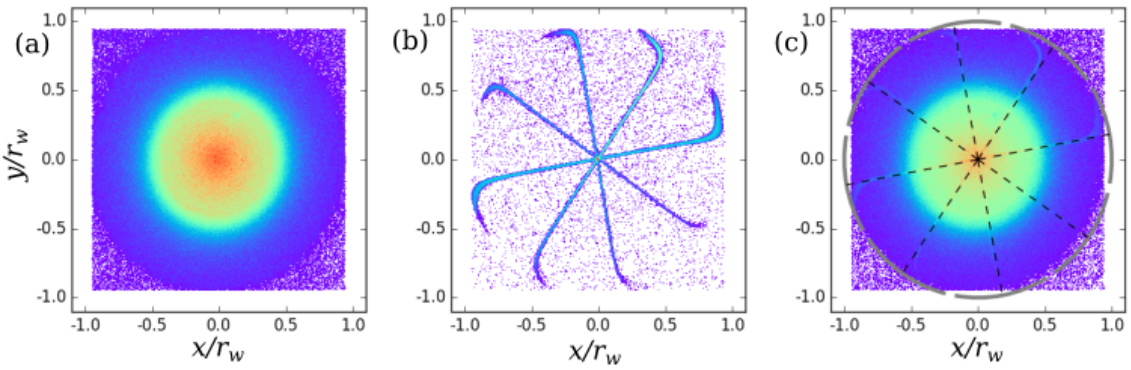

Figure 2.10: Spatial calibration of the CCD diagnostic. (a) an image of plasma filling the entire trap volume; (b) overlaid images of four plasmas during destruction by an external strain flow; (c) data from panels (a) and (b) fitted with the 8-segment electrodes (gray) and their orientations (black dashed lines).

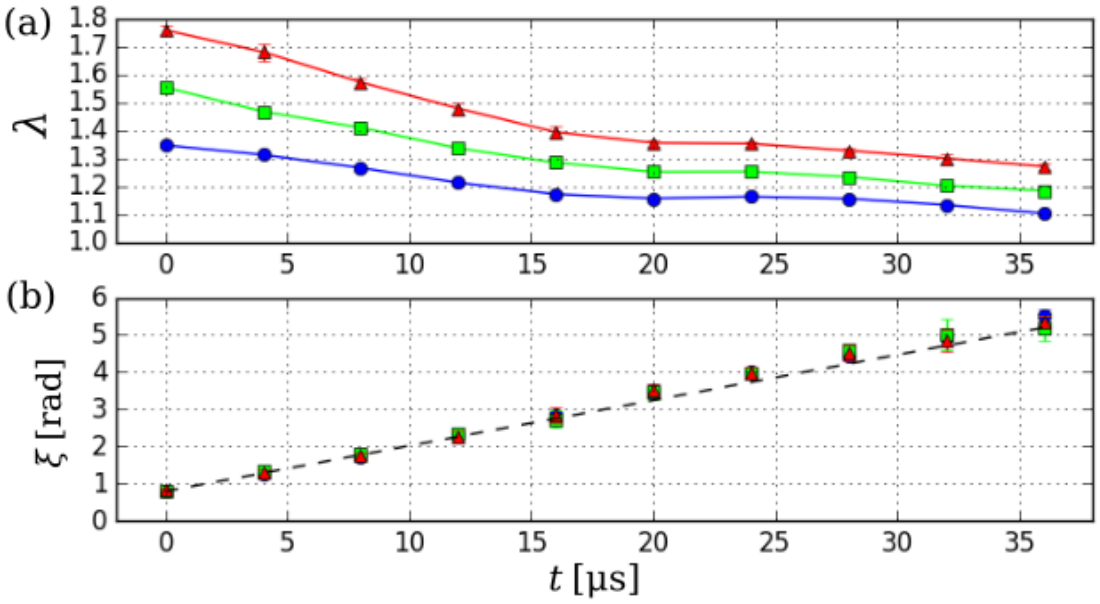

Figure 2.11: Vorticity calibration process. (a) $\lambda(t)$ and (b) $\xi(t)$ are shown for a freely rotating quasi-flat vortex excited to three different initial values of λ. Included in panel (b) is a linear fit (dashed) to the $\xi(t)$ data for $0 \leq t \leq 16$ μs, where $\omega_0 = 488$ krad/s.

quantitative studies. Possible reasons for the discrepancy are discussed here, although a clear answer has yet to be found.

A uniform flow (i.e., with a dominant $m = 1$ component) such as that shown in Fig. 2.4 (a), when imposed suddenly, will cause the plasma to translate rigidly at velocity $v = A_1/Br_w$. This velocity can be measured using the phosphor screen, thus providing a measurement of the ratio A_1/Br_w. Alternatively, the simple strain flow [Fig. 2.4 (c)] with dominant $m = 2$ component can be used to directly calibrate the strain rate ε. When the normalized strain ε^* is sufficiently large, the plasma will behave passively, distorting elliptically with aspect ratio [39]

$$\lambda(t) = \exp(2\varepsilon t). \tag{2.7}$$

The time dependence of the aspect ratio can be measured using the elliptical fitting routine described above, providing a direct measurement of ε.

Similar techniques using slowly ramped (i.e., adiabatic) uniform flows and simple strain flows also yield calibrations of the external flow. When an $m = 1$ flow is gradually imposed, the plasma moves away from the trap axis adiabatically, and remains in an off-axis equilibrium where the external flow is balanced by image fields [85]. When an $m = 2$ simple strain flow is applied gradually, the expected equilibrium ellipticity is given by Ref. [8] (these elliptical equilibrium states are discussed in greater detail in Chapters 3 & 4). Thus, calibrations can be performed using both instantaneously imposed and gradually ramped flows, either with an $m = 1$ or 2 flow pattern.

Figure 2.12 shows measurements of the strain magnitude using a simple strain

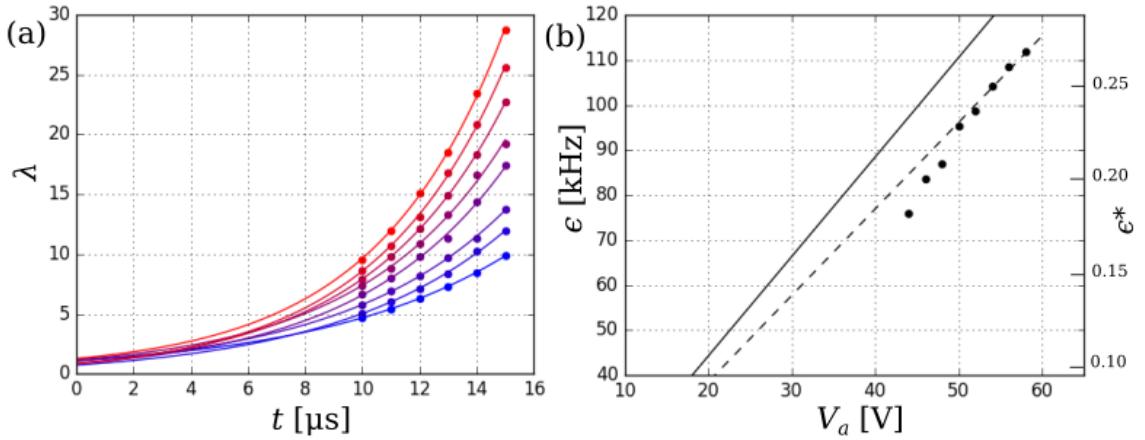

Figure 2.12: Strain calibration process. (a) measurements of $\lambda(t)$ for $\varepsilon^* = 0.18 - 0.27$ (blue to red), with $\omega_0 = 420$ krad/s; (b) measurements of $\varepsilon(V_a)$ given by exponential fits to $\lambda(t)$. The calibrated strain to voltage ratio (dashed) is compared to the calculated value (solid).

flow imposed instantaneously on an initially axisymmetric plasma. In panel (a), exponential curves are fitted to $\lambda(t)$ data to extract ε. In panel (b), the measured ε is plotted against the applied voltage V_a, showing a linear dependence for $\varepsilon^* \gtrsim 0.23$ with slope $\varepsilon/V_a = 1923\ (\mathrm{Vs})^{-1}$, consistent with the assumption that the plasma is behaving passively. However, the calculated value is $\varepsilon/V_a = 2219\ (\mathrm{Vs})^{-1}$ based on the aforementioned values of B, r_w, and A_2, giving a discrepancy of -13%.

This issue is further complicated by the fact that the calibration ε/V_a has actually changed a few times over the course of about a year and a half of 8ST experiments. For example, in Ref. [83] the calibration was measured to be $\varepsilon/V_a = 2390\ \mathrm{Vs}^{-1}$, or $+7\%$. Thus, the strain magnitude has been measured to be *both above and below the predicted value* by as much as 13%, but more typically in the range 5-10%. In general, once the calibration has shifted, it is consistent from day to day. At least one instance of the calibration

shift was correlated with erratic behavior of laboratory equipment (in this case, a power supply for the magnet), although in other cases the calibration has shifted for no apparent reason. Recently, the calibration has been steady at $\varepsilon/V_a \approx 2060$ (-7%) for about half a year. Although the strain calibration technique shown in Fig. 2.12 provides the most direct measurement of ε, other techniques using $m = 1$ flows and ramped flows have given calibrations which are roughly consistent with the strain calibration results. Thus, the strain calibration technique appears to give robust results.

In order to investigate the source of this discrepancy in the strain calibration, the magnetic field, applied voltage, and electrode geometry were scrutinized. Deviation from the expected magnetic field would produce the observed shift in external flow magnitude, since B appears in the denominator of all $\mathbf{E} \times \mathbf{B}$ flows. However, the 8ST apparatus was removed and the magnetic field measured directly, with no significant discrepancy observed. Furthermore, calibrations were performed at a lower magnetic field ($B = 3.5$ T) and the calibration shift was still apparent. A systematic error in the voltage applied to the segments of electrode II could also be responsible for the shift. For example, a contact resistance or a finite resistance to ground could alter the applied voltages. The electrode voltages were measured directly under atmospheric pressure, and no shift was observed. Further experiments under vacuum indicated that the circuit was behaving properly. Finally, the shift could be due to geometric errors involved with construction of the 8ST apparatus. For example, due to relatively large tolerances on certain parts of the design, some segments of electrode II were noticeably shifted both azimuthally and radially, as shown in the photograph in Fig. 2.13. However, direct measurements of r_w were made and precise

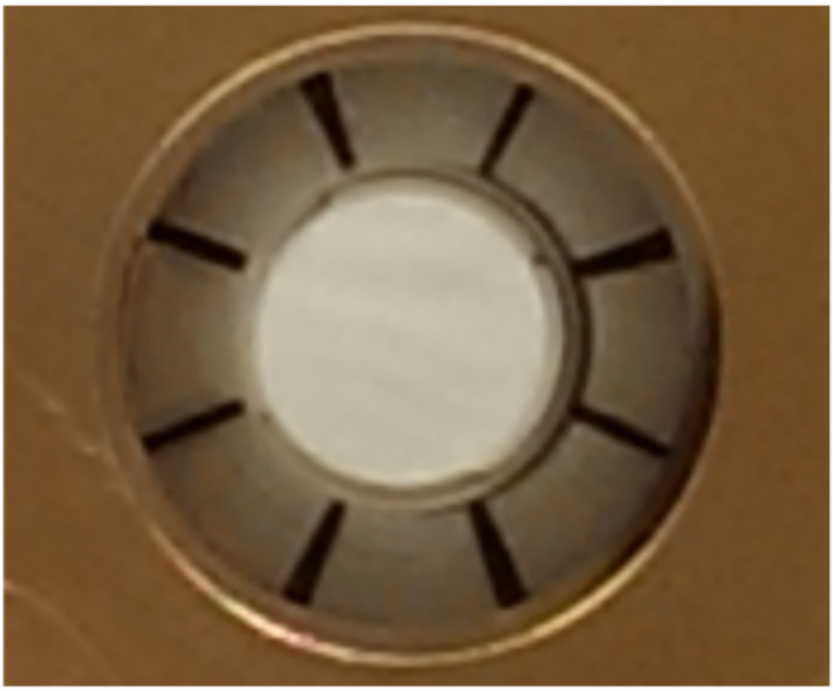

Figure 2.13: Photograph of the segments of electrode II. Slight misalignment and imperfections in the assembly are observed, which could impact the exact value of the applied strain magnitude.

calculations of A_2 were conducted, with neither quantity deviating sufficiently to explain the calibration shift. In summary, systematic errors of many types were investigated, but none of these are likely to produce a shift in strain magnitude greater than about 5%, and so the source of the discrepancy remains a mystery.

2.7 Non-fluid behavior

In order for the plasma/fluid analogy to be valid, the perpendicular dynamics of the plasma must follow the Drift-Poisson equations (Eqs. 2.2). This amounts to a separation of spatial and temporal scales, which is discussed in Sec. 2.1. However, it is important

to understand the plasma behavior when these conditions are violated. Described here are non-ideal, non-2D, and non-fluid effects which arise when the scale separations are not satisfied. Also given are the degrees to which these assumptions are valid in the 8ST.

- **3D effects.** The confinement electrodes (I, III, and V) produce a radial vacuum electric field which gives rise to an $\mathbf{E} \times \mathbf{B}$ background rotation known as the "magnetron" drift [80]. This effect is minimized by using a large aspect ratio trap, with $r_w \ll L$. In the 8ST, $r_w/L = 10$ and the magnetron rotation frequency near the origin is both measured and calculated to be ~ 150 Hz, three orders of magnitude below f_v. Additionally, 3D geometric effects can be introduced by a misalignment of the electrode axis with the magnetic field. Such a misalignment would also adversely impact the confinement properties of the plasma and operation of the RW. The alignment is adjusted in order to minimize the asymmetry-induced radial transport of the plasma, and to optimize the RW operation. We estimate that the magnetic field is aligned with the electrodes to within an error of $\lesssim 3$ mrad.

- **Small spatial scales.** At small spatial scales, the fluid analogy can be broken by finite gyroradius effects and discrete particle effects. In the 8ST the gyroradius is $r_g = 0.5$ μm, 2 orders of magnitude below the CCD resolution. Discrete particle effects are expected at spatial scales approaching the inter-particle spacing, which is $(nL_p)^{-1/2} = (\omega B \varepsilon_0 L/e)^{-1/2} \approx 0.125\ \omega^{-1/2}$ mm. Therefore, the inter-particle spacing approaches the CCD pixel size for $\omega \approx 14$ rad/s, 4 orders of magnitude lower than the typical central vorticity. Such a signal would be well below the CCD noise

floor, which is typically ~ 10 krad/s.

- **Viscosity.** Viscosity is present in a pure electron plasma as a result of electron-electron collisions; however it differs fundamentally from the hydrodynamic viscosity appearing in the Navier-Stokes equations. In general, the viscosity varies with electron density inside the plasma, and it is a complicated function of the various system parameters (magnetic field, density, temperature, etc.). There is no viscosity outside of the plasma (i.e., in irrotational regions of the flow), and so the system obeys free-slip boundary conditions. For a more detailed discussion of electron plasma viscosity, see Ref. [23].

- **Plasma expansion.** For a plasma isolated from an axisymmetric (circular) boundary, viscosity itself cannot drive net radial vorticity transport since the global angular momentum is conserved [88]. In contrast, viscous hydrodynamic vortices are characterized by an outward radial diffusion of circulation (i.e., the Lamb-Oseen vortex [9]). In practice, small asymmetries and construction errors in the apparatus (for example, gaps between the segmented electrodes) can drive outward radial transport of the plasma [89], thus behaving like an effective viscosity. In the 8ST, the ratio of the decay time of the central vorticity to the vortex rotation period is $> 10^6$, as shown in Fig. 2.14; this quantity can be interpreted as an effective Reynolds number.

- **Plasma re-entry.** For sufficiently large values of the strain magnitude, some or all of the electron distribution may be advected out of the trap through the small gaps between the 8-segment electrodes [83]. It is routinely observed that some electrons

orbit the biased segment and return into the trap, as shown in Fig. 2.15. Apparently, these particles are confined axially and obey $\mathbf{E} \times \mathbf{B}$ drift dynamics in the vacuum region outside the segmented electrodes. Although interesting, this behavior can be detrimental to the experiments, since the re-entrant circulation can modify the dynamics of the remaining circulation.

- **Dump rotation.** During the imaging process, the electrons must travel axially from the 8-segment region to the phosphor screen. In this time, the density distribution continues to drift in the plane perpendicular to $\mathbf{B}$. For example, an elliptical vortex may rotate as much as 10° during diagnosis [83]. The amount of rotation is determined by measuring the orientation of an elliptical vortex in equilibrium with the strain [8], and comparing this to the known electrode geometry. The data are corrected accordingly when necessary, in order to recover the ellipse orientation just prior to diagnosis.

The effects described in this section break the 2D fluid analogy, and so care must be taken to avoid them. In most cases, this can be accomplished by choosing appropriate values of the vorticity and experiment duration, such that the necessary separation of scales is acheived.

2.8 Vortex-in-cell simulations

To support and extend the 8ST experimental results, numerical simulations were conducted using the vortex-in-cell technique [58]. Here, the vorticity distribution is ap-

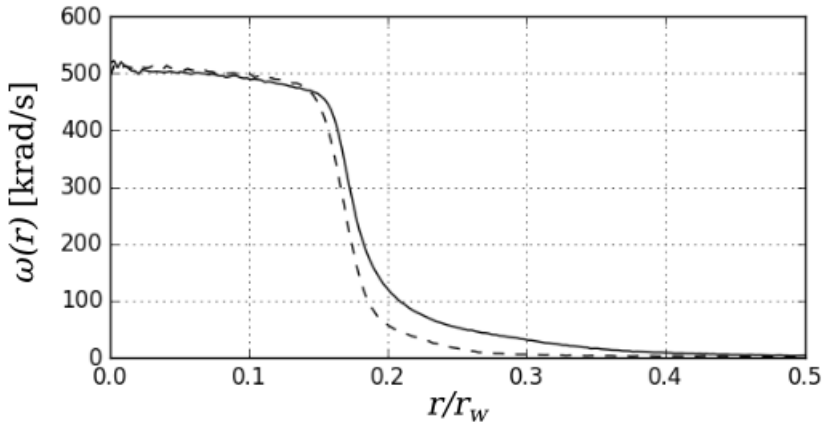

Figure 2.14: A quasi-flat initial vorticity profile (solid), and the same profile after 10 s of free relaxation in the absence of strain (dashed). A small amount of circulation near the edge of the vortex is lost to the wall, likely due to asymmetry transport, but the core remains approximately unchanged.

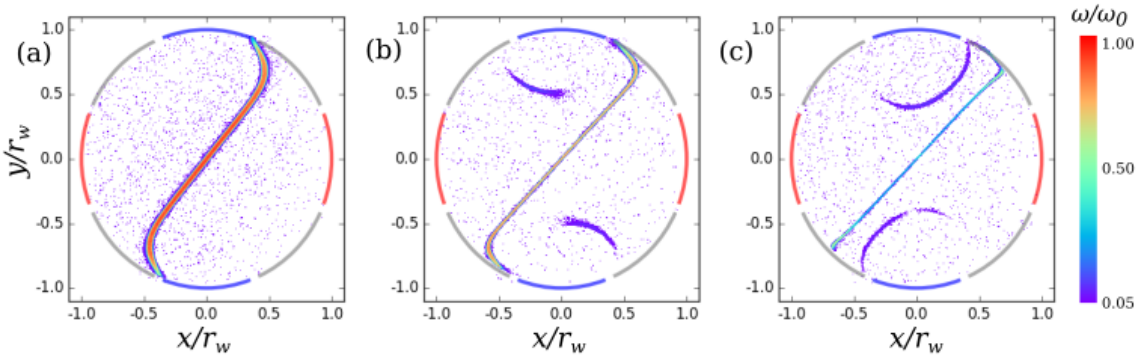

Figure 2.15: Demonstration of electron re-entry after a straining event. Here, $\varepsilon^* = 0.25$ and $\omega_0 = 520$ krad/s, and the vorticity evolution is shown at times $t =$ (a) 20, (b) 30, and (c) 40 μs. Electrons are advected through gaps between segmented electrodes, then drift around the biased segment and eventually return to the trap volume.

proximated by a number of discrete point vortices of equal strength. A Monte Carlo method is used to arrange the point vortices to achieve the desired initial profile. Typically, profiles given by Eq. 2.6 are used, where the vortex radius r_v and the smoothness exponent α are chosen. Alternatively, experimentally measured vorticity profiles can be loaded into the simulation. At each time step, the Poisson equation is solved on a grid using a finite-difference method, subject to the same boundary conditions used in the experiments (see Fig. 2.4). The stream function at the location of each point vortex is calculated using a linear interpolation between grid points, and time is advanced using a 4th order Runge-Kutta technique. Typical simulation parameters are the number of point vortices $N = 10^5$, grid size $r_w/300$, and a time step $\Delta t \sim 0.05\omega_0^{-1}$. The displacement of the entire vorticity distribution is feedback-damped artificially in the simulation in order to avoid the $m = 1$ translation instability due to the external flow, thus allowing for longer timescales than are possible in the experiments.

Examples of the results of vortex-in-cell simulations are shown in Fig. 2.16, corresponding directly to the data in Fig. 1.3, with $\varepsilon^* =$ (a) 0.116 and (b) 0.13. The simulation results in Fig. 2.16 appear to be in good qualitative agreement with the experimental results in Fig. 1.3. Notable differences are that the experimental vortices are rotated counter-clockwise slightly due to the diagnosis process, and the thin filaments are more difficult to observe in the laboratory due to noise acquired by the CCD.

Some of the work and discussion in Chapter 2 is taken from N. C. Hurst, J. R. Danielson, and C. M. Surko, "An electron plasma experiment to study vortex dynamics subject to externally imposed flows," *AIP Conf. Proc.* **1928**, 020007 (2017). The author of

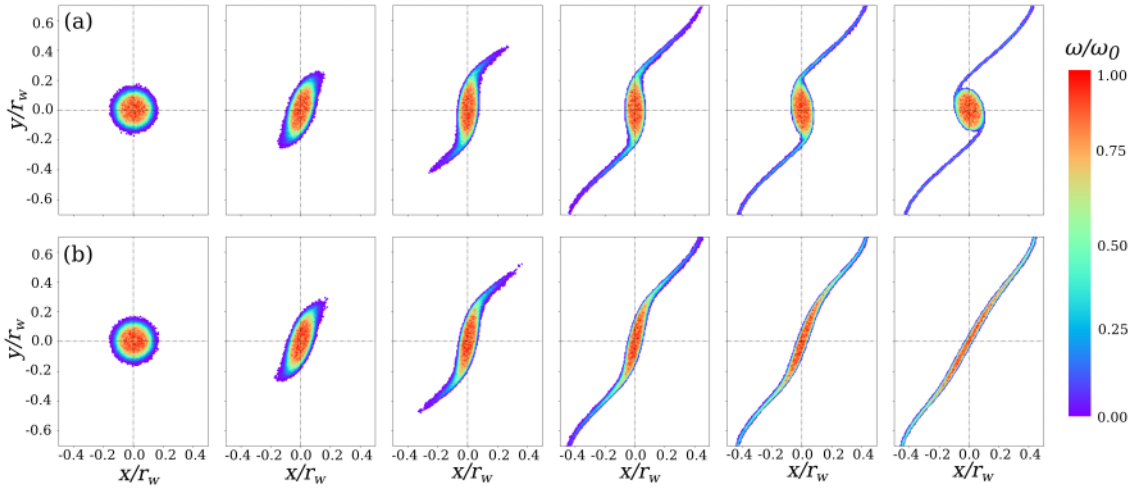

Figure 2.16: Vortex-in-cell simulations of a quasi-flat vortex subject to applied strain. Here, $\varepsilon^* =$ (a) 0.116 and (b) 0.13, and $0 \leq t \leq 22.8\omega_0^{-1}$. These results correspond directly to the experimental data in Fig. 1.3.

the dissertation led the research and was the primary investigator and author of this paper.

Chapter 3

Theoretical description of vortices in strain flows

3.1 Introduction

Ideal 2D fluids are described by the 2D Euler equations, Eqs. 1.2. The flow field $\mathbf{v} = -\nabla\psi \times \hat{\mathbf{z}}$ is uniquely specified at an instant by the vorticity and the boundary conditions *via* the Poisson equation, $\nabla^2\psi = \omega$, and the vorticity is advected without dissipation by the flow field, $(\partial_t + \mathbf{v}\cdot\nabla)\omega = 0$ [which can be written as $\partial_t\omega + J(\psi,\omega) = 0$, where J is the Jacobian operator]. Thus, the vorticity is a constant in the Lagrangian frame (i.e., the frame moving with the fluid). Equations 1.2 form an infinite-dimensional Hamiltonian system, where the continuous spatial coordinates (x,y) are one choice of the canonical momentum and coordinate. Alternatively, the the polar coordinates (r^2,θ) are another choice of canonical coordinates which are also action-angle coordinates [41]. The dissipationless

flow conserves internal energy along streamlines, so thermal forces are absent. Due to incompressibility, sound waves are absent. The pressure plays the role of a Lagrange multiplier, and can be calculated directly from the flow field [90]. In this dissertation, bounded fluids with non-uniform boundary conditions are considered, and so it is useful to decompose the stream function into homogeneous and particular solutions, $\psi = \psi_s + \psi_v$ where ψ_s describes irrotational flow associated with boundary conditions and ψ_v describes flow associated with the vorticity. The ideal 2D fluid equations conserve total energy, angular momentum, circulation, and a set of Casimir invariants which are moments of the vorticity [4].

A key theme in this work is the competition between strain and vorticity in a 2D fluid. The velocity gradient tensor at any point $\nabla\mathbf{v}(x,y,t)$ can be decomposed into its symmetric part

$$\sigma \equiv \frac{1}{2}[\nabla\mathbf{v} + (\nabla\mathbf{v})^{\mathrm{T}}] \tag{3.1}$$

which is called the strain tensor, and its antisymmetric part

$$\Omega \equiv \frac{1}{2}[\nabla\mathbf{v} - (\nabla\mathbf{v})^{\mathrm{T}}] \tag{3.2}$$

which is called the vorticity tensor, where the superscript T denotes the transpose operation. The vorticity tensor has complex-conjugate eigenvalues with magnitude equal to the vorticity ω in the $\hat{\mathbf{z}}$ direction. Assuming incompressibility ($\nabla \cdot \mathbf{v} = 0$), the strain tensor is traceless with real eigenvalues $\pm s$, where

$$s = [4\psi_{xy}^2 + (\psi_{xx} - \psi_{yy})^2]^{\frac{1}{2}}, \tag{3.3}$$

with partial deriatives indicated by subscripts. The magnitude of the strain and vorticity eigenvalues can be combined to form a dimensionless parameter $s^* = s/\omega$, which quantifies the local competition between strain and vorticity, with $s^* \gg 1$ corresponding to strain-dominated hyperbolic fluid motion, and $s^* \ll 1$ corresponding to vorticity-dominated periodic fluid motion.

Here we consider an initially axisymmetric, monotonically decreasing vorticity distribution $\omega(r)$ in a 2D ideal fluid, subject to an externally imposed irrotational simple strain flow as defined by Eq. 1.3. The external strain flow ψ_s has a uniform strain tensor everywhere, for which the eigenvalue is $s = 2\varepsilon$, and the orientation angle of the strain axis (i.e., the direction of the positive eigenvector) is chosen to be $\pi/4$[1]. When ψ_s is superposed with the flow ψ_v due to the vortex, s may vary across the domain, since ψ_v can contribute to the strain tensor. The vorticity is taken to be of a single sign, $\omega \geq 0$, as is the case for electron plasmas.

The primary goal of this work is to study the behavior of quasi-flat radial vorticity profiles, where $\omega(r)$ is a constant in the core, and then decreases quickly to zero at the edge of the vortex [c.f. Fig. 2.8 (b)]. In this case, the elliptical vortex patch theory is expected to be an accurate description. A secondary goal is to study how the dynamics depend on the degree of flatness of the profile. When the profile is relatively smooth [c.f. Fig. 2.8 (a)], departures from the elliptical patch theory are expected. In this chapter, details of the vortex patch model and its predictions are presented, and theoretical efforts regarding

[1]Here, ε is used rather than s for historical purposes, namely because MS71, K81, and others have used this convention as well. The strain orientation is irrelevant to the dynamics, so this value is chosen mainly for cosmetic purposes.

smooth profiles are discussed. These theoretical results are compared to experimental and numerical data in Chapter 4.

3.2 The elliptical patch model

A particularly useful theoretical description of 2D ideal vortices is the so-called elliptical patch model. Here, the vorticity is treated as piecewise constant inside an elliptical boundary, namely the vorticity distribution is given by $\omega(x,y) = \omega_0$ when

$$\frac{1}{2}\left[\frac{(x+y)\cos\xi - (x-y)\sin\xi}{a}\right]^2 + \frac{1}{2}\left[\frac{-(x+y)\sin\xi - (x-y)\cos\xi}{b}\right]^2 \leq 1 \qquad (3.4)$$

and $\omega(x,y) = 0$ elsewhere. Here, ξ is the orientation of the ellipse with respect to the strain axis (at 45°), and a and b are the semimajor and semiminor axes. Uniform translations have been neglected, so the ellipse remains centered on the origin and the vorticity centroid is $\int dA\ \mathbf{r}\omega = \mathbf{0}$. Imposing incompressibility, the area of the ellipse πab is a constant, and so we need only consider the aspect ratio of the ellipse, $\lambda = a/b$. This geometry is shown schematically in relation to the applied strain flow in Fig. 3.1.

The elliptical patch model was first studied by Kirchoff, who found exact solutions to the 2D Euler equations where the patch rotates freely in the absence of external flow with $d\lambda/dt = 0$ and [9]

$$\frac{d\xi}{dt} = \omega_0 \frac{\lambda}{(\lambda+1)^2}. \qquad (3.5)$$

This solution can be thought of as a nonlinear generalization of the linear Kelvin modes [91] on a vortex patch for azimuthal wavenumber $m = 2$ and axial wavenumber $k_z = 0$.

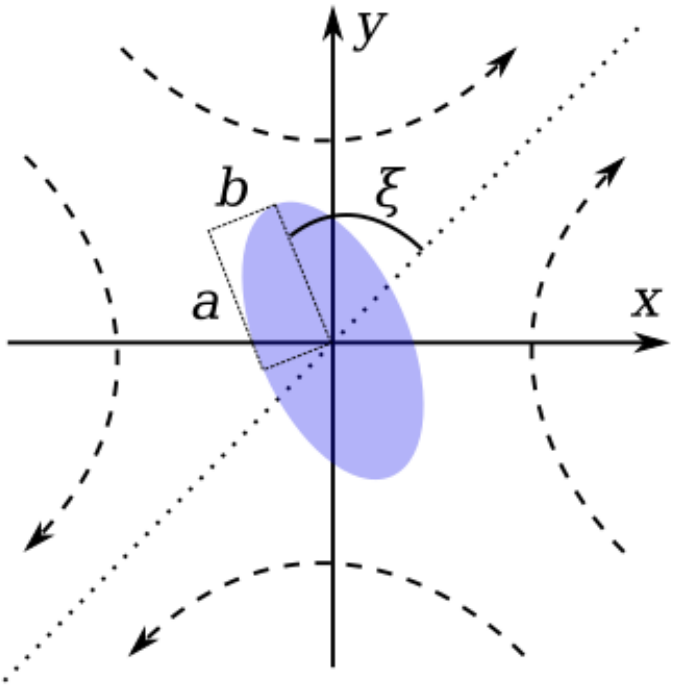

Figure 3.1: Geometry of an elliptical vortex in a background simple strain flow. Streamlines of the strain flow are depicted (dashed arrows), as is the strain axis (dotted) which is oriented at 45° with respect to the coordinate axes. The ellipse is shown in blue, with indications for the semimajor and semiminor axes a and b, and the orientation with respect to the strain axis ξ.

3.2.1 The K81 system under constant strain

In the presence of the time-independent, simple strain flow (Eq. 1.3, where ε is a constant), the behavior of the elliptical vortex patch was solved exactly by Kida [39]; this work is referred to here as K81. The dynamical equations for the aspect ratio and orientation are given by

$$\frac{d\lambda}{dt} = 2\lambda\varepsilon\cos 2\xi, \tag{3.6}$$

$$\frac{d\xi}{dt} = -\varepsilon\sin 2\xi\frac{\lambda^2+1}{\lambda^2-1} + \omega_0\frac{\lambda}{(\lambda+1)^2}. \tag{3.7}$$

These equations were solved by eliminating the time dependence, giving trajectories of the form

$$\varepsilon\sin 2\xi = \omega_0\Big[\frac{\lambda}{\lambda^2-1}\ln\frac{(\lambda+1)^2}{4C\lambda}\Big], \tag{3.8}$$

where C is an integration constant associated with the initial conditions, with $C = 1$ corresponding to an initially circular vortex [i.e., $\lambda(t=0) = 1$]. This case is particularly important here since the 8ST produces initially axisymmetric vortices, as described in Chapter 2.

Since the Euler flow is dissipationless, the K81 system preserves the total energy, and so the Hamiltonian

$$H(\lambda,\xi) = 2\varepsilon\sin 2\xi\frac{1-\lambda^2}{\lambda} + 2\omega_0\ln\Big[\frac{(1+\lambda)^2}{\lambda}\Big] \tag{3.9}$$

is invariant along a trajectory in phase space [92], and $C = \frac{1}{4}\exp(H/2\omega_0)$. Although (λ,ξ) are physically intuitive quantities, they are not canonical coordinates for this system, and they are degenerate under the transformations $(\lambda,\xi) \to (1/\lambda, \xi+\pi/2)$ and $\xi \to \xi+\pi$. A

suitable choice of canonical momentum and coordinate is [40]

$$p = \frac{(\lambda-1)^2}{\lambda},\ q = 2\xi, \tag{3.10}$$

yielding the Hamiltonian and equations of motion

$$H(p,q) = -2\varepsilon \sin q\sqrt{p^2+4p} + 2\omega \ln(p+4). \tag{3.11}$$

$$\frac{\mathrm{d}p}{\mathrm{d}t} = -2\varepsilon \sin q\sqrt{p^2+4p}, \tag{3.12}$$

$$\frac{\mathrm{d}q}{\mathrm{d}t} = -\varepsilon \cos q\frac{2p+4}{\sqrt{p^2+4p}} + \frac{2\omega}{p+4}. \tag{3.13}$$

In this dissertation, the coordinates (λ,ξ) are primarily used, where $1 \leq \lambda$ and $0 \leq \xi < \pi$. However, the canonical coordinates (p,q) are also discussed since they are useful from a theoretical perspective.

The timescale of the dynamics is set by ω_0^{-1}, so time can be normalized as $t^* \equiv t\omega_0$. The first term on the right side of Eq. 3.9 is the interaction energy between the patch and the strain, and the second term is the self-energy associated with elliptical distortion of the patch [93] (note that the second term on the right side of Eq. 3.7 is given by Eq. 3.5). Thus the dynamics can be described qualitatively as a competition between the two terms in the Hamiltonian representing stretching and rotation of the patch. This competition is parameterized by the (global) strain-to-vorticity ratio $\varepsilon^* \equiv \varepsilon/\omega_0$.

Contours of the K81 Hamiltonian (Eq. 3.9) are shown in (λ,ξ) space in Fig. 3.2 for four different values of the strain $\varepsilon^* = 0.05$, 0.11, 0.135, and 0.155. The separatrix is shown in black, closed orbits within the separatrix are shown in red, open orbits outside the separatrix are shown in blue, and the orbit corresponding to $C = 1$ (the circular condition)

is shown in magenta. Here, $H(\lambda < 1, \xi)$ is not shown since it is symmetric to $H(\lambda > 1, \xi + \pi/2)$, although the symmetry $\xi \to \xi + \pi$ is still evident. Alternatively, Fig. 3.3 shows contours of H in (p,q) space, as given by Eq. 3.11, for the same values of ε^*. Usage of the canonical coordinates eliminates the degeneracy, however the phase space is difficult to visualize when p is small. For this reason, it is convenient to visualize the phase space in the coordinates $(\lambda - 1, q)$, as shown in Fig. 3.4 (again, for the same values of ε^*). With positive vorticity, the closed orbits proceed in a counter-clockwise sense.

Some general observations can be made by inspecting these phase space plots. For panels (a) – (c), there exists a separatrix which is defined by an unstable saddle point at $q = \pi/2$. The separatrix encloses a set of periodic orbits surrounding a stable center point, also located at $q = \pi/2$. The separatrix is absent at $\varepsilon^* = 0.155$ in panel (d), implying that a saddle-node bifurcation occurs as the control parameter ε^* is varied. Above this critical value of ε^*, no periodic (stable) orbits exist, all orbits are open (unstable). Furthermore, the $C = 1$ orbit is unstable at $\varepsilon^* = 0.135$ in panel (c), implying that the separatrix coincides with the $C = 1$ orbit at some point below the bifurcation threshold. In Fig. 3.5, colormaps of H [for $\varepsilon^* =$ (a) 0.11 and (b) 0.155] show that the stable center point (marked by a green dot) is a local energy minimum.

It was found in K81 that the solutions (Eq. 3.8) come in a few different types, depending on the initial conditions and the value of ε^*: rotations, nutations, stationary modes, and unstable modes. Physically, a closed orbit which does not enclose the origin corresponds to a nutation of the ellipse where ξ is bounded, and one enclosing the origin corresponds to rotation of the ellipse where ξ increases monotonically. The orbit with

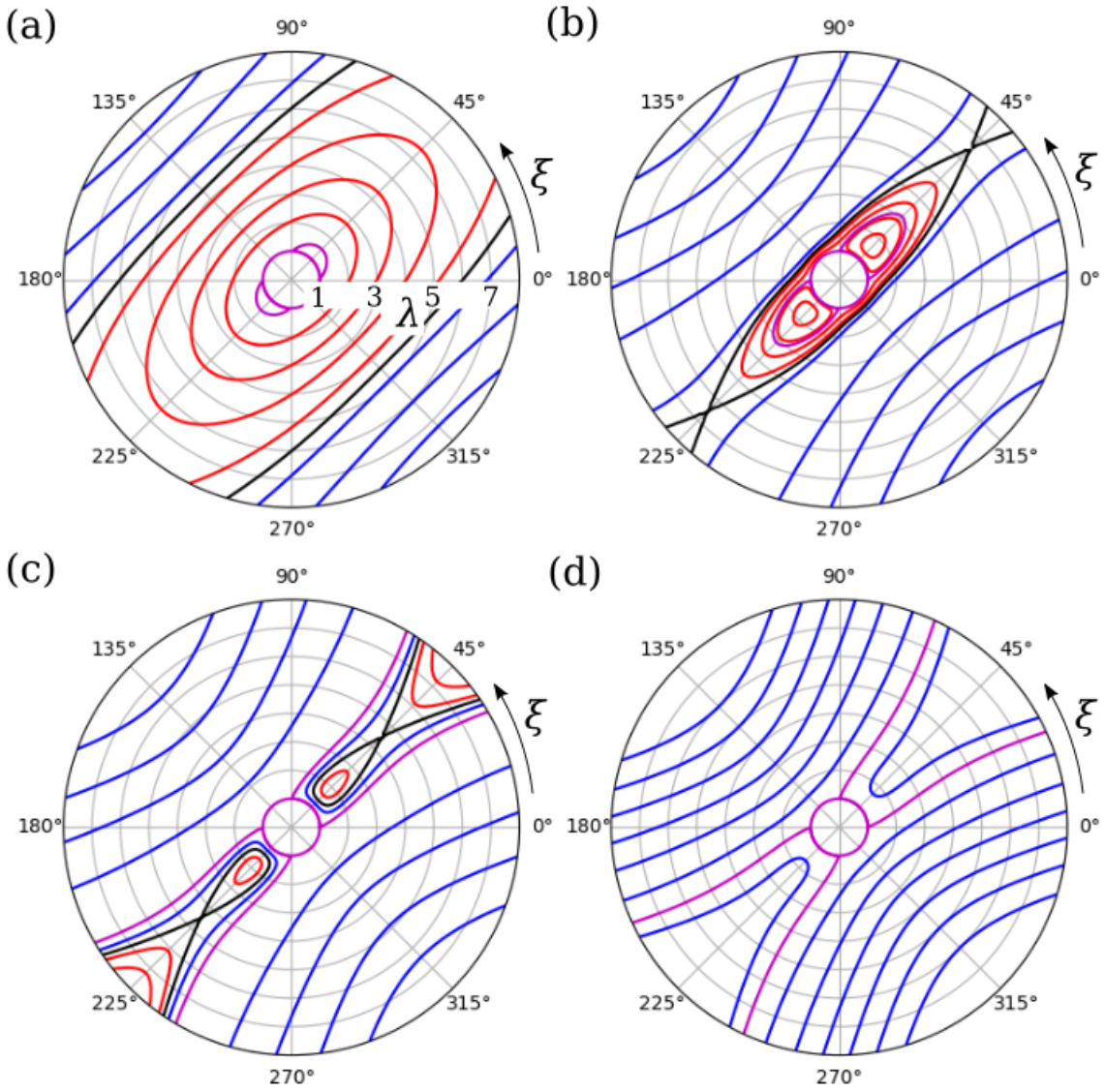

Figure 3.2: Contours of the K81 Hamiltonian (Eq. 3.9) in polar $(\lambda \geq 1, \xi)$ space. Here, $\varepsilon^* =$ (a) 0.05; (b) 0.115; (c) 0.135; and (d) 0.155. Shown are closed orbits (red), open orbits (blue), the separatrix (black), and the $C = 1$ orbit (magenta).

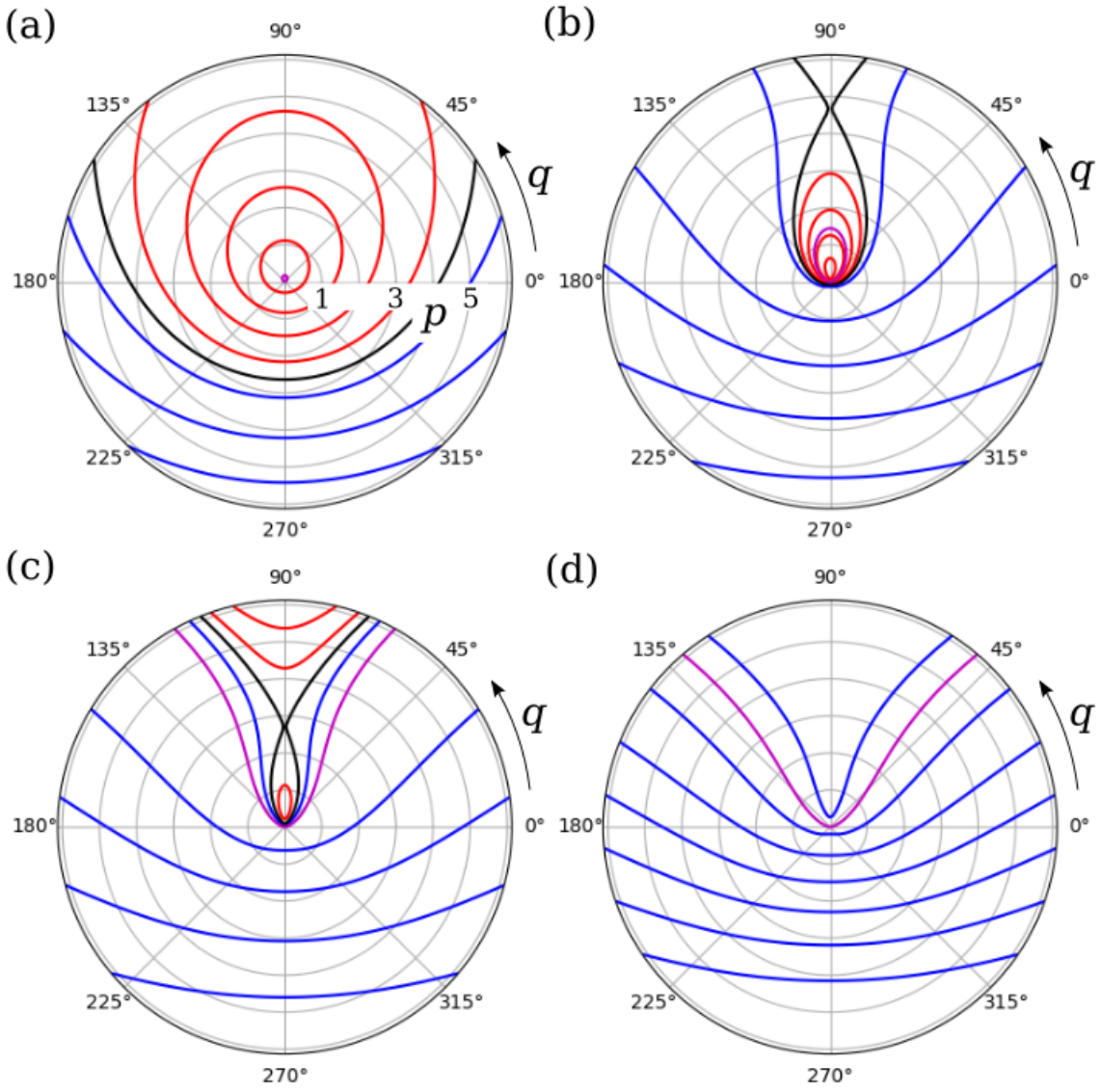

Figure 3.3: Contours of the K81 Hamiltonian (Eq. 3.11) in polar (p,q) space. Here, $\varepsilon^* =$ (a) 0.05; (b) 0.115; (c) 0.135; and (d) 0.155. Shown are closed orbits (red), open orbits (blue), the separatrix (black), and the $C = 1$ orbit (magenta).

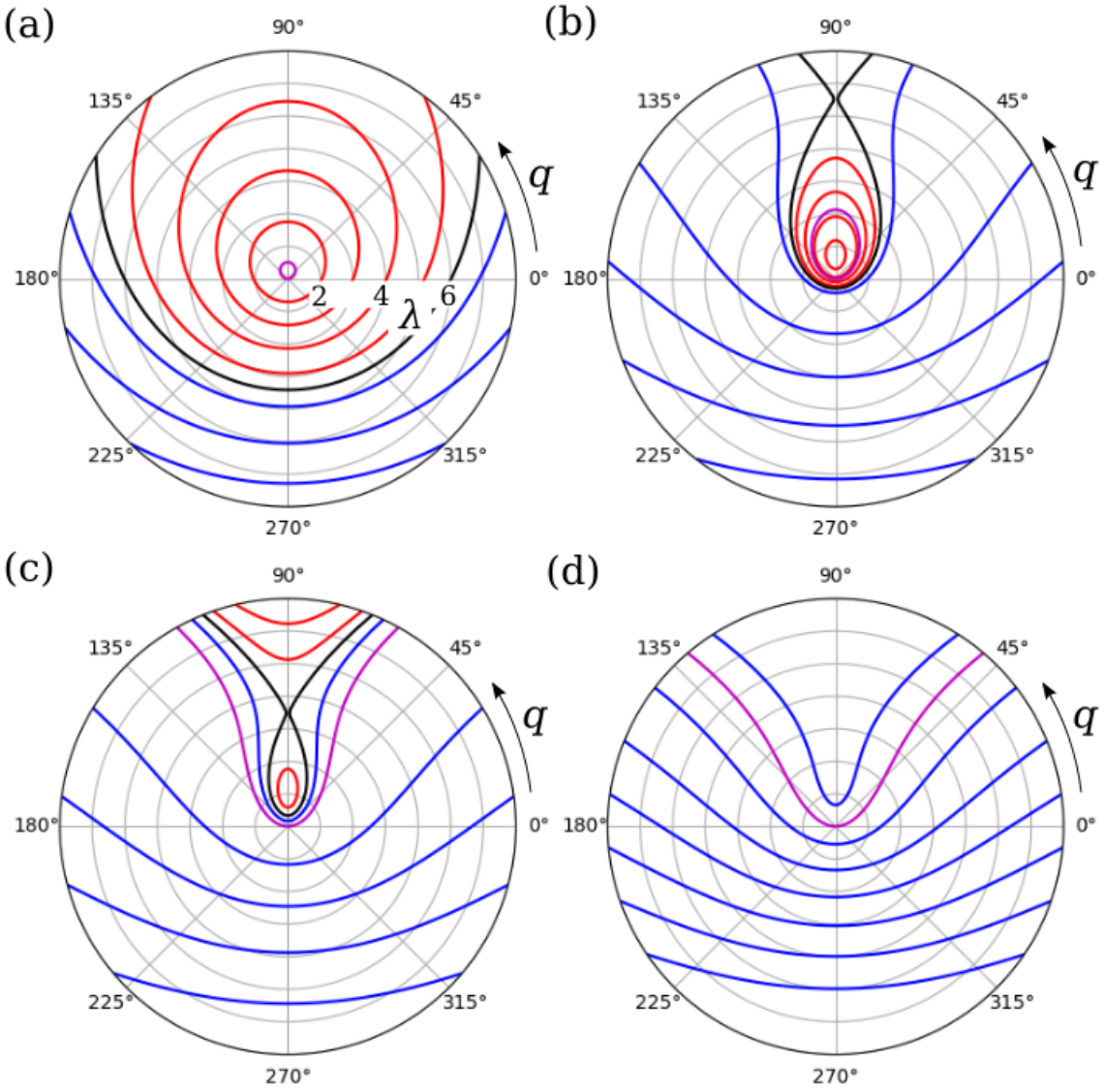

Figure 3.4: Contours of the K81 Hamiltonian (Eq. 3.9) in polar $(\lambda - 1, q)$ space. Here, $\varepsilon^* =$ (a) 0.05; (b) 0.115; (c) 0.135; and (d) 0.155. Shown are closed orbits (red), open orbits (blue), the separatrix (black), and the $C = 1$ orbit (magenta).

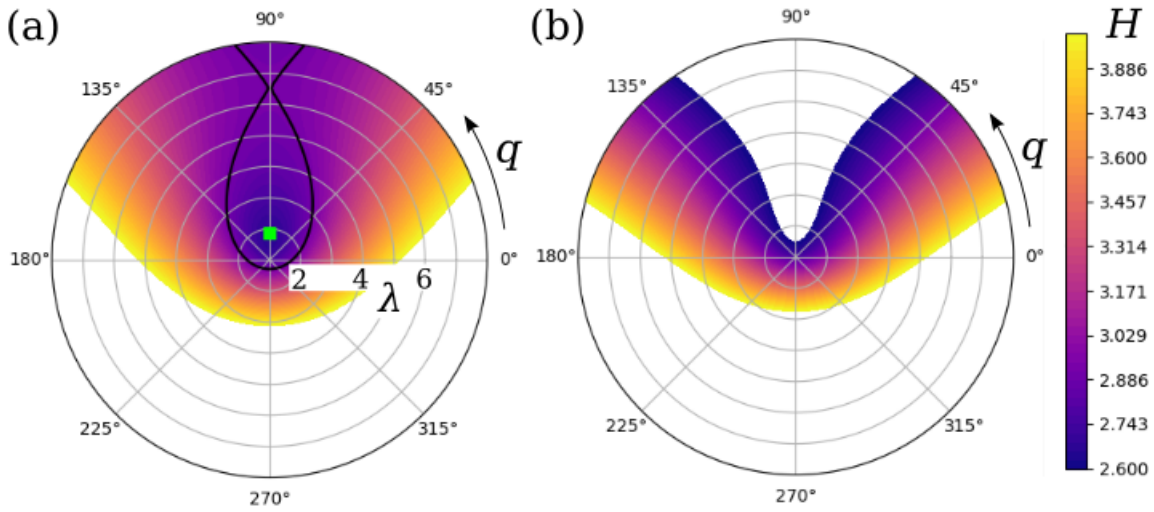

Figure 3.5: Color maps of the K81 Hamiltonian H (Eq. 3.9) in polar $(\lambda-1, q)$ space. Here, $\varepsilon^* =$ (a) 0.11 and (b) 0.155. In panel (a), there exists a separatrix (black line) enclosing a stable center point (green dot) which corresponds to a local energy minimum; in panel (b), no fixed points or separatrices exist.

circular initial condition ($C = 1$) marks the boundary between rotations and nutations. Since it returns after each period exactly to $\lambda = 1$ where ξ is degenerate, it cannot be strictly classified as either a rotation or a nutation. Open orbits correspond to unstable destruction modes of the vortex; here, ξ is bounded, λ is unbounded from above, and the vortex is stretched into an ever-thinning filament aligned with the strain axis ($\lambda \to \infty, \xi \to 0$).

The qualitative behavior of the K81 system is dictated by its fixed points (λ_0, ξ_0), which are defined by $d\lambda/dt = d\xi/dt = 0$, resulting in $\xi_0 = \pi/4$ and λ_0 given by the solution to

$$\frac{\lambda_0(\lambda_0 - 1)}{(\lambda_0 + 1)(\lambda_0^2 + 1)} = \varepsilon^*. \tag{3.14}$$

This formula was first derived by MS71 (prior to K81), and later, independently, in the context of electron plasmas by Backhaus, et. al. [94]. For $\varepsilon^* < \varepsilon_c^*$, Eq. 3.14 has two solutions, where $\varepsilon_c^* \approx 0.15$ is the critical strain value. At ε_c^* the two branches meet and the saddle-

node bifurcation occurs; above ε_c^* there are no solutions to Eq. 3.14. The lower branch of Eq. 3.14 is plotted in Fig. 3.6 as a solid line, and the upper branch as a dashed line. The lower and upper branches correspond to the center and saddle points (respectively) shown in Figs. 3.2 – 3.4. Therefore, the location of these points can be calculated from Eq. 3.14, and then the value of $H(\lambda_0, \xi_0)$ at the separatrix or the local minimum can be calculated. It is helpful to picture a three-dimensional space $H(\lambda, \xi, \varepsilon^*)$, where Figs. 3.2 – 3.4 are slices of constant ε^* and Fig. 3.6 is a slice of constant $\xi = \pi/4$.

A K81 orbit is uniquely defined by the constant C and the normalized strain ε^*. For a given value of C, there exists a critical value of the strain which we call the dynamical stability limit $\varepsilon_d^*(C)$ where the orbit coincides with the separatrix. The orbit is closed if $\varepsilon^* < \varepsilon_d^*$ and open if $\varepsilon^* > \varepsilon_d^*$. The dynamical stability limit can be calculated by determining when the maximum value λ_m of the aspect ratio reached in the orbit coincides with the upper branch of Eq. 3.14. At this point, $\mathrm{d}\lambda/\mathrm{d}t = 0$, yielding $\xi = \pi/4$, and λ_m is given by the solution to

$$\left(\frac{\lambda_m}{\lambda_m^2 - 1}\right) \ln\left[\frac{(\lambda_m + 1)^2}{4C\lambda_m}\right] = \varepsilon^*. \tag{3.15}$$

When the left sides of Eqs. 3.14 and 3.15 are equated and C is specified, the solution for λ can be used to find the stability limit $\varepsilon_d^*(C)$. This is shown graphically in Fig. 3.6, where λ_m is plotted (dotted lines, given by Eq. 3.15) over the MS71 equilibria (Eq. 3.14) for three different initial conditions, $C = 1$, 1.12, and 1.335. The λ_m curves meet the unstable branch of Eq. 3.14 at the points $\varepsilon_d^*(C)$, at which point the orbits become unstable and so λ_m is undefined (the orbit is said to be "homoclinic" when it coincides with the separatrix).

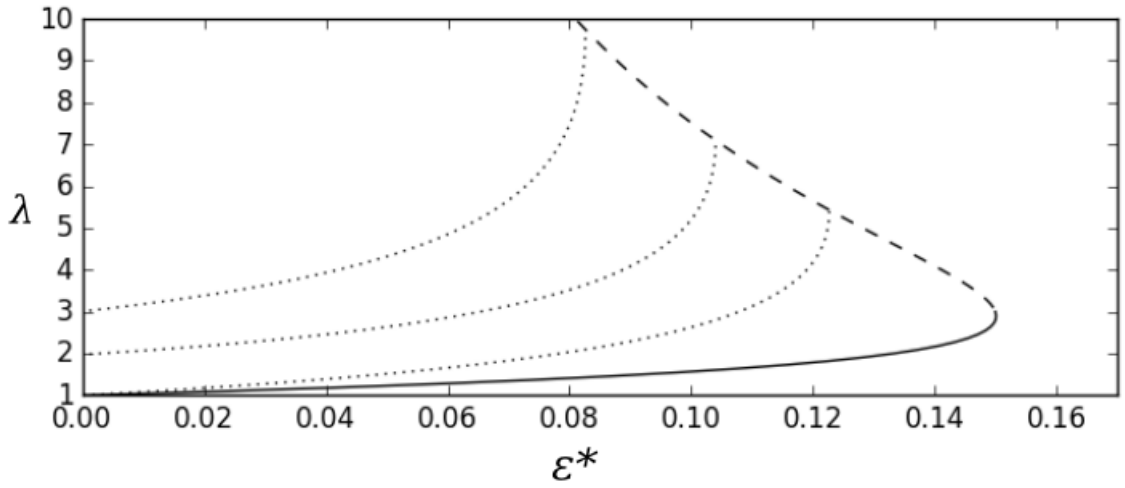

Figure 3.6: Fixed points of the K81 system and maximum aspect ratio curves. Shown are the values of λ as a function of ε corresponding to the saddle point (dashed) and the center point (solid), as given by Eq. 3.14, where $\xi = \pi/4$. Also shown are the values of $\lambda_m(\varepsilon^*)$ (dotted) as given by Eq. 3.15 for $C = 1$, 1.12, and 1.135.

For $C = 1$, $\varepsilon_d^* \approx 0.123$, which corresponds to $\lambda_m \approx 5.4$. Thus an initially circular vortex patch subject to constant strain is destroyed at a smaller value of strain than the critical value $\varepsilon_c^* \approx 0.15$, and in general ε_d^* can vary with C across the interval $[0, \varepsilon_c^*]$. The strain values shown in Figs. 3.2 – 3.4 are chosen such that for the lowest two [panels (a) and (b)] $\varepsilon^* < 0.123$ with $C = 1$ corresponding to a closed orbit; then in panel (c) $0.123 < \varepsilon^* < 0.15$ where $C = 1$ is an open orbit; and in panel (d) $\varepsilon^* > \varepsilon_c^*$ above the bifurcation threshold, so all orbits are unstable.

The temporal behavior of K81 orbits are shown in Fig. 3.7, with $C = 1$ and $\varepsilon^* =$ 0.05, 0.11, 0.123, 0.135, and 0.155 (the same values considered above), including (a) $\lambda(t^*)$, (b) $\xi(t^*)$, (c) $p(t^*)$, and (d) $q(t^*)$. At low values of ε^*, the elliptical distortions are weak, and so the orbital period approaches the linear value $T = 8\pi/\omega_0$. In this case, $p(t)$ is approximately sinusoidal. For all closed orbits, $p(t)$ is smooth near $p = 0$, while $\lambda(t)$

has a kink at $\lambda = 1$ (i.e., $d\lambda/dt$ is discontinuous). As ε^* increases, the orbital period is lengthened, as would be expected for a highly distorted ellipse based on Eq. 3.5, until the period becomes infinite at $\varepsilon_d^*(C = 1) \approx 0.123$. At this point, the system moves along the separatrix and approaches the saddle point, as shown by the dashed line in Fig. 3.7. Above ε_d^*, the orbits are unstable and λ increases without bound.

The K81 system can be simplified substantially by neglecting one of the two terms in the Hamiltonian. The rotation term dominates when λ is near 1; however for $C = 1$ with sufficiently large ε^*, $d\lambda/dt \gg d\xi/dt$, and λ quickly grows to a value where the strain term dominates. In this case, $\xi(t) \approx 0$, the rotation term is negligible, and the vorticity is advected as a passive scalar. Thus the solution to Eqn. 3.6 is approximately given by Eq. 2.7. On the other hand, in the limit of small ε^*, the rotation term dominates over the strain, and the orbits are simply perturbed Kelvin waves. Examples of open K81 orbits for $\varepsilon^* > \varepsilon_d^*(C = 1)$ are shown in Fig. 3.8, including (a) $\lambda(t^*)$ and (b) $\xi(t^*)$. Here, the homoclinic orbit is shown as a dotted line ($\varepsilon^* = 0.12271$), and other K81 solutions are shown as solid lines for $\varepsilon^* = 0.15$ (blue), 0.120 (magenta), and 0.125 (red). Also shown are the corresponding exponential curves (dashed) given by Eq. 2.7 (i.e., assuming passive vorticity). The K81 solutions approach the exponential curves in panel (a), and the amplitude of ξ decreases in panel (b) as ε^* increases.

3.2.2 The K81 system under time-dependent strain

When the strain magnitude is allowed to vary in time, the Hamiltonian is no longer conserved, and the phase space structure changes as the system evolves. Although time-

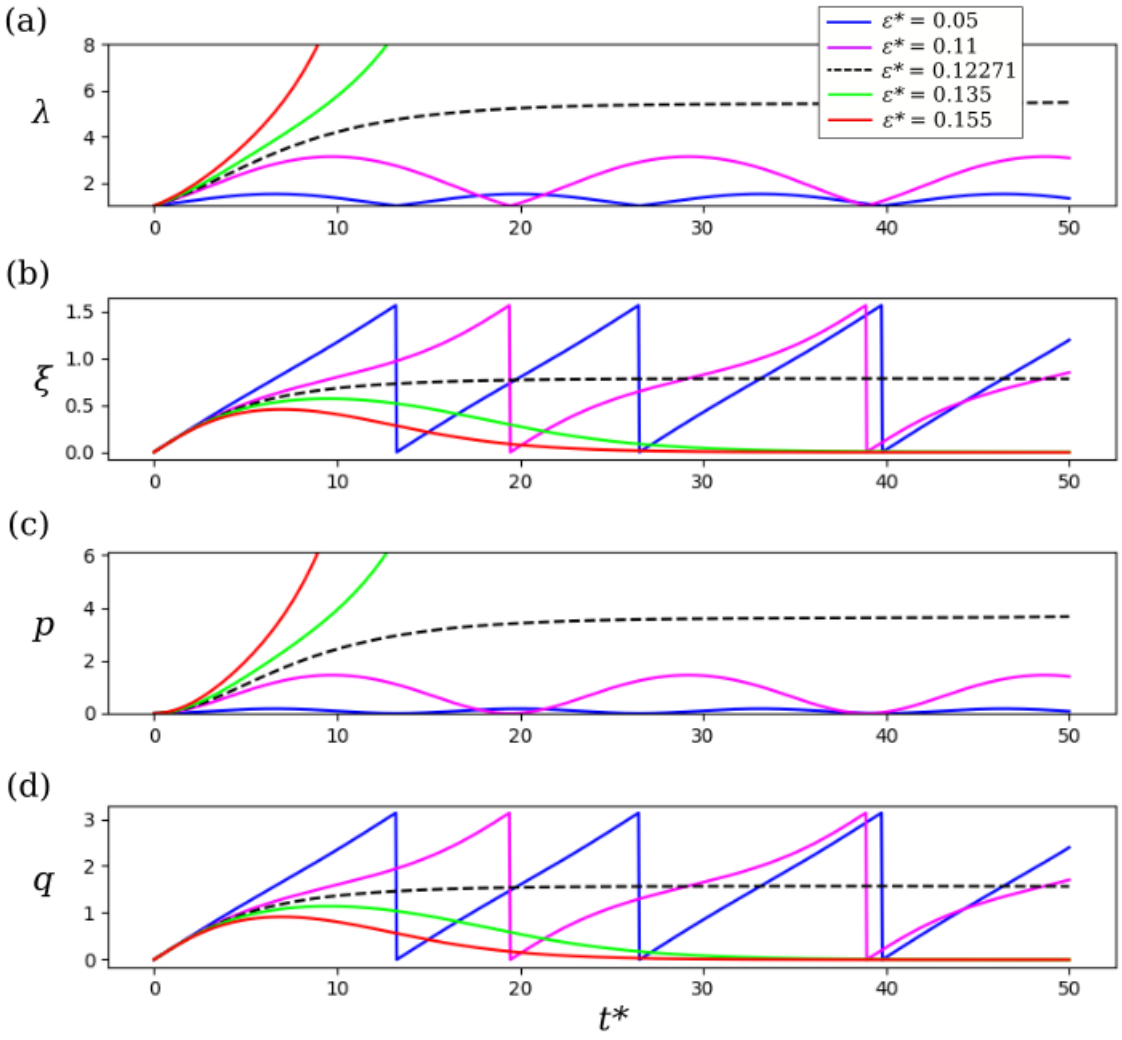

Figure 3.7: Temporal behavior of K81 orbits with circular initial condition. Shown are $\varepsilon^* = 0.05$ (blue), 0.11 (magenta), 0.135 (green), and 0.155 (red), including (a) $\lambda(t^*)$; (b) $\xi(t^*)$; (c) $p(t^*)$; and (d) $q(t^*)$. The homoclinic orbit is also shown (black dashed line, $\varepsilon^* = 0.12271$).

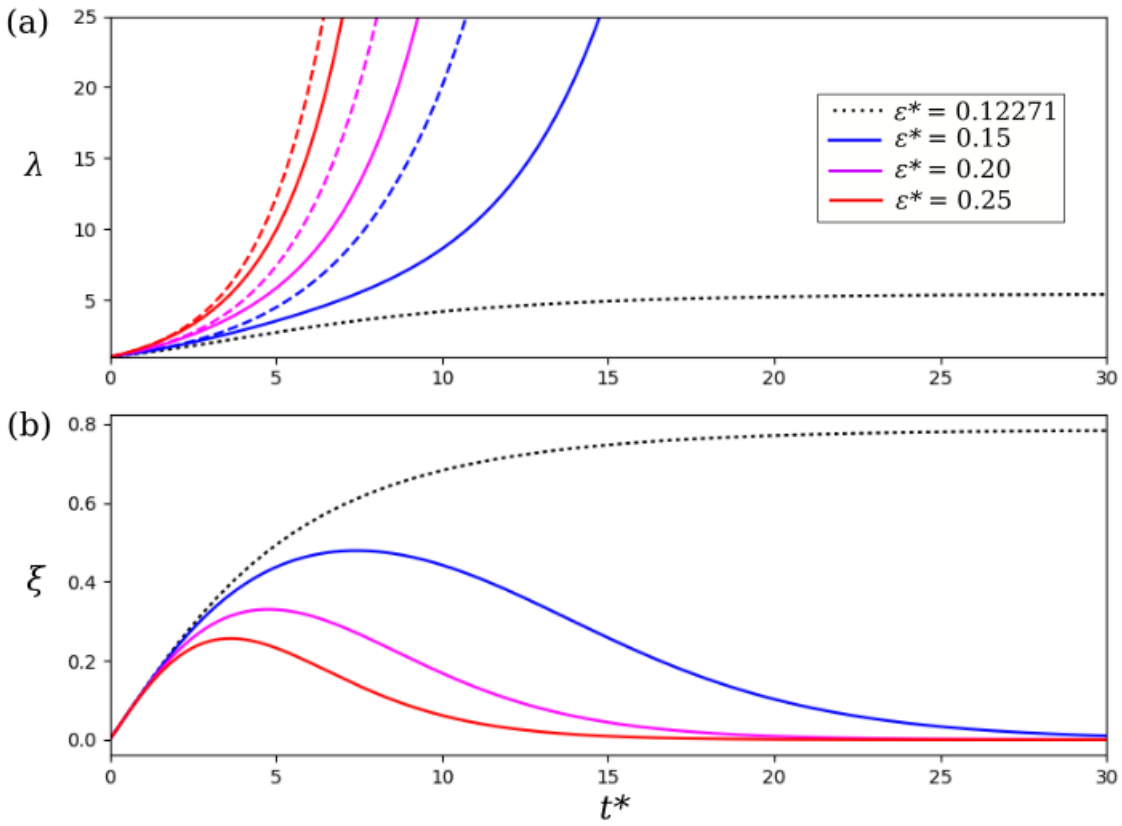

Figure 3.8: Temporal behavior of open (unstable) K81 orbits with circular initial condition. Shown are $\varepsilon^* = 0.15$ (blue), 0.20 (magenta), and 0.25 (red), including (a) $\lambda(t)$ and (b) $\xi(t)$. Also shown are the homoclinic orbit (black dotted line, $\varepsilon^* = 0.12271$) and exponential curves (dashed) given by Eq. 2.7 for corresponding values of ε^*.

dependent strain was not discussed by K81 or MS71, the K81 dynamical equations (Eqs. 3.6 & 3.7) are valid for time-dependent ε^*. If the applied strain varies slowly in time relative to the vortex rotation, the system preserves the adiabatic invariant $J = \oint p \, \mathrm{d}q$, which is the area enclosed by the orbit in (p,q) space [95]. Since the circular initial condition occupies only a point in the phase space for $\varepsilon^* = 0$, then as the strain is gradually increased, the system evolves in equilibrium along the lower branch of Eqn. 3.14 with $J \approx 0$. As ε^* approaches the limit ε_c^*, the center point and saddle point annihilate, and the vortex loses stability *via* a saddle-node bifurcation. For an initial condition with $J \neq 0$, as the strain is gradually increased, J is preserved until the orbit collides with the separatrix and the system loses stability *via* a homoclinic bifurcation. For sufficiently rapid changes in ε^*, the adiabaticity is broken, and $\mathrm{d}J/\mathrm{d}t \neq 0$.

Examples of the K81 dynamics under time-dependent strain are shown in Figs. 3.9 & 3.10. Figure 3.9 shows $\lambda(t)$ and $\xi(t)$ in response to a strain flow which is ramped up linearly from zero at rates $\mathrm{d}\varepsilon^*/\mathrm{d}t^* = 0.002$, 0.004, and 0.006. Also shown, as dashed lines, are the equilibrium values of $\lambda_0(\varepsilon^*)$ as calculated by Eq. 3.14. If the system behaves adiabatically, it is expected to follow these equilibrium curves. The lowest ramp rate shown in Fig. 3.9 closely follows the equilibrium, while the higher ramp rates show a greater level of divergence. However, a small orbit amplitude can be observed even for the lowest ramp rate. This is likely due to the kink in $\varepsilon^*(t)$ as the ramp begins, and can be eliminated by using a smooth function [96].

In Fig. 3.10, Gaussian time dependence is used,

$$\varepsilon(t) = \varepsilon_0 \exp\Big[-\Big(\frac{t-t_0}{\tau_s}\Big)^2\Big], \tag{3.16}$$

where the maximum strain $\varepsilon_0^* = 0.05$ occurs at $t_0^* \equiv t_0\omega_0 = 25$. Three different Gaussian pulse widths are used, $\tau_s^* \equiv \tau_s\omega_0 = 4$ (blue), 8 (magenta), and 12 (red). Here, since the pulse is smooth, adiabatic behavior can be observed for the widest pulse (red). In this case, the vortex distorts elliptically as the strain is applied, then returns to axisymmetry as the strain is removed. However, for more narrow pulses (magenta and blue), adiabaticity is broken, leaving the vortex with a residual finite-amplitude Kirchoff mode (Eq. 3.5) after the strain pulse has receded to zero.

The nonlinear dynamics of vortices under time-dependent external flow can be quite complicated, and in particular, chaotic [97]. Such behavior can be studied in the 8ST using, for example, a sinusoidal time dependence for the applied strain. Detailed experiments of this nature have yet to be conducted, although an example of preliminary data is shown in Chapter 5. A rigorous study of adiabatic behavior and chaotic dynamics under time-dependent flows is left for future work.

3.2.3 Instabilities

The K81 solutions described above are possible because an initially elliptical vortex patch remains elliptical at all times under the action of a simple strain flow such as Eq. 1.3. However, perturbations to the elliptical shape may be unstable. Perturbations about the freely rotating Kirchoff elliptical patch vortex (Eq. 3.5) were considered by Love (i.e., in

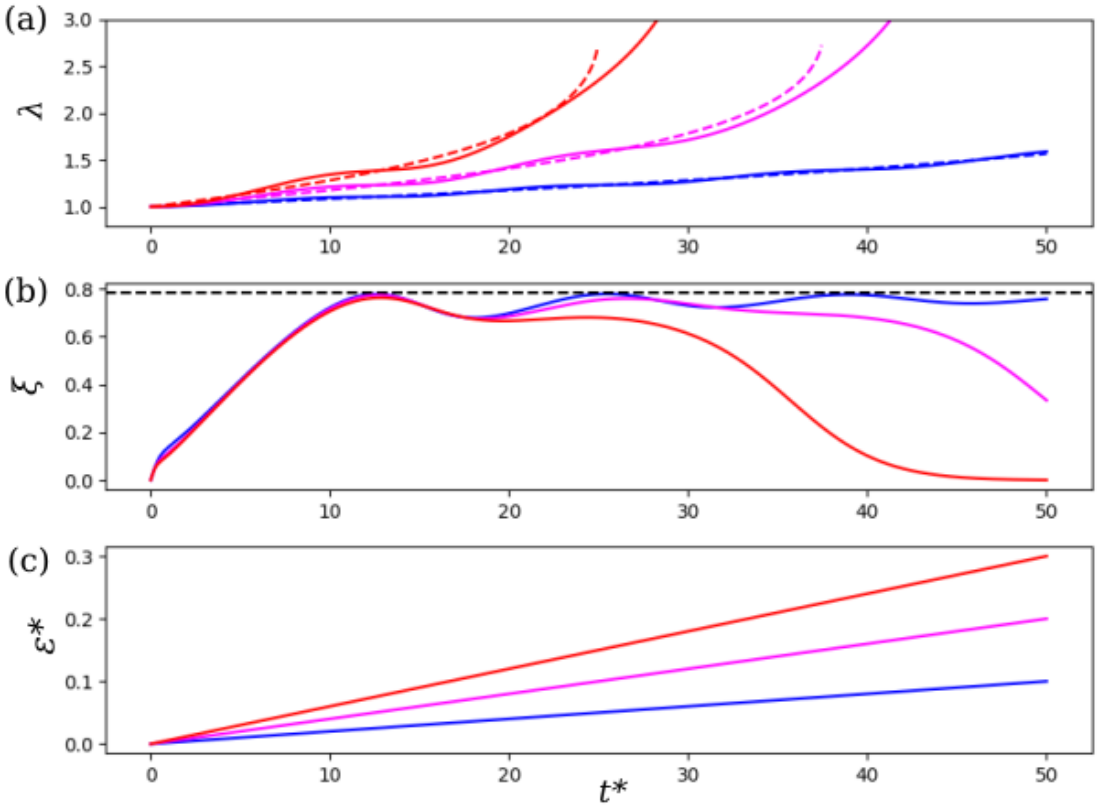

Figure 3.9: Response of the K81 system to an external strain which is ramped up linearly in time. The ramp rates are $d\varepsilon^*/dt^* = 0.002$ (blue), 0.004 (magenta), and 0.006 (red). The corresponding equilibria are shown as dashed lines.

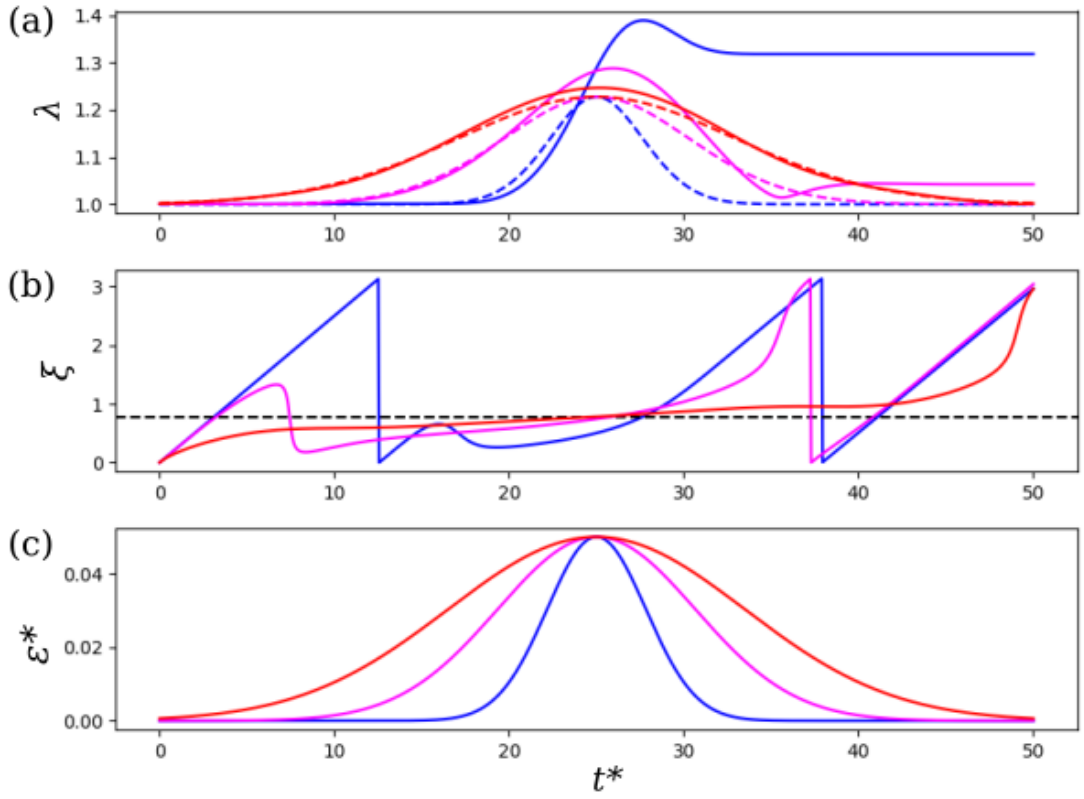

Figure 3.10: Response of the K81 system to an external strain with Gaussian time dependence. The normalized pulse width is $\tau_s^* = 4$ (blue), 8 (magenta), and 12 (red). The corresponding equilibria are shown as dashed lines.

the absence of external flow), who found that modes grow as $\exp(-i\eta t)$ where [98]

$$\eta^{*2} = \frac{1}{4}\left[\left[\frac{2m\lambda}{(\lambda+1)^2} - 1\right]^2 - \left(\frac{\lambda-1}{\lambda+1}\right)^{2m}\right], \tag{3.17}$$

with azimuthal wavenumber m, and normalized growth rate $\eta^* \equiv \eta/\omega_0$. MS71 considered the stability of their elliptical vortex equilibria (Eq. 3.14) in the presence of external shear and strain. For the case of applied strain, they found the growth rates to be [8]

$$\eta^{*2} = \frac{1}{4}\left[\left(\frac{2m\lambda}{\lambda^2+1} - 1\right)^2 - \left(\frac{\lambda-1}{\lambda+1}\right)^{2m}\right]. \tag{3.18}$$

Interestingly, the Love and MS71 results differ only in the denominator of the first term, presumably since the free Kirchoff vortex rotates whereas the MS71 strained vortex is stationary. These growth rates are plotted versus λ for a few of the lowest wavenumbers in Fig. 3.11. The $m = 2$ mode is marginally stable for Eq. 3.17, corresponding simply to the Kirchoff solution. For the MS71 instabilities, the $m = 2$ mode becomes unstable past $\lambda \approx 2.9$, which corresponds to the critical strain value $\varepsilon_c^* \approx 0.15$. Generally, higher wavenumbers become unstable as the vortex aspect ratio increases.

In the limit $\lambda \to \infty$, the vortex can be regarded as a thin shear layer (i.e., a filament). In this case, the Love instabilities can be identified with the familiar Kelvin-Helmholtz (KH) instability, whereas the MS71 instabilites can be thought of as KH instabilities under the influence of a background strain of a particular strength (a situation which was studied in detail by Dritschel [99]). While the KH instability was first studied in the context of an infinitely thin vortex sheet, Rayleigh [100] first considered the linear stability of a finite strip of piecewise constant vorticity; a useful recap is given by Dritschel [101]. The growth

rate of a mode on such a strip with wavenumber k is given by

$$\eta^{*2} = \frac{1}{4}\Big[(1-2bk)^2 - \exp(-4bk)\Big], \tag{3.19}$$

where b is the half-thickness of the strip, in analogy with the semiminor axis of an ellipse. Equation 3.19 is plotted in Fig. 3.12. Unstable modes exist for $0 < 2bk \lesssim 1.278$, and the fastest growing unstable mode occurs at $2bk \approx 0.7968$.

3.3 Vortex dynamics beyond the patch model

3.3.1 Overview of methodology

In the preceding section, the dynamics of the elliptical patch vortex were described entirely in terms of the two variables (λ, ξ), without discussion of the continuous flow field $\mathbf{v}(x,y)$. This is possible because the K81 solutions exactly satisfy the Euler equations, and so a higher-dimensional model is unnecessary (neglecting the aforementioned instabilities). However, the patch model is unphysical in that the vorticity gradient is infinite. Therefore, it is important to also consider the dynamics of smooth vorticity profiles in continuous fluids. An important theme here is that the competition between strain and vorticity is locally quantified by $s^*(x,y)$, as opposed to the patch description where the dynamics are set by the global parameter ε^*. Such a description is further motivated by prior experimental and numerical results, most notably the vortex stripping and filamentation phenomenon observed in water tank experiments [21] and contour dynamics simulations [54]. Filamentation presents a significant theoretical challenge, since it involves the nonlinear transfer of

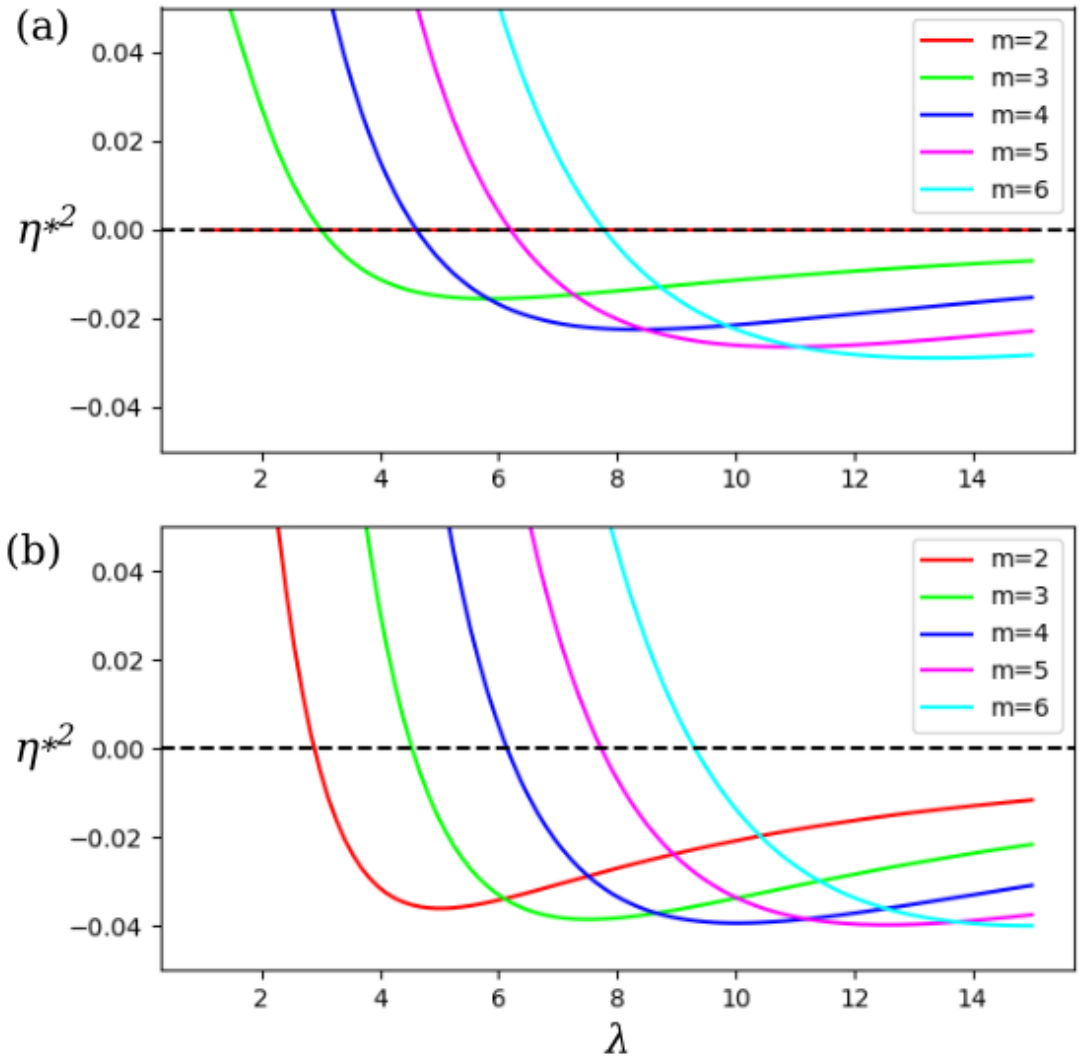

Figure 3.11: Normalized squared growth rates versus λ for (a) Love instabilities, and (b) MS71 instabilities. Shown are azimuthal wavenumbers $m = 2 - 6$. A black dashed line at $\eta^{*2} = 0$ indicates the stability boundary, where $\eta^{*2} < 0$ corresponds to unstable modes.

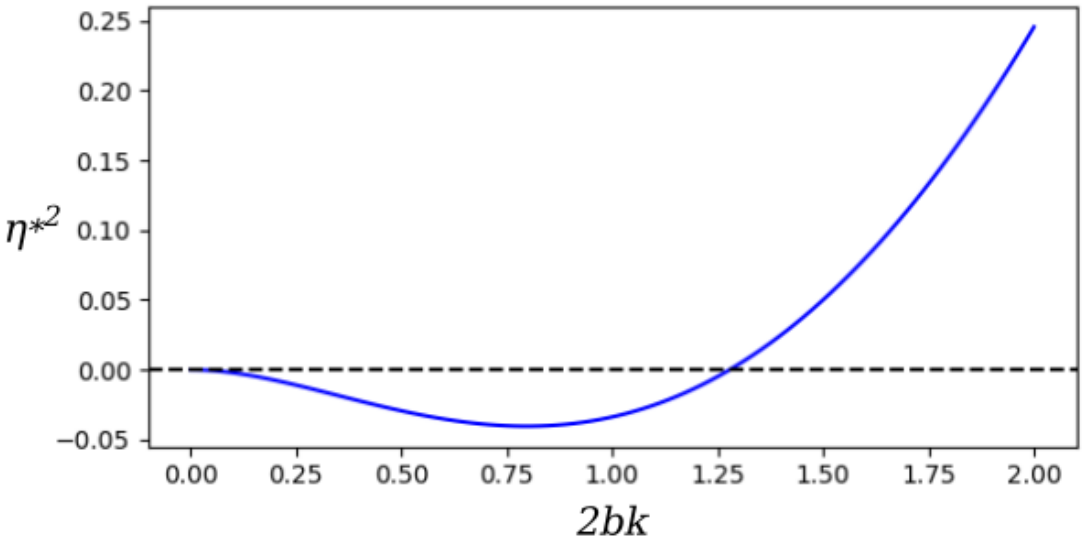

Figure 3.12: Normalized squared growth rates versus normalized wavenumber $2bk$ for the KH instability on a strip of piecewise constant vorticity. Instability occurs for $\eta^{*2} < 0$.

vorticity structures across a broad range of scales. This behavior is believed to be a key ingredient of the forward enstrophy cascade familiar to 2D turbulence theory [102, 4].

The dynamics of smooth vorticity distributions are in general strongly nonlinear and difficult to solve, so certain approximations must be used in order to make progress. For example, the Euler equations can be linearized in the limit of weak or strong strain, or in the limit of short timescales. In the case of weak applied strain, perturbations to the vorticity distribution are small, and so the Euler equations can be linearized about the steady-state axisymmetric vortex solution. For the case of strong strain, the dynamics can be linearized by neglecting the particular solution to the Poisson equation ψ_v, such that the vorticity is advected as a passive scalar (so-called rapid distortion theory [45]).

A few authors [42, 43, 44] have used these perturbative techniques in order to describe low-amplitude elliptical excitations of a smooth vortex. In each case, the motivation

was to study the damping properties of the excitation, although each used a slightly different approach. For example, Schecter [44] considered a weak strain which is applied impulsively (i.e., over a duration which is short compared to the vortex rotation period); Balmforth [43] considered a weak strain which rotates along with the vortex; and Lingevitch [42] considered a weak strain whose magnitude oscillates slowly with respect to the vortex rotation. Common to each approach is the idea that the applied strain excites a "quasi-mode" which can become decoherent over time due to filamentation behavior and/or differential rotation of the vortex.

However, in this dissertation, we consider marginal strain (i.e., near the critical strain threshold), so neither the strain nor the vorticity may be treated perturbatively. In this case, it can be instructive to analyze the flow behavior on short timescales. A linear description can be obtained by neglecting the feedback of the vorticity on the flow field; this amounts to considering the passive advection of the vorticity by the initial flow field. On longer timescales, the changing vorticity distribution influences the flow field as the nonlinearity becomes important.

3.3.2 The Okubo-Weiss criterion

By studying spatial derivatives of the velocity field, Okubo [46] and Weiss [47] (independently) derived approximate short-term descriptions of the 2D Euler equations which have been widely studied in the context of 2D turbulence. Local solutions are found for the evolution of the vorticity gradient $\nabla\omega$ in the Lagrangian frame, under the assumption

that strain and vorticity vary slowly relative to $\nabla\omega$. The solutions take the form

$$\frac{\mathrm{d}}{\mathrm{d}t}\nabla\omega \propto \exp Q^{\frac{1}{2}}t, \tag{3.20}$$

where $Q = \psi_{xy}^2 - \psi_{xx}\psi_{yy}$ is the Okubo-Weiss parameter, with subscripts indicating partial derivatives. Q is identified as the square of the eigenvalues of the velocity gradient tensor $\nabla\mathbf{v}$, which is equal to the difference of the squared strain magnitude and the squared vorticity, $Q = s^2 - \omega^2$. Normalizing to the vorticity yields $Q/\omega^2 \equiv Q^* = s^{*2} - 1$, so Q is a measure of the local strain-to-vorticity ratio. Eq. 3.20 admits oscillatory solutions when the vorticity dominates ($s^* < 1$), and exponential solutions when the strain dominates ($s^* > 1$). The oscillatory solutions are associated with stable vortices, and the exponential solutions are associated with filamentation behavior. Although the assumption used to derive Eq. 3.20 was found to be valid only in certain regions of flow [48], the Okubo-Weiss result has been extended to higher orders of approximation and to 3D [49, 50], and is widely used to differentiate stable vortex structures from regions of turbulent cascade activity.

3.3.3 A few examples

In the 8ST, the initial vorticity profiles are generally well approximated by Eq. 2.6, where $\alpha \to \infty$ corresponds to the vortex patch and $\alpha = 2$ to the Gaussian profile. Experimentally, α can be varied approximately from 2 to 10, where $\alpha \geq 5$ is loosely referred to as a "quasi-flat" profile due to good agreement with the elliptical patch theory (see Chapter 4). However, Eq. 2.6 is not localized, and is therefore difficult to handle mathematically. An alternative approach is to consider piecewise vorticity profiles which are monotonically de-

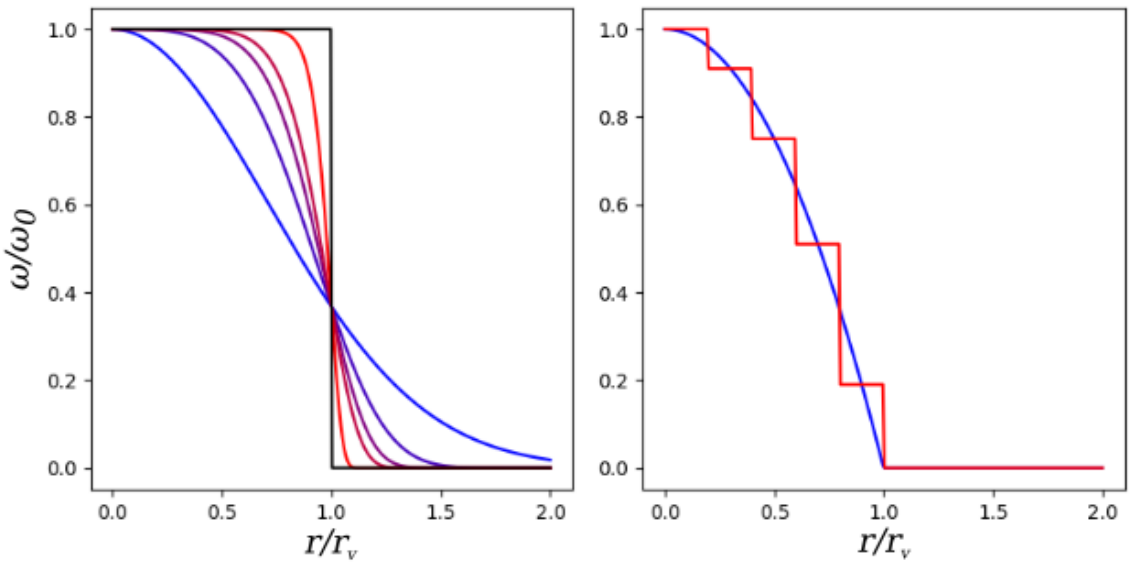

Figure 3.13: Examples of theoretical vorticity profiles. (a) profiles given by Eq. 2.6 for α =2, 4, 6, 8, and 20 (blue to red), and the patch profile (black); (b) a piecewise parabolic profile (blue) and an approximation using discrete steps [i.e., nested contours (red)].

creasing for $r < r_v$ and zero for $r > r_v$ [43, 44]. Another approach is the contour dynamics method, where smooth vorticity profiles are approximated using discrete steps [53, 55, 51]. Some examples of these profiles are shown in Fig. 3.13.

For example, consider the flow fields of a circular vortex patch profile and a piecewise parabolic profile. Taking $\omega_0 = 1$ and $r_v = 1$, the vorticity of the patch profile and the associated stream function is given by

$$\omega(r) = \begin{cases} 1 & r \leq 1 \\ 0 & r > 1 \end{cases} \tag{3.21}$$

$$\psi_v(r) = \begin{cases} \frac{1}{4}r^2 & r \leq 1 \\ \frac{1}{2}\ln r + \frac{1}{4} & r > 1. \end{cases} \tag{3.22}$$

For the piecewise parabolic profile,

$$\omega(r) = \begin{cases} 1 - r^2 & r \leq 1 \\ 0 & r > 1 \end{cases} \tag{3.23}$$

$$\psi_v(r) = \begin{cases} \frac{1}{4}r^2 - \frac{1}{16}r^4 & r \leq 1 \\ \frac{1}{4}\ln r + \frac{3}{16} & r > 1. \end{cases} \tag{3.24}$$

Here, the streamlines associated with ψ_v are all circular, and there exists a single stagnation point (defined by $\mathbf{v} = \mathbf{0}$) at the origin. However, when ψ_v is superposed with a strain flow ψ_s given by Eq. 1.3, the flow contains additional stagnation points for certain values of ε^*. The flow geometry for these two cases is shown in Fig. 3.14 for $\varepsilon^* = 0.2$, 0.4, and 0.6.

For the circular patch, two saddle points exist outside the vortex at location (x_0, y_0) where $x_0 = 0$ and $y_0 = \pm(2\varepsilon^*)^{-1/2}$, and one center point exists at the origin. The saddle points define a separatrix in the flow field that divides open, hyperbolic streamlines from closed, elliptical ones. As ε^* increases from zero, the stagnation points move toward the origin along the $y-$axis. When $\varepsilon^* = 1/2$, the stagnation points coincide with the edge of the vortex, and the streamlines inside the vortex are vertical. When $\varepsilon^* > 1/2$, there is a single stagnation point at the origin, but it is a saddle point. Thus, as ε^* is increased through $1/2$, the saddle points jump immediately to the origin and annihilate the stable point, changing the topology of the stream function. The separatrix intersects the vorticity distribution along the $x-$axis for $\varepsilon^* \gtrsim 0.14$, and it shrinks as ε^* is increased before disappearing at $\varepsilon^* = 1/2$. The Okubo-Weiss stability boundary, defined by $Q = 0$, coincides with the vortex boundary (a circle of unit radius) for $0 < \varepsilon^* < 1/2$, otherwise Q is everywhere positive and

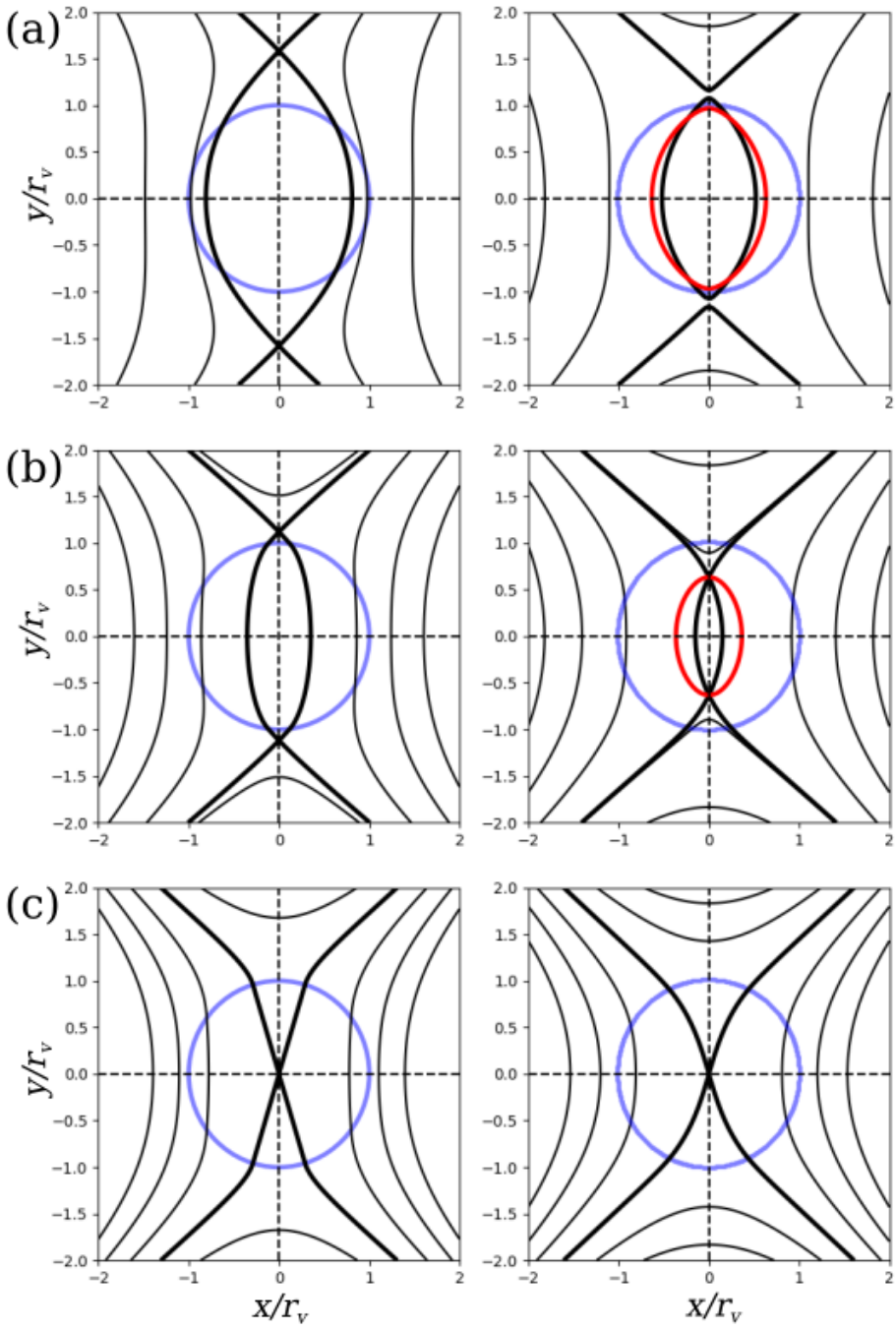

Figure 3.14: Flow geometry for a circular vortex patch (left) and a parabolic vorticity distribution (right). The applied strain magnitude is $\varepsilon^* =$ (a) 0.2, (b) 0.4, and (c) 0.6. Shown are streamlines (black) including the separatrix (thick black), the boundary of the vortices (thick blue), and the Okubo-Weiss stability boundary defined by $Q = 0$ (thick red).

the entire flow field is hyperbolic. Further discussion of topological changes in 2D fluid flows can be found in Refs. [103, 104].

In the case of the parabolic profile, stagnation points exterior to the vortex are given by $x_0 = 0$, $y_0 = \pm(4\varepsilon^*)^{-1/2}$. For $\varepsilon^* > 1/4$, the stagnation points intersect the vorticity distribution, and their locations are instead given by the solution to $y_0(y_0^2/4 + \varepsilon^* - 1/2)$. If $1/4 < \varepsilon^* < 1/2$, then $y_0 = 0$, $\pm[4(1/2 - \varepsilon^*)]^{-1/2}$, where the point at the origin is stable and the other two are symmetric saddles. Again, the flow topology changes at the critical value $\varepsilon^* = 1/2$ as the saddles annihilate the stable point. However, with a smooth profile, the saddles move smoothly toward the origin as ε^* is increased rather than jumping. The Okubo-Weiss stability boundary is shown for the parabolic profiles in Fig. 3.14; it shrinks as ε^* increases before disappearing completely as the topology changes.

Both the stream function separatrix and the Okubo-Weiss criterion serve as approximate predictors of the local stability of the vorticity. Knowledge of the full flow field is necessary to find the stream function separatrix, whereas the Okubo-Weiss stability criterion can be calculated locally by differentiating the velocity field. Both criteria are valid on short timescales where the vorticity is approximately static. On longer timescales the nonlinear evolution of the vorticity field must be taken into account, and so these stability criteria may be inaccurate.

For example, the center of a circular vortex patch with $0.123 < \varepsilon^* < 0.5$ initially follows closed streamlines, whereas the nonlinear K81 theory predicts eventual destruction. As the patch distorts elliptically, it contributes to the strain tensor. Based on the particular solution to the Poisson equation ψ_v, an elliptical vortex patch produces a constant strain

within the patch with eigenvalue

$$s_v = \omega_0 \left(\frac{\lambda - 1}{\lambda + 1}\right) \tag{3.25}$$

and orientation $\xi - \pi/4$. Therefore, the total strain inside the vortex patch can be much larger than the applied strain. For example, a patch in equilibrium just below the threshold has $\varepsilon^* \approx 0.15$, $\lambda \approx 2.9$, and $s_v/2 \approx 0.25$, so the self-strain exceeds the applied strain significantly.

Chapter 4

Experiments with constant strain flows

Experimental data for the evolution of an initially axisymmetric electron plasma vortex in response to a simple strain flow were shown in Fig. 1.3 for two values of normalized strain, $\varepsilon^* = 0.116$ and 0.13, that are below and above the critical strain threshold. In this chapter, we compare these and other data, and corresponding vortex-in-cell simulations, with theoretical predictions of the elliptical patch model. Additionally, departures from the elliptical patch theory are studied using smooth profiles.

4.1 Tests of the elliptical patch model

Data are presented here from experiments with the 8ST comparing elliptical distortions of a strained vortex to predictions of the elliptical patch theory [8, 39]. Ellipses are fit to the measured half-maximum vorticity contours using the numerical routine described in Chapter 2. This yields experimentally determined values of the aspect ratio of the ellipse λ

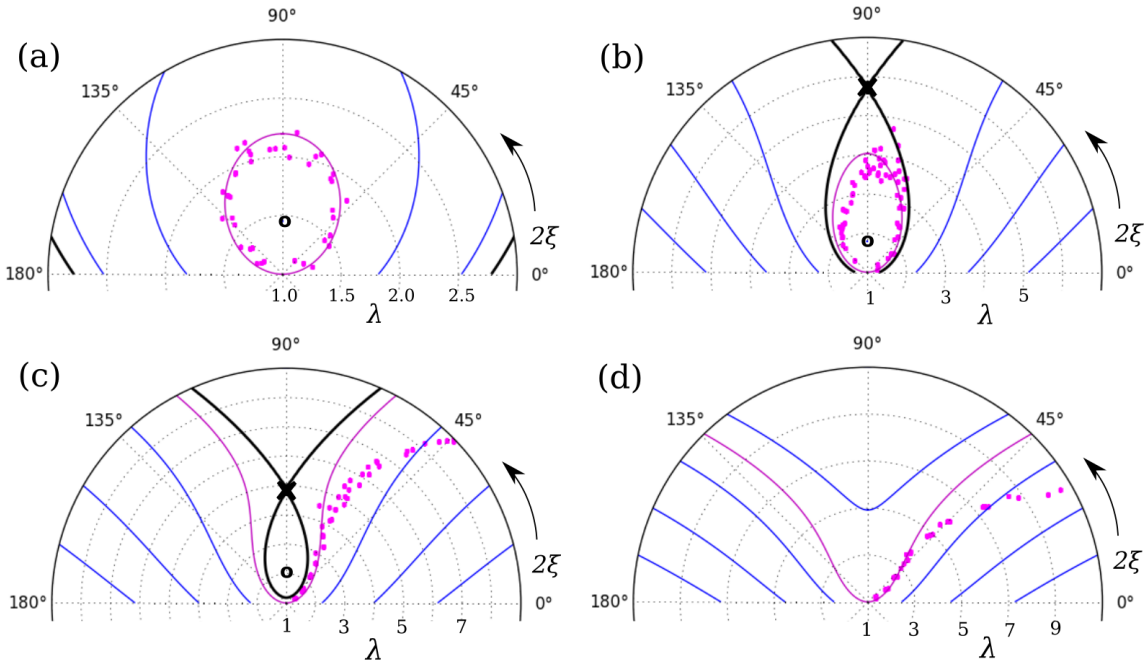

Figure 4.1: Comparison of experimental data and K81 predictions for dynamical orbits in $(\lambda, 2\xi)$ space. Here, $\varepsilon^* =$ (a) 0.087, (b) 0.116, (c) 0.13, and (d) 0.152. Contours of the K81 Hamiltonian are shown (solid lines), including open orbits (blue lines), the separatrix (thick black line), and the $C = 1$ orbit (magenta line). Fixed points of the K81 system are shown as (X) and (O), and experimental data are shown as magenta circles.

and the orientation ξ with respect to the applied strain axis. These quantities are compared directly to the theory with no fitted parameters. For comparison to the patch model, quasi-flat initial vorticity profiles are used, where $\omega(r)$ is approximately given by Eq. 2.6 with smoothness exponent $\alpha \geq 5$.

4.1.1 K81 orbits

The measured evolution of an initially axisymmetric vortex subject to a constant external strain flow is shown in Fig. 4.1. The initial vorticity profile is well described by Eq. 2.6 with $\alpha \approx 6$ [c.f. Fig. 2.8 (b)], and the strain flow is given by Eq. 1.3. The ellipse

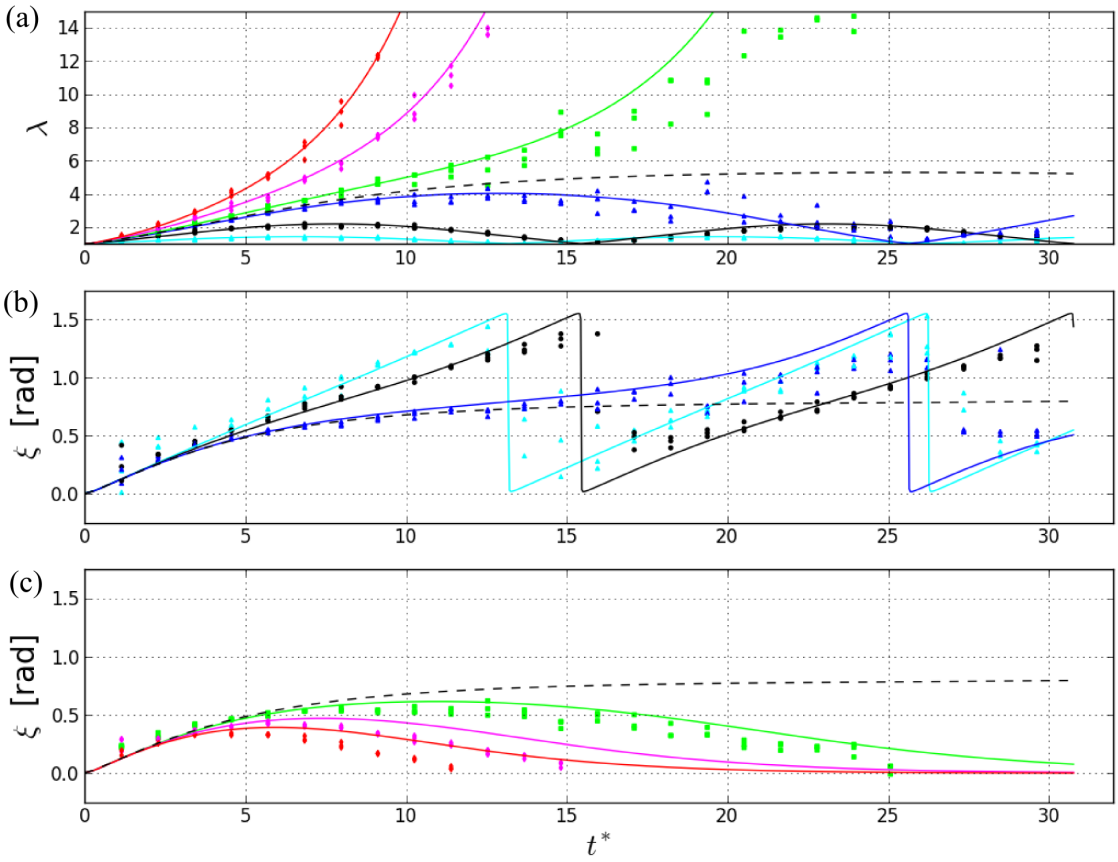

Figure 4.2: Comparison of experimental data and K81 predictions for $\lambda(t^*)$ and $\xi(t^*)$. (a) $\lambda(t^*)$, (b) $\xi(t^*)$ (closed orbits), and (c) $\xi(t^*)$ (open orbits), where $t^* = t\omega_0$ and $\omega_0 = 228$ krad/s, for normalized strains $\varepsilon^* = 0.044$ (cyan), 0.087 (black), 0.116 (blue), 0.13 (green), 0.152 (magenta), and 0.173 (red). Predictions of K81 elliptical patch theory are shown as solid lines, including the threshold orbit $\varepsilon^* = 0.123$ (black dashed line).

parameters $(\lambda, 2\xi)$ are plotted in Fig. 4.1 for normalized strain $\varepsilon^* = 0.087$, 0.116, 0.13, and 0.152 [panels (a)-(d), respectively], with central vorticity $\omega_0 = 228$ krad/s. Data are taken at intervals of 5 μs (1.1 ω_0^{-1}), and repeated three times for statistics. These data are compared to the K81 prediction for $C = 1$. Contours of the K81 Hamiltonian (Eq. 3.9) are plotted over the data including open orbits, the $C = 1$ orbit, and the separatrix. Note that in Fig. 4.1 (c), the circular initial condition is unstable, although closed orbits still exist inside the separatrix; whereas in panel (d) the separatrix has disappeared.

These data are also plotted versus normalized time in Fig. 4.2. Shown are $\lambda(t^*)$ in panel (a), and $\xi(t^*)$ in panels (b) and (c), for six values of strain, $\varepsilon^* = 0.044$, 0.087, 0.116, 0.13, 0.152, and 0.173. Predictions of the K81 theory for $C = 1$ are shown as solid lines. The lowest strain values $\varepsilon^* = 0.044$, 0.087, and 0.116 are below the dynamical stability threshold $\varepsilon_d^*(C = 1) \approx 0.123$ (which is shown as a dashed line), so the system executes periodic orbits in (λ, ξ) space. The higher strain values $\varepsilon^* = 0.13$, 0.152, and 0.173 are above the threshold, and so λ grows without bound as ξ approaches 0.

The data in Figs. 4.1 and 4.2 generally agree with the theory, with a few exceptions. Since behavior of the K81 system is unstable near the separatrix, data for the strain values just above and below the threshold (i.e., $\varepsilon^* = 0.116$ and 0.13) become noisy at later times. For the above-threshold cases ($\varepsilon^* = 0.13$, 0.152, and 0.173), the experimentally measured ξ diverges from that of the theory when λ is large. This is a manifestation of the dump rotation effect discussed in Sec. 2.2. Since the ellipse continues to rotate slightly during the diagnostic process, the data here are corrected using a uniform shift of $\Delta\xi = -10^\circ$; however, the rotation shift decreases as the vortex distorts, similar to the trend in Eq. 3.5.

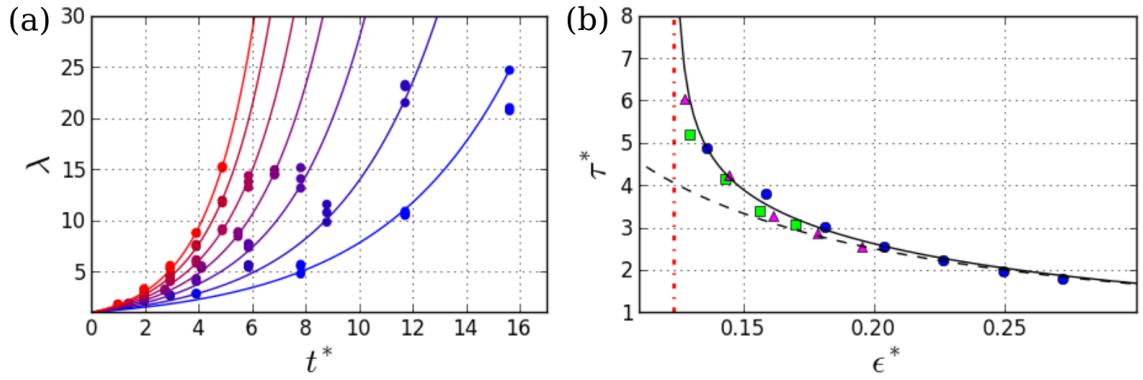

Figure 4.3: Dynamics of unstable elliptical vortices above the critical strain threshold. (a) data (circles) for $\lambda(t^*)$ for $\varepsilon^* = 0.136, 0.159, 0.181, 0.204, 0.227, 0.249, 0.272$ (blue to red), with exponential fits (lines), where $\omega_0 = 195$ krad/s. (b) normalized time constant of the exponential fits $\tau^* \equiv \tau\omega_0$ for $\omega_0 = 195$ (blue), 260 (green), and 326 (magenta) krad/s. Also shown are the K81 theory (solid black line), assuming passive vorticity $\tau^* = 1/2\varepsilon^*$ (dashed line), and the stability boundary $\varepsilon_d^* = 0.123$ (dotted line).

Well above the critical strain threshold $\varepsilon^* \gg \varepsilon_d^*$, K81 elliptical patch theory predicts an exponential behavior $\lambda(t) = \exp(t/\tau)$, where $\tau = 1/2\varepsilon$ (Eq. 2.7). For $\varepsilon^* > \varepsilon_d^*$, exponential curves are fit to data for $\lambda(t)$ to find τ. Figure 4.3 (a) shows measurements of $\lambda(t)$ for $\omega_0 = 150$ krad/s and $\varepsilon^* = 0.136, 0.159, 0.181, 0.204, 0.227, 0.249, 0.272$ (blue to red) with exponential fits as solid lines. Figure 4.3 (b) shows the normalized time constant $\tau^* \equiv \tau\omega_0$ associated with the exponential fits as a function of ε^* for $\omega_0 = 195$, 260, and 326 krad/s, compared to the K81 prediction (solid line). The prediction assuming passive vorticity ($\tau^* = 1/2\varepsilon^*$) is shown as a dashed line, and the K81 stability limit $\varepsilon_d^*(C = 1)$ is shown as a vertical dotted line. Figure 4.3 shows that the assumption of passive vorticity is accurate for roughly $\varepsilon^* > 0.20$; whereas for $0.123 < \varepsilon^* < 0.20$ the stretching rate is reduced (i.e., the lifetime of the vortex is extended), and $\lambda(t)$ is not exactly exponential because the system stalls near the saddle point.

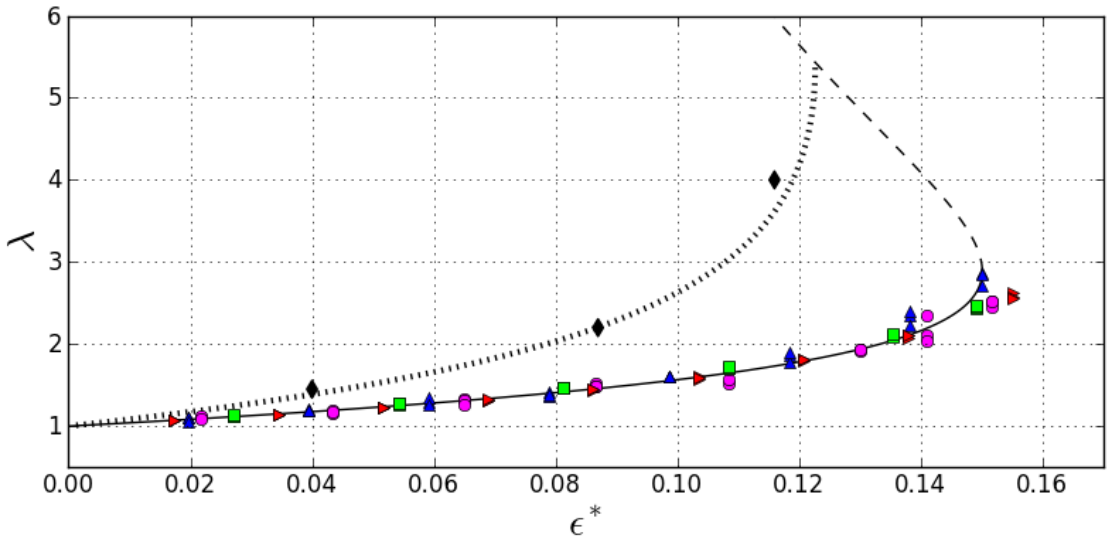

Figure 4.4: Demonstration of MS71 strained vortex equilibria. Data are obtained using a slow linear ramp function $\varepsilon^* \propto t$, for $\omega_0 = 143$ krad/s (red), 182 krad/s (green), 228 krad/s (magenta), and 313 krad/s (blue). They are compared to the stable branch (solid line) of the MS71 theory (Eq. 3.14). The unstable branch is also shown (dashed line). Data and predictions for the maximum aspect ratio in a K81 orbit λ_m are shown as well, with theory given by Eq. 3.15 (dotted line) and data (black diamonds).

4.1.2 MS71 equilibria

For the case of constant strain imposed on an initially axisymmetric vortex, as in Fig. 4.1, stationary solutions are not possible. However, if the strain is gradually increased, the system can be expected to behave adiabatically. In this case, the action J remains approximately zero, such that the (λ, ξ) are given by the MS71 equilibrium solution (Eq. 3.14). Data are shown in Fig. 4.4, where λ is studied by the imposition of a slow, linearly ramped strain, for $\omega_0 = 143$, 182, 228, and 313 krad/s, and ramp rates in the range $d\varepsilon^*/dt^* = 0.0025$ - 0.005. The theoretical MS71 equilibria are shown, including both the stable (solid) and unstable (dashed) branches. The data agree with the theory, to within the experimental uncertainty, up to the stability limit $\varepsilon_c^* \approx 0.15$. This implies that the system

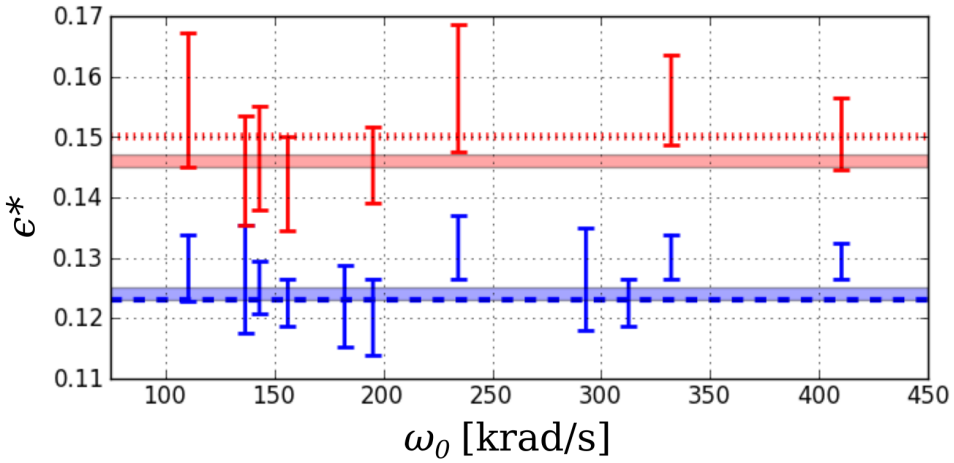

Figure 4.5: Stability threshold measurements versus peak vorticity. The thresholds $\varepsilon_d^*(C = 1)$ for initially axisymmetric vortices subject to constant strain are shown (blue). Also shown are those for vortex equilibria ε_c^* using a linearly ramped strain (red). K81 and MS71 predictions are shown ($\varepsilon^* = 0.123$, dashed, and 0.15, dotted), as are results of vortex-in-cell simulations (shaded). The experimental measurements are indicated by error bars (see text for details).

is behaving adiabatically. However, numerical solutions to Eqs. 3.6 & 3.7 indicate that a small amplitude orbit may be excited due to the kink in $\varepsilon(t)$ as the linear ramp begins (c.f. Fig. 3.9) [96].

Also shown in Fig. 4.4 is the maximum aspect ratio λ_m reached by a K81 orbit with $C = 1$ (Eq. 3.15, dotted line), with data for $\varepsilon^* = 0.045$, 0.087, and 0.116, corresponding to the orbits shown in Fig. 4.1. Again, the data and theory are in close agreement.

4.1.3 Stability threshold measurements

Shown in Fig. 4.5 are experimental measurements of both the equilibrium and dynamical stability thresholds for quasi-flat vortices with $\alpha \geq 5$ (red and blue error bars, respectively). These data are compared to results of vortex-in-cell simulations (shaded

bars), and predictions of the elliptical patch theory $\varepsilon_c^* \approx 0.15$ (dotted) and $\varepsilon_d^*(C=1) \approx 0.123$ (dashed). Experimentally, the dynamical stability threshold is found by varying ε^* and observing λ at late times in the evolution ($t \sim 20\omega_0^{-1}$), such that the stability or lack thereof is evident (c.f. Fig. 4.2). The measurements of $\varepsilon_d^*(C=1)$ are plotted against the peak vorticity ω_0 in Fig. 4.5, where the bottom (top) end of the error bar corresponds to a strain where five consecutive runs show stable (unstable) behavior. A similar technique is used to measure the equilibrium stability limit ε_c^*. In this case, the strain is slowly increased using a linear-ramp time dependence with $d\varepsilon^*/dt^* \sim 0.005$ (c.f. Fig. 4.4), and then held at a particular value of ε^* to determine the stability. The stability thresholds are found in a similar manner using vortex-in-cell simulations. The experimental measurements give $\varepsilon_c^* = 0.15 \pm 0.01$ and $\varepsilon_d^*(C=1) = 0.124 \pm 0.006$. The simulations give $\varepsilon_c^* = 0.145 - 0.147$ and $\varepsilon_d^*(C=1) = 0.123 - 0.125$.

Thus the stability threshold observed in experiments and simulations are in good agreement with the predictions of elliptical patch theory, except for a slightly reduced value of ε_c^* in the simulations. Small deviations such as this may be associated with the smoothness of the profile at the edge of the vortex. Alternatively, the finite ramp time of the strain could lead to breaking of the adiabaticity and therefore to slightly reduced stability limits. The dependence of the stability limits on profile smoothness is investigated in further detail in Fig. 4.8. Constancy of the experimental results over a wide range of ω_0 lends confidence that non-ideal or 3D effects depending on the electron density are negligible.

In conclusion, many aspects of the elliptical vortex patch model studied by K81 and MS71 have been tested using realistic, quasi-flat vorticity profiles that are subjected

to external strain. In general, the global dynamics of the vortex cores are found to be in good agreement with the theory. However, the analysis so far considered only the ellipse parameters (λ, ξ) obtained using the elliptical fitting routine, whereas the CCD images contain information of the full vorticity field. In the next section, we consider the dynamics of the continuous vorticity distribution, which is beyond the scope of the elliptical patch model.

4.2 Physics beyond the elliptical patch model

The agreement between the experiments and the elliptical patch theory for quasi-flat profiles raises the following questions: How "flat" must the profile be in order to agree with the theory? How are the vortex dynamics modified relative to the patch theory predictions when the profile is not sufficiently flat? These questions are addressed here by studying the full flow field as described by the 2D Euler equations (Eqs. 1.2), and by studying non-flat profiles.

4.2.1 The stream function separatrix and the Okubo-Weiss criterion

The vorticity evolution data shown in Fig. 1.3 for $\varepsilon^* = 0.116$ and 0.13 are plotted again in Fig. 4.6, with overlaid streamlines, the separatrix (thick), and the Okubo-Weiss stability criterion $Q = 0$ (dashed). At $t = 0$, a small amount of circulation exists outside the separatrix; and as the vorticity evolves, the separatrix changes accordingly. Below the critical strain threshold [panel (a)], peripheral vorticity is carried into filaments exterior

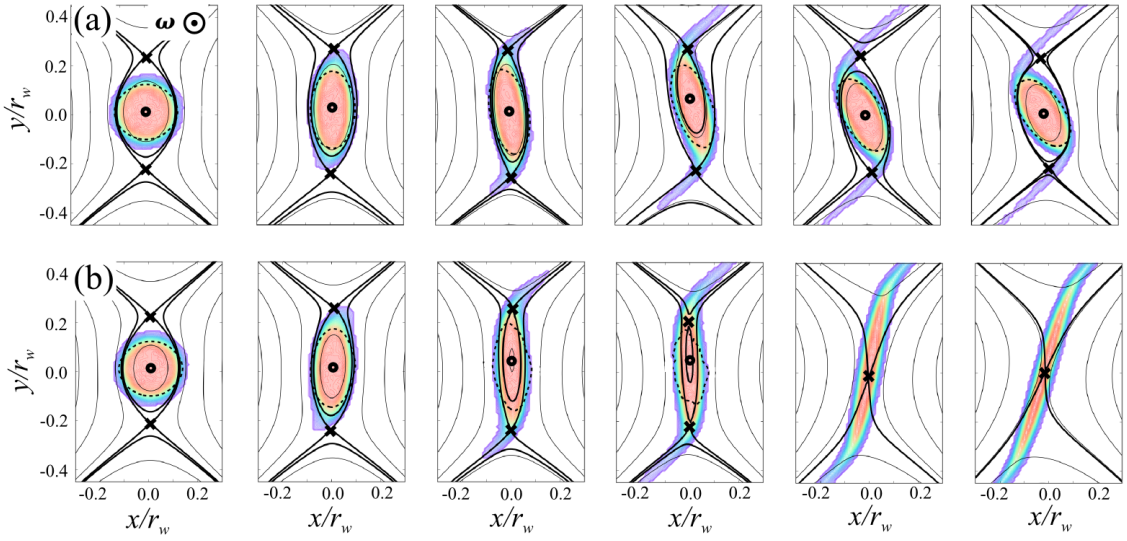

Figure 4.6: Evolution of the vorticity distribution, stream function, and Okubo-Weiss criterion. Vorticity data are shown (color maps) for $\varepsilon^* = 0.116$ (a) and 0.13 (b) at increments of 20 μs ($4.56\omega_0^{-1}$). Streamlines are overlaid (black lines), as are the separatrix (thick black line), saddle points (X), center points (O), and the Okubo-Weiss stability boundary defined by $Q = 0$ (dashed line). Note the topological change of the stream function between 4th and 5th panels in row (b).

to the separatrix, while the majority of the circulation remains on closed streamlines inside the separatrix. Above the critical threshold [panel (b)], the separatrix shrinks as the vortex distorts. The saddle points move inward and annihilate the center point at the origin between the fourth and fifth panels, thus changing the stream function topology as the vortex is destroyed. The Okubo-Weiss local stability criterion shows qualitatively similar behavior to the separatrix, disappearing at the same point in Fig. 4.6 (b). Quantitatively, however, stable regions predicted by the separatrix and the Okubo-Weiss theory are slightly different in shape and spatial extent. Notably, according to the stream function separatrix, there may exist regions which are vorticity-dominated where the local vorticity is small or zero (specifically, above and below the vortex, near the X-points) due to nonlocality of the Poisson equation; whereas these regions are classified as stable by the Okubo-Weiss criterion.

The temporal evolution of these data are studied quantitatively in Fig. 4.7 for six values of ε^*. Shown are (a) the total normalized circulation integrated over the domain Γ/Γ_0; (b) the circulation $\Gamma_{\text{sep}}/\Gamma_0$ contained inside the separatrix; (c) the circulation Γ_Q/Γ_0 inside the $Q = 0$ surface; and (d) the normalized Okubo-Weiss parameter Q_0^* evaluated at the origin (c.f. Eq. 3.20), where the stability boundary $Q_0^* = 0$ is shown as a black dashed line. Here, Γ_{sep} and Γ_Q are calculated as $\int_S \omega dA$ where S corresponds to the region enclosed by the separatrix or the $Q = 0$ surface. Error bars show averages over three data points. These results are calculated from the same data shown in Figs. 1.3, 4.1, and 4.2. At late times, Fig. 4.7 (a) demonstrates loss of circulation to the wall gaps (note that for the three strain values above the threshold, Γ/Γ_0 eventually tends to zero). Panels (b) and

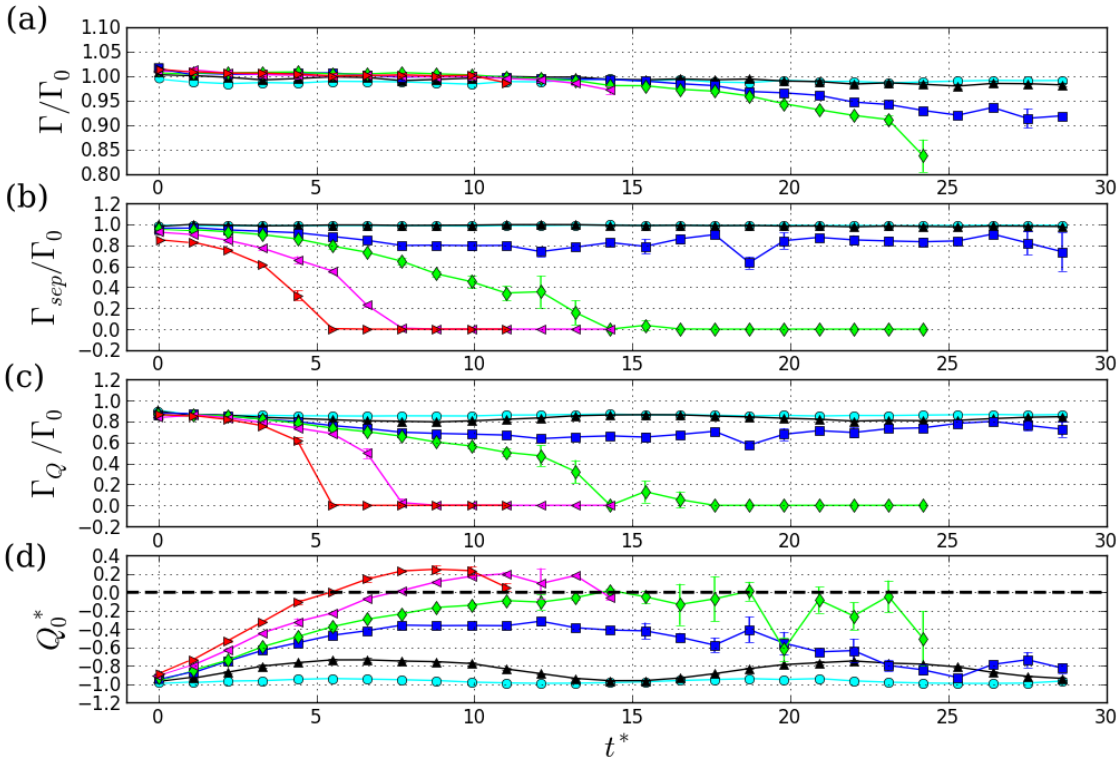

Figure 4.7: Local stability inside a vortex versus time. Here, $\varepsilon^* = 0.045$ (cyan), 0.087 (black), 0.116 (blue), 0.13 (green), 0.152 (magenta), and 0.173 (red). (a) the normalized total circulation, (b) circulation inside the separatrix, (c) circulation inside the Okubo-Weiss stability boundary, and (d) value of the normalized Okubo-Weiss parameter at the origin, compared to the stability threshold (dashed line). Note that $\Gamma_{sep}, \Gamma_Q \to 0$, and Q_0^* crossing zero indicate a change of the stream function topology.

(c) show the shrinking and disappearance of the separatrix and Okubo-Weiss stable region for the cases above the strain threshold and destabilization of peripheral circulation for the case slightly below the threshold. In Fig. 4.7 (d), $Q_0^* = s^{*2} - 1$ increases dramatically from its initial value $4\varepsilon^{*2} - 1$ due to the self-strain s_v as the vortex distorts. For the three strain values above the threshold, Q_0^* crosses the stability boundary as the stream function changes topology. Thus, the initial stream function separatrix and the Okubo-Weiss criteria fail to predict the eventual destruction of the vortex due to nonlinear evolution of the vorticity. The temporal behavior of Γ_{sep} and Γ_Q are comparable, although not exactly in agreement. Further study of these local stability criteria is left for future work.

4.2.2 Shifted stability limits

Reference [83] demonstrated a slightly reduced critical strain threshold for smooth, Gaussian vorticity profiles relative to quasi-flat ones. This effect is analyzed further in Fig. 4.8, which shows the dynamical threshold $\varepsilon_d^*(C = 1)$ versus the smoothness exponent α. Experimental and numerical data are shown, as is the K81 strain threshold $\varepsilon_d^*(C = 1)$. The error bars are found in the same manner described above in the discussion of Fig. 4.5. Here, the simulations use profiles given by Eq. 2.6, with α varying from 2 to 10. For the experimental data, α is found using a fit to Eq. 2.6. Both the experimental and numerical data show a clear shift to lower stability threshold at low α (i.e., approaching Gaussian profiles). Data are taken here for $\omega_0 = 347$ - 571 krad/s, and radius $r_v = 0.1$ - $0.2\ r_w$. The experimental profiles agree closely with Eq. 2.6. Other data (not shown) suggest that the threshold is lowered by about 10% for $r_v \approx 0.3 r_w$, likely due to the influence of the wall.

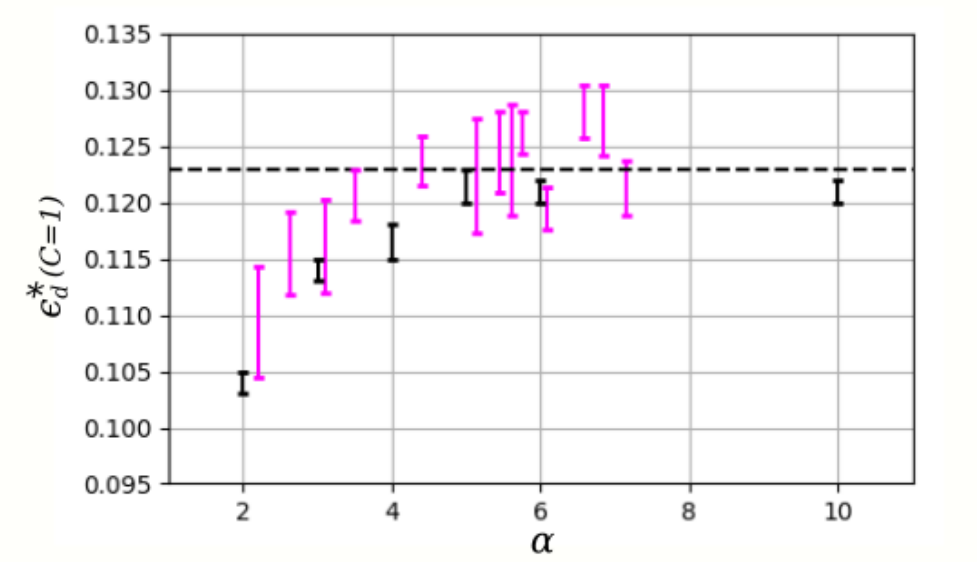

Figure 4.8: Dynamical stability threshold $\varepsilon_d^*(C=1)$ for constant strain versus smoothness exponent α. The K81 theoretical stability limit for $\alpha \to \infty$ is shown (dashed line), as are simulations (black) and experimental data (magenta).

Additionally, results (also not shown) for profiles which are not good fits to Eq. 2.6 indicate that the threshold can be sensitive to specific details of the profile.

Vorticity and stream function data for the evolution of a Gaussian vortex relative to a quasi-flat vortex are shown in Fig. 4.9. Here, (a) shows a Gaussian vortex with $\alpha \approx 2$, and (b) shows a quasi-flat vortex with $\alpha \approx 8$. For both profiles, $\omega_0 = 785$ krad/s and $\varepsilon^* = 0.112$. Consecutive panels are separated by time $t^* = 12.56$, beginning at $t^* = 0$. The strain magnitude is chosen just slightly below the K81 threshold, such that the flat vortex survives. However, the Gaussian vortex is destroyed, thus demonstrating the threshold shift shown in Fig. 4.8. A plausible explanation for this shift is that the smooth profiles have substantial filamentary structures near the saddle points which augment the total strain in the vortex core. In contrast, although quasi-flat profiles may also show filamentary behavior, the circulation contained in these filaments is small; and therefore, the effect of the filaments

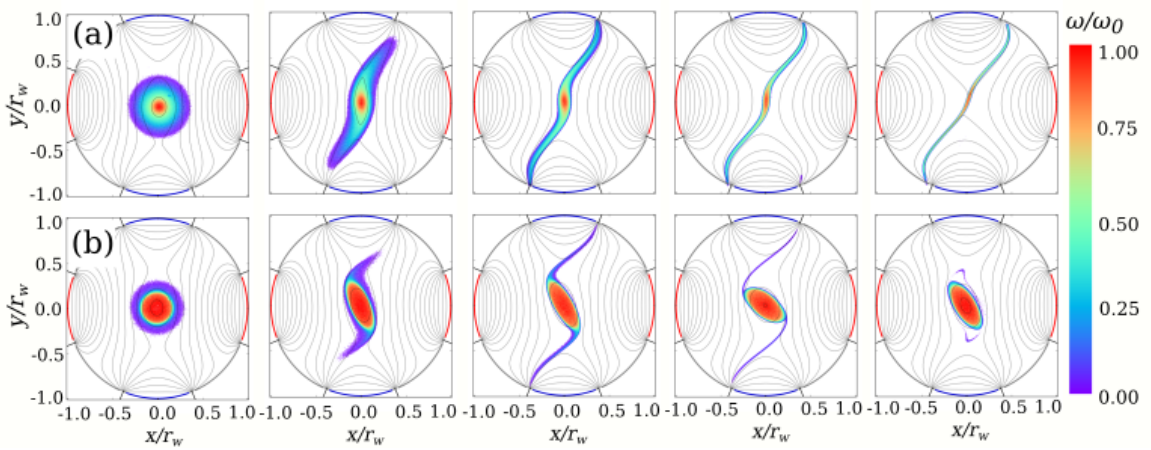

Figure 4.9: Experimental evolution of vorticity (color maps) and stream function (lines) for (a) a Gaussian profile, and (b) a quasi-flat profile with $\alpha \approx 8$. Both rows (a) and (b) correspond to $\omega_0 = 785$ krad/s, $\varepsilon^* = 0.112$, and panels are separated by time $t^* = 12.56$ beginning with $t^* = 0$.

on the core is negligible.

4.2.3 Stripping of peripheral circulation

For a smooth vortex below the critical destruction threshold, although the core may survive, some of the outer circulation can be stripped away. Figure 4.10 shows the total remaining circulation in a vortex subjected to constant strain for a duration $t = 25\omega_0^{-1}$. Experimental data (magenta) agree well with simulations (black, with guide lines) for both a quasi-flat profile with $\alpha \approx 7$ and a smooth profile with $\alpha = 2$. The K81 destruction threshold is shown as well (black dashed line). The data show that smooth vortices suffer heavy stripping due to the external strain, even well below the destruction threshold.

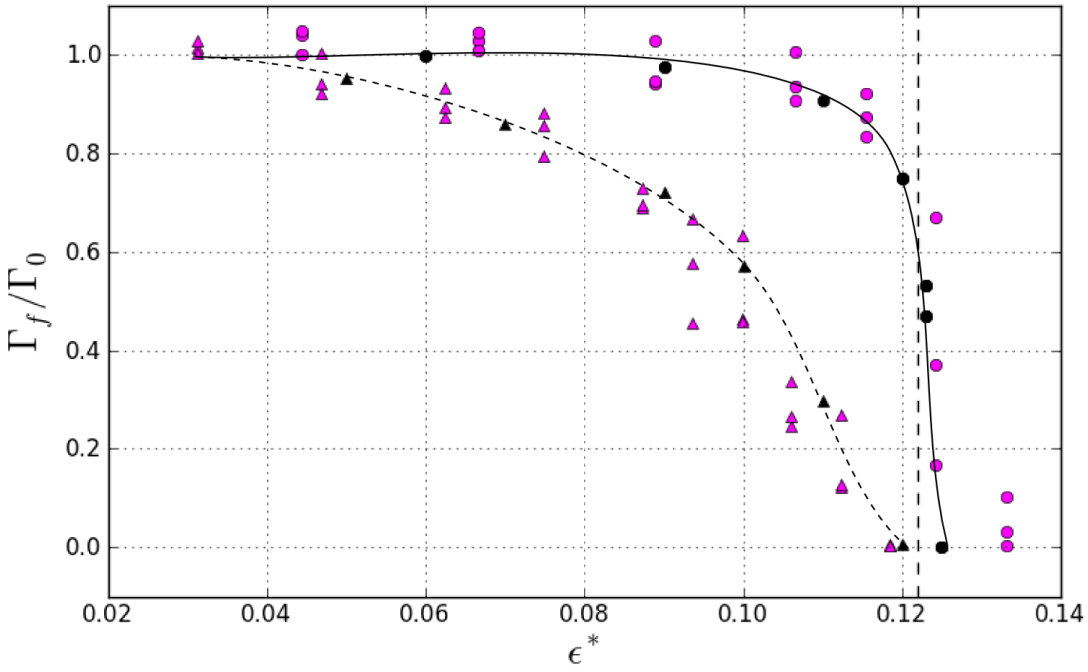

Figure 4.10: Fraction of the circulation remaining in a vortex after a straining event. Shown are experimental (magenta) and numerical (black) data, for a quasi-flat vortex with $\alpha \approx 7$ (circles) and a smooth vortex with $\alpha = 2$ (triangles). Also shown are guides to the eye (black lines), and the K81 stability threshold (vertical black dashed line).

4.2.4 Inviscid damping of K81 orbits

The K81 elliptical patch model preserves energy; and therefore, the trajectories in phase space are given by contours of the Hamiltonian (Eq. 3.9). However, it is observed that these orbits can undergo inviscid damping (i.e., spatial Landau damping [44]) when the vorticity profile is sufficiently non-flat. This effect is demonstrated in Fig. 4.11 using an initial profile which has a flat core ($\alpha \approx 8$) and a low-vorticity tail exterior to the core [c.f. Fig. 2.8 (c)]. Figures 4.11 (a)-(c) show evolution of the ellipse parameters (λ, ξ) in response to constant strain of magnitudes $\varepsilon^* = 0.045$, 0.09, and 0.108, respectively. Shown here are experimental data (magenta circles) and simulation data (black circles). The simulations use an initial vorticity profile identical to the experimental one. The data are compared to the $C = 1$ contour of the K81 Hamiltonian (magenta line). The energy H is calculated from (λ, ξ), and plotted versus time in Fig. 4.11(d)-(f) for experimental and numerical data, corresponding to the damped orbits in panels (a)-(c). The amount of remaining circulation at the end of each data set is $\Gamma_f/\Gamma_0 \approx 1$ in panel (a), 0.95 in panel (b), and 0.9 in panel (c). The evolution of the vorticity and stream function is shown for two damped orbits in Fig. 4.12 with $\varepsilon^* = 0.045$ and 0.09 [i.e., corresponding to the data in Figs. 4.11 (a) and (b), respectively]. Both cases clearly show filamentation behavior within the separatrix, and panel (b) also shows circulation loss to the wall.

Here, the energy H (given by Eq. 3.9) associated with the $m = 2$ elliptical distortions decreases as energy is transferred to other wavenumbers, either by differential rotation or filamentation [44]. In this way, the $C = 1$ orbit evolves toward the local minimum of H

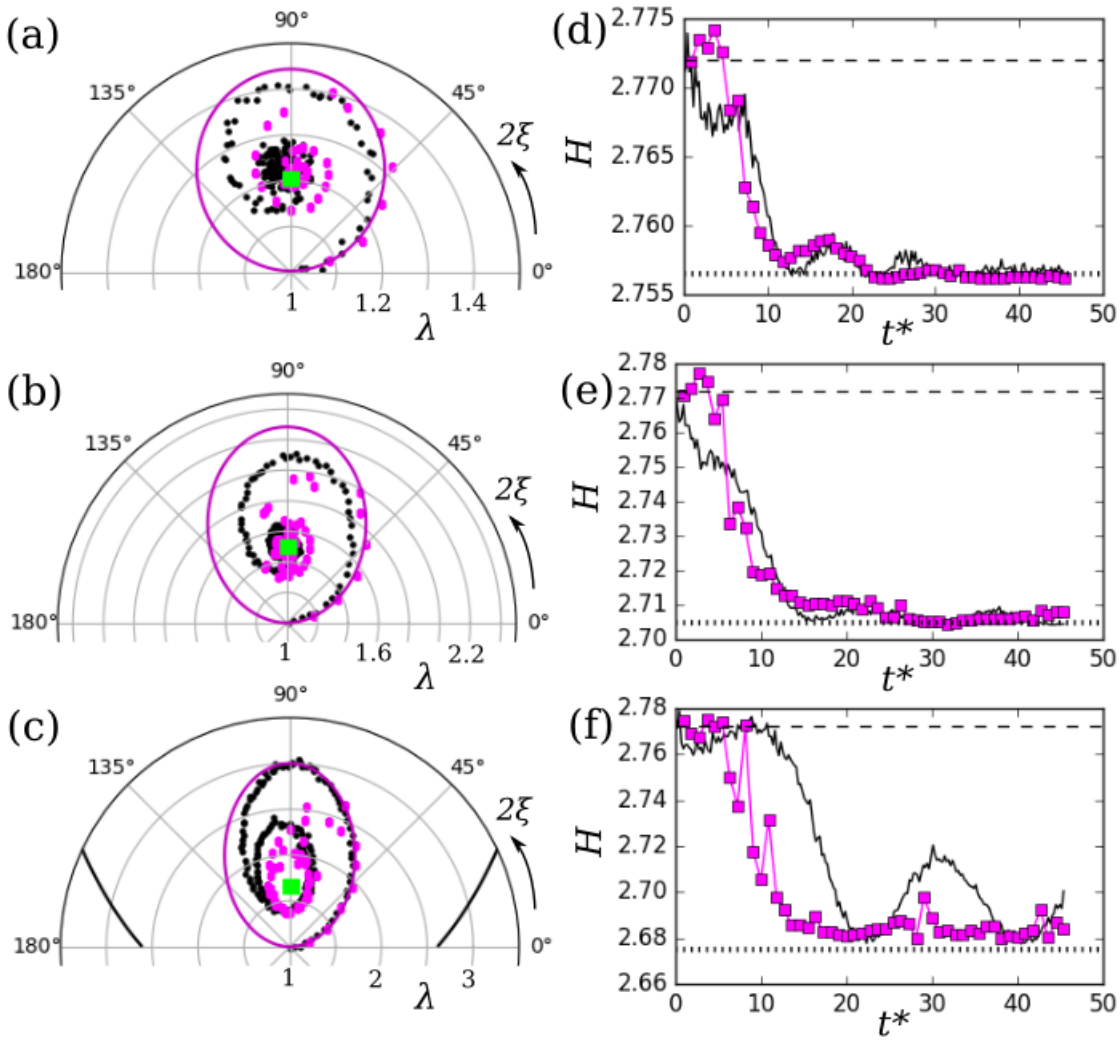

Figure 4.11: Evidence of inviscid damping of K81 orbits in $(\lambda, 2\xi)$ space. Panels (a)-(c) show experimental results (magenta circles) and simulation results (black circles), plotted over Hamiltonian contours for the $C = 1$ orbit (magenta line), the separatrix (black line), and the equilibrium point (green square), for $\varepsilon^* =$ (a) 0.045, (b) 0.09, and (c) 0.108. Panels (d)-(f) show the corresponding temporal evolution of H, relative to the initial value (dashed) and the value at the stable equilibrium (dotted).

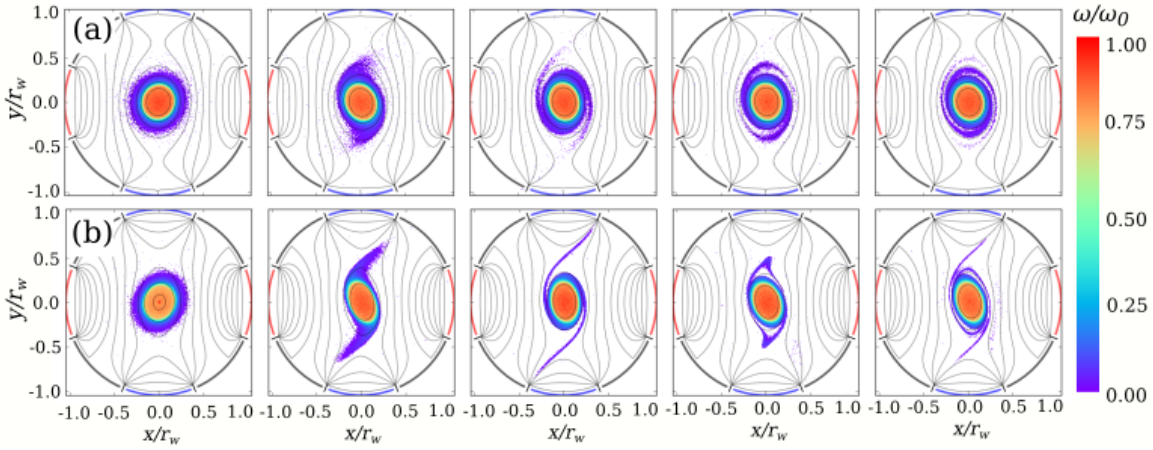

Figure 4.12: Vorticity (color maps) and stream function (black lines) evolution during inviscid damping of the K81 orbit. Here, $\varepsilon^* = 0.045$ (a) and 0.09 (b). Here, $\omega_0 = 458$ krad/s, and data are shown at time intervals $\Delta t^* = 9.16$ beginning with $t^* = 0.916$.

at the stable center point given by the lower branch of Eq. 3.14. In Fig. 4.11 (a) and (b), the damping drives the system close to the equilibrium. However in panel (c), the damping saturates at a finite orbit amplitude. In this case, the tail is stripped away suddenly, the damping shuts off, and the remaining flat core executes nutations. Both the experiments and simulations show similar behavior, although the onset and rate of damping is slightly different.

Based on these observations, inviscid Landau damping of an elliptical vortex in the presence of external strain differs qualitatively from the freely relaxing case studied previously in Ref. [44] in two major ways. First, rather than damping toward axisymmetry, the system damps toward a steady elliptical state similar to the stable equilibria described by MS71. In the case of zero strain, the damping may saturate as a rotation mode; whereas with nonzero strain, the saturated state corresponds to a nutation. Secondly, circulation may be stripped and lost to the wall due to the external strain. Thus, in addition to damping *via*

differential rotation and filamentation, damping may also occur through an "evaporative" process associated with circulation crossing the separatrix. Circulation loss was observed for the data in Fig. 4.11 (b) and (c), implying that the evaporative damping mechanism is active; whereas in panel (a), no circulation loss is observed. Here, inviscid damping of the K81 orbit is demonstrated for a profile which is quasi-flat in the core, but with a tail of circulation at the edge of the vortex, as shown in Fig. 2.8 (c). However, various other data from the 8ST indicate that damping may occur for a broad range of non-flat profiles.

Some of the work and discussion in Chapter 4 is taken from N. C. Hurst, J. R. Danielson, D. H. E. Dubin, and C. M. Surko, "Experimental study of the stability and dynamics of a two-dimensional ideal vortex under external strain," submitted to *J. Fluid Mech.* (2017). The author of the dissertation led the research and was the primary investigator and author of this paper.

Chapter 5

Experiments with time-dependent strain flows

5.1 Introduction

In the preceding chapter, the discussion was restricted primarily to experiments where the applied strain magnitude ε was a constant. This was a logical first step in the 8ST research program due to its simplicity. In this case, the system energy is conserved, a valuable constraint which allowed K81 to obtain exact solutions using the elliptical patch model. Time-dependent strain, where $\varepsilon = \varepsilon(t)$, was considered only once in Chapter 4, in the context of the MS71 equilibria (which are fixed points of the K81 system). Although the strain varied in time, the vortex response was approximately adiabatic, and so the behavior was relatively simple and well-understood. For more general time dependence, theoretical results are hard to come by. In this chapter, we discuss a set of preliminary experiments

which begin to explore the vast parameter space of time-dependent strain flows. Given the preliminary nature of the data, the discussion that follows will be somewhat speculative.

A few basic types of time dependence, shown in Fig. 5.1, are considered here. Panel (a) shows a linear ramp time dependence,

$$\varepsilon(t) = \frac{\varepsilon_0\, t}{t_f}, \tag{5.1}$$

which is considered briefly in Chapter 4, where ε_0 is a constant and t_f is the time at which the experiment is concluded and the vorticity diagnosed. However, here $\varepsilon(t)$ has a kink at $t = 0$ (i.e., $\mathrm{d}\varepsilon/\mathrm{d}t$ is discontinuous). Alternatively, a smooth ramp can be generated using a hyperbolic tangent function. An example is shown in panel (b), where the strain is given by

$$\varepsilon(t) = \frac{1}{2}\left[\tanh\left(\frac{t-t_0}{\tau_s}\right) - 1\right]. \tag{5.2}$$

Here, the strain reaches its half-maximum value at time $t = t_0$, and the rate of change is controlled by the parameter τ_s. Although not discussed further here, smooth ramps such as this will be useful for future studies of adiabaticity.

Panel (c) shows a square-pulse strain time dependence,

$$\varepsilon(t) = \varepsilon_0 \Theta(t)\Theta(t_0 - t), \tag{5.3}$$

where Θ is the Heaviside step function. Here, the strain is turned on for some time t_0, and then turned off for the remainder of the experiment until the vorticity is diagnosed at time $t = t_f$. Thus, the vortex experiences a transient K81 straining event followed by a period of free relaxation. We also consider a "double square-pulse" time dependence, shown in

panel (d):

$$\varepsilon(t) = \varepsilon_1 \Theta(t)\Theta(t_0 - t) + \varepsilon_2 \Theta(t - t_0)\Theta(t_f - t). \tag{5.4}$$

Here, after the initial square pulse with magnitude ε_1, the strain is reduced to a constant, intermediate value $0 < \varepsilon_2 < \varepsilon_1$. In this way, the dynamics on the time interval $[0, t_0]$ are given by a K81 orbit with circular initial condition and strain ε_1. The value of the ellipse parameters (λ, ξ) at $t = t_0$ then serves as an initial condition for a second K81 orbit with strain ε_2 on the interval $[t_0, t_f]$.

Gaussian pulses are also used [shown in panel (e)], where the strain time dependence is given by Eq. 3.16. The Gaussian pulse represents a smooth, transient straining event, a situation which is more physically realistic than that of the square pulse. Finally, sinusoidal time dependence is considered [shown in panel (f)],

$$V_a(t) = V_0 \sin(\Omega_s t), \tag{5.5}$$

where the applied voltage V_a varies harmonically at frequency Ω_s. Here, the strain magnitude is proportional to the absolute value of the voltage, $\varepsilon \propto |V_a|$. Positive voltage $V_a > 0$ corresponds to a strain flow where $\varepsilon \propto V_a$ and the orientation of the strain axis (i.e., the direction of the positive eigenvector) is $\pi/4$ with respect to the (x, y) coordinate system; and $V_a < 0$ corresponds to a flow with orientation $-\pi/4$. This type of situation could arise, for example, when a vortex is trapped in a periodic orbit.

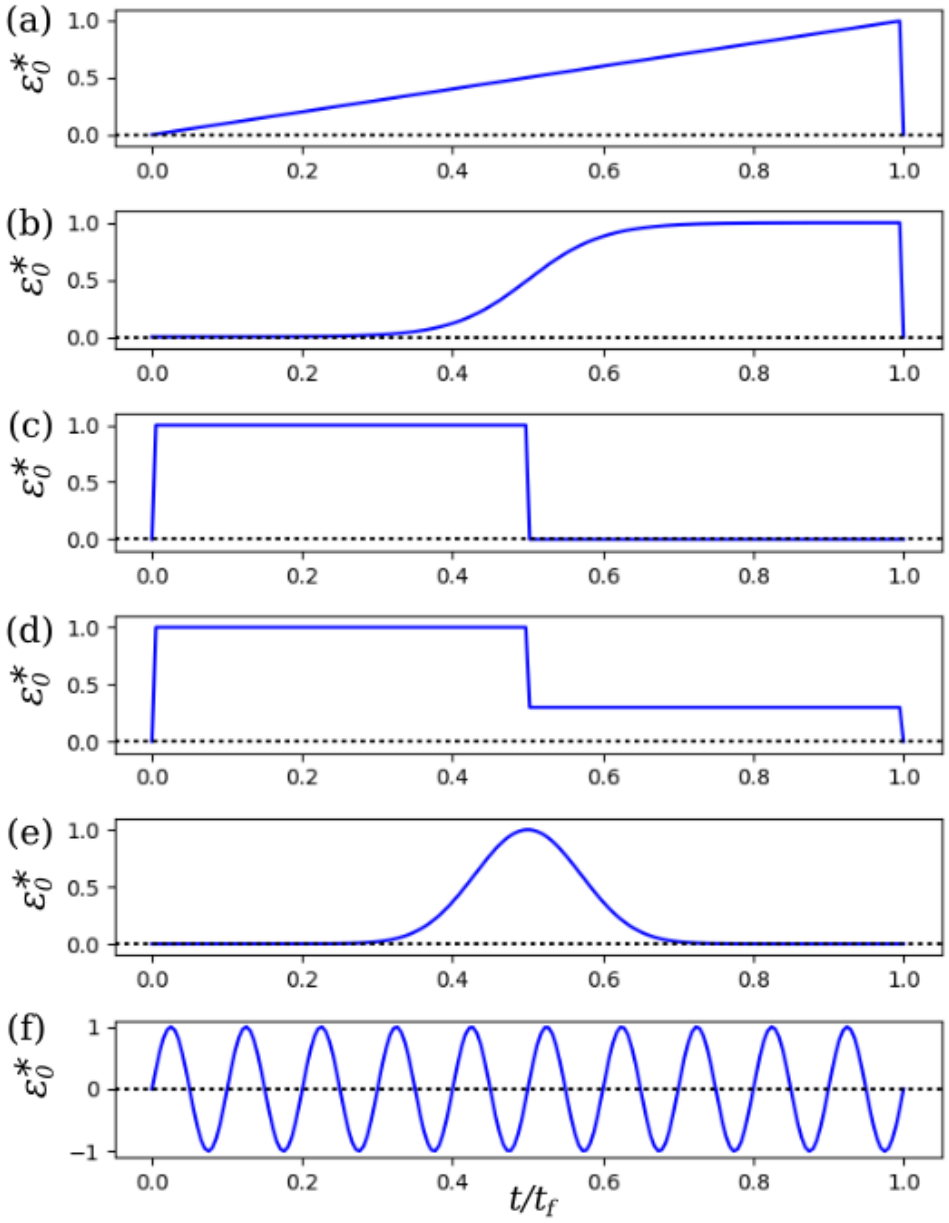

Figure 5.1: Various time dependencies of the applied strain flow. Shown are (a) a linear ramp function, (b) a hyperbolic tangent ramp, (c) a square pulse, (d) a double square pulse, (e) a Gaussian pulse, and (f) a sinusoidal function.

5.2 Square pulses

Here we consider an external strain with square-pulse time dependence, given by Eq. 5.3 and shown in Fig. 5.1(c). The vortex evolves under constant strain on the time interval $[0,t_0]$, then evolves freely (in the absence of strain) for some time until it is diagnosed at $t_f > t_0$. The evolution under constant strain was studied in detail in Chapter 4. The dynamics are given by a K81 orbit for $0 < t < t_0$. The state of the system at $t = t_0$ is that of an elliptical vortex described by the aspect ratio λ and orientation ξ. Since the subsequent evolution on the time interval $[t_0,t_f]$ takes place without strain, the boundary conditions are symmetric and so the orientation is irrelevant. The resulting dynamics are therefore given by the free relaxation of an elliptical vortex, and the character of the evolution depends on $\lambda(t_0)$. For patch-like profiles, the evolution is that of a Kirchoff vortex (Eq. 3.5) which may be subject to Love instabilities (Eq. 3.17). However, if the vorticity profile is sufficiently smooth, some level of inviscid damping is expected [44].

In order to best control the vorticity distribution at $t = t_0$, a large value of strain is used, $\varepsilon_0^* \approx 0.25 \gg \varepsilon_d^*$. In this way, the vorticity behaves passively, and $\lambda(t_0)$ is given approximately by Eq. 2.7. At some point in time, the tips of the vortex along the semimajor axis contact the wall at the gaps between the segmented electrodes. This occurs when the semimajor axis is $a = r_w$, or when $\lambda = r_w^2/r_v^2$. Past this point, the vorticity distribution is better described near the center of the trap as a filament of constant thickness $2b$ (i.e., a finite-width vortex sheet, or a shear layer), rather than as an ellipse. The free evolution of a vorticity filament is characterized by the well-known Kelvin-Helmholtz (KH) instability

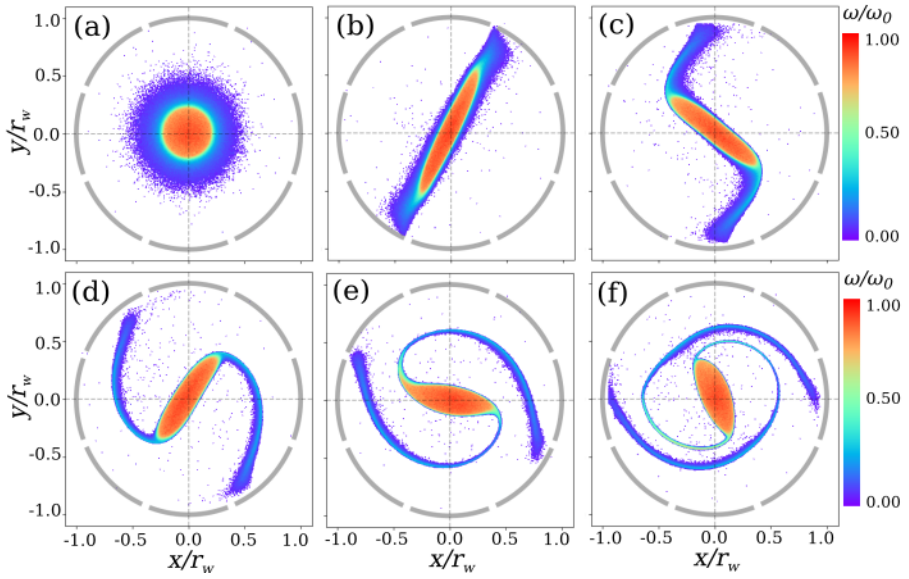

Figure 5.2: Free relaxation of a stretched vortex with $\omega_0 = 440$ krad/s and initial aspect ratio $\lambda \approx 7.5$. Images are taken at $t =$ (a) 0, (b) $t_0 = 11$ μ s, (c) $t = t_0 + 25$ μs, (d) $t = t_0 + 50$ μs, (e) $t = t_0 + 75$ μs, and (f) $t = t_0 + 100$ μs, where the applied strain is $\varepsilon^* = 0.24$ on the interval $0 \leq t \leq t_0$. The vortex is subject to Love instabilities, and it ultimately forms a cat's-eye structure.

[9], which can be thought of as a generalization of the Love instability for $\lambda \to \infty$.

Data are shown for the free relaxation of elliptical vortices with $\lambda(t_0) \approx 7.5$ in Fig. 5.2, and $\lambda(t_0) \approx 11.5$ in Fig. 5.3. Here, the diffuse, peripheral circulation surrounding the vortex core has begun to contact the wall gaps, although the half-maximum vorticity contour has not. Snapshots of the vorticity are shown at $t = 0$, $t = t_0$ (at the end of the strain pulse), and then at $t = t_0 + 25$ μs intervals (11 ω_0^{-1}) up to $t_0 + 100$ μs (44 ω_0^{-1}) during the free relaxtion period. In Fig. 5.2, the vortex experiences inviscid damping, and ultimately saturates as a quasi-elliptical distribution with sharp edges and $\lambda \approx 3$. Filamentary structures exterior to the core are wrapped around the core, generating a cat's-eye structure. In Fig. 5.3, the evolution is that of a vortex splitting (fission) event with two daughter vortices,

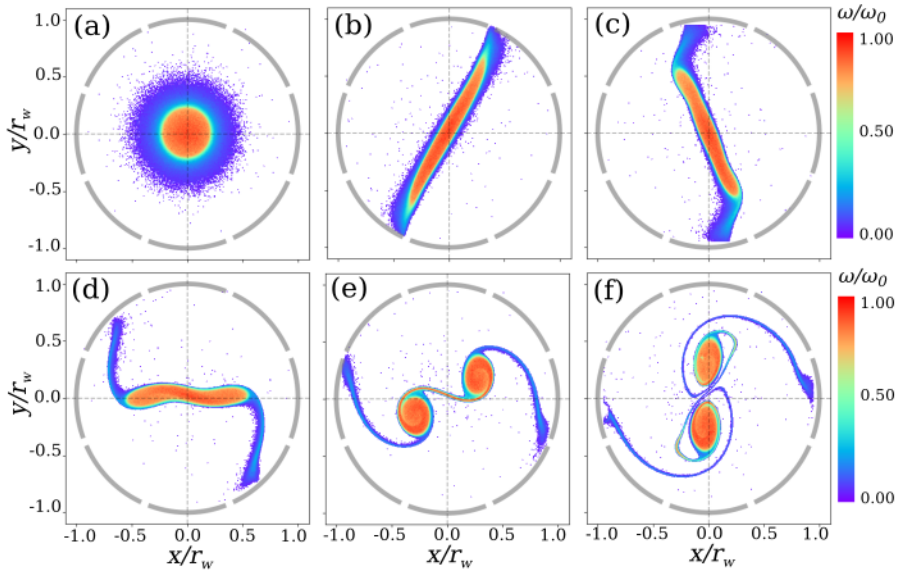

Figure 5.3: Free relaxation of a stretched vortex with $\omega_0 = 440$ krad/s and initial aspect ratio $\lambda \approx 11.5$. Images are taken at $t =$ (a) 0, (b) $t_0 = 13\ \mu$ s, (c) $t = t_0 + 25\ \mu$s, (d) $t = t_0 + 50\ \mu$s, (e) $t = t_0 + 75\ \mu$s, and (f) $t = t_0 + 100\ \mu$s, where the applied strain is $\varepsilon^* = 0.24$ on the interval $0 \leq t \leq t_0$. The vortex is subject to Love instabilities, ultimately leading to a vortex splitting event.

which corresponds to the nonlinear saturation of the Love instability with wavenumber $m = 4$ [98].

Wavenumber $m = 4$ is the fastest growing unstable Love mode in the range $6 < \lambda < 8$ (c.f. Fig. 3.11). Numerical experiments by Mitchell [98] and simple arguments by Dritschel [105] support the idea that an elliptical patch vortex becomes unstable to fission when $\lambda \gtrsim 6.04$, although Mitchell showed that the threshold could be reduced by introducing an $m = 4$ seed perturbation on the initial vortex. The data in Figs. 5.2 and 5.3 show the fission threshold to be in the range $7.5 < \lambda < 11.5$, which is significantly higher than that found by Mitchell and Dritschel.

It is well-known that $m = 2$ modes on a vortex can be subject to inviscid damping

if the profile is smooth (c.f. Fig. 4.11); and it seems plausible that other modes may obey similar physics. In this manner, the $m = 4$ mode could damp away rather than growing to a saturated state, thus raising the threshold for vortex splitting events. The data presented in Figs. 5.2 show that an $m = 4$ mode grows and then damps away in favor of lower modes. Similarly, in the case of Fig. 5.3, an $m = 6$ mode grows, and then damps away in favor of the $m = 4$ mode.

Similar experiments were conducted for vortices that were stretched into thin filaments spanning the trap. In this case, the evolution is better described as a Kelvin-Helmholtz instability as opposed to the Love instabilities shown in Figs. 5.2 and 5.3. Data are shown in Fig. 5.4 for filaments of three different initial half-thicknesses, $b/r_w =$ (a) 0.036, (b) 0.014, and (c) 0.007, which relax to states with N_d daughter vortices, where $N_d = 3$, ~ 10, and ~ 25, respectively. Panel (d) shows a close-up view of the vorticity evolution in panel (c). The data in rows (b) and (c) show evidence of re-entrant circulation, which could perturb the dynamics of the filament. Furthermore, the effect of the image fields is clear: vortices form at the tips of the filament near the wall long before the free KH instability creates vortices near the origin. The increased roll-up rate near the wall can be expected, since the image vorticity generates a cooperative shear. In panel (d), there is evidence of a secondary pairing instability, where two adjacent KH vortices enter into orbits about each other and may eventually merge.

The nonlinear saturation of the KH instability on a vorticity filament was studied further by measuring the number of daughter vortices N_d as a function of filament thickness, as shown in Fig. 5.5. Here, a quasi-flat vortex with $\omega_0 = 520$ krad/s and $r_v/r_w \approx 1/8$ was

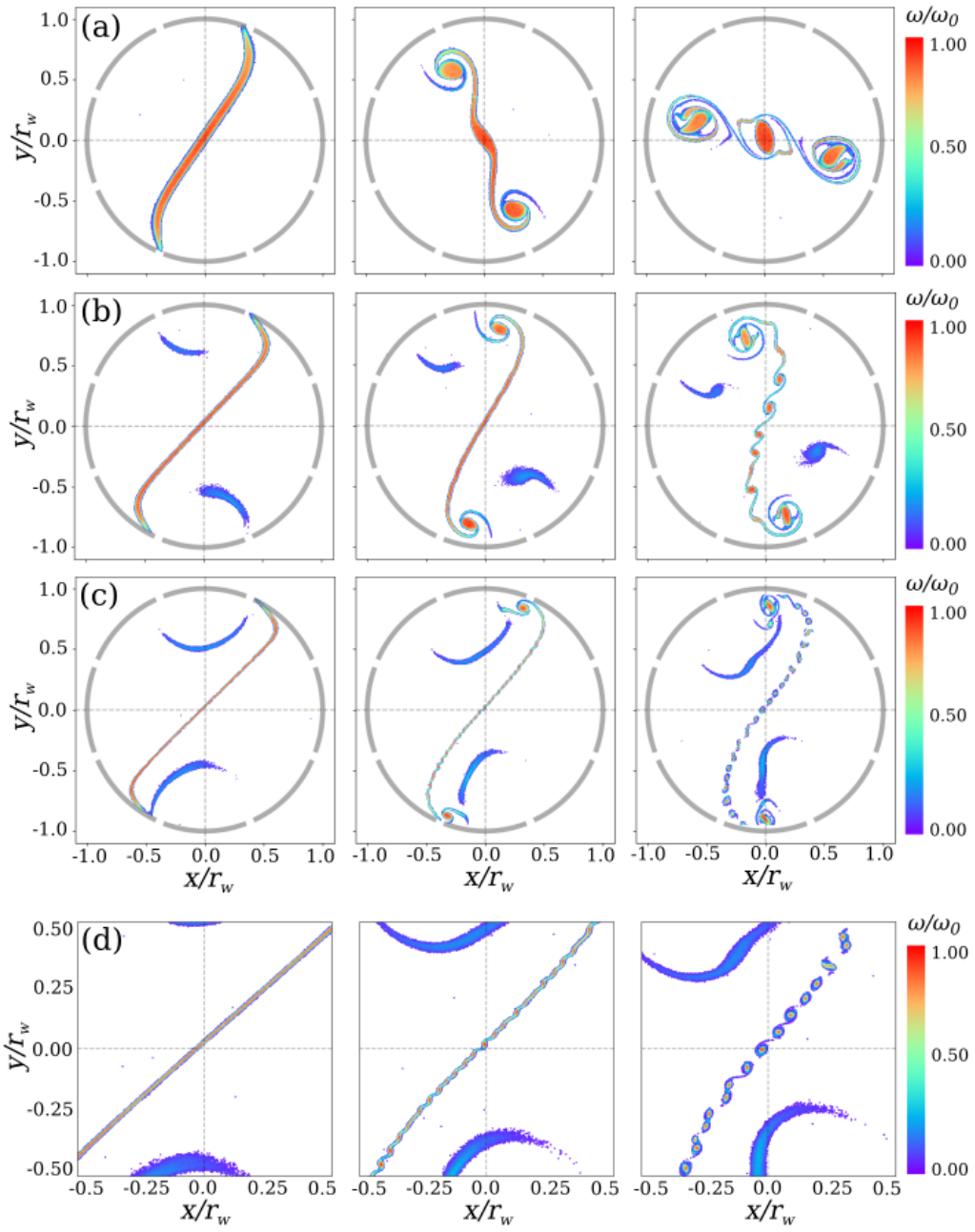

Figure 5.4: Free relaxation of vorticity filaments for $\omega_0 = 440$ krad/s and filament half-thickness $b/r_w =$ (a) 0.036; (b) 0.014; (c) 0.007. The first image in each row is taken at the moment the strain is turned off, and subsequent images are separated by 50 μs (22 ω_0^{-1}). The filaments are subject to Kelvin-Helmholtz instabilites, causing them to break up into a number N_d of daughter vortices, where $N_d =$ (a) 3; (b) ~ 10; (c) ~ 25. Row (d) shows a close-up view of row (c). The blobs of vorticity on either side of the filaments are re-entrant electrons (see Fig. 2.15).

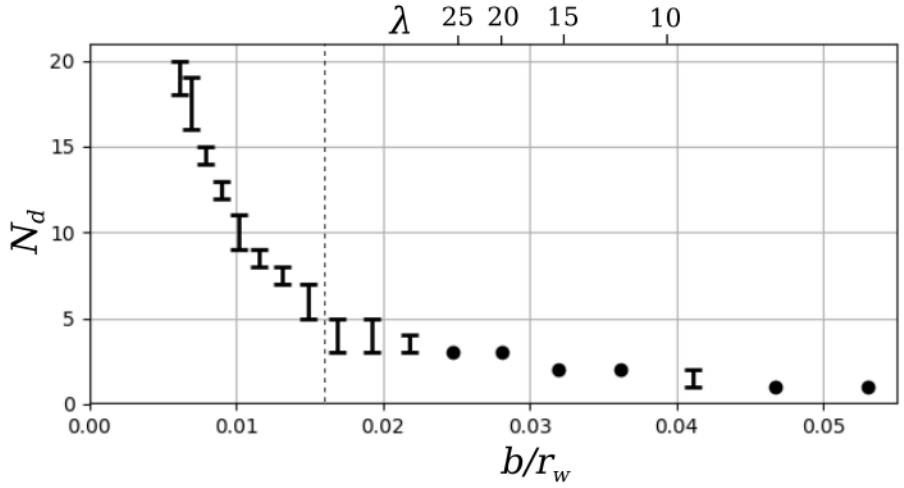

Figure 5.5: Number of daughter vortices N_d versus normalized filament half-thickness b/r_w, or aspect ratio λ. Each error bar represents the variation in N_d observed over three runs (dots are shown if no variation was observed). The semimajor axis contacts the wall at roughly $b/r_w = 0.016$, denoted by a vertical dashed line.

stretched into an ellipse, and further into a filament spanning the trap. It was then allowed to relax for a time $\sim 50\omega_0^{-1}$ (i.e., sufficiently long that the saturated state was evident), and N_d was observed visually. The point where the half-maximum vorticity contour contacts the wall, $b/r_w \approx 0.0156$, is shown in Fig. 5.5 as a vertical dashed line. Error bars are determined by conducting three consecutive runs and observing a range of N_d. When each of the three runs results in the same N_d, a dot is plotted rather than an error bar. These data can be compared roughly to predictions based on the fastest-growing mode in the KH spectrum, which occurs for wavenumber $2bk \approx 0.8$. Assuming each wave period develops into a daughter vortex, one would expect $N_d \sim (16b/r_w)^{-1}$. The data disagree with this prediction by about a factor of two, the reason for which is presently unknown.

5.3 Double square pulse

Following a square pulse of strain, the elliptically distorted vortex or filament may be subject to Love or KH instabilities, as shown in the preceding section. However, it is known that these instabilities can be stabilized by an external strain flow [99]. Thus, we now consider a "double square-pulse" strain time dependence, where immediately following the initial square pulse is a second square pulse of weaker strain [c.f. Fig. 5.1(d)]. The first pulse stretches the initially axisymmetric vortex into a filament roughly aligned with the strain axis, as seen in the first column of Fig. 5.4. The second pulse provides stabilization against the KH instability. The double square pulse technique can also be used to study K81 orbits with a non-circular initial condition, although this idea is not explored further here.

Data are shown in Fig. 5.6 for a filament with $\omega_0 = 440$ krad/s and $b/r_w = 0.014$ [c.f. Fig. 5.4(b)] evolving under the influence of applied strain with $\varepsilon^* =$ (a) 0.01, (b) 0.02, and (c) 0.03. In row (a), the strain has little effect, and the filament rolls up into daughter vortices as would be expected. In row (b), and to an even greater extent in row (c), the KH roll-up is significantly suppressed by the applied strain. The number and spatial extent of the daughter vortices is diminished. The strain affects the KH modes in two ways: the waves are squashed (i.e., the amplitude is reduced) by the strain in the direction perpendicular to the filament; and they are stretched in the parallel direction, such that the wavenumber of a seed wave decreases over time. The linear problem was analyzed by Dritschel [99], who numerically calculated the extent to which a seed wave was amplified

by the KH mechanism before eventually succumbing to the strain. More relevant here is the question of whether KH waves grow to the point where they can saturate by forming vortices, which seems to be the case to some extent in all three rows of Fig. 5.6.

5.4 Gaussian pulses

We now turn our attention to an applied strain with a Gaussian time dependence, These Gaussian pulses can be thought of as smooth relatives of the square pulses considered earlier in this section; during the pulse, the behavior is similar to that of a K81 vortex, and on the trailing edge of the pulse, instabilities begin to set in. When the peak strain is sufficiently small (i.e., $\varepsilon_0^* < \varepsilon_c^*$), at no point during the pulse is the vortex destabilized in the sense of a K81 destruction mode, and so $\lambda(t)$ is bounded below about 5. Based on the data shown above in Figs. 5.2 and 5.3, these vortices are not expected to undergo fission, and so the final state of the vortex core should be quasi-elliptical, possibly with filamentation at the periphery. When the pulse half-width τ_s is long compared to the vortex rotation period $\tau_v = 4\pi/\omega_0$, the behavior should be adiabatic, such that the vortex remains in equilibrium with the strain throughout the pulse, and so the vortex is expected to return to axisymmetry after the pulse has passed. When τ_s is short compared to τ_v, the behavior is non-adiabatic, and so the vortex may be left with a residual elliptical distortion after the pulse has receded. Finally, resonant behavior is expected when $\tau_s \sim \tau_v$.

These effects are studied in Fig. 5.7, where Gaussian pulses of varying width are applied to a vortex with $\omega_0 = 228$ krad/s for $\varepsilon_0^* =$ (a) 0.054 and (b) 0.108. Here, $t_0 = 100$

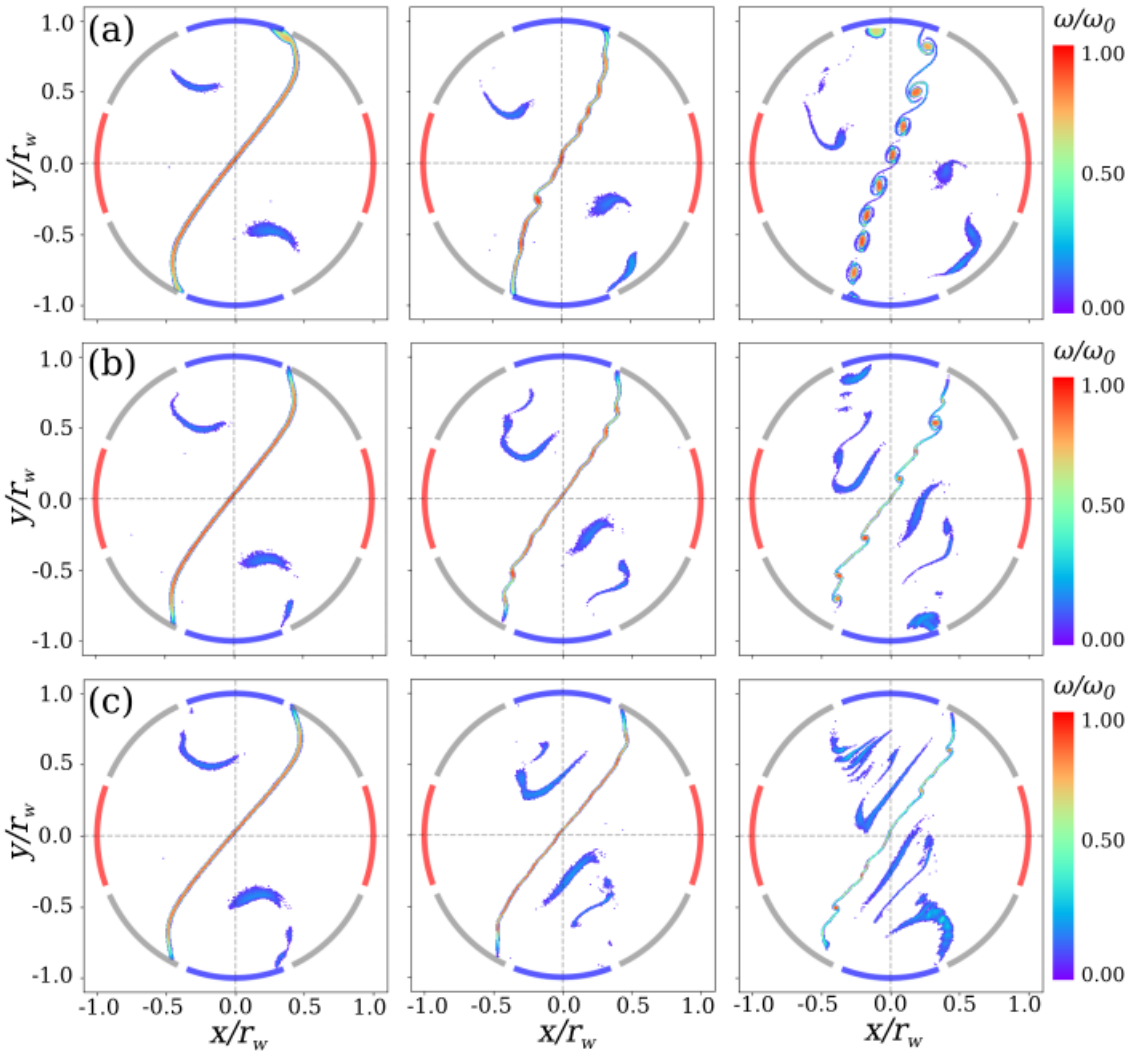

Figure 5.6: The Kelvin-Helmholtz instability under applied strain. A filament with $\omega_0 =$ 440 krad/s and half-thickness $b/r_w = 0.014$ [c.f. Fig. 5.4(b)] is generated by an initial strain pulse. Then, it evolves under the influence of a second strain pulse with $\varepsilon^* =$ (a) 0.01; (b) 0.02; (c) 0.03. The three panels in each row correspond to 40, 80, and 120 μs of evolution (intervals of $17.6\omega_0^{-1}$). Re-entrant vorticity can be observed on either side of the filament (see Fig. 2.15).

μs (22.8 ω_0^{-1}), and the aspect ratio of the ellipse λ is diagnosed at $t_f = 200$ μs (45.6 ω_0^{-1}) while the pulse half-width τ_s is varied. Each data point is repeated five times for statistical purposes and compared to predictions based on numerical solutions to the K81 equations (c.f. Fig. 3.10). In all cases, the final vorticity distribution is close to circular for pulses with $\tau_s^{-1} \ll \omega_0$, as expected for adiabatic behavior. For short pulses with $\tau_s^{-1} \gg \omega_0$, the final aspect ratio is close to unity, simply because the strain is not on long enough for λ to grow significantly. For intermediate pulse widths, a resonance peak of sorts is observed at $\tau_s^* \equiv \tau_s \omega_0 \sim 3$ in both the data and the K81 predictions. However, the experimentally observed residual ellipticity is significantly smaller than that predicted by K81. The reason for this is likely inviscid damping [44], which takes place after the pulse has receded.

Figure 5.8 shows vortex behavior in response to Gaussian strain pulses, as a function of the normalized pulse half-width τ_s^* (on the vertical axis) and the amplitude ε_0^* (on the horizontal axis). Different types of behavior are observed across the two-dimensional parameter space $(\tau_s^*, \varepsilon_0^*)$. They are plotted as colored symbols in panel (a). Panel (b) shows an example of a vorticity distribution corresponding to each of the colored symbols. Black squares correspond to circular vortices; they are observed for $\varepsilon_0^* < \varepsilon_c^*$ and $\tau_s^{-1} \ll \omega_0$, so that the vortex behaves adiabatically, below the critical strain threshold. Red circles correspond to vortices with residual elliptical distortions, which can occur due to non-adiabaticity (c.f. Fig. 5.7). Under more severe conditions, non-adiabatic behavior at higher values of strain can lead to stripping at the periphery of the vortex, or inviscid damping can set in to produce cat-eye structures; these behaviors are indicated by green triangles. Cases where the ellipse becomes highly distorted due to Love instabilities are shown as blue triangles. When the in-

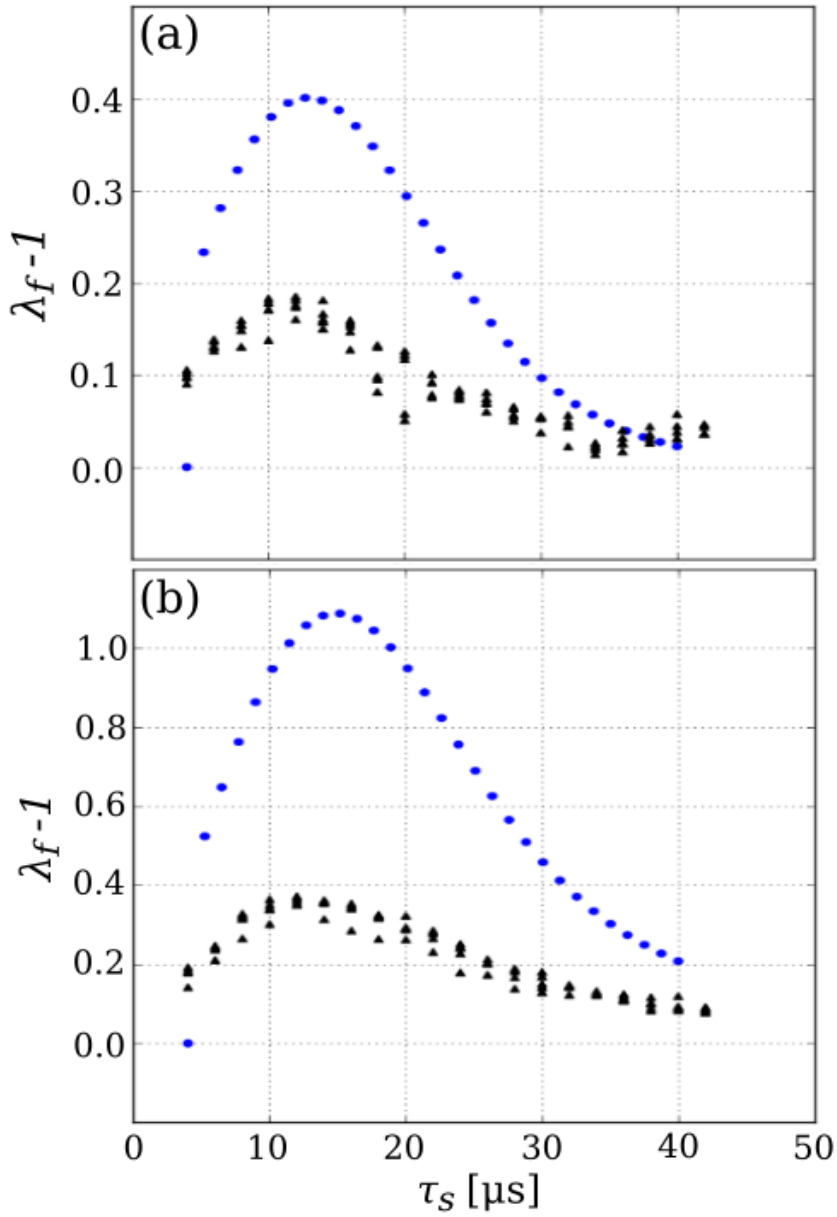

Figure 5.7: Residual elliptical distortion of a vortex with $\omega_0 = 228$ krad/s following a Gaussian strain pulse of varying width. The peak strain is $\varepsilon_0^* =$ (a) 0.054; (b) 0.108, and the pulse half-width is τ_s. Data for the final aspect ratio λ_f (black triangles) are obtained using the elliptical fitting routine, and compared to numerical solutions of the K81 system (blue circles).

stability is sufficiently strong, fission events occur, and the vortex splits into two daughters; these conditions are indicated by magenta triangles. Finally, when the strain is sufficiently strong and the pulse duration is sufficiently long, the vortex can be stretched into a filament, which then relaxes to a state of multiple daughters (i.e., $N_d > 2$); these cases are shown as cyan diamonds.

5.5 Sinusoidal strain

When the strain time dependence is taken to be sinusoidal, the dynamics can be quite complicated. For example, each half-cycle of the wave can be thought of as a strain pulse, and so the vortex responds to the sinusoidal strain by a sequence of K81-like stretching events, and subsequent relaxation periods where instabilities can grow. In principle, one can envision a diagram similar to that of Fig. 5.8(a), where the vortex response to a sinusoidal strain pattern is described as a function of the amplitude and frequency variables $(\varepsilon_0^*, \Omega_s)$. For example, when $\varepsilon_0^* < \varepsilon_c^*$ and $\Omega_s \ll \omega$, adiabatic behavior can be expected. Similarly, when $\Omega_s \gg \omega$, the vortex response should be small due to time-averaging (similar to cutoff phenomena in forced oscillators). However, when the right conditions are chosen, the vortex can resonate with the strain and produce chaotic dynamics.

An example of a vorticity distribution resulting from such conditions is shown in Fig. 5.9. Here, the vortex has been repeatedly stretched and allowed to relax over the course of six periods, effectively "stirring" the vortex and generating a patch of turbulence where there was once a quiescent vortex. This process is described further in Fig. 5.10, where the

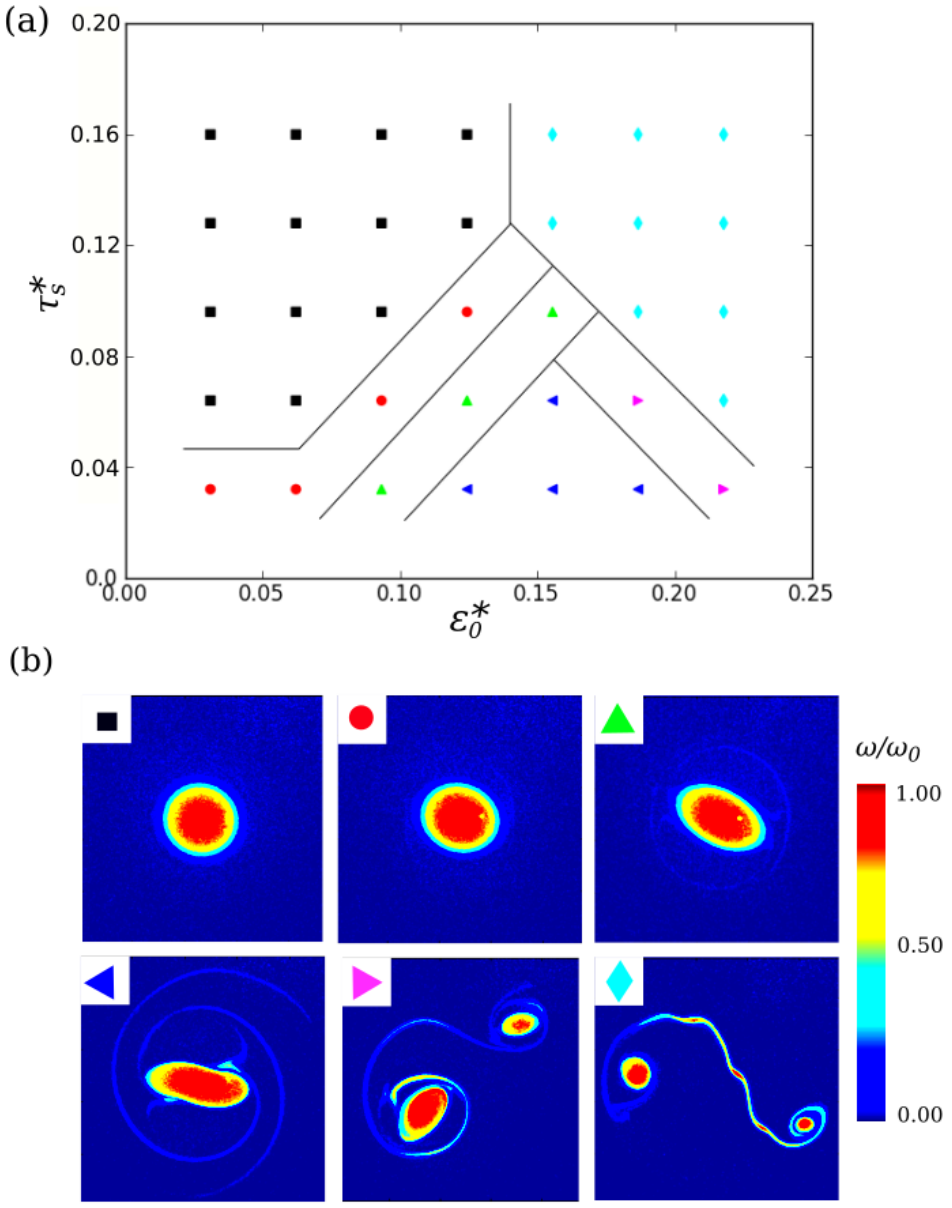

Figure 5.8: Map of vortex response to a Gaussian strain pulse. (a) map of behaviors observed as a function of the half-width τ_s and amplitude ε_0^* of the strain pulse; (b) examples of late-time vorticity distributions corresponding to regions of panel (a). Counter-clockwise from the top left panel of (a): circular states (black squares); pure elliptical states (red circles); elliptical states with filamentation/stripping (green triangles); distorted ellipses with significant filamentation (blue triangles); split states with two daughters (magenta triangles); and filamentary structures (cyan diamonds).

vorticity evolution is depicted schematically in response to a single cycle of periodic strain. As the strain grows, the initially circular vortex is stretched into an ellipse [c.f. Fig. 5.10 (a), i-ii]; then, as the strain decreases to zero, the distorted vortex is split due to Love instabilities (ii-iii). The two daughter vortices then experience a similar scenario where $V_a < 0$ and the orientation of the strain axis is $-\pi/4$ (iv-v), which leads to further splitting events. In principle, this process could continue over many cycles, leading to a large number of small-scale vortices. However, the simple physical picture presented in Fig. 5.10 neglects interactions between vortices, which can, for example, affect the straining rates and the growth rates of the instabilities, and lead to vortex pairing and merging events.

The results described in this section, although interesting, are preliminary and deserving of further analysis. It is anticipated that future work will address the issues raised here in a more rigorous and quantitative way.

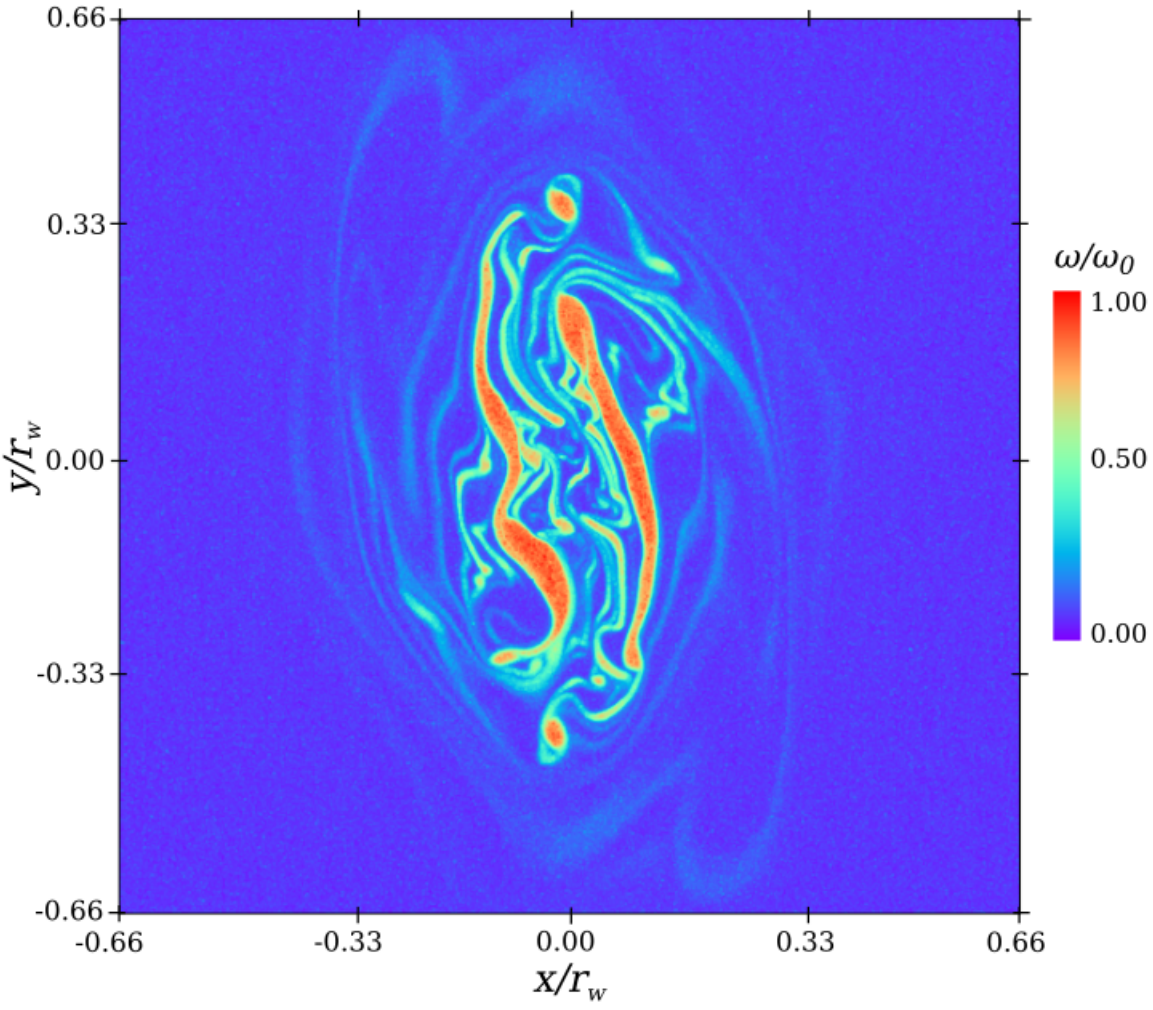

Figure 5.9: A vortex subjected to six periods of sinusoidal strain. Here, $f_s \equiv \Omega_s/2\pi = 20$ kHz, $\omega_0 = 240$ krad/s, and $\varepsilon_0^* = 0.175$. A series of straining events and instabilities results in a complicated vorticity distribution; one could say the vortex has been "stirred" into a state of turbulence.

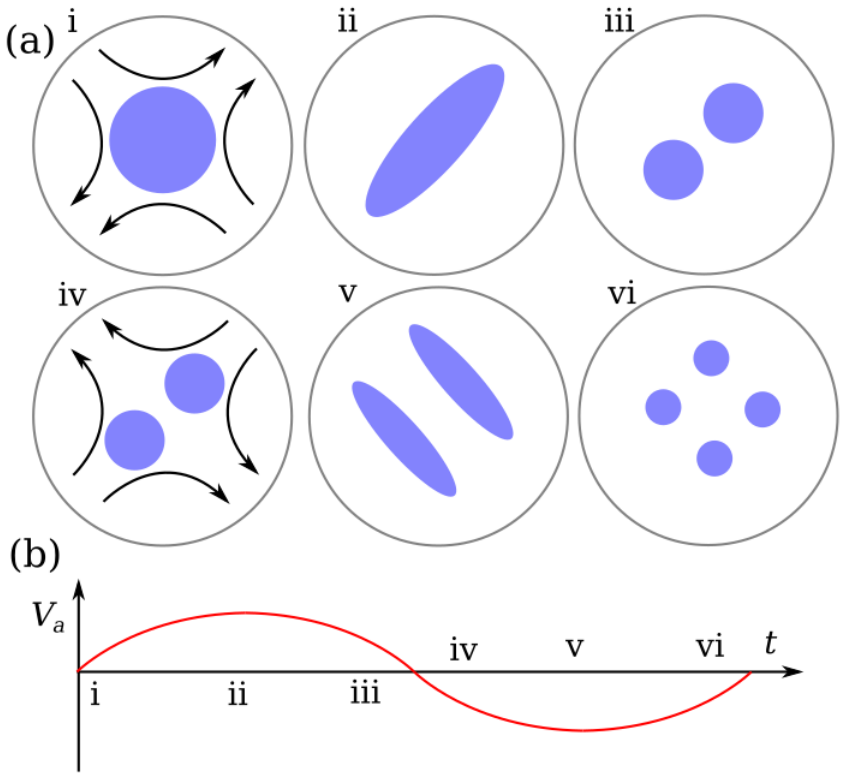

Figure 5.10: Cartoon of vortex behavior under periodic strain. Panel (a) shows the vorticity evolution (blue) at various points in time (i-vi) throughout a single strain cycle, where the time dependence of the applied voltage V_a is shown in panel (b). Here, vortex structures undergo periods of stretching under strong strain, and subsequent periods of relaxation where Love instabilities result in vortex splitting events.

Chapter 6

Summary and conclusions

6.1 Recap of the strained vortex problem

2D fluids exist in natural and man-made systems across a wide range of scales. It is important to understand their dynamics from both a scientific and a practical perspective. Perhaps the most striking example is the quasi-2D motion of air and water across the surface of the Earth [27]. These dynamics have a profound impact on our lives, through the weather we experience every day, as well as long-term climate behavior. Other important quasi-2D flows are found in aircraft wakes [8] and mixing applications [37], and in magnetized laboratory plasmas for nuclear fusion research [13, 36]. More exotic scenarios include disk-like flow geometry found in astrophysical settings, for example in galaxies and accretion disks [35, 34].

Many of these systems are characterized by high Reynolds numbers, in which case external forcing can create vortices and turbulence. For example, solar heating drives tur-

bulence in Earth's oceans and atmosphere, just as external heating drives plasma turbulence in fusion devices. Transport in these systems is enhanced significantly by the formation of vortices which carry heat, momentum, and passive tracers as they move through the fluid. However, these vortices can be perturbed and even destroyed by other flow structures that they encounter along their journey. Large-scale jets, such as Earth's jet stream or zonal flows in fusion devices, can suppress transport by decorrelating vortices. Furthermore, interactions between vortices can lead to deformation, destruction, and vortex merger events.

These behaviors can be studied in a controlled manner by considering the canonical example of a single isolated vortex subject to an externally imposed flow. Here, the spatiotemporal form of the external flow can be chosen to mimic the effect of other vortices, large-scale flows, or boundaries. The simplest case is that of an initially axisymmetric vortex in a 2D ideal fluid, subjected to an irrotational simple strain flow, that is, a hyperbolic external flow with azimuthal wavenumber $m = 2$. When the flow is static and the initial vorticity profile is flat, a simple theoretical description is possible in terms of the so-called elliptical patch model studied by K81 [39], MS71 [8], and many others. Here, the vorticity is treated as piecewise constant inside an elliptical boundary. In this way, the system is described completely by two dynamical variables, the aspect ratio λ and the orientation ξ of the ellipse, thus reducing the dimensionality and making the problem tractable.

Although this simple scenario is both soluble and understandable, the assumptions involved are sometimes not physically realistic. Often, vorticity profiles in nature are smooth, and the environment in which they exist is chaotic. In this dissertation, the K81 system is studied experimentally, and the results are used as a starting point to inves-

tigate the dynamics of smooth vorticity profiles under strain. Furthermore, intuition gained from studying the K81 system is used to extrapolate to time-dependent flows, which more accurately model the experiences of a vortex in a natural system.

6.2 Summary of experimental data and results

6.2.1 Development of an apparatus for strained vortex experiments

In order to conduct the studies described above, a novel electron plasma apparatus called the Eight-Segment Trap (8ST) was designed and built, and experimental techniques and protocols were developed [106]. The experiments make use of an isomorphism between the Drift-Poisson equations describing the dynamics of a single-component plasma perpendicular to the magnetic field, and the 2D Euler equations describing ideal fluid flow [17]. Here, the electron density plays the role of the fluid vorticity, and the electric potential is analogous to the fluid stream function. The 8ST was designed such that plasmas could be contained under a long, eight-fold azimuthally segmented electrode. In this way, external flows could be implemented by electrically biasing the segments without introducing 3D effects. In contrast, other electron plasma devices feature short segmented electrodes, which limits the ability to apply external flows. The plasma must be long relative to the transverse dimensions in order to behave as a 2D fluid, as described in Chapter 2. Additionally, axial electric fields are generated which introduce 3D physics such as axial particle trapping. Thus, the 8ST is uniquely capable of creating external flows which are within the bounds of the plasma/fluid analogy.

In the 8ST, prior to application of the external flow, fluid vortices are prepared by manipulating the trapped electron plasmas. Most importantly, the rotating wall technique is used to control the radial vorticity profile. In this way, profiles ranging from smooth to quasi-flat can be obtained. Once the electron plasma has the desired profile and other properties (density, temperature) necessary for a fluid description, then the external flow is created by biasing the electrode segments. The vorticity distribution evolves under the flow for some time, then the flow is removed and the distribution is immediately diagnosed using a phosphor screen and a CCD camera. By repeating this protocol many times, the evolution of the vorticity distribution $\omega(x,y,t)$ can be determined. The evolution can be studied as a function of the profile smoothness, the strain magnitude ε^*, and the time dependence of the strain $\varepsilon^*(t)$. Although this dissertation focuses only on the simple strain flow, other types of flow geometry are possible by biasing the segments in a different pattern. The vortex dynamics observed in the 8ST are complemented by numerical experiments using a vortex-in-cell code [58], which serve to reinforce the experimental results and to explore a wider parameter space than is possible experimentally.

6.2.2 Experiments with quasi-flat profiles

The first set of experiments conducted in the 8ST focused on the dynamics of quasi-flat initial vorticity profiles, which are easily prepared using the rotating wall technique. The motivation was to test the predictions of the elliptical patch theories of K81 and MS71. The experimental data show that, for constant strain ε^* below the dynamical stability threshold $\varepsilon_d^*(C=1)$, the vortices distort elliptically in a periodic manner, executing closed orbits

in (λ, ξ) space. For $\varepsilon^* > \varepsilon_d^*$, it is observed that the vortices experience indefinite stretching as the strain overcomes the vorticity; hence, the vortices are effectively destroyed. The shape of the orbits in (λ, ξ) space and the temporal behavior of the system are in quantitative agreement with predictions of the K81 model. When the strain is gradually increased from zero, it is found that the vortices behave adiabatically, remaining in equilibrium with the strain. The stationary states obtained in this manner are in quantitative agreement with the equilibria given by MS71, which are fixed points of the K81 equations. The stability threshold is measured for both the dynamical case (constant strain) and the equilibrium case (ramped strain), and the results match the predictions of the elliptical patch theory.

6.2.3 Experiments with smooth profiles

When smooth profiles are studied, the behavior of the vortices differs in certain ways from the patch model. A key theme is that the stability of the vorticity becomes a local matter, rather than a global one. This simple fact opens the door for partial vortex destruction events, also known as "vortex stripping" events. In this case, although the strain is not strong enough to completely destroy the vortex core, it can destabilize low-vorticity circulation around the edge of the vortex. This circulation is carried into filamentary structures which are then advected away from the core by the strain. The amount of circulation which is stripped away is a function of the applied strain magnitude and the profile smoothness. These basic ideas were discovered previously through water tank experiments and contour dynamics simulations [21, 54]; however, the 8ST offered a higher level of precision which has allowed us to conduct more quantitative experiments. It was discovered using the 8ST

that smooth profiles have modified stability properties relative to flat ones. Specifically, for the case of constant strain applied to an initially axisymmetric vortex, it was found that Gaussian profiles are destroyed for strain magnitudes which are about 15% lower than that for quasi-flat profiles. The reason for this seems to be associated with the formation of substantial filamentary structures which modify the strain experienced by the vortex core.

Perhaps the most important result from the 8ST experiments regarding smooth profiles is that the K81-like elliptical oscillations undergo inviscid damping which drives the system toward the stable, elliptical equilibria given by MS71. This phenomenon is closely related to the free damping of a smooth, elliptical vortex, a case which was studied in Refs. [10, 44, 43], among others. However, due to the presence of the external strain, a few important differences arise. For a free elliptical vortex, the system "axisymmetrizes," or damps toward an axisymmetric state, although nonlinear effects can cause the system to saturate as a steady cat's-eye distribution. In contrast, under strain, the system damps toward a steady elliptical state, and may saturate as a finite-amplitude K81 nutation mode (or, conceivably, a rotation mode). Another key difference is associated with the vortex stripping phenomenon; under strain, the vortex can experience circulation loss, especially along the semimajor axis near the saddle points, and this can result in a type of "evaporative" damping.

6.2.4 Experiments with time-dependent strain

The most recent (albeit preliminary) experiments in the 8ST involved time-dependent strain flows, mostly in the context of quasi-flat vortices. A number of different cases were

considered, including square pulses, Gaussian pulses, and sinusoids. During a square pulse, the vortex evolution is well-described by the K81 phenomenology; as such, the state at the end of the pulse is that of an elliptically distorted vortex. Following the square pulse, the free evolution of that elliptical state was observed. At relatively small values of λ, the observed dynamics are similar to that of Ref. [44]. At higher values of λ, rather than damping to an elliptical state, the Love instability with azimuthal wavenumber $m = 4$ grows into a state of nonlinear saturation; this is identified as a vortex splitting event which produces two daughter vortices. As λ is increased further, the number of daughter vortices rises. As the vortex is stretched further, the semimajor axis reaches the wall, at which point the distribution is best described as a finite strip of vorticity spanning the fluid domain. In this case, linear evolution of the strip is that of a Kelvin-Helmholtz (KH) instability, which again produces a number of daughter vortices in the saturated state. In the 8ST, as many as ~ 30 daughter vortices were observed for very thin filaments. Furthermore, a secondary pairing instability was observed, where neighboring daughter vortices enter into binary orbits about each other, and may eventually merge.

Other experiments were conducted where the strain was reduced after the initial square pulse not to zero, but to some intermediate value. Here, the evolution is that of a filament of vorticity relaxing under weak external strain. The question becomes: what value of strain is necessary to stabilize the filament against KH roll-up? Although the data are preliminary, it is clear that even small values of strain $\varepsilon^* \sim 0.02 - 0.03$ can drastically alter the dynamics; although even then, a few small daughter vortices are observed.

Another set of experiments involved strain pulses with Gaussian time dependence.

Qualitatively, the observed dynamics were similar to that of the square pulses: a combination of K81-like dynamics during the pulse, followed by Love instabilities after the pulse had receded. The key difference is that the Gaussian pulse is smooth, and so adiabatic behavior is possible. Different types of vortex behavior were observed, depending on the amplitude and width of the Gaussian strain pulse. They include axisymmetric states corresponding to adiabatic behavior, slightly elliptical states where adiabaticity is broken, cat-eye states for larger strain values, highly distorted vortices which have suffered Love instabilities, and split states where the number of daughter vortices ranges from two upwards.

When a strain flow which is sinusoidal in time is applied, the dynamics can be very complicated and even chaotic. Specifically, for some range of parameters (frequency and amplitude of the sinusoid), the vortex can be "stirred" into a patch of turbulence. In this scenario, a half cycle of the applied strain stretches the vortex, and then instabilities set in while the strain passes through zero, and this procedure is then repeated. Although detailed experiments have yet to be conducted, we also can expect adiabatic behavior for low-frequency sinusoids, as well as a weak response when the frequency is too high due to time-averaging.

6.3 Implications for other quasi-2D fluid systems

The results discussed in this dissertation for ideal 2D fluids may be useful in understanding a variety of other quasi-2D fluid systems, including geophysical fluids, magne-

tized plasmas, and astrophysical disks. However, these systems are more complicated than the simple 2D fluids studied here: often 3D and non-ideal effects are present at some level. In this section, I will speculate as to how the results of the dissertation pertain to various other related fluid systems.

A common theme among many quasi-2D fluid systems is that of "potential vorticity" (PV) conservation. Whereas the 2D Euler equations preserve the vorticity ω in the Lagrangian frame, other systems preserve some other form of generalized vorticity. Potential vorticity models are often used to describe the behavior of geophysical fluid flow on the surface of rotating planets [30], as well as quasi-2D drift wave turbulence in magnetized quasi-neutral fusion plasmas [12].

Whereas the 2D Euler system tends to evolve toward a state of isolated, quasi-axisymmetric vortices, PV systems tend to favor strip-like vorticity structures called "zonal flows," which are clearly observed in images of Jupiter, for example. Thus, the PV dynamics seem to have a stabilizing effect on filamentary structures and a destabilizing effect on vortex structures. If a vortex is to persist in such an environment, it must be intense, and even then, it may be subject to elliptical distortions; the Great Red Spot of Jupiter is a clear example [107]. In this sense, one could imagine that the breakdown of a vortex might be facilitated in a PV environment, thus lowering the strain destruction threshold ε_d^* relative to its value in the Euler system. However, near the poles of rotating planets, the opposite is true – the planetary rotation leads to the formation and persistence of "polar vortex" structures which are routinely observed on Earth and other planets. The PV dynamics due to the rotation have a stabilizing effect on these structures, therefore more extreme straining

events may be necessary to destabilize the polar vortices. Reference [7] discusses a rare event in 2002 where Earth's antarctic polar vortex was destabilized in this way.

Turbulent transport in a 2D ideal fluid is facilitated by the motion of vortices, which are capable of carrying heat, momentum, and tracers quickly over large distances. However, in a PV system, the transport can be suppressed as vortices are destabilized by large-scale zonal flows. As such, the transport rate should scale inversely with the ratio of the zonal flow strain to the vorticity (i.e., an analog of ε^*). These ideas are of great importance to the magnetic fusion research community [13, 36], since the suppression of transport can lead to high-confinement states with high plasma temperature and pressure. More specifically, a vortex which encounters a shear layer associated with a zonal flow (also called a "transport barrier" in the literature) will likely experience some type of time-dependent strain similar to the strain pulses studied in Chapter 5. The question then becomes whether the magnitude and duration of the strain pulse is sufficient to "destroy" the vortex. If so, it seems plausible that the resulting filament of vorticity would simply reinforce the shear layer rather than fragmenting into daughter vortices.

A similar situation arises in the context of astrophysical disks. At the simplest level, hydrodynamical flow within these disks can be described using the so-called "shearing box" geometry, where the flow evolves under the influence of a background shear associated with the Keplerian rotation of the disk [33]. When the radial variation of the fluid density is considered, the disk also follows a type of PV dynamics [31]. Thus, the ideas considered above in the context of geophysical fluids and fusion plasmas may be applicable. For example, it is thought that vortices in stellar accretion disks could enhance planet formation processes

[34]. The background Keplerian shear and/or PV dynamics may have a destabilizing effect on the vortices, which could reduce the likelihood of planet formation.

6.4 Ideas for future experiments

So far, experiments with the 8ST have focused primarily on the case of time-independent strain flows, a particularly simple case for which the data can be compared directly to the K81 theory. Interesting discrepancies with the K81 theory have been observed when smooth vorticity profiles are used, including modified stability properties and inviscid damping of the orbits. These topics deserve further, quantitative study. It would be worthwhile to measure precisely the damping rate of the orbit for a range of vorticity profiles, and attempt to quantify the conditions necessary for the damping to be shut off before reaching a steady elliptical state. By conducting a perturbation analysis about such an elliptical state, it might be possible to also compute theoretically the damping rate and compare to experimental data. Although the Okubo-Weiss local stability criterion [46, 47] and its variants [49, 50] are often implemented for turbulent flows, it would be interesting to study these predictions further for the simple case of a single strained vortex.

Data were presented in Chapter 5 for certain cases of time-dependent strain, including square pulses, Gaussian pulses, and sinusoids. However, these data were preliminary, and the parameter space of possible time dependencies is vast. A logical next step in the 8ST research program is to document precisely the behavior of the vortices in response to a wide range of time-dependent strain flows of varying magnitude and frequency scale (i.e.,

in the spirit of Fig. 5.8). Wherever possible, the data should be compared with theoretical results. For example, when the strain varies slowly, adiabatic behavior is expected, and so future experiments should focus on studying the equilibria occuring under these conditions, as well as the manner in which adiabaticity is broken when the frequency scale of the strain is increased. Of particular interest is the case of the sinusoidal strain, where the vortex can be "stirred" into a state of driven turbulence; here, the transition to chaotic behavior could be studied in detail. Furthermore, it would be interesting to then cease the sinusoidal time dependence in favor of a constant one, and study the relaxation of the turbulence in the presence of a background (static) strain flow.

The parameter space of possible experiments in the 8ST could be further expanded by considering other spatial dependencies of the applied flow (i.e., boundary conditions other than the quadrupolar one used to generate the simple strain flow). Whereas this dissertation focuses primarily on elliptical $m = 2$ vortex modes, attempts could be made to excite and study $m = 3$ or $m = 4$ modes as well. The effect of applied irrotational shear on a vortex could be studied by using the flow pattern shown in Fig. 2.4(b), although in this case the timescale of the experiment is limited due to translation of the vortex toward the wall. On a slightly more complicated level, when a quadrupolar voltage pattern is rotated about the trap, the external flow appears as a simple shear flow in the rotating frame, and so this could be an interesting direction for research.

Finally, looking beyond the 8ST, it would be valuable to consider ways to simulate other types of quasi-2D fluid behavior using electrons. For example, it could be possible to create a PV-like situation if the trapping length of the apparatus was a function of the

perpendicular spatial coordinates, $L = L(x, y)$; here, the circulation associated with a given electron would change as it drifts about the trap. Although such experiments would be difficult or impossible using the current 8ST apparatus, this could be implemented on a future device. Experiments of this type would be of greater relevance to the dynamics of geophysical fluids, laboratory fusion plasmas, and astrophysical disks. Complementary studies would also be relatively simple to carry out using a modified version of the vortex-in-cell code.

Appendix A

Experiments with the multi-cell trap

A.1 Introduction

Prior to construction of the 8ST, experiments were conducted using a different non-neutral plasma confinement apparatus called the Multi-Cell Trap (MCT). The goal of these experiments was to develop a high storage capacity PM trap capable of confining large numbers of charged particles for a long period of time. They constitute the first laboratory studies of the multi-cell concept originally proposed by Surko and Greaves [108], in which single-component plasmas are transferred into off-axis Penning-Malmberg (PM) traps and stored in parallel. Contrary to the 8ST experiments, the conditions for the plasma/fluid analogy are often violated here. Collisional and 3D effects play an important role in the dynamics of MCT plasmas. However, in many cases the plasmas exhibit vortex-like behavior (i.e., due to the plasma rotation and the rapid axial bounce motion) – in fact, the 8ST concept was motivated by a set of experiments performed in the MCT.

The primary constraint on storage capacity in a PM trap is the "space charge" potential generated by the plasma through Poisson's equation. The space charge potential has its maximum absolute value at the center of the plasma where the particle density is highest, given by

$$|\phi_0| = \frac{eN}{4\pi L\varepsilon_0}\left[1+2\ln\left(\frac{r_w}{r_p}\right)\right], \tag{A.1}$$

where r_p is the radius of the plasma and a flat plasma density profile is assumed [109]. In order to confine the plasma axially, the electrostatic potentials generated by the confinement electrodes must exceed the plasma space-charge potential, otherwise particles will leak out of the ends of the trap until the plasma potential and confinement potential are equal. This places a practical limit on the number of particles that can be confined in a single PM trap. The confinement electrodes are biased to voltage V_c by a power supply. These voltages must be switched quickly in order to both trap and deliver particles. While confinement voltages of order $V_c \sim 1$ kV are manageable, one would like to avoid larger voltages due to a number of factors including electrical breakdown and plasma heating. Additionally, r_p/r_w and L must be relatively small in order to avoid expansion and heating of the plasma, and therefore maximize its lifetime in the trap. The MCT concept addresses these problems by separating the plasma into a few smaller plasmas which are confined individually in a series of smaller, parallel PM traps. In this way, the separate plasmas are shielded from each other by conducting walls, thus allowing for a greater number of particles to be stored in a similar volume.

The multicell concept was developed in order to store and manipulate large num-

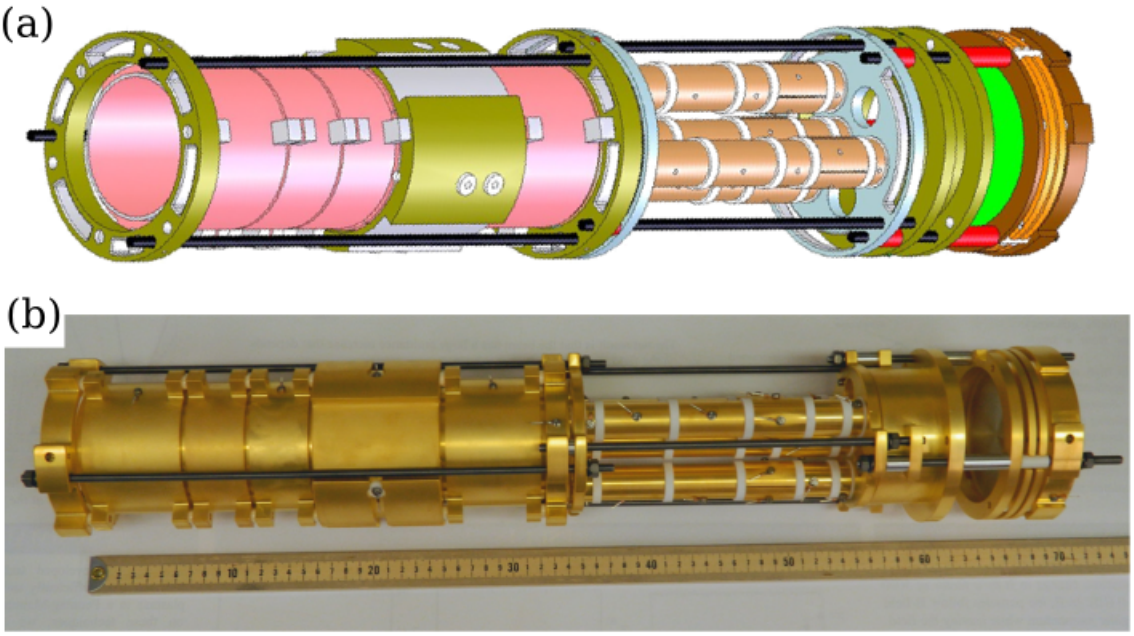

Figure A.1: Computer model (a) and photograph (b) of the MCT electrode structure. The large-diameter master cell is located on the left, the storage cell array is in the middle, and the phosphor screen assembly is on the right.

bers of positrons (i.e., anti-electrons) for a variety of antimatter applications. These include efforts to create an electron-positron plasma in the laboratory [110], and other applications where large bursts of positrons are needed [111]. The MCT experiments discussed here were performed using electrons, with the idea that the techniques developed could also be used to manipulate positron plasmas. Due to its unusual geometry, experiments with the MCT led to a number of interesting discoveries in the context of non-neutral plasma physics, which are presented here. Also discussed are the successes and failures of this MCT device with regard to the goal of high-capacity antimatter storage, and recommendations for future devices are given.

Pictures of the MCT apparatus are shown in Fig. A.1, including a computer model and a photograph of the assembled device after gold-plating. The MCT consists of a large-

diameter "master cell" PM trap (left side), and a series of four small-diameter, parallel "storage cells" (right). One storage cell, labeled "cell A," shares an axis with the master cell, while the axes of the other three cells (B, C, and D) are parallel to but displaced radially by 30 mm from the master cell axis, and evenly spaced in azimuthal location. The wall radius of the master cell is 38 mm. The radius of cells A, B, C, and D are 8, 8, 6, and 4 mm. The storage cells were designed and built with different radii, so as determine how small the cells can be made without adversely impacting the confinement properties. The length of the confinement region is about 200 mm for the master cell, and 170 mm for all of the storage cells.

Each cell (including the master) is equipped with a few solid annular electrodes for axial confinement, and a four-fold azimuthally segmented electrode which can be used for improved plasma confinement *via* the Rotating Wall (RW) technique [24]. The entire electrode structure was mounted inside the same vacuum chamber and magnet system used for the 8ST experiments, with vacuum pressure $\sim$ nanotorr and magnetic field $B = 4.8$ T. The same electron source was used to generate plasmas, and the same phosphor screen and CCD camera were used to diagnose the electron density (although the optical setup was slightly different).

The procedure for injecting electron plasmas into the MCT storage cells is shown schematically in Fig. A.2. First, plasmas are generated ("filled") in the master cell with the heated cathode source using the procedure described in Chapter 2. The number of electrons N can be controlled by the electrode voltages and the duration of the fill process. The plasma must be small in radius so as to eventually fit into the smaller storage cells, and

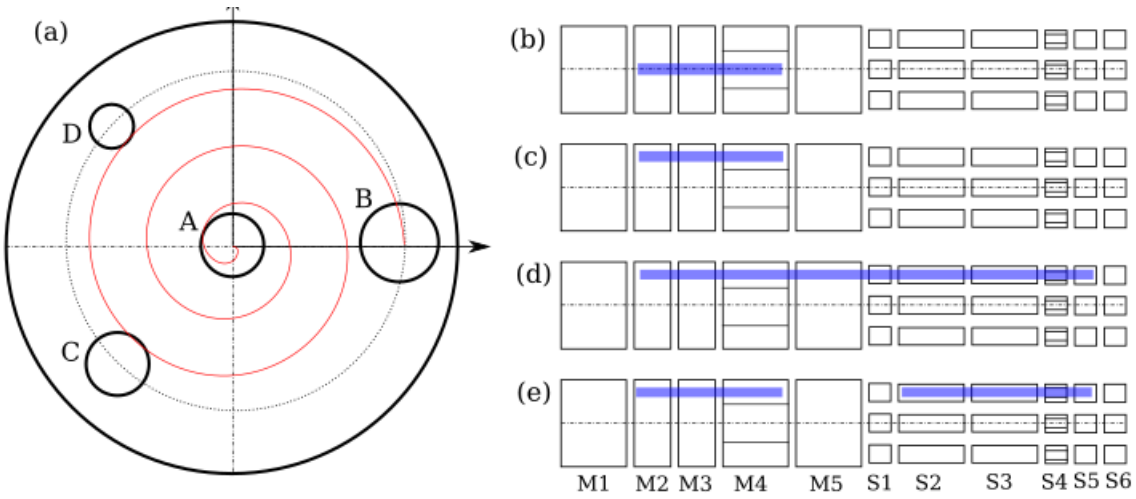

Figure A.2: Schematic diagram of the MCT geometry and procedure. (a) view of the master and storage cells in the plane perpendicular to **B**, including a spiral plasma trajectory from the master cell axis to the axis of cell B (red). (b)-(e) side view of the electrodes with labels M1-5 (master) and S1-6 (storage). Plasmas beginning on the master cell axis (b) are moved across the field using the autoresonant diocotron drive (c), injected into an off-axis cell (d) and stored (e).

high in density in order to maximize the number of stored particles. This was accomplished by compressing the plasma with the RW technique using the segmented electrodes (M4). In order to transfer the plasma into cell A (on-axis), the confinement potentials are simply adjusted so that the plasma streams into the cell along the magnetic field. In order to transfer the plasma into the off-axis cells, the plasma must be displaced across the magnetic field. This was done by applying a chirped voltage signal (i.e., a sinusoid where the frequency increases with time) to one of the segments of electrode M4 in order to drive the plasma outward in radius. Here, the nonlinear $m = 1$ diocotron mode of the plasma locks to the drive signal through a process called autoresonance, as described in Refs. [112, 109, 25]. When the plasma displacement reaches the radius of the off-axis cells, the drive signal is removed, and the plasma orbits the master cell at a fixed radius. As the plasma transits

the desired off-axis cell, the confinement potentials are adjusted so that the plasma streams along the magnetic field into the storage cell. Then, the plasma in the storage cell is isolated by once again raising the confinement potentials, and plasma expansion is countered in the storage cell by implementing the RW technique using the segmented electrodes (S4). In this way, plasmas can be injected into the storage cells, both on and off the axis of the master cell, and confined for long periods of time using the RW.

In general, to transfer and confine a plasma in a storage cell requires a number of steps, where the performance at each step can have a significant impact on the following steps. The research program with the MCT can be summarized as a series of experiments aimed at understanding the plasma dynamics through each step from filling the master cell to RW confinement in the storage cell. This appendix is organized such that each section focuses on a particular step in this process.

A.2 Plasma pinning during the fill process

The trap is filled with plasma using a heated cathode source which produces a magnetized beam of electrons. The cathode is located in the flaring region of the magnetic field where $B_z \sim 0.02$ T, and biased to a negative voltage V_e in order to generate a beam. As the electrons travel into the high field region where the MCT electrodes are located, parallel energy is converted to perpendicular in order to conserve the magnetic moment adiabatic invariant $E_\perp/B$ [19]. The first master cell confinement electrode M1 (closest to the cathode) is biased to the "lip voltage" V_l, which is chosen to be slightly less than the parallel energy

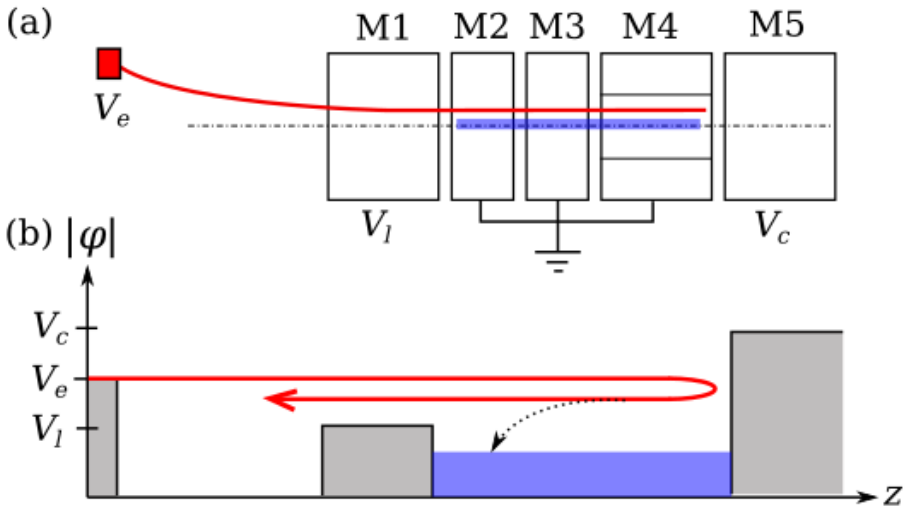

Figure A.3: Schematic diagram of the plasma generation process. (a) a heated cathode (red) produces an electron beam which passes through the master cell. (b) the beam (red) has sufficient energy to transit electrode M1, but is reflected by electrode M5. Scattering events can cause electrons to become trapped (black arrow), and the trapped electrons can form a plasma (blue).

of the beam, so that the electrons are just barely able to pass through the lip electrode into the trap region. The last master cell electrode M5 is biased to the confinement voltage $V_c = -100$ V such that the incoming beam particles are reflected. As the particles transit the master cell confinement region, they can scatter parallel energy into the perpendicular direction, either through binary collisions or, conceivably, through a two-stream instability [86]. In this way, the parallel energy can be reduced to below eV_l so that the particles become trapped in the master cell. A schematic of the plasma filling process is shown in Fig. A.3. This process continues until the desired number of trapped electrons N is reached. At this point, the lip electrode M1 is ramped to voltage V_c so the incoming beam is blocked, and the plasma is isolated inside the master cell.

In practice, the voltages V_l and V_e and the fill time are adjusted until the desired

plasma is achieved. However, small variations in the intial plasma can have a significant effect on the dynamics later in the experimental procedure. Thus it is important to develop a better understanding of how the plasmas are generated in order to achieve better reproducibility.

The above description of the fill process considers only the axial dynamics. In principle, the distribution of electrons perpendicular to the magnetic field is of little importance since the profile can be adjusted with the RW. However, the performance of the RW compression can be sensitive to the initial electron distribution. It was found in the MCT that the initial density profile was in turn sensitive to where in the perpendicular plane the electron beam passed through the master cell electrodes. For example, a beam which was well centered on the axis of the master cell tended to result in plasmas with small radius and high density, whereas a beam which was offset from the axis resulted in broad, low-density plasmas. In the latter case, electrons are deposited at the beam location away from the trap axis.

Eventually, the trapped particles settle into a collective rotational motion as would be expected for an electron plasma. However, during the early stages of the fill process, very few particles are trapped, and so the collective rotation of the trapped particles (which may not yet constitute a plasma) is weak. It was observed in the MCT that early in the fill process, the trapped particles were "pinned" to the beam location. As the particle number N grew over time, a transition occurred where the trapped population separated from the beam and began to execute an $m = 1$ diocotron mode.

Data are shown in Fig. A.4 (a) for the location of the beam and plasma during

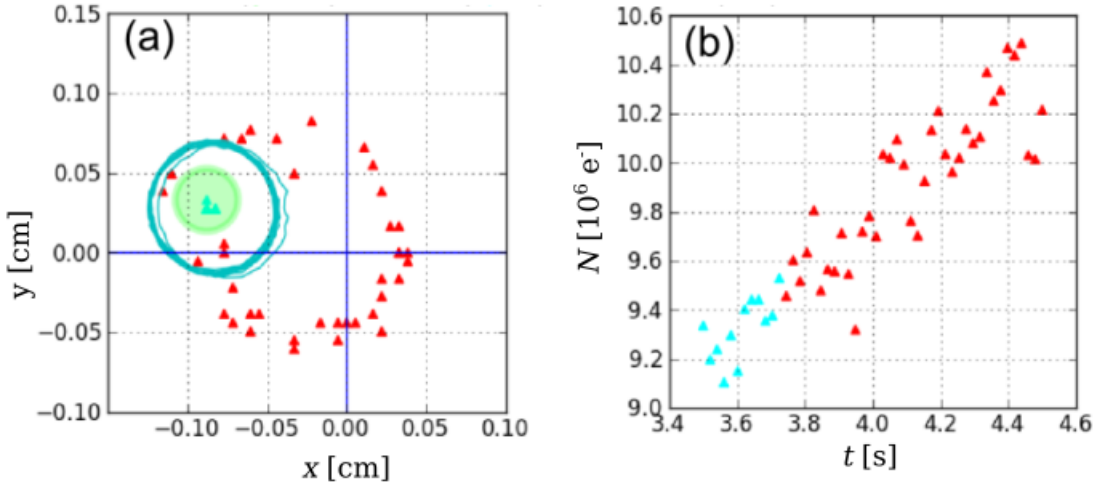

Figure A.4: Data showing the de-pinning of the trapped electron population as its particle number increases. (a) location (triangles) and spatial extent (contours) of the beam (green circle), pinned plasmas (cyan), and de-pinned plasmas (red); (b) particle number as a function of the fill time.

the fill process in the master cell. Here, the beam location and width is diagnosed by direct imaging with the phosphor screen (the beam is allowed to pass through the electrodes briefly so as not to damage the screen). The beam is shown in Fig. A.4 (a) as a green shaded circle; its width is ~ 0.25 mm, and it is located approximately 1 mm from the trap axis. Plasmas are created and diagnosed at various times throughout the fill process. Panel (a) shows the location of the plasma density centroid (triangles) for pinned (cyan) and unpinned (red) plasmas. Also shown is the spatial extent of the pinned plasmas (cyan contours corresponding to 5% of the peak density). Panel (b) shows the total trapped particle number N as a function of the fill time t. The data show that below a certain threshold, the plasma location is coincident with that of the beam; whereas above the threshold, the plasma becomes decoupled from the beam and performs a quasi-circular diocotron orbit about the trap axis.

The pinning behavior can be understood in terms of a simple 2D fluid model, where the plasma and the beam are treated as individual point vortices. As discussed in Chapter 2, a single electron can be treated as a point vortex (under certain conditions), where the charge per unit length is analogous to the vortex circulation. For a plasma consisting of N electrons, if the internal degrees of freedom (i.e., elliptical distortions, etc.) are neglected, the perpendicular dynamics are that of a point vortex with circulation $\Gamma_p = eN/L$ which can move across the magnetic field according to the $\mathbf{E}\times\mathbf{B}$ drift. The passing beam particles quickly transit the master cell in a single bounce, therefore the perpendicular drift motion is insignificant and the beam can be treated as a stationary point vortex. The circulation associated with the beam is given by the number of passing electrons in the trap at any given time, which is $N_b = I/ef_b = 2LI/ev_{\|}$ where $I \sim 0.1$ μA is the beam current, so the beam circulation is $\Gamma_b = 2I/v_{\|}$.

We construct a Hamiltonian describing the drift dynamics of the trapped plasma located at (r,θ) under the influence of the beam and its own image field,

$$H(r,\theta) = \Gamma_b\Gamma_p \ln\left[r_w^{-1}(r^2 + x_b^2 - 2rx_b\cos\theta)^{\frac{1}{2}}\right] + \Gamma_p^2 \ln(1 - r^2/r_w^2), \qquad \text{(A.2)}$$

where the beam is located at distance x_b along the positive $x-$axis, and the canonical co-ordinates are (p_θ,θ), where $p_\theta = eBr^2/2L$. The first term in Eq. A.2 is the interaction energy between the beam and the plasma; it describes orbital motion of the plasma about the beam, since the beam location is fixed. The second term is the interaction energy of the plasma with its image charge induced in the wall; it describes circular orbital motion about the trap axis (i.e., the $m = 1$ diocotron mode). The system is parameterized by the

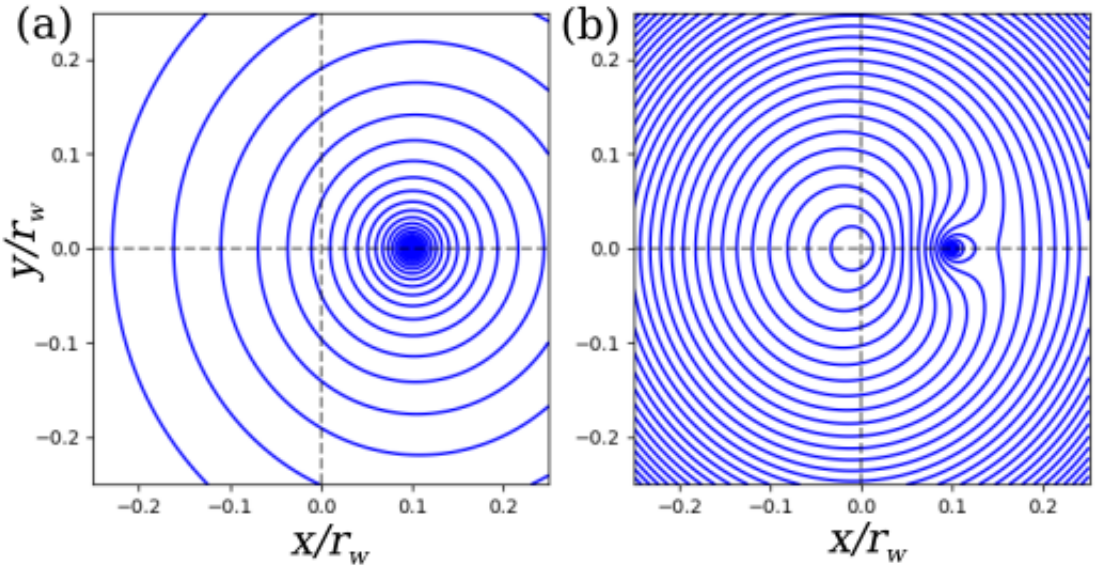

Figure A.5: Contours of the beam-plasma Hamiltonian given by Eq. A.2. Here, $x_b = 0.1$, and $\Gamma_p/\Gamma_b =$ (a) 0.1, and (b) 10, corresponding to beam-dominated and plasma-dominated behavior, respectively. A bifurcation occurs as the parameter Γ_p/Γ_b is varied.

ratio of circulations Γ_p/Γ_b. Contours of the Hamiltonian in Eq. A.2 are plotted in Fig. A.5 for $x_b/r_w = 0.1$, and $\Gamma_p/\Gamma_b =$ (a) 0.1, and (b) 10. For small Γ_p/Γ_b, the plasma orbits are centered on the beam. As Γ_p/Γ_b increases, a bifurcation occurs, and the plasma can orbit either the beam, the trap axis, or both. Thus, as the particle number associated with the plasma grows, the plasma can be de-pinned when Γ_p/Γ_b reaches its critical value.

This simple model captures qualitative aspects of the plasma pinning phenomenon. These ideas are useful in understanding the early stages of the plasma filling process. Additionally, the pinning behavior could potentially be used as a technique to better control the transverse location of small trapped plasmas.

A.3 Cell-to-cell transfer

After generating a plasma, the RW technique is used to compress the plasma as needed. The RW method has been studied widely and is well understood [113, 24], so it is not discussed in detail here. Following the RW compression, the plasma can be either transferred directly into the on-axis cell (A), or moved across the field and injected into one of the off-axis cells (B, C, or D). Although plasma transfers have been performed in other devices, they are unique in the MCT. Coaxial transfers (into cell A) are unique in that the storage cell has a much smaller transverse dimension than the master cell. Transfer into the off-axis cells provides an additional level of complication, since, in addition to the axial motion, the plasma is inclined to drift around the trap due to image fields. Due to their relative simplicity, coaxial transfers were studied first in the MCT in order to understand the effect of the differing trap dimensions.

Experiments with coaxial transfers were conducted by preparing a plasma in the master cell, then simply grounding the gate between the master and storage cell (electrodes M5 and A1) for some time t, after which the gate was raised again, thus isolating the transferred plasma from that remaining in the master cell. Then, the transferred plasma was diagnosed using the CCD camera. This procedure is shown schematically in Fig. A.6, where we allow for a uniform bias V_s applied to all storage cell electrodes. It was found that the spatial distribution of the transferred plasma was similar to that of the original plasma, so the perpendicular dynamics are unimportant. The primary metric for these experiments was the ratio of the number of particles in the transferred plasma N_s to that of the original

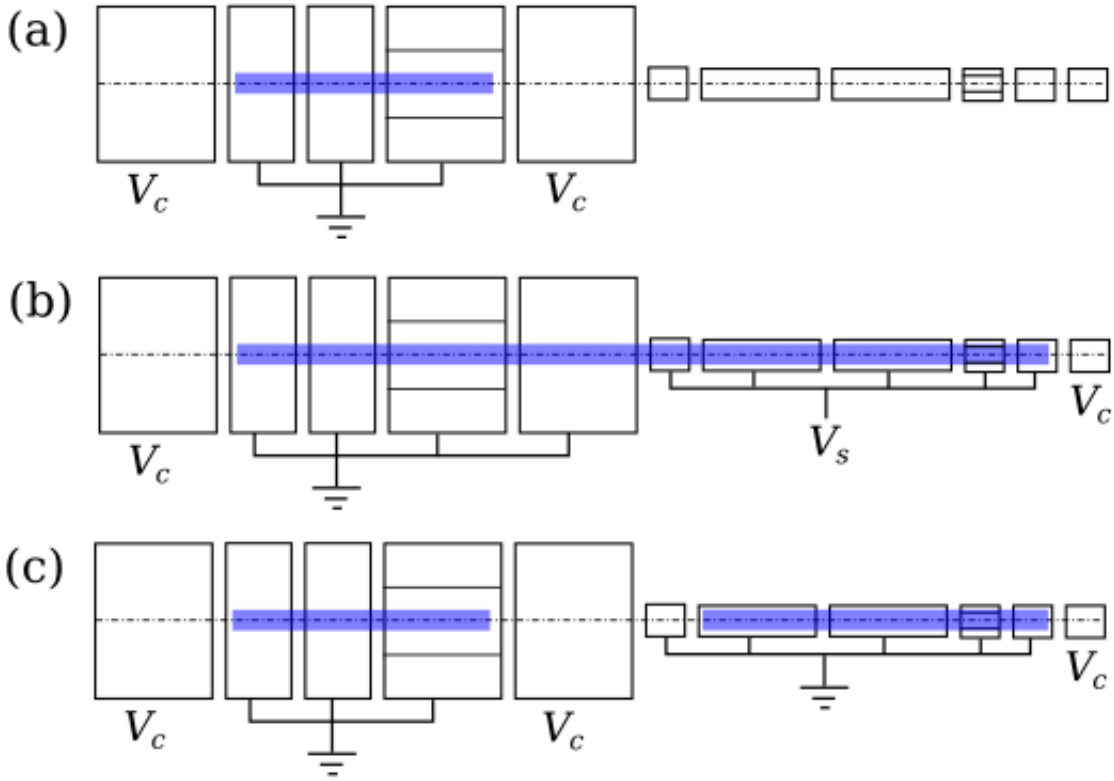

Figure A.6: Schematic diagram of transferring plasma into an on-axis storage cell. The experiments begin with (a) a plasma confined in the master cell, then (b) the plasma is allowed to stream into the storage cell, then (c) the storage cell plasma is isolated and diagnosed.

plasma N_0, which we will call the transfer efficiency N_s/N_0. The goal was to maximize the transfer efficiency so as to increase the number of particles trapped in the storage cells[1].

Data are shown in Fig. A.7 (a) for the transfer efficiency as a function of the the gate time t, for two different initial plasmas with $r_p \sim 1$ mm and $N_0 = 4 \times 10^6$ (magenta) and 6×10^6 (blue) e^-. Although not shown in the data, plasma initially streams into the storage cell on the order of the bounce time $1/f_b = 2L/v_T$, which is approximately 1 μs. The plasma quickly develops a collisionless steady state where $N_s/N_0 \sim 0.2 - 0.3$. For $t \gtrsim 1$ ms, the transfer efficiency is increased to $N_s/N_0 > 0.5$ as the plasma relaxes into the storage cell through collisions. The efficiency is comparable for the two different plasmas, indicating that the curve in Fig. A.7 (a) may be independent of the specific details of the plasma.

The collisionless steady state can be understood using a simple kinetic model. Here, the dynamics are described by a phenomenon called "anti-shielding" [114], where the plasma density is reduced in the vicinity of a positive test charge since the collisionless particles are accelerated. We consider a 1D system where particles bounce across both the master cell and the storage cell. The master cell plasma and the storage cell plasmas are described by their particle numbers N_m, N_s and lengths L_m, L_s. Initially, before the transfer begins, $N_m = N_0$, the total number of particles, and the particle energy is $\phi_0 = -(e/4\pi\varepsilon_0) n_m \gamma_m$, where $n_m \equiv N_m/L_m$ is the 1D density, and $\gamma_m = 1 + 2\log(r_w/r_m)$ (c.f. Eq. A.1). Here, we have assumed that the plasma temperature is small compared to

[1] One possibility is to conduct multiple sequential transfer events, which is called "plasma stacking". In this case, the initial transfer efficiency is not as important. However, subsequent transfer events are complicated by the preexisting plasma in the storage cell. Stacking events are not discussed further here, although this may be an interesting direction of research.

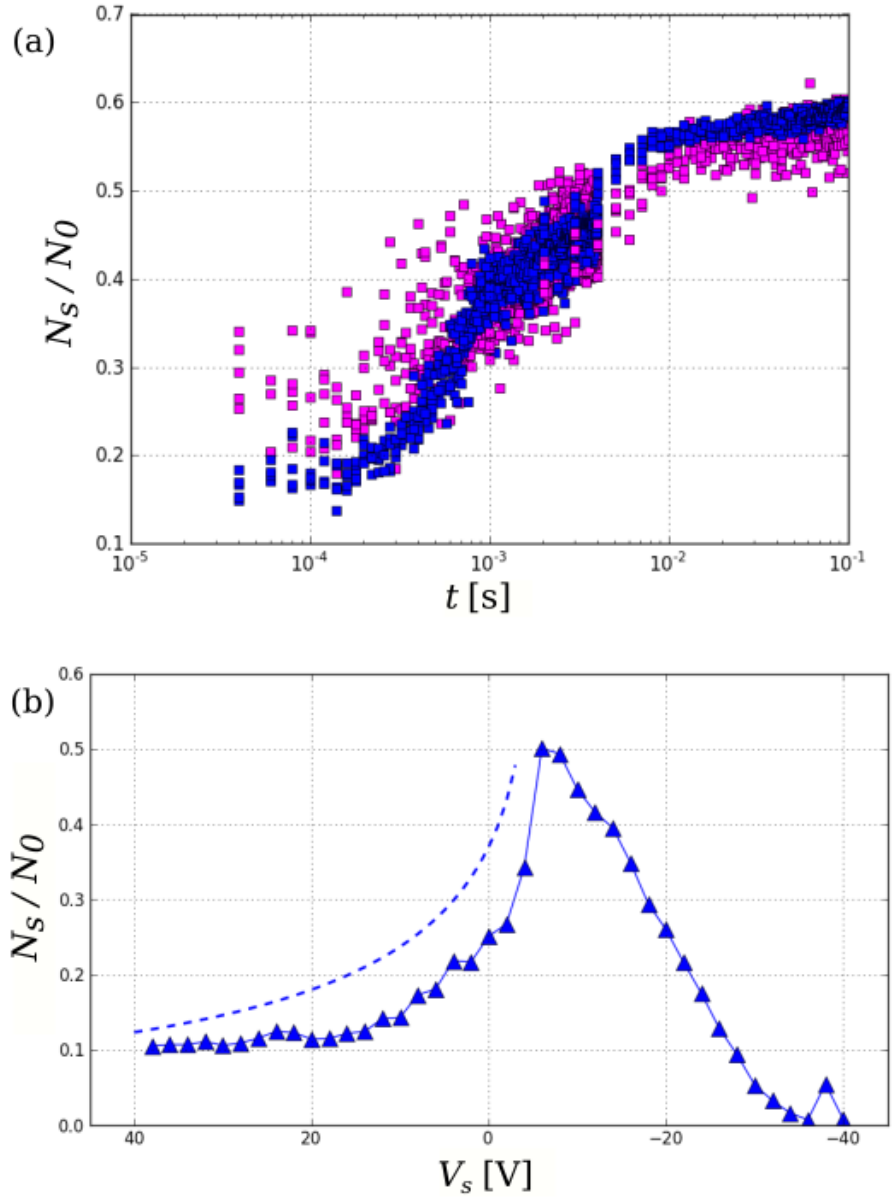

Figure A.7: Data showing the efficiency of transferring plasma into an on-axis storage cell, as a function of (a) time, and (b) voltage applied to the storage cell electrodes. Panel (a) shows data for two different plasmas with $r_p \sim 1$ mm and $N_0 = 4 \times 10^6$ (magenta) and 6×10^6 (blue) e^-. In panel (b), data for $N_0 = 6 \times 10^6$ e^- are compared to a simple kinetic model (dashed) which is described in the text.

the space charge potential, $e\phi/T \gg 1$.

When the gate between the master and storage cells is lowered, particles stream into the storage cell, and then eventually bounce back into the master cell. Once a collisionless steady state is reached, the net flux of particles across the boundary between the two traps is zero. This amounts to a continuity condition $n_m v_m = n_s v_s$, with v the axial velocity of the particles in each trap region. Energy conservation dictates that $m_e v_m^2/2 = \phi_0 - \phi_m$, and $m_e v_s^2/2 = \phi_0 - \phi_s - V_s$ (since the storage cell can be biased). Finally, conservation of particle number dictates that $N_m + N_s = N_0$. Imposing these three conditions, we obtain a quadratic equation for the particle number in the storage cell:

$$\left[\frac{\gamma_m}{L_m^3} + \frac{\gamma_s}{L_s^3}\right] N_s^2 - \left[\frac{4\pi\varepsilon_0 V_s}{eL_s^2} + \frac{2N_0\gamma_m}{L_m^3} + \frac{N_0\gamma_m}{L_m L_s^2}\right] N_s + \frac{N_0^2\gamma_m}{L_m^3} = 0 \tag{A.3}$$

The solution of this equation, scaled to the initial particle number N_0, gives the transfer efficiency. All of the coefficients in Eq. A.3 are constants, except that the storage cell voltage V_s can be varied. When $V_s = 0$, the solution is $N_s/N_0 \approx 0.37$, which is slightly greater than the observed efficiency on collisionless timescales [c.f. Fig. A.7 (a)].

Physically, this model describes a situation where the storage cell density is reduced relative to that of the master cell mainly due to the factor γ which depends on the wall radius. Since $r_s < r_m$, the potential in the storage cell is reduced and so particles are accelerated into the storage cell by the electric field at the interface. Thus, the particles transit the storage cell faster than the master cell – that is, the storage region is anti-shielded by the plasma – and so the storage cell density is reduced. This is detrimental to the goal of maximizing transfer efficiency. However, by applying a negative voltage V_s to the storage

cell electrodes, particles are slowed down in the storage cell, thus increasing the efficiency (up to a certain point where the voltage begins to block the incoming particles).

In Fig. A.7 (b), data are shown for the collisionless transfer efficiency (i.e., with $t \sim 50$ μs) as a function of the voltage applied to the storage cell for a plasma with $r_p \sim 1$ mm and $N = 6 \times 10^8$ e$^-$. It is observed that the efficiency decreases when $V_s > 0$, since the electrons are accelerated through the storage cell. Similarly, the efficiency increases when small negative voltages are applied. The efficiency then decreases again with sufficiently large negative voltages, since electrons are simply blocked from entering the storage cell. The solution to Eq. A.3 (dashed) is compared to the data, up to the point at which the quadratic solution becomes imaginary ($V_s \sim -3$ V). Although the model tends to overpredict the transfer efficiency, it seems to capture qualitatively the key aspects of the anti-shielding phenomenon.

In summary, when transferring plasma into a smaller cell on short timescales, it may be advantageous to apply a small, negative voltage to the electrodes in order to maximize the efficiency. On longer timescales $t \gtrsim 1$ ms, particle collisions become important. Collisional dissipation drives the plasma toward a state of uniform potential across the trap interface, $\phi_m = \phi_s$. In this case, the transfer efficiency is actually increased in the smaller cell,

$$\frac{N_s}{N_0} = \frac{1}{1 + \gamma_s L_m / \gamma_m L_s} \approx 0.6, \tag{A.4}$$

in agreement with the observed efficiency on longer timescales [c.f. Fig. A.7 (a)]. Although interesting, this is somewhat irrelevant, since on collisional timescales, the efficiency can

be set to unity by applying a sufficiently deep potential well $+V_s$.

A.4 Autoresonant plasma positioning

In order to transfer plasma into the off-axis storage cells, it must first be displaced across the magnetic field. This is done by exciting an $m = 1$ diocotron mode autoresonantly, where a chirped voltage signal (where the frequency grows in time) is applied to one of the segmented electrodes in the master cell [25]. Autoresonance is a phenomenon occuring in nonlinear oscillators, where the amplitude of the oscillator will adjust itself in order to match the frequency of an applied drive signal. Thus, by varying the frequency of the drive signal, the amplitude of the oscillator can be varied as well.

The $m = 1$ diocotron mode is a nonlinear oscillation, where the frequency is given by

$$f_d = \frac{cNe}{\pi LBr_w^2}\left[\frac{1}{1-(d/r_w)^2}\right], \tag{A.5}$$

where d is the radial displacement of the plasma centroid [109]. For $d/r_w \ll 1$, the bracketed quantity in Eq. A.5 is ≈ 1, so the linear frequency is $f_1 = cNe/\pi LBr_w^2$. It increases with d/r_w, until $d + r_p \sim r_w$, at which point the plasma distorts elliptically[2]and Eq. A.5 is not accurate.

The initial plasma is located near the axis of the master cell. A chirped voltage signal is applied where the starting frequency is less than f_1. As the chirp frequency increases

[2]These elliptical distortions of plasmas near the wall are analogous to the elliptical vortex distortions discussed in the body of the dissertation. Here, the plasma is subject to an external, irrotational shear flow due to its own image charge induced in the wall.

through f_1, the diocotron mode locks to the signal, and the radial location of the plasma increases autoresonantly as the frequency increases. In this case, the plasma trajectory is an outward spiral, as depicted in Fig. A.2 (a). The drive signal is removed when the plasma displacement reaches the radial location of the off-axis cells, that is, when $d = 30$ mm. At this point, $d/r_m \approx 0.79$ and $f_d \approx 2.66 f_1$ according to Eq. A.5. Once the drive signal is removed, the plasma performs a circular diocotron orbit over which it transits the three off-axis cells.

However, the observed diocotron frequency in the MCT master cell was not exactly in agreement with Eq. A.5. Thus, a more detailed model of the diocotron mode was needed in order to position the plasma at the correct radius. In previous work [115], an analytical theory for the diocotron mode frequency was given, including the effect of the "magnetron" drift due to the vacuum electric fields produced by the confinement electrodes. In order to obtain this result, Ref. [115] assumed that $r_p/r_w \ll 1$, $d/r_w \ll 1$, $r_w/L \ll 1$, and $\phi_0/V_c \ll 1$. In the MCT, these assumptions are all routinely violated except for $r_p/r_w \ll 1$. Therefore, a model was developed where the plasma is treated as a line charge, but no other assumptions are made. This problem was solved numerically to find the diocotron frequency as a function of N and d.

Given N, d, and the electrode geometry, the length L of the plasma can be calculated numerically by comparing the plasma potential (Eq. A.1) to the confinement potentials. Results are shown in Fig. A.8 for the master cell geometry and the storage cell geometry, where contours of the electrostatic potentials due to the end confinement electrodes are shown. The axial coordiante z is measured from the center of the trap; only half of the trap

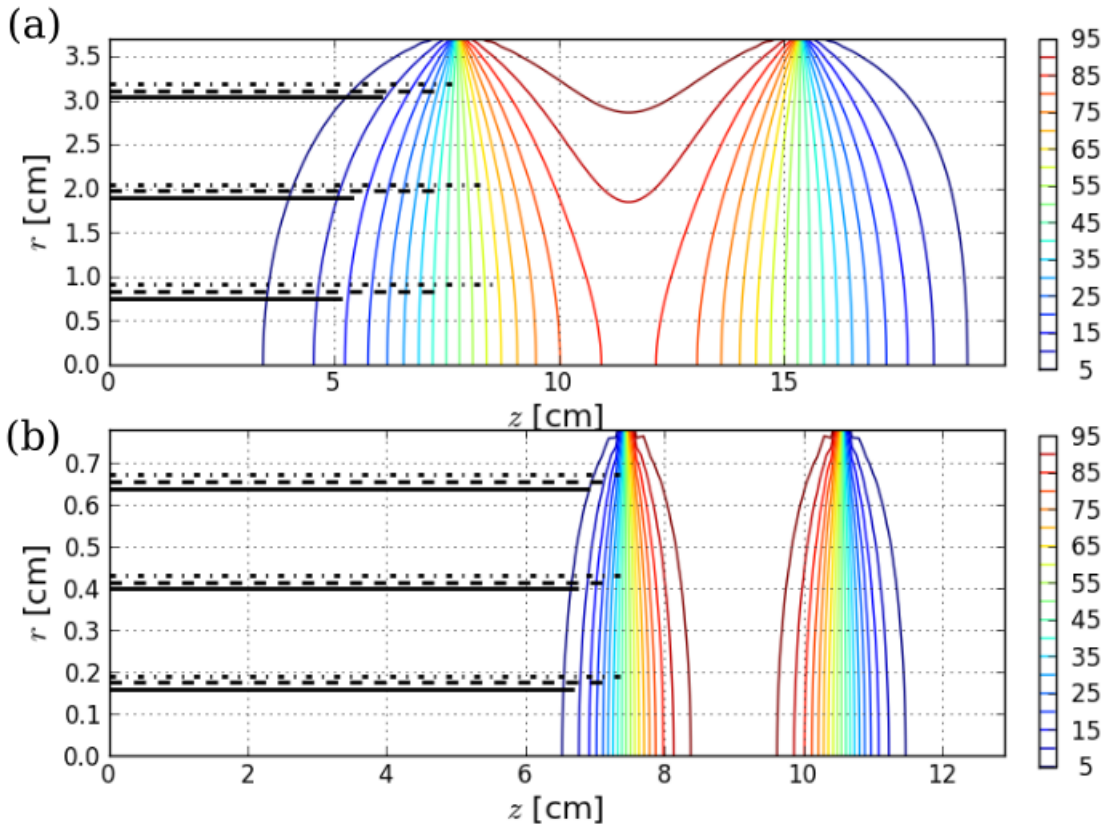

Figure A.8: Calculated plasma length plotted over vacuum electric potentials for the master cell (a) and a storage cell (b). Here, the vacuum equipotential contours are plotted due to end confinement electrodes, which are biased to $-V_c = -100$ V. Plasmas are shown for $N = 2 \times 10^8$ (solid), $N = 9 \times 10^8$ (dashed), and $N = 16 \times 10^8$ (dash-dot), at three different values of d.

is shown, since it is symmetric. Plasmas with three different values of N are shown as lines, for three different values of d, where the length of the line corresponds to the calculated plasma length L. For larger values of N, the plasma pushes further into the confinement field, and so the magnetron effect is emphasized. Furthermore, it is clear that the magnetron effect is significantly more important in the master cell than in the storage cell, due to the larger aspect ratio r_w/L.

After calculating L, the diocotron frequency is calculated numerically in the spirit of Ref. [115], including contributions from both the image fields and the confinement fields. These predictions are compared to experimental data in Fig. A.9 as a function of N and d. The numerical model discussed here (solid) is in good quantitative agreement with the data, whereas the predictions of Ref. [115] diverge, since the assumptions used in that calculation are violated.

Using this numerical model, the diocotron mode frequency corresponding to the off-axis cell location can be calculated, and the drive signal can be removed upon reaching this frequency. At this point, the plasmas can be transferred into the off-axis cells. In order to complete the transfer, the plasmas must be small in spatial extent so as to fit smoothly into the storage cells. In order to do this, the plasmas were compressed using the RW technique on the axis of the master cell. However, it was found that the plasmas expanded significantly during the autoresonant diocotron excitation (i.e., over the course of the spiral trajectory) [25]. This work studied the dependence of the expansion on other system parameters, and identified ways to minimize its effect.

Some of the work and discussion in this section is taken from N. C. Hurst, J. R.

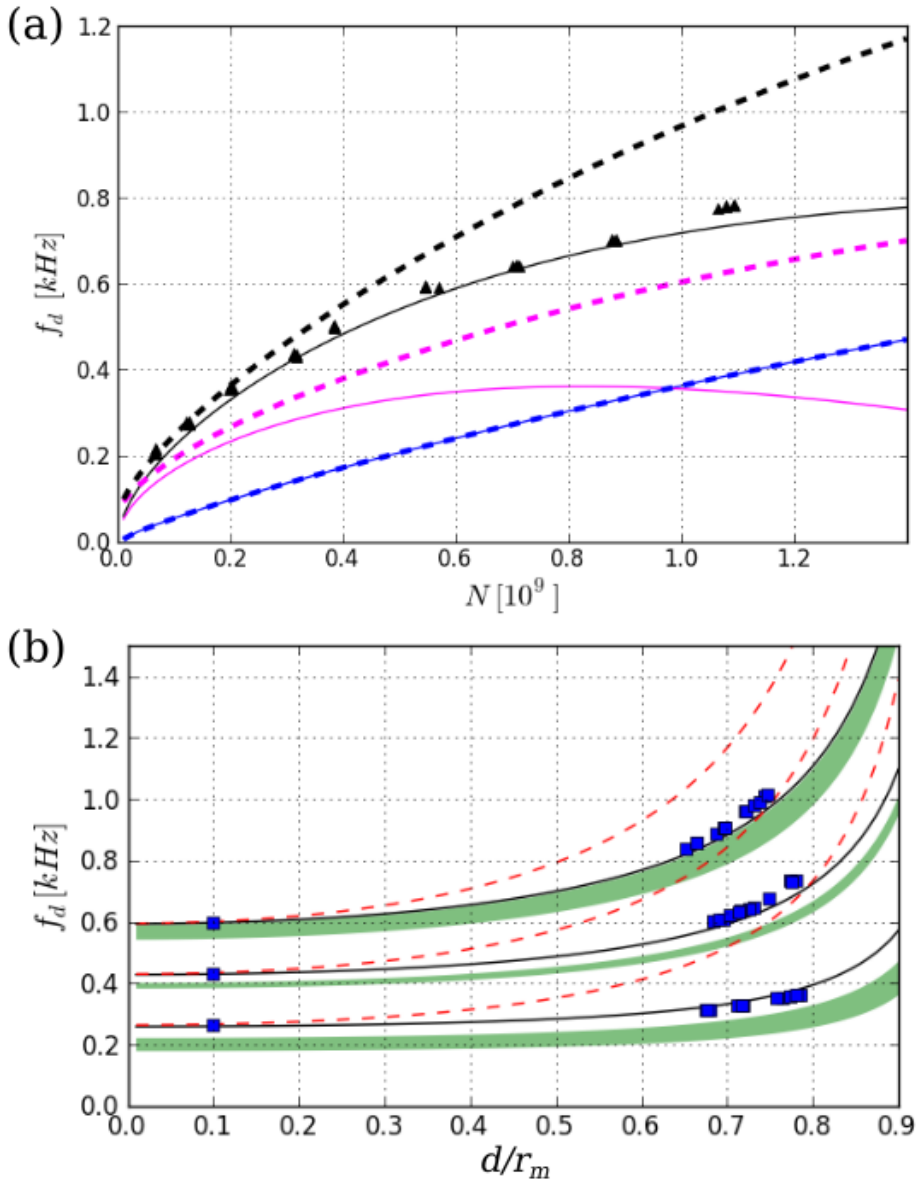

Figure A.9: Comparison of diocotron frequency data with a numerical model (solid) and an analytical one (dashed) in the master cell. (a) frequency as a function of particle number. Shown are the image field contribution (blue), the magnetron contribution (magenta), and the sum of the two (black). (b) frequency as a function of displacement, including fitted (black) and unfitted (green) numerical predictions, and analytical ones (dashed, red).

Danielson, C. J. Baker, C. M. Surko, "Finite-length, large-amplitude diocotron mode dynamics," *AIP Conf. Proc.* **1668**, 020003 (2015). The author of the dissertation led the research and was the primary investigator and author of this paper.

A.5 Bounce-average orbits

As the plasma executes a circular diocotron mode at $d \approx 30$ mm, it transits the location of each of the off-axis cells (B, C, and D). In order to transfer the plasma into these cells, the confinement potential separating the two traps is removed so that the plasma streams along the magnetic field into the storage cell, as depicted in Fig. A.2 (d). However, this situation is more complicated than the on-axis transfer discussed above, since the plasma continues to execute a diocotron orbit while the transfer takes place. Prior to conducting these experiments, it was naively thought that the transfer would be interrupted when the master cell diocotron motion carried it away from the storage cell location.

In fact, experiments with off-axis plasma transfer in the MCT showed that during the transfer process, the plasmas actually perform quasi-elliptical diocotron-like drift orbits within the bounds of the storage cell. This phenomenon is demonstrated using experimental data and a simple model (magenta lines) in Fig. A.10. Panel (d) shows the trajectory of the plasma density centroid in the frame of the storage cell (cell C), where the master cell axis is located along the negative $x-$axis; panel (f) shows CCD images of the plasma density over one period of the orbit. The particle number, mean-square radius, and displacement of the plasma in the storage cell are shown in panels (a)-(c). Evidently some particles in

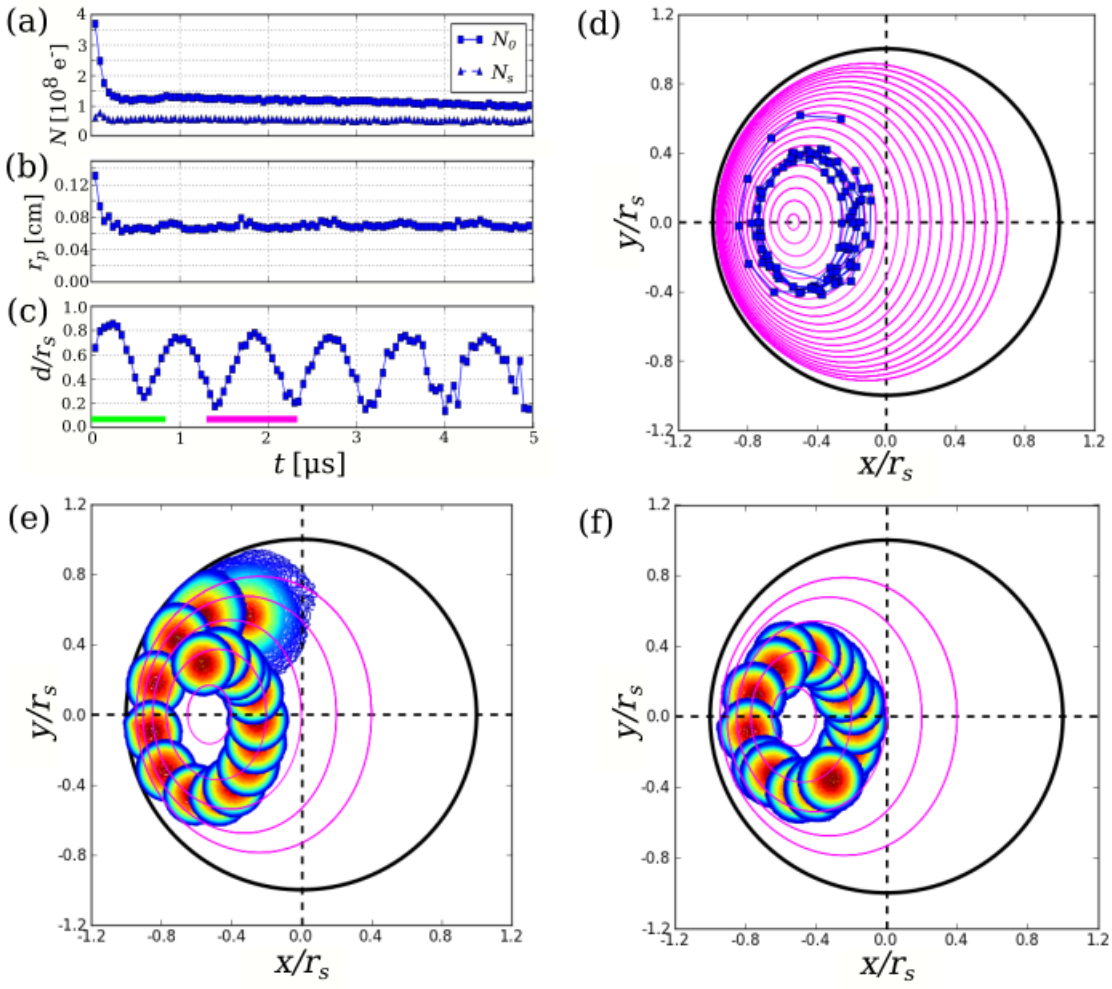

Figure A.10: Data and a simple model of bounce-average diocotron orbits for plasmas spanning the master and storage cells. Shown are (a) the number of particles inside the storage cell N_s, and total, N_0; (b) plasma radius; (c) displacement in the storage cell frame; (d) trajectory of the plasma centroid (blue) and orbit predictions of a simple model (magenta); (e) plasma images over the first orbit; (f) plasma images over the third orbit. Panels (e) and (f) correspond to the green and magenta bars in panel (c).

the outer region of the plasma are lost during a transient event as the transfer begins, after which the plasma settles into a steady orbit. CCD images of the plasma density during the transient are shown in panel (e).

This interesting orbital behavior of the plasma can be modeled simply according to bounce-average drift dynamics, as would be a normal diocotron orbit in a single cell. Since the bounce motion of the particles is rapid compared to the drift motion, the plasma behaves as a rigid column. Thus, the perpendicular drift motion of a particle is given by the average electric field experienced across a full bounce cycle spanning both cells, and so we average the drift velocity vectors, weighted by the instantaneous fraction of particles existing in each cell. Since the orbit spans a large range of displacement in the storage cell, $0 \leq d_s/r_s \lesssim 0.8$, the full nonlinear dioctron formula must be considered (Eq. A.5). However, the orbit extends over a small range of displacement in the master cell, that is $d_m/r_m \approx$ constant, so the contribution from the master cell can be modeled as a uniform drift velocity. These dynamics are referred to as "bounce-average orbits".

Working in the frame of the storage cell, we treat the plasma as a line charge and describe its drift dynamics using the Hamiltonian

$$H = -\frac{\kappa d_s}{r_s}\cos\theta_s + \log\left[1 - \left(\frac{d_s}{r_s}\right)^2\right], \tag{A.6}$$

where κ is a parameter describing the relative weighting of the master cell drift to that of the storage cell. Unfortunately, κ is difficult to calculate, so the model is fitted to the data using κ as an adjustable parameter. Contours of the Hamiltonian (which correspond to plasma orbits) are shown as magenta lines in Fig. A.10. The shape of the orbits predicted

by this model is in close agreement with the experimental data.

The standard diocotron mode has a stable stationary point at the origin, where the image field is identically zero; Eq. A.6 has a stationary point which is offset from the origin, given by $\theta_s = \pi$,

$$\frac{d_s}{r_s} = -\frac{1}{\kappa} + \left(\frac{1}{\kappa^2} + 1\right)^{\frac{1}{2}}. \tag{A.7}$$

Near the stationary point, the orbits are approximately elliptical; whereas for larger orbit amplitude, the orbit shape is more circular. However, the finite plasma radius places a limit on the possible orbit amplitude, since the edge of the plasma approaches the wall. By selecting the location where the plasma transfer begins, the plasma can be positioned near the stationary point, where, in principle, it should remain static. In this way, the off-axis transfer can proceed similarly to the on-axis case, without the additional complication of the orbital motion. Data are shown in Fig. A.11 for a bounce-average plasma spanning both cells which is situated near the stationary point. Shown are the location of the plasma density centroid [panel (a)], the particle number, plasma radius, and displacement [panels (b)-(d)], and CCD images of the plasma density at times $t = 15$, 30, and 45 ms [panels (e)-(g)]. The data show that the plasma remains at the stationary point, although it expands and loses particles at an enhanced rate due to the unusual trapping geometry. Other data (not shown here) indicate that plasmas executing bounce-average orbits can be damped toward the stationary point using a feedback circuit connected to the segmented electrode on the storage cell. Additionally, the exact location of the stationary point can be tuned by applying a static asymmetric potential using the storage cell segmented electrode.

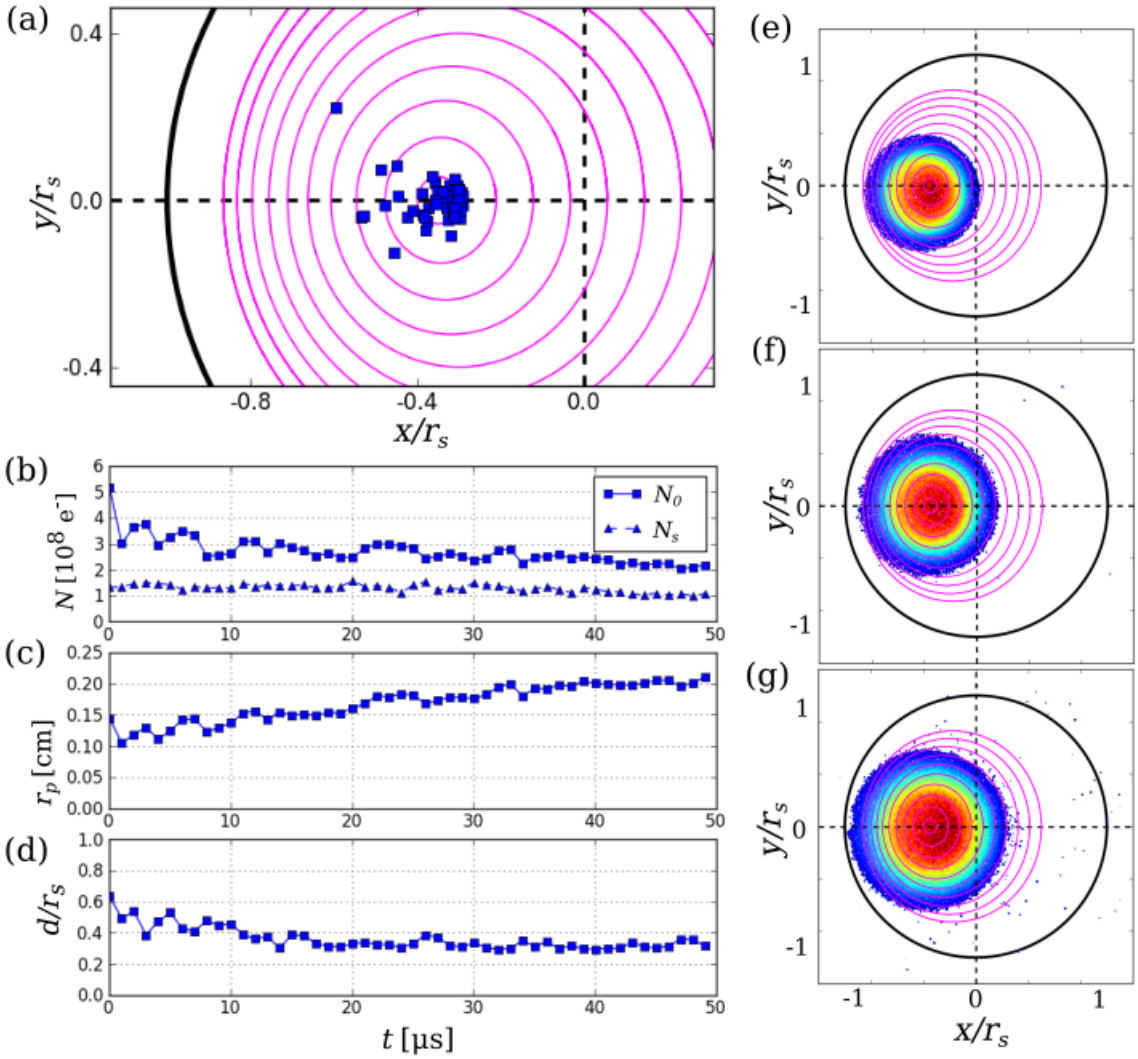

Figure A.11: Data for a bounce-average plasma located at the stationary point. (a) location of the plasma centroid over 50 ms, including predictions of a simple model; (b) total particle number N_0 and number in the storage cell N_s; (c) plasma radius; (d) displacement in the storage cell frame; (e)-(g) CCD images of stationary plasmas at $t = 15$, 30, and 45 s.

The feasibility of performing off-axis transfers is improved significantly due to the bounce-average orbit behavior. Rather than having to complete the transfer while the master cell diocotron orbit transits the storage cell (~ 100 μs), the transfer can be completed over the course of ~ 10 ms while the plasma sits at the stationary point given by Eq. A.7. In this way, the transfer events can be performed on collisional timescales, and are therefore not subject to the anti-shielding effect shown in Fig. A.7. By applying a positive voltage to the electrodes of the storage cell, off-axis transfers approaching 100 % efficiency could be performed.

Some of the work and discussion in this section is taken from N. C. Hurst, J. R. Danielson, C. J. Baker, C. M. Surko, "Electron plasma orbits from competing diocotron drifts," *Phys. Rev. Lett.* **113**, 025004 (2014). The author of the dissertation led the research and was the primary investigator and author of this paper.

A.6 Trapped off-axis plasmas

During an off-axis transfer, the bounce-average orbit dynamics are allowed to proceed for some time, then the gate electrodes separating the storage cell from the master cell are biased to the confinement voltage $-V_c$. This isolates the transferred plasma in the storage cell. The plasma remaining in the master cell continues to execute a large-amplitude diocotron mode; it can be either discarded, or returned to the master cell axis using autoresonance or feedback damping. Thus, the primary goal of the MCT, to transfer plasmas into off-axis cells, was realized. Plasmas were transferred into the on-axis storage cell, and each

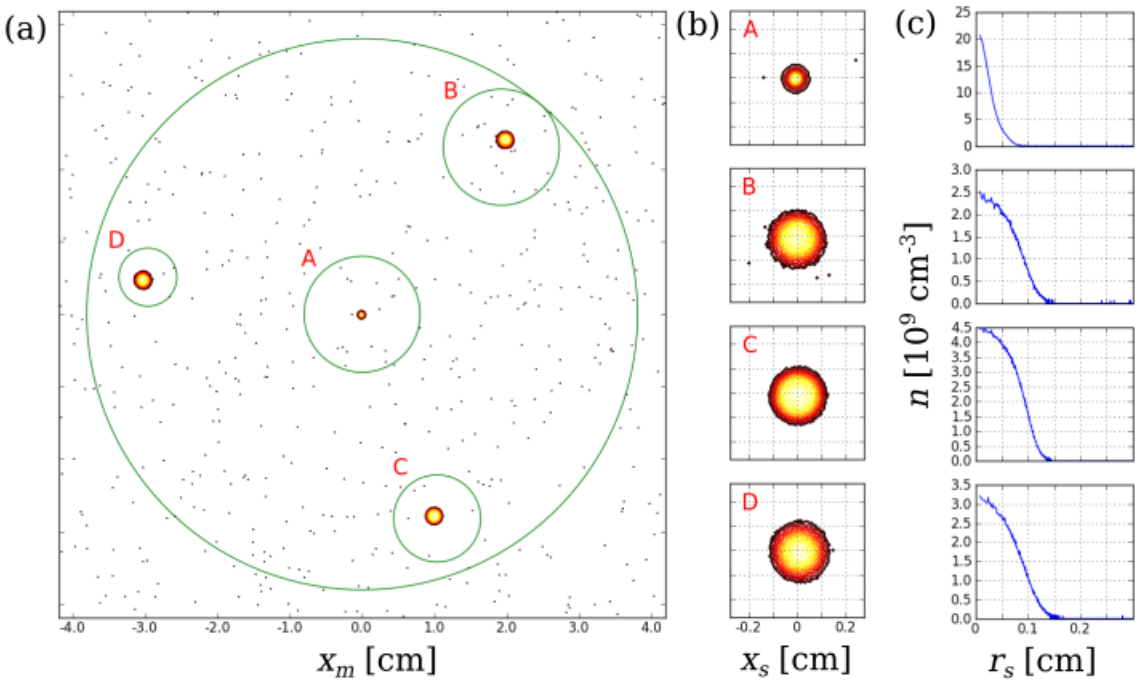

Figure A.12: Images of plasmas trapped in each of the storage cells (not simultaneously). (a) combined, and (b) individual images of all four trapped plasmas; (c) radial density profiles of each plasma.

of the off-axis ones (although not simultaneously). Images of these plasmas are combined and shown in Fig. A.12. Here, the off-axis plasmas have larger radii and lower density compared to the on-axis plasma, due to expansion during the diocotron excitation and the bounce-average orbits.

A secondary goal of the MCT research program was to hold plasmas in off-axis cells for long periods of time. In principle, while a plasma is held in an off-axis cell, other plasmas could be injected into other cells, so as to obtain simultaneous long-term confinement of multiple different off-axis plasmas. This was not accomplished in the MCT experiments described here, primarily due to technical limitations and hardware availability. However, the transport properties of confined off-axis plasmas were studied.

Figure A.13 shows the evolution of a plasma trapped in the off-axis cell C over half a minute using the RW technique to combat expansion (blue). Other data are shown (magenta), where the RW compression is turned off after 15 s and the plasma is allowed to relax freely. The data show that the RW compression can take 5 - 10 s to reach a steady state, and that the free expansion rate of the plasma is about 5 s. Similar methods were used to measure the lifetime of plasmas (without RW compression) in each of the off-axis cells for a range of plasma parameters. In cell A and cell B, the measured lifetime was ~ 15 s; in cell C, $\sim 5-10$ s; and in cell D, < 1 s.

A few conclusions can be made here. Since cells A and B (which have the same wall radius) show similar transport properties, the transport does not seem to be any worse for the off-axis cell. However, the transport does depend strongly on the radius of the cell (i.e., for a fixed plasma radius), specifically the transport is much more rapid in the smallest cell (cell D) than in the others. When the RW is used to counter the expansion, plasmas can be stored without particle loss in cells A and B for over a day. Similarly, plasmas were held in cell C without loss for about two hours, although this is likely not the limit. However, the transport in cell D was so rapid that the RW method was unable to counter the expansion, thus plasmas could not be held in cell D for longer than about 1 s.

A.7 High-voltage experiments

All of the experiments discussed in this dissertation use axial confinement voltages of $V_c = -100$ V, except for the experiments presented in this section. Since the goal is

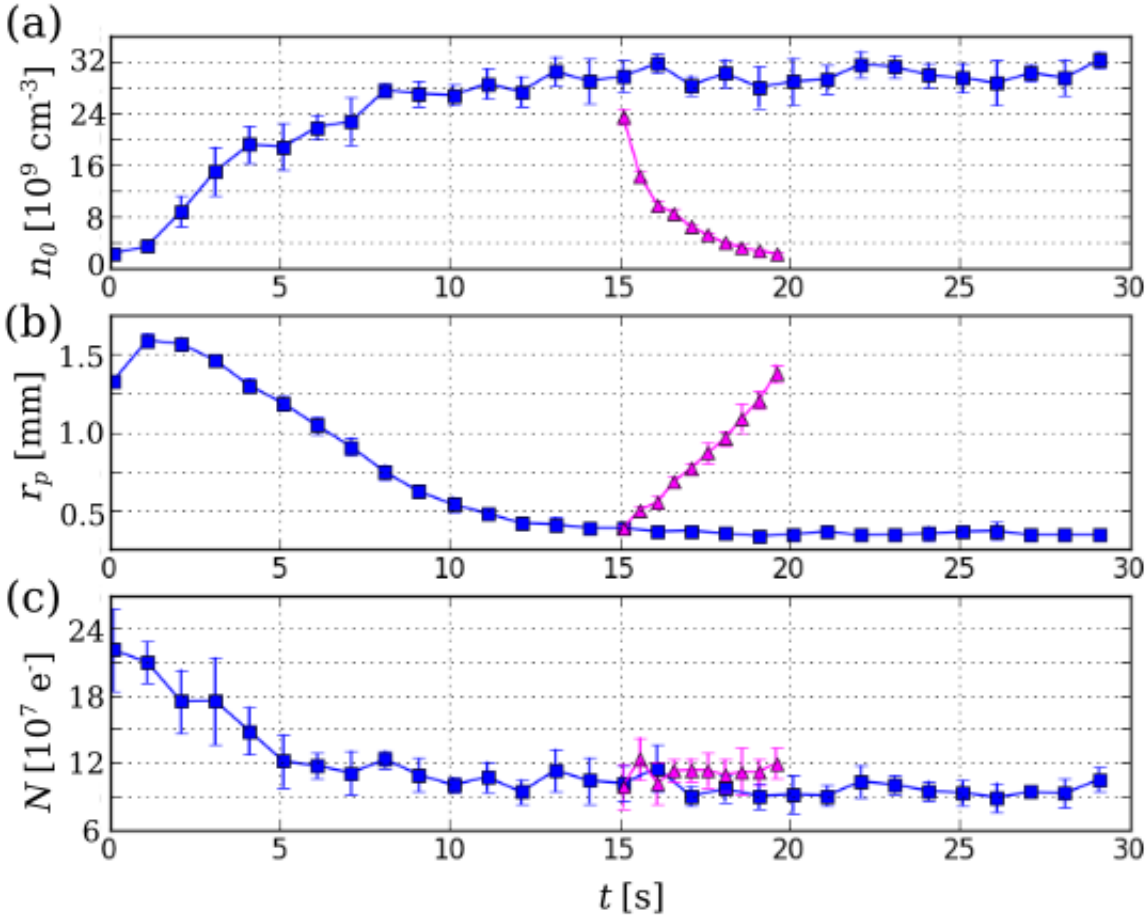

Figure A.13: Data showing the RW compression and free expansion of an off-axis plasma. (a) evolution of the peak density for a plasma under RW compression (blue), and one where the RW is turned off at $t = 15$ s (magenta); (b) plasma radius; (c) total particle number. The data are taken in cell C, and the free expansion time is found to be ~ 5 s.

to maximize the trap capacity, the confining potential well should be as deep as possible. Therefore, experiments were performed in cell A where the confinement voltages were chosen to be $V_c = -1$ kV. The main goal of these experiments was to study the fill process and the confinement properties of plasmas with $\sim$ kV space charge.

In order to generate kV plasmas, electrodes A1 and A6 were connected to specialized power supplies capable of producing ± 2 kV voltages which could be varied quickly. Electrodes A2-A5 were connected to a third power supply. The fill procedure was identical to that described above, except that the interior electrodes were biased to the "well" voltage V_w. At some time, the beam was blocked to stop the filling, and electrodes A1 and A6 were raised to $V_c = -1$ kV. Shortly thereafter, electrodes A2-A5 were raised to ground. Then, the plasma was imaged by grounding electrode A6.

Data are shown in Fig. A.14 for the radial density profile of plasmas during the fill process, and during subsequent free relaxation, for well depths of $V_w = 0$, 0.5, and 1 kV. For $V_w = 0$ V, the fill and relaxation proceeds as usual, where asymmetry-induced transport drives a flux of particles to the wall on a ~ 10 s timescale. For $V_w = 0.5$ kV, the transport is strong enough that a particle flux to the wall develops during the fill process, and continues after the fill has concluded. For $V_w = 1$ kV, interesting behavior is observed. Here, the plasma again develops a flux to the wall during the fill. However, after the fill is concluded, the plasma maintains a steady state profile reaching all the way to the wall. At lower V_w, the profiles decayed as particles were absorbed by the wall, but here the profile is static. Figure A.15 shows the total particle number during the fill and relaxation periods for different well depths. The cases with $V_w \leq 0.5$ kV show decay at late times as particles are absorbed by

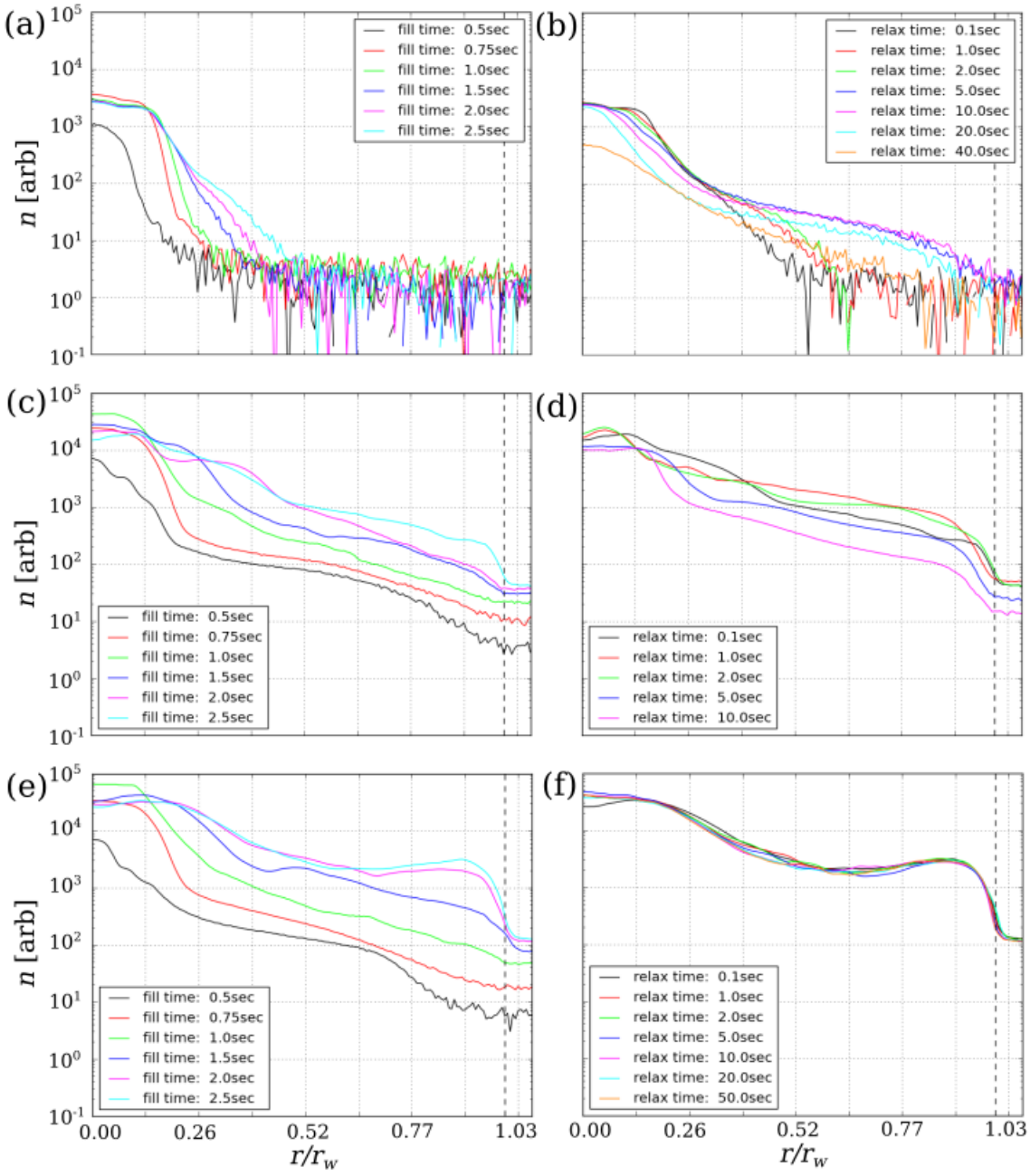

Figure A.14: Radial profiles of high-voltage plasmas during filling and relaxation. Panels (a) and (b) correspond to $V_w = 0$ V, (c) and (d) to $V_w = 0.5$ kV, and (e) and (f) to $V_w = 1$ kV. The left column shows the profile evolution over 2.5 s of filling; the right column shows the subsequent free relaxation of these profiles. The wall radius is indicated by a dashed line.

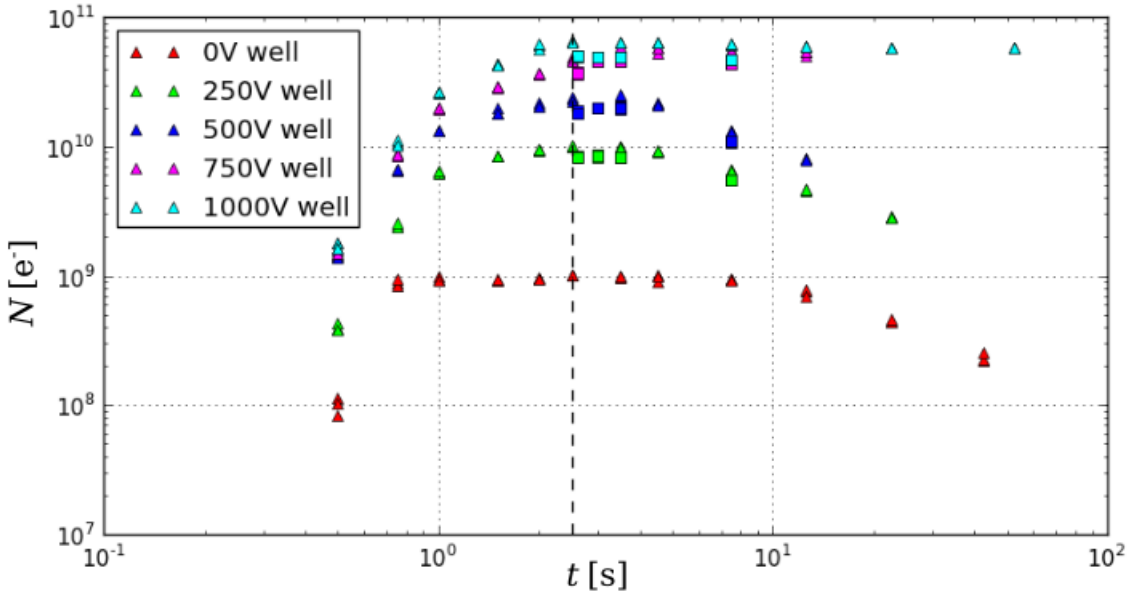

Figure A.15: Evolution of trapped particle number for high-voltage plasmas. Measurements of N are shown for plasmas with $V_w = 0$, 0.25, 0.5, 0.75, and 1 kV. The fill proceeds for 2.5 s, up to the dashed line; afterwards, the plasma is allowed to freely relax. For $V_w =$ 0.75 and 1 kV, the plasma develops a steady state where $N \approx$ constant.

the wall; the cases $V_w = 0.75$ and 1 kV show a static particle number at late times. Other experiments were performed where the $m = 1$ diocotron signal was monitored as a gauge of the plasma state over long time periods, showing that the plasma maintained the steady state for at least an hour.

Since these steady profiles extend all the way to the wall, it is clear that there must be a particle flux to the wall. This implies that, in order to maintain the steady profile, there must also be a source of electrons. Although this phenomenon was not studied in greater detail, our hypothesis is that the plasma was continuously resupplied with electrons by ionizing the background neutral gas in the vacuum chamber. Generally, at low confinement voltages $V_c = -100$ V, the plasma often cools to a temperature $T < 1$ eV due to cyclotron radiation. However, with $V_c \sim 1$ kV and N approaching 10^{11}, the radial transport rate is

much higher. As electrons move outward in radius, electrostatic energy is liberated, which heats the plasma. The hot plasma in turn can ionize the background gas, providing a source of electrons. The potential well is filled by these electrons until the well is filled (i.e., the plasma space charge potential is equal to V_c). The ions, presumably, are accelerated by the negative endcap potentials, where they can either become trapped, or ejected from the system along the magnetic field. When the potential well was full, a flux of electrons onto the phosphor screen was observed during the steady state, showing that electrons were lost axially through the confinement electrodes, as well as radially to the wall.

Further insight can be gained by studying the spatial density distribution during the steady state discharge. CCD images are shown in Fig. A.16 for plasmas with $V_w = 0.25$ kV (left) and 0.75 kV (right), after 2 s of filling (top) and after 2.5 s of filling and 2 s of free relaxation (bottom). Whereas Fig. A.14 shows the evolution of azimuthally averaged radial density profiles, Fig. A.16 shows that the plasmas feature non-axisymmetric structures. For example, in Fig. A.16 (a), a clear $m = 4$ mode is observed, whereas the structures are more complicated in the other images. These data indicate that the radial transport may be occuring due to the growth and breaking of diocotron-like waves on the plasma surface. Thus the transport is somewhat turbulent and fluid-like, rather than diffusive. It is interesting to draw an analogy with the behavior of toroidal fusion plasmas, where radial transport is driven largely by turbulent behavior rather than diffusive processes.

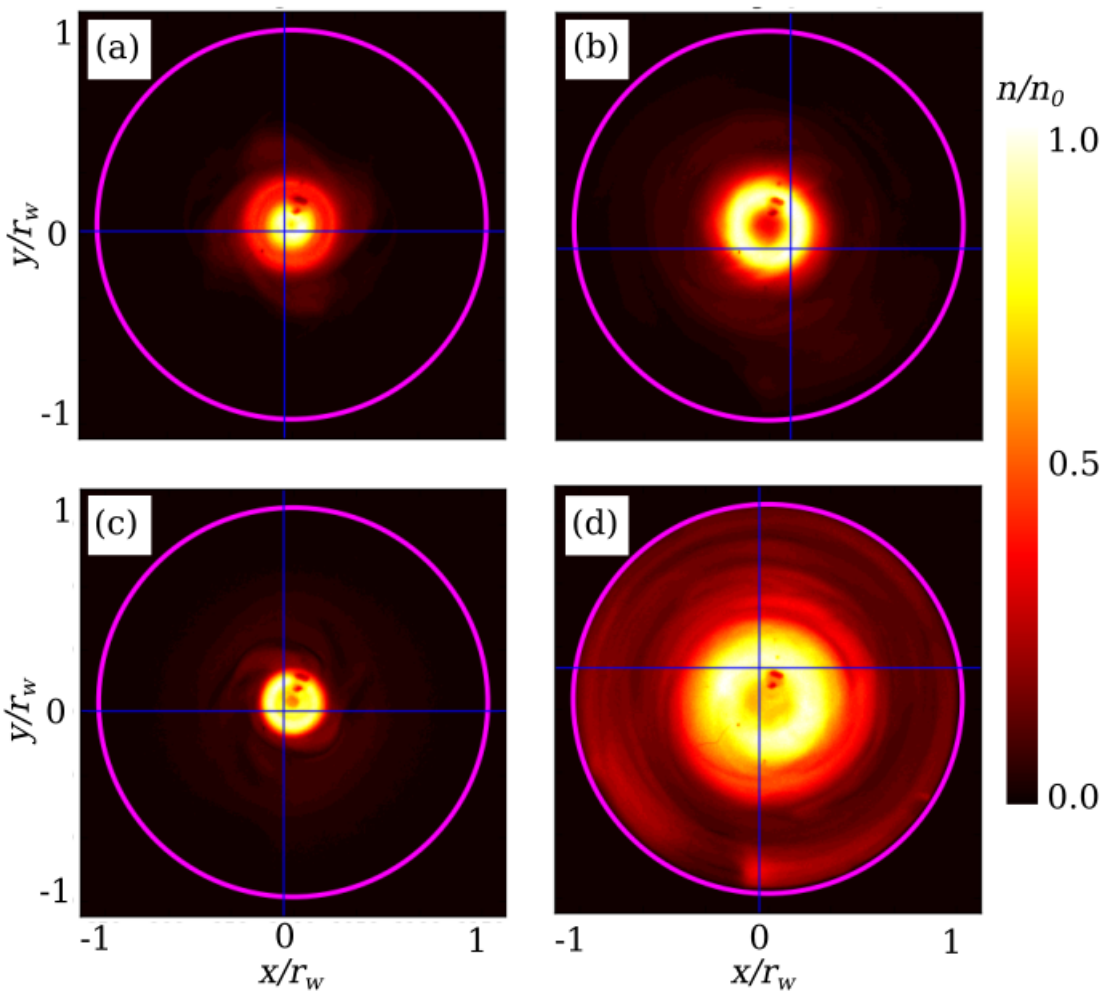

Figure A.16: Images of the electron density distribution of high-voltage plasmas during the fill and relaxation periods. Panels (a) and (c) correspond to $V_w = 0.25$ kV, and panels (b) and (d) to $V_w = 0.75$ kV. Panels (a) and (b) show the density after 2 s of filling; panels (c) and (d) show the density after 2.5 s of filling and 2 s of free relaxation. The dark spot at $(x/r_w, y/r_w) \approx (0.1, 0.1)$ is an artifact due to a defect on the phosphor screen.

A.8 Vortex destruction in the MCT

Reference [25] found an upper limit to the diocotron mode amplitude that could be excited using the autoresonant drive technique. When the plasmas reached $d_m/r_m \sim 0.85$-0.9, they would become deformed and disappear. This process was difficult to diagnose, since the master cell plasmas could only be imaged by passing through the storage cells. We hypothesized that the plasmas were being deformed and destroyed by the electric field due to the autoresonant drive electrode. Although the amplitude of the signal was typically < 5 V, the electric field is concentrated near the gaps between the segmented electrode. Plasmas with large-amplitude diocotron modes pass close by these gaps, and are therefore subject to strong electric fields.

In order to test these ideas, plasmas were trapped in cell A (where the entire density distribution could be diagnosed) and subjected to strong electric fields by biasing one segment of electrode A4 to a positive voltage V_a. These data are shown in Fig. A.17, where the biased electrode is shown in magenta. The outer region of the plasma is stripped away by the $\mathbf{E} \times \mathbf{B}$ drift flow due to the applied electric field. In Fig. A.17 about 20 % of the original particles are lost during the stripping event.

These events are similar to the vortex stripping phenomena which have been observed in laboratory water tanks [21]. However, these plasmas are not well-described as 2D fluids, since the asymmetry potential is applied to a segment which extends only over a portion of the plasma length. It was found that the asymmetry potential gave rise to axial trapping of plasma particles. For example, with $V_a > 0$, the plasma particles were divided

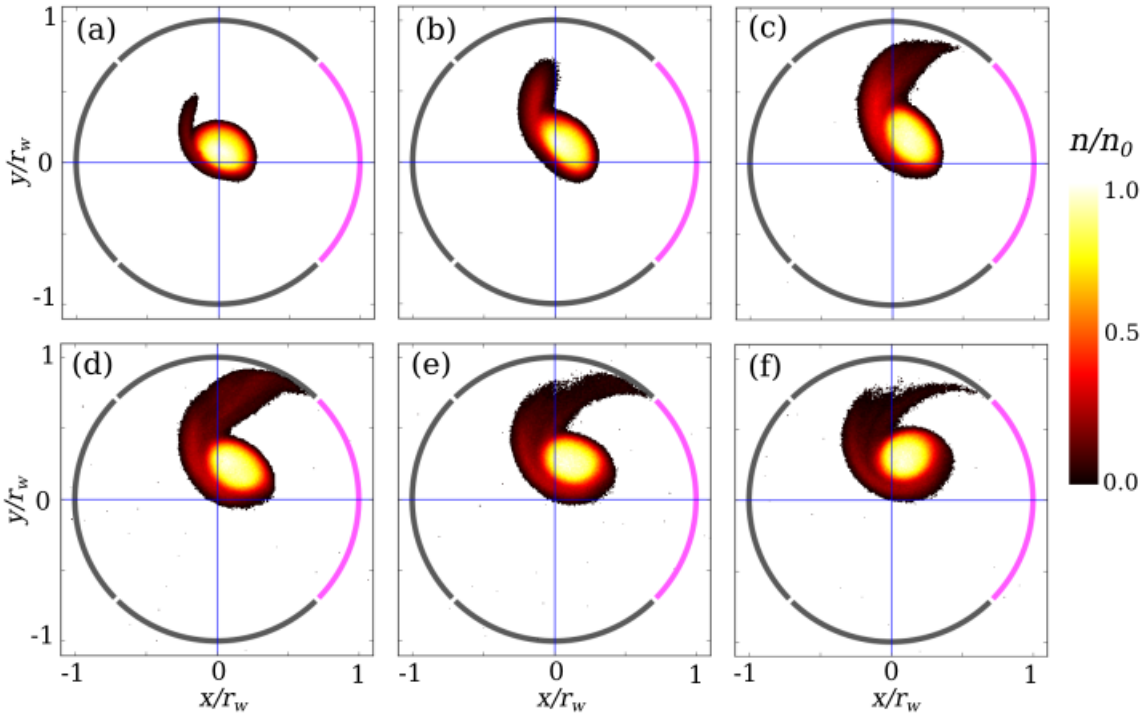

Figure A.17: Stripping of a plasma in the MCT due to an applied asymmetric potential. Electron density maps are shown at times $t = 2$, 8, 14, 20, 26, and 32 μs (a)-(f) when a constant voltage is applied to one segment (magenta) of electrode A4. This and other data provided the motivation for the 8ST device.

into two populations, those trapped axially under the electrode A4, and those confined between electrodes A1 and A6 (i.e., passing particles). The passing particles experienced a much weaker electric field than the trapped particles due to bounce-averaging; therefore, the trapped plasma could be heavily deformed or destroyed, while the passing plasma was just weakly deformed. When $V_a < 0$, particles could be excluded from electrode A4 altogether, and thus the asymmetry potential had little effect. Other experiments were done where the segments of electrode A4 were biased in a quadrupole pattern, generating a simple strain flow (as discussed in the body of the dissertation). In this way, the $m = 0$ component of the asymmetric potential was zero, so particles on the trap axis would not experience axial trapping. However, trapping effects were still observed for off-axis particles.

Due to these 3D effects, we were unable to develop a theoretical model which could quantitatively describe the behavior. Therefore, a new set of electrodes was designed and built, where the segmented electrode was made to be long in order to study pure 2D fluid physics with external flows – the 8ST. The data in Chapter 4 are generally in quantitative agreement with 2D fluid theory, thus the 8ST design is sufficient to avoid the 3D effects from which the MCT "vortex" experiments suffered.

A.9 Summary and Conclusions

A series of experiments were conducted with the MCT electron plasma confinement device, in order to study the feasibility of trapping large numbers of charged particles in a

set of small, parallel PM traps. In order to trap plasmas in off-axis cells, plasmas must first be generated in the master cell, compressed using the RW technique, displaced off-axis in the master using the autoresonant diocotron drive, transferred axially into the storage cell, and finally compressed and held in the storage cell using the RW. Each of these steps was studied in detail, and interesting physical processes were observed during each step.

When filling plasma into the master cell, it was found that early in the fill process, the plasma was pinned to the location of the incoming beam. When the plasma developed a sufficiently large particle number, it decoupled from the beam. When transferring plasma into the on-axis cell (cell A), it was found that the plasma developed a collisionless steady state where the plasma density in the storage cell was reduced due to anti-shielding. This density could be adjusted by applying a uniform potential to the storage cell electrodes. On longer timescales, the storage cell density during the transfer increased due to collisional effects.

During the autoresonant diocotron excitation, it was observed that the plasma expanded significantly, and was eventually destroyed upon reaching displacements of $d_m/r_m \sim 0.9$. Moreover, the observed diocotron mode frequency was not in agreement with any known theory, so a numerical model was constructed which accurately predicts the frequency. When plasmas were transferred into the off-axis cells, they performed quasi-elliptical bounce-average orbits due to the differing electric fields in the master and storage cells. These bounce-average plasmas could also be held in stationary states by positioning them at a stationary point where the master and storage cell drifts cancel.

It was determined that, without using the RW technique to counter expansion, the

lifetime of plasmas in the storage cells was about 15 s in cells A and B ($r_w = 8$ mm), 5-10 s in cell C ($r_w = 6$ mm), and < 1 s in cell D ($r_w = 4$ mm). With the RW, plasmas could be confined more or less indefinitely in cells A, B, and C; however in cell D, the expansion was too rapid and could not be countered with the RW. Experiments with kilovolt confinement potentials in cell A showed that the expansion rate was so large that the plasma heated and ultimately ionized the background neutral gas.

Future attempts to develop multi-cell PM trap devices should consider these results and adapt the design accordingly. The plasma manipulation techniques have been shown to work, including on-axis and off-axis transfers and the autoresonant diocotron excitation; although care must be taken to properly compress the plasma using the RW technique, and to minimize the expansion during other stages. According to the data presented here, the primary problem with operation a multi-cell device is the strong radial transport which is observed at large particle number N, and at large scaled plasma radius r_p/r_w. In the regime of kilovolt plasma potentials, the transport may be too strong to counteract with the RW. The same is true for small-radius traps such as cell D.

Best practices in order to reduce the radial transport are two-fold. First, the plasmas must be compressed to a small radius relative to the trap dimensions, ideally $r_p/r_w \lesssim 0.2$. The extent to which the plasma can be compressed will dictate the wall radius needed for successful containment. Secondly, the transport can be minimized by carefully designing the trap(s) to obtain a high degree of symmetry. Details of the MCT storage cell construction resulted in cells which were slightly distorted from the ideal cylindrical geometry; this is thought to have driven much of the observed transport. This could be avoided with a

more robust trap design.

Finally, experiments were conducted in the MCT demonstrating the stripping and destruction of electron plasmas in response to applied asymmetric potentials. These experiments were subject to 3D effects, which complicated the dynamics. This motivated the design and construction of the 8ST, where experiments could be conducted purely in 2D.

Appendix B

List of mathematical symbols

Given in Tbl. B.1 is a list of mathematical symbols and abbreviations used in the dissertation, and a brief description of each. They are organized approximately in order of appearance.

Table B.1: List of mathematical symbols and abbreviations.

Symbol	Description
$\mathbf{v}$	Fluid velocity
ρ	Fluid mass density
p	Fluid pressure
ω	Scalar fluid vorticity in 2D
ψ	Fluid stream function
Continued on next page	

Table B.1 – continued from previous page

Symbol	Description
PM	Penning-Malmberg trap (non-neutral plasma device)
E	Electric field
B	Magnetic field
Re	Reynolds number
ν	Kinematic viscosity
ω_0	Peak (central) vorticity
ε	Strain rate
ε^*	Strain rate normalized to peak vorticity
PV, ζ	Potential Vorticity
β	Coriolis parameter
m	Azimuthal wavenumber
MS71	A scientific paper by Moore and Saffman, 1971 [8]
K81	A scientific paper by Kida, 1981 [39]
N	Total number of particles
VIC	Vortex-In-Cell (numerical point-vortex method)
ϕ	Electric potential
T	Plasma temperature
r_g	Electron gyroradius

Continued on next page

Table B.1 – continued from previous page

Symbol	Description
e	Electron charge
m_e	Electron mass
v_T	Thermal velocity
n	Electron density
ε_0	Permittivity of free space
r_v	Vortex radius
f_v	Vortex rotation frequency
f_b	Axial bounce frequency
L	Plasma length
r_w	Wall radius
H	Hamiltonian (system energy)
ϕ_s	Vacuum potential in 2D (due to boundary conditions)
p_θ	Canonical angular momentum
(x, y)	Cartesian coordinates
(r, θ)	Polar coordinates
8ST	Eight-Segment Trap (PM trap device for fluid experiments)
δB	Magnetic field variation
V_c	Axial confinement voltage

Continued on next page

Table B.1 – continued from previous page

Symbol	Description
RW	Rotating Wall (method for compressing non-neutral plasmas)
n_0	Peak (central) density
SNR	Signal to Noise Ratio
A_m, B_m	Vacuum potential expansion coefficients
V_a	Asymmetry voltage
V_l	Lip voltage (used during plasma filling process)
V_e	Electron source voltage
f_w	Rotating wall frequency
τ_c	Cyclotron cooling time ($\sim$ 150 ms for $B = 4.8$ T)
s	Magnitude of eigenvalues of strain tensor
Q	Okubo-Weiss parameter
α	Profile smoothness exponent
Γ	Circulation
a, b	Semimajor and semiminor axis of ellipse
λ	Aspect ratio of ellipse
ξ	Orientation of ellipse semimajor axis
ψ_v	Stream function associated with vorticity
ψ_s	Stream function associated with boundary conditions

Continued on next page

Table B.1 – continued from previous page

Symbol	Description
σ	Strain tensor
Ω	Vorticity tensor
s^*	Normalized local strain
C	Integration constant, K81 initial condition
(p,q)	Ellipse canonical variables
(λ_0,ξ_0)	Fixed points of K81 system
ε_c^*	Critical strain (equilibrium)
ε_d^*	Critical strain (dynamical)
λ_m	Maximum aspect ratio during a K81 orbit
J	Action associated with a K81 orbit (also, the Jacobian operator)
t_0	Time parameter for time-dependent strain flows
τ_s	Pulse width parameter for time-dependent strain flows
ε_0	Amplitude of time-dependent strain flow
KH	Kelvin-Helmholtz (shear instability)
η	Growth rate for Love and KH instabilities
k	Cartesian wavenumber
(x_0,y_0)	Stagnation points
s_v	Self-strain (generated by a distorted vortex)

Continued on next page

Table B.1 – continued from previous page

Symbol	Description
τ	Vortex stretching rate
Γ_0	Circulation integrated across the domain
Γ_{sep}	Circulation inside the stream function separatrix
Γ_Q	Circulation inside the Okubo-Weiss stable region
Q_0^*	Normalized Okubo-Weiss parameter evaluated at the origin
Γ_f	Final circulation remaining after a straining event
t_f	Total duration of a time-dependent strain flow
Ω_s	Frequency of a harmonic time-dependent strain flow
N_d	Number of daughter vortices resulting from an instability
τ_v	Vortex rotation period
ϕ_0	On-axis space charge potential
r_p	Plasma radius
MCT	Multi-Cell Trap (PM trap device with multiple cells)
$E_\perp$	Perpendicular energy
Γ_p	Circulation associated with a point plasma
Γ_b	Circulation associated with a beam
x_b	Location where the beam enters the master cell
N_0	Initial particle number of plasma

Continued on next page

Table B.1 – continued from previous page

Symbol	Description
N_m, N_s	Number of particles in the master, storage cell
$v_{\|\|}$	Parallel velocity
γ_m, γ_s	Geometric factor in the space charge formula
ϕ_m, ϕ_s	Space charge potential inside the master, storage cell
V_s	Uniform voltage applied to storage cell electrodes
f_d	$m = 1$ diocotron frequency
d_m, d_s	Radial plasma displacement in the master and storage cells
κ	Ratio of master cell drift to storage cell drift (bounce-average orbits)
V_w	Positive well voltage used for generating high-voltage plasmas
V_a	Asymmetry voltage used for MCT “vortex” experiments

Bibliography

[1] G. A. Tokaty. A History and Philosophy of Fluid Mechanics. Dover Publications, Inc. (New York), 1971.

[2] L. Euler. Principes generaux du mouvement des fluides. *Memoires de l'academie des sciences de Berlin*, 11:274–315, 1757.

[3] L. Landau and E. Lifschitz. Fluid Mechanics. Pergamon Press, 1959.

[4] P. Tabeling. Two-dimensional turbulence: a physicist approach. *Phys. Reports*, 362:1–62, 2002.

[5] J. C. McWilliams. The emergence of isolated coherent vortices in turbulent flow. *J. Fluid Mech.*, 146:21–43, 1984.

[6] A. Andersen, T. Bohr, B. Stenum, and J. Juul Rasmussen. The bathtub vortex in a rotating container. *J. Fluid Mech.*, 556:121–146, 2006.

[7] A. J. Charlton, A. O'Neill, W. A. Lahoz, and P. Berrisford. The splitting of the stratospheric polar vortex in the southern hemisphere, september 2002: Dynamical evolution. *J. Atmos. Sci.*, 62:590–602, 2005.

[8] D. W. Moore and P. G. Saffman. Structure of a line vortex in an imposed strain. In M. Rogers J. H. Olsen, A. Goldburg, editor, *Aircraft wake turbulence and its detection*, pages 339–354. Plenum Press, New York, 1971.

[9] P. G. Saffman. Vortex Dynamics. Cambridge University Press, 1992.

[10] M. V. Melander, J. C. McWilliams, and N. J. Zabusky. Axisymmetrization and vorticity-gradient intensification of an isolated two-dimensional vortex through filamentation. *J. Fluid Mech.*, 178:137–159, 1987.

[11] D. Montgomery and L. Turner. Two-dimensional electrostatic turbulence with variable density and pressure. *Phys. Fluids*, 23:2:264–268, 1980.

[12] A. Hasegawa and K. Mima. Pseudo-three-dimensional turbulence in magnetized nonuniform plasma. *Phys. Fluids*, 21:87:87–92, 1978.

[13] P. W. Terry. Suppression of turbulence and transport by sheared flow. *Rev. Mod. Phys.*, 72:1:109–165, 2000.

[14] A. J. Cerfon. Vortex dynamics and shear-layer instability in high-intensity cyclotrons. *Phys. Rev. Lett.*, 116:174801, 2016.

[15] R. C. Davidson. Physics of Nonneutral Plasmas. Addison-Wesley, Redwood City, CA, 1990.

[16] R. H. Levy. Diocotron instability in a cylindrical geometry. *Phys. Fluids*, 8:7:1288–1295, 1965.

[17] C. F. Driscoll and K. S. Fine. Experiments on vortex dynamics in pure electron plasmas. *Phys. Fluids B*, 2:1359–1366, 1990.

[18] T. M. O'Neil. Trapped plasmas with a single sign of charge (from coulomb crystals to 2d turbulence and vortex dynamics). *Phys. Today*, 52:24:24–30, 1999.

[19] F. F. Chen. Introduction to plasma physics and controlled fusion, 2nd ed. Plenum Press, New York, 1984.

[20] Y. D. Afanasyev, P. B. Rhines, and E. G. Lindahl. Velocity and potential vorticity fields measured by altimetric imaging velocimetry in the rotating fluid. *Exp. in Fluids*, 47:913, 2009.

[21] R. R. Trieling, M. Beckers, and G. J. F. Van Heijst. Dynamics of monopolar vortices in a strain flow. *J. Fluid Mech.*, 345:165–201, 1997.

[22] R. Salmon. Lectures on Geophysical Fluid Dynamics. Oxford University Press (New York), 1998.

[23] J. M. Kriesel and C. F. Driscoll. Measurements of viscosity in pure-electron plasmas. *Phys. Rev. Lett.*, 87:135003, 2001.

[24] J. R. Danielson, C. M. Surko, and T. M. O'Neil. High-density fixed point for radially compressed single-component plasmas. *Phys. Rev. Lett.*, 99:135005, 2007.

[25] C. J. Baker, J. R. Danielson, N. C. Hurst, and C. M. Surko. Electron plasma dynamics during autoresonant excitation of the diocotron mode. *Phys. Plasmas*, 22:022302, 2015.

[26] C. A. Kapetanakos and A. W. Trivelpiece. Diagnostics of non-neutral plasmas using an induced-current electrostatic probe. *J. Appl. Phys.*, 42:12:4841 –4847, 1971.

[27] D. G. Dritschel and B. Legras. Modeling oceanic and atmospheric vortices. *Phys. Today*, 46:3:44–51, 1993.

[28] E. A. Spiegel and J. P. Zahn. The solar tachocline. *Astronomy and Astrophysics*, 265:1:106–114, 1992.

[29] A. Adams, P. M. Chesler, and H. Liu. Holographic turbulence. *Phys. Rev. Lett.*, 112:151602, 2014.

[30] P. B. Rhines. Waves and turbulence on a beta-plane. *J. Fluid Mech.*, 69:3:417–443, 1975.

[31] R. V. E. Lovelace, H. Li, S. A. Colgate, and A. F. Nelson. Rossby wave instability of keplerian accretion disks. *Astrophys. Journal*, 513:805–810, 1999.

[32] J. Binney and S. Tremaine. Galactic Dynamics. Princeton University Press, 2008.

[33] Y. Lithwick. Nonlinear evolution of hydrodynamical shear flows in two dimensions. *Astrophys. Journal*, 670:789–804, 2007.

[34] Y. Lithwick. Formation, survival, and destruction of vortices in accretion disks. *Astrophys. Journal*, 693:1:85–96, 2009.

[35] P. Godon and M. Livio. Vortices in protoplanetary disks. *Astrophys. Journal*, 523:1:350–356, 1999.

[36] P. Manz, M. Ramisch, and U. Stroth. Physical mechanism behind zonal-flow generation in drift-wave turbulence. *Phys. Rev. Lett.*, 103:165004, 2009.

[37] G. A. Voth, G. Haller, and J. P. Gollub. Experimental measurements of stretching fields in fluid mixing. *Phys. Rev. Lett.*, 88:25:254501, 2002.

[38] H. Lamb. Hydrodynamics. Cambridge University Press, 1932.

[39] S. Kida. Motion of an elliptic vortex in a uniform shear flow. *J. Phys. Soc. Japan*, 50:10:3517–3520, 1981.

[40] M. V. Melander, N. J. Zabusky, and A. S. Styczek. A moment model for vortex interactions of the two-dimensional euler equations. part 1. computational validation of a hamiltonian elliptical representation. *J. Fluid Mech.*, 167:95–115, 1986.

[41] P. J. Morrison. Hamiltonian description of the ideal fluid. *Rev. Mod. Phys.*, 70:2:467–521, 1998.

[42] J. F. Lingevitch and A. J. Bernoff. Distortion and evolution of a localized vortex in an irrotational flow. *Phys. Fluids*, 7:5:1015–1026, 1995.

[43] N. J. Balmforth, S. G. L. Smith, and W. R. Young. Disturbing vortices. *J. Fluid Mech.*, 426:95–133, 2001.

[44] D. A. Schecter, D. H. E. Dubin, A. C. Cass, C. F. Driscoll, I. M. Lansky, and T. M. O'Neil. Inviscid damping of asymmetries on a two-dimensional vortex. *Phys. Fluids*, 12:10:2397–2412, 2000.

[45] J. C. R. Hunt and D. J. Carruthers. Rapid distortion theory and the 'problems' of turbulence. *J. Fluid Mech.*, 212:497–532, 1990.

[46] A. Okubo. Horizontal dispersion of floatable particles in the vicinity of velocity singularities such as convergences. *Deep Sea Research and Oceanographic Abstracts*, 17:3:445–454, 1970.

[47] J. Weiss. The dynamics of enstrophy transfer in two-dimensional hydrodynamics. *Physica D*, 48:273–294, 1991.

[48] C. Basdevant and T. Philipovitch. On the validity of the "weiss criterion" in two-dimensional turbulence. *Physica D*, 73:17–30, 1970.

[49] B. L. Hua and P. Klein. An exact criterion for the stirring properties of nearly two-dimensional turbulence. *Physica D*, 113:98–110, 1998.

[50] G. Haller. An objective definition of a vortex. *J. Fluid Mech.*, 525:1–26, 2005.

[51] L. M. Polvani and G. R. Flierl. Generalized kirchoff vortices. *Phys. Fluids*, 29:2376–2379, 1986.

[52] B. Legras and D. Dritschel. Vortex stripping and the generation of high vorticity gradients in two-dimensional flows. *Appl. Sci. Research*, 51:445–455, 1993.

[53] N. J. Zabusky. Contour dynamics for the euler equations in two dimensions. *J. Comp. Phys.*, 30:1:96–106, 1979.

[54] A. Mariotti, B. Legras, and D. G. Dritschel. Vortex stripping and the erosion of coherent structures in two-dimensional flows. *Phys. Fluids*, 6:12:3954–3962, 1994.

[55] D. G. Dritschel. Contour dynamics and contour surgery: numerical algorithms for extended, high-resolution modelling of vortex dynamics in two dimensional, inviscid, incompressible flows. *Comp. Phys. Reports*, 10:77–146, 1989.

[56] J. Goodman, T. Y. Hou, and J. Lowengrub. Convergence of the point vortex method for the 2-D Euler equations. In *Communications on Pure and Applied Mathematics, Vol. XLIII*. John Wiley and Sons, Inc., 1990.

[57] H. Aref. Chaos in the dynamics of a few vortices - fundamentals and applications. In F. I. Niordson and N. Olhoff, editors, *Theoretical and Applied Mechanics.*, pages 43–68. Elsevier Science Publishers B. V. (North-Holland), 1985.

[58] A. Leonard. Vortex methods for flow simulation. *J. Comp. Phys.*, 37:3:289–335, 1980.

[59] O. Paireau, P. Tabeling, and B. Legras. A vortex subjected to a shear: an experimental study. *J. Fluid Mech.*, 351:1–16, 1997.

[60] M. A. Rutgers, X. L. Wu, and W. B. Daniel. Conducting fluid dynamics experiments with vertically falling soap films. *Rev. Sci. Instruments*, 72:7:3025–3037, 2001.

[61] K. S. Fine, C. F. Driscoll, J. H. Malmberg, and T. B. Mitchell. Measurements of symmetric vortex merger. *Phys. Rev. Lett.*, 67:5:588–591, 1991.

[62] T. B. Mitchell and C. F. Driscoll. Electron vortex orbits and merger. *Phys. Fluids*, 8:7:1828–1841, 1996.

[63] M. Amoretti, D. Durkin, J. Fajans, R. Pozzoli, and M. Rome. Asymmetric vortex merger: Experiments and simulations. *Phys. Plasmas*, 8:9:3865–3868, 2001.

[64] Y. Soga, Y. Kiwamoto, A. Sanpei, and J. Aoki. Merger and binary structure formation of two discrete vortices in a background vorticity distribution of a pure electron plasma. *Phys. Plasmas*, 10:3922, 2003.

[65] K. S. Fine, A. C. Cass, W. G. Flynn, and C. F. Driscoll. Relaxation of 2d turbulence to vortex crystals. *Phys. Rev. Lett.*, 75:18:3277–3280, 1995.

[66] D. A. Schecter, D. H. E. Dubin, K. S. Fine, and C. F. Driscoll. Vortex crystals from 2d euler flow: Experiment and simulation. *Phys. Fluids*, 11:4:905–914, 1999.

[67] Y. Kiwamoto, N. Hashizume, Y. Soga, J. Aoki, and Y. Kawai. Formation and relaxation of two-dimensional vortex crystals in a magnetized pure-electron plasma. *Phys. Rev. Lett.*, 99:115002, 2007.

[68] D. Durkin and J. Fajans. Experiments on two-dimensional vortex patterns. *Phys. Fluids*, 12:2:289–293, 2000.

[69] Y. Kawai, Y. Kiwamoto, Y. Soga, and J. Aoki. Turbulent cascade in vortex dynamics of magnetized pure electron plasmas. *Phys. Rev. E*, 75:066404, 2007.

[70] F. Lepreti, M. Rome, G. Maero, B. Paroli, R. Pozzoli, and V. Carbone. Scaling properties and intermittency of two-dimensional turbulence in pure electron plasmas. *Phys. Rev. E*, 87:063110, 2013.

[71] X. P. Huang and C. F. Driscoll. Relaxation of 2d turbulence to a meta-equilibrium near the minimum enstrophy state. *Phys. Rev. Lett.*, 72:14:2187–2190, 1994.

[72] D. J. rodgers, S. Servidio, W. H. Matthaeus, D. C. Montgomery, T. B. Mitchell, and T. Aziz. Hydrodynamic relaxation of an electron plasma to a near-maximum entropy state. *Phys. Rev. Lett.*, 102:244501, 2009.

[73] A. J. Peurrung and J. Fajans. Experimental dynamics of an annulus of vorticity in a pure electron plasma. *Phys. Fluids*, 5:2:493–499, 1993.

[74] C. F. Driscoll. Observation of an unstable l=1 diocotron mode on a hollow electron column. *Phys. Rev. Lett.*, 64:6:645–648, 1990.

[75] R. Chu, J. S. Wurtele, J. Notte, A. J. Peurrung, and J. Fajans. Pure electron plasmas in asymmetric traps. *Phys. Fluids B*, 5:7:2378–2386, 1993.

[76] J. Fajans, E. Yu. Backhaus, and E. Gilson. Bifurcations in elliptical, asymmetric non-neutral plasmas. *Phys. Plasmas*, 7:10:3929–3933, 2000.

[77] S. Chen, G. Maero, and M. Rome. Spectral analysis of forced turbulence in a non-neutral plasma. *J. Plasma Phys.*, 83:3:705830303, 2017.

[78] D. Eggleston. Experimental study of two-dimensional electron vortex dynamics in an applied irrotational shear flow. *Phys. Plasmas.*, 1:12:3850–3856, 1994.

[79] D. H. E. Dubin and T. M. O'Neil. Trapped nonneutral plasmas, liquids, and crystals (the thermal equilibrium states). *Rev. Mod. Phys.*, 71:1:87–172, 1999.

[80] J. R. Danielson, D. H. E. Dubin, R. G. Greaves, and C. M. Surko. Plasma and trap-based techiques for science with positrons. *Rev. Mod. Phys.*, 87:1:247–306, 2015.

[81] D. H. E. Dubin. Collisional transport in non-neutral plasmas. *Phys. Plasmas*, 5:5:1688–1694, 1998.

[82] D. H. E. Dubin. Collisional diffusion in a two-dimensional point vortex gas or a two-dimensional plasma. *Phys. Plasmas*, 10:5:1338–1350, 2003.

[83] N. C. Hurst, J. R. Danielson, D. H. E. Dubin, and C. M. Surko. Evolution of a vortex in a strain flow. *Phys. Rev. Lett.*, 117:235001, 2016.

[84] N. C. Hurst, J. R. Danielson, D. H. E. Dubin, and C. M. Surko. Experimental study of the stability and dynamics of a 2d ideal vortex under external strain. *Submitted to J. Fluid Mech.*, 2018.

[85] N. C. Hurst, J. R. Danielson, C. J. Baker, and C. M. Surko. Electron plasma orbits from competing diocotron drifts. *Phys. Rev. Lett.*, 113:025004, 2014.

[86] T. Mohamed, H. Imao, N. Oshima, A. Mohri, and Y. Yamazaki. Fast electron accumulation and its mechanism in a harmonic trap under ultrahigh vacuum conditions. *Phys. Plasmas*, 18:3:032507, 2011.

[87] T. M. O'Neil. Cooling of a pure electron plasma by cyclotron radiation. *Phys. Fluids*, 23:4:725–731, 1980.

[88] T. M. O'Neil. A confinement theorem for nonneutral plasmas. *Phys. Fluids*, 23:11:2216–2218, 1980.

[89] J. M. Kriesel and C. F. Driscoll. Two regimes of asymmetry-induced transport in non-neutral plasmas. *Phys. Rev. Lett.*, 85:12:2510–2513, 2000.

[90] A. J. Majda and A. L. Bertozzi. Vorticity and incompressible flow. Cambridge University Press, 2002.

[91] Sir William Thomson. Vibrations of a columnar vortex. *The London, Edinburgh, and Dublin Philosophical Magazine and Journal of Science*, 10:61:155–168, 1880.

[92] S. P. Meacham, P. J. Morrison, and G. R. Flierl. Hamiltonian moment reduction for describing vortices in shear. *Phys. Fluids*, 9:8:2310–2328, 1997.

[93] J. Vanneste and W. R. Young. On the energy of elliptical vortices. *Phys. Fluids*, 22:081701, 2010.

[94] E. Yu. Backhaus, J. Fajans, and J. S. Wurtele. Stability of highly asymmetric non-neutral plasmas. *Phys. Plasmas*, 6:1:19–30, 1999.

[95] A. Crosby, E. R. Johnson, and P. J. Morrison. Deformation of vortex patches by boundaries. *Phys. Fluids*, 25:023602, 2013.

[96] J. Notte, J. Fajans, R. Chu, and J. S. Wurtele. Experimental breaking of an adiabatic invariant. *Phys. Rev. Lett.*, 70:25:3900–3903, 1993.

[97] E. A. Ryzhov. Nonlinear dynamics of an elliptic vortex embedded in an oscillatory shear flow. *Chaos*, 27:113101, 2017.

[98] T. B. Mitchell and L. F. Rossi. The evolution of kirchoff elliptic vortices. *Phys. Fluids*, 20:054103, 2008.

[99] D. G. Dritschel, P. H. Haynes, M. N. Juckes, and T. G. Shepherd. The stability of a two-dimensional vorticity filament under uniform strain. *J. Fluid Mech.*, 230:647–665, 1991.

[100] Lord Rayleigh. On the stability, or instability, of certain fluid motions. *Proc. Lond. Math Soc.*, 19:67–74, 1887.

[101] D. G. Dritschel. On the stabilization of a two-dimensional vortex strip by adverse shear. *J. Fluid Mech.*, 206:193–221, 1989.

[102] R. H. Kraichnan. Inertial ranges in two-dimensional turbulence. *Phys. Fluids*, 10:7:1417–1423, 1967.

[103] H. K. Moffatt. The topology of scalar fields in 2D and 3D turbulence. In T. Kambe, T. Nakano, and T. Miyauchi, editors, *IUTAM Symposium on Geometry and Statistics of Turbulence.*, pages 13–22. Kluwer Academic Publishers, 2001.

[104] M. Ghil, T. Ma, and S. Wang. Structural bifurcation of 2-d incompressible flows. *Indiana University Mathematics Journal*, 50:1:159–180, 2001.

[105] D. G. Dritschel. The stability and energetics of corotating uniform vortices. *J. Fluid Mech.*, 157:95–134, 1985.

[106] N. C. Hurst, J. R. Danielson, and C. M. Surko. An electron plasma experiment to study vortex dynamics subject to externally imposed flows. *AIP Conf. Proc.*, 1928:020007, 2018.

[107] P. S. Marcus. Jupiter's great red spot and other vortices. *Annu. Rev. Astron. Astrophys.*, 31:523–573, 1993.

[108] C. M. Surko and R. G. Greaves. A multicell trap to confine large numbers of positrons. *Rad. Phys. and Chem.*, 68:419–425, 2003.

[109] J. R. Danielson, T. R. Weber, and C. M. Surko. Plasma manipulation techniques for positron storage in a multicell trap. *Phys. Plasmas*, 13:123502, 2006.

[110] H. Saitoh, T. S. Pedersen, U. Hergenhahn, E. V. Stenson, N. Paschkowski, and C. Hugenschmidt. Recent status of a positron-electron experiment (apex). *J. Phys. Conf. Ser.*, 505:012045, 2014.

[111] C. M. Surko and R. G. Greaves. Emerging science and technology of antimatter plasmas and trap-based beams. *Phys. Plasmas*, 11:5:2333–2348, 2004.

[112] J. Fajans, E. Gilson, and L. Friedland. Autoresonant (nonstationary) excitation of the diocotron mode in non-neutral plasmas. *Phys. Rev. Lett.*, 82:22:4444–4447, 1999.

[113] E. M. Hollmann, F. Anderegg, and C. F. Driscoll. Confinement and manipulation of non-neutral plasmas using rotating wall electric fields. *Phys. Plasmas*, 7:7:2776–2789, 2000.

[114] C. Hansen and J. Fajans. Dynamic and debye shielding and antishielding in magnetized, collisionless plasmas. *Phys. Rev. Lett.*, 74:21:4209–4212, 1995.

[115] K. S. Fine and C. F. Driscoll. The finite length diocotron mode. *Phys. Plasmas*, 5:3:601–607, 1998.